DEVELOPMENT OF SCANNING ION CONDUCTANCE MICROSCOPY FOR BIOMEDICAL APPLICATIONS

by

Andriy I. Shevchuk M.Sc.

A thesis submitted to the University of London

for the degree of Doctor of Philosophy

Cellular and Molecular Endocrinology Group

Faculty of Medicine

Imperial College London

2003

Abstract

This thesis describes the development of multifunctional high-resolution scanning ion conductance microscopy (SICM) and its application to the study of various living cell properties.

High-resolution imaging of live biological samples, as an extreme example of soft responsive materials, poses a significant technical challenge. A number of microscopy techniques have been developed with the aim of visualizing small biological objects, but few are suitable for live cell imaging. SICM is probably the best method developed to date. Although, since its invention SICM has been adapted for biological experiments a reliable distance control algorithm and methods to simultaneously obtain functional as well as topographic information are still required.

In this study, the SICM scanning procedure was successfully improved with the development of a distance modulated protocol that allowed long-term imaging and the measurement of fast and slow membrane dynamics in living cells. Furthermore, the new robust SICM control system enabled the development of new hybrid techniques which we have called: “scanning surface confocal microscopy” and “scanning patch-clamp” by combining SICM with confocal microscopy and patch-clamp respectively. These new and powerful SICM-based techniques were applied to a wide range of biomedical studies. Scanning surface confocal microscopy was used to study abnormal cardiac myocyte contraction, and test potential anti-arrhythmic drugs. It was also used to image the interaction between fluorescently-labelled virus-like particles and the cell membrane, and follow the process of their internalisation. Scanning patch-clamp enabled recording of ion channels in small cells such as sperm, and subcellular structures such as epithelial microvilli and neural dendrites. In addition, it provided means of mapping of different ion channel distribution in the cell membrane in relation to cell surface topography and studying the role of their distribution in cell functioning.

The results obtained in this study provided new insights into cell function and allowed us to propose potential models of cell behaviour.

Acknowledgements

Thanks go out to following people:

My supervisors, Dr. Yuri Korchev and Prof. Dr. Max J. Lab for their guidance, patience and supervision throughout.

My co-supervisor, Dr. David Klenerman for his constructive suggestions, and critical reading of this thesis.

My supervisors, co-supervisor and Dr. Guy Moss for correcting my English in this thesis.

Dr. Julia Gorelik for her instructions regarding cell culture maintenance and preparation.

The work presented in this thesis is my own, however the majority of the experiments presented here were complex and required gross statistics, so the involvement of more than few people was necessary.

The experiments with new born cardiomyocytes in the study of changes in rat cardiomyocyte contraction and calcium dynamics induced by taurocholate were made in collaboration with Dr. Julia Gorelik. The experiments with adult cardiomyocytes were performed in collaboration with Prof. Dr. Sian E. Harding.

All ion channel studies with a Scanning Patch-Clamp system were performed in collaboration with Dr. Julia Gorelik, Dr. Yuchun Gu and Hilmar A. Spohr.

The study of single virus-like particle entry into a cell was undertaken in collaboration with Dr. Julia Gorelik (Scanning Surface Confocal Microscopy experiments), M. Romalho, Dr. N. Krauzewicz (Fluorescent Microscopy experiments, cells and virus-like particles preparation), Dr. M. Elliott and Dr. C. Lei (Atomic Force Microscopy experiments).

The study of microvillar dynamics was made in collaboration with Dr. Julia Gorelik (Scanning Ion Conductance Microscopy experiments), Gregory I. Frolenkov (Scanning Electron Microscopy experiments).

The experiments with DNA deposition were performed in collaboration with Dr. Andreas Bruckbauer, Dr. Alison M. Rothery and Dr. David Klenerman.

Contents

List of figures

Abbreviations

ADC	Analog to Digital Converter
AFM	Atomic Force Microscopy
DAC	Digital to Analog Converter
DIC	Differential Interference Contrast
DMEM	Dulbecco's Modified Eagle Medium
DNA	Deoxyribonucleic Acid
DPN	Dip-pen Nanolithography
DSP	Digital Signal Processor
EGTA	Ethylene glycol-bis(2-aminoethylether)-N,N,N',N'-tetraacetic acid
ESEM	Environmental Scanning Electron Microscopy
HEPES	N-(2-Hydroxyethyl)piperazine-N'-(2-ethanesulfonic acid); 4-(2-Hydroxyethyl)piperazine-1-ethanesulfonic acid
ID	Inner Diameter
mCP	Microcontact Printing
mFDs	Microfluidic Devices
NEAA	Non-Essential Amino Acids
NMDG	N-Methyl-D-glucamine
NTA	Nitrilotriacetic Acid
OC	Obstetric Cholestasis
OD	Outer Diameter
PCI	Personal Computer Interface
PET	Polyethylene Terephthalate
PSD	Phase Sensitive Detector
SCG	Superior Cervical Ganglion
SCM	Scanning Confocal Microscopy
SECM	Scanning Electrochemical Microscopy
SEM	Scanning Electron Microscopy
SICM	Scanning Ion Conductance Microscopy
SITS	Disodium 4-acetamido-4'-isothiocyanato-stilben-2,2'-disulfonate
SNOM	Scanning Near-Field Optical Microscopy
SP	Set Point

SPM	Scanning Probe Microscopy
SR	Sarcoplasmic Reticulum
SSCM	Scanning Surface Confocal Microscopy
ssDNA	Single-Stranded Deoxyribonucleic Acid
STEM	Scanning Transmission Electron Microscopy
STM	Scanning Tunneling Microscopy
TC	Taurocholate
TEA	Tetraethylammonium Acetate
TEM	Transmission Electron Microscopy
VLP	Virus-Like Particle

Introduction

Observation is the first stage of study; therefore the study of biological cells is impossible with the naked eye due to their small dimensions. Optical microscopy, especially fluorescent microscopy, has proven to be an extremely versatile tool for cell biologists to study live cells. However, its resolution is restricted to the diffraction limit of light and also it provides limited possibilities to visualise cell surface structures and to actively interrogate the sample. In principle, scanning probe microscopy (SPM) techniques, such as atomic force microscopy (AFM) (Binning and Quate, 1986), provide a means of imaging and manipulating objects down to an atomic scale. Unfortunately, in practice their application in the field of biology has been limited to studying various macromolecules deposited on hard surfaces, fixed cell preparations and measurement of adhesion forces (Lesniewska et al., 1998;You and Yu, 1999). This is mainly because of the direct physical contact that scanning probe makes with the sample, which is destructive to soft cell membranes. Scanning near-field optical microscopy (SNOM) (Subramaniam et al., 1998) combines non-invasive imaging light and the high resolution of scanning probe microscopy and potentially should provide a universal imaging tool. Nevertheless, this technique has difficulties in reliably regulating the distance between the scanning probe and the soft and responsive cell surface. Scanning ion conductance microscopy (Hansma et al., 1989) is another representative of the SPM group whose remarkable feature is a scanning algorithm, which, in contrast with other SPM techniques, maintains the working distance between the probe and the sample such that they do not make direct physical contact with each other.

Although since its invention SICM has been adapted for biological experiments (Korchev et al., 1997b;Korchev et al., 1997a) it still requires a reliable scanning algorithm.

This thesis

The work presented in this thesis describes the development of two multifunctional scanning ion conductance microscopes and their application to several cellular studies.

All experiments described in this thesis, except the early stages of modulated control testing and a part of the scanning patch-clamp recordings, were performed on the SICM stage that I have developed.

Most of the results described were published and presented on conferences, so the references will be given where possible.

The first SICM I built was made on the basis of a prototype with the use of similar control hardware and the same major mechanical components, so the home-built current amplifier and general design were the only differences. Then this microscope was equipped with a photomultiplier and two lasers that enabled fluorescent confocal measurements in combination with SICM imaging. Later, for the purpose of electrophysiological studies the home-built current amplifier was replaced with a commercial patch-clamp amplifier. All these modifications made it possible the combination of SICM with major microscopy and electrophysiology techniques to perform exciting experiments such as the study of cardiac myocyte contraction abnormalities caused by diseases and the testing of potential anti-arrhythmic drugs, the mapping of different ion channels distribution and studying the role of their distribution in cell functioning, the imaging of fluorescently-labelled particles, such as virus-like particles, their interaction with the cell membrane and process of particle internalisation and finally the measurement of fast and slow cell membrane dynamics.

With time, partially because of the limitation of the existing microscope control hardware, and partially because of increasing demands due to the expansion of our laboratory, we needed a new microscope. Development and construction of the new SICM was time consuming. It took half a year before the first image with the new microscope was achieved. Since then, we have heavily exploited the new SICM, which is faster because of the new hardware and more flexible because it is easily programmable in comparison with the prototype. With the new microscope we have measured fast microvillar dynamics in living epithelial cells and developed a technique for molecule deposition with sub-micron resolution in an ink-jet printer fashion. Later, a third microscope was built in our laboratory based on the control system that I developed.

Nowadays, researchers around the world show great interest in SICM. As an example, recently one SICM based on the control system that I have developed was

built with our assistance in Department of Cell Physiology, National Institute for Physiological Sciences, Okazaki, Aichi, Japan. Also, during my study we had many visitors in our laboratory that interested in the SICM technique, often discussions resulted in collaborative research projects. Some of our collaborators requested from me a comprehensive description of the SICM setup and principles of its operation because they are not fully described in papers. Because of these requests I decided to dedicate a substantial part of my thesis to the description of the SICM.

Overall structure and objectives of the thesis

This thesis starts with an introductory chapter to various microscopy techniques, their principles of operation and a discussion of their strengths and weaknesses for live cell imaging. As a result of this discussion the major requirements for a live cell imaging technique are determined.

In the second chapter scanning ion conductance microscopy (SICM) is described. This chapter is focused on the key features and the advantages of SICM in comparison with the other microscopy techniques, explaining why SICM is preferable for application to some biological tasks. The chapter is also dedicated to various applications of the SICM with examples provided.

The third chapter presents the first SICM setup that I have developed during this study. Also, a comprehensive description of its architecture is given followed by a chapter on all modifications that I have done to the SICM hardware and software with the aim of improving the scanning protocol and multifunctionality of the system.

The fifth chapter is dedicated to the study of the contracting cardiac myocytes. Obtained results clearly demonstrate the improved scanning abilities of SICM that made possible simultaneous high-resolution contraction amplitude and local calcium transients measurements. The following chapter will show how the improved SICM can be implemented to studying contraction abnormalities caused by diseases and to test potential anti-arrhythmic drugs.

The seventh chapter describes a new Scanning Patch-Clamp technique developed on a basis of combination of SICM and the patch-clamp and its application to the study of ion channels in small cells and sub-cellular structures. The next chapter illustrates how the Scanning Patch-Clamp was utilized to map the distribution of calcium and chloride channels in the cardiac myocyte sarcolemma.

The ninth chapter shows how the virus-like particle entry into a cell can be studied with a new Scanning Surface Confocal Microscopy technique - a combination of SICM and laser scanning confocal microscopy.

The tenth chapter describes the development of the second SICM that I have built in our laboratory. This microscope is equipped with completely new control hardware that I have chosen and software that I have specially written.

The two following chapters present the experiments and results achieved with the second SICM setup. The SICM was applied to the study of fast microvilli dynamics in epithelial cells. The new, improved SICM made if possible to directly measure the important parameters of microvilli such as growth and retraction rate, lifetime etc. for the first time. Also, controlled deposition and printing with different molecules using the SICM scanning micropipette as a delivery tool is shown.

The final chapters summarize the study, making conclusions about the work and suggest future directions.

Chapter 1 Microscopy techniques overview towards imaging of live biological samples

1.1 Introduction

In this chapter different types of microscopy techniques are introduced in the context of their applicability to the study of biological samples. The history of their development is also briefly described. Finally, in this chapter the strengths and weaknesses of various imaging methods are discussed, concluding with the requirements with which the most suitable technique should comply.

1.2 Optical microscopy and its derivatives

The adaptation of an optical microscope and observations made by Leeuwenhoek revolutionized the world of bio-related sciences. His lenses made it possible to study living microorganisms that cannot be seen by the naked eye. Since that time, a large number of different microscopy techniques have been developed. The majority of modern microscopes are relatively complicated instruments with high resolution, and the fact that the optical microscopy is still widely used by scientists demonstrates its usefulness. Furthermore, the optical microscope even became a symbol of science for many years.

What is the key feature that makes the application of the light microscopy to biology so effective? Presumably, it is the possibility to observe living objects in real time and in conditions close to their natural environment, thus making it possible to study their properties, and their behaviour as the result of various stimuli. Such observations are mostly non-perturbative i.e. have no harmful influences on the specimen.

However, there are also problems with the application of optical microscopy to biological samples. In conventional optical microscopy an image is presented due to differences in brightness. This is created by reduction of the light wave amplitude while passing through the light-absorbing and scattering features of the sample. Therefore, if

the sample is relatively transparent, that is often the case in biological preparations, the optical microscope image has poor contrast. Fortunately, although transparent objects have very little effect on the amplitude of the light they do change the light wave's phase by delaying it. This property of a substance can be expressed in terms of the refractive index: that is the ratio of the velocity of the light in a vacuum to its velocity in the substance. It is also the ratio of the sine of the angle of incidence to the sine of the angle of refraction. However, objects with different values of refractive index could not be visualized by the optical microscope since neither the eye nor photograph film can perceive the phase difference.

The effect of refraction was successfully utilized by F. Zernike in 1935 who converted the phase difference into an amplitude difference by a system later named "phase contrast". Zernike positioned a special condenser with a ring-shaped mask in the pathway of the illuminating light, and a phase-ring at the back focal plane of the objective. The phase-ring is designed so that it delays the phase of light by $\lambda/4$ (where λ is the wavelength of light). The refractive index of most biological objects is such that they also delay the phase of light by $\lambda/4$ or less, so the complete phase delay of the light through the phase-ring and the object is less than or equal to $\lambda/2$. When delayed and not delayed light meet at the focal plane they compensate each other resulting in brightness that is inversely proportional to the refractive index of the object. The disadvantage of the phase contrast is appearance of a 'halo' around the object that lowers the resolution.

In 1940s the first differential interference contrast microscope (DIC), based on the phase contrast principles, was developed by F. Smith and M. Francon. In DIC a single ray of light is polarized and spit into two individual rays, one traversing and the other missing the specimen. After passing the sample rays are recombined and interact with the image plane where interference of these rays creates contrast (Fig. 1.1).

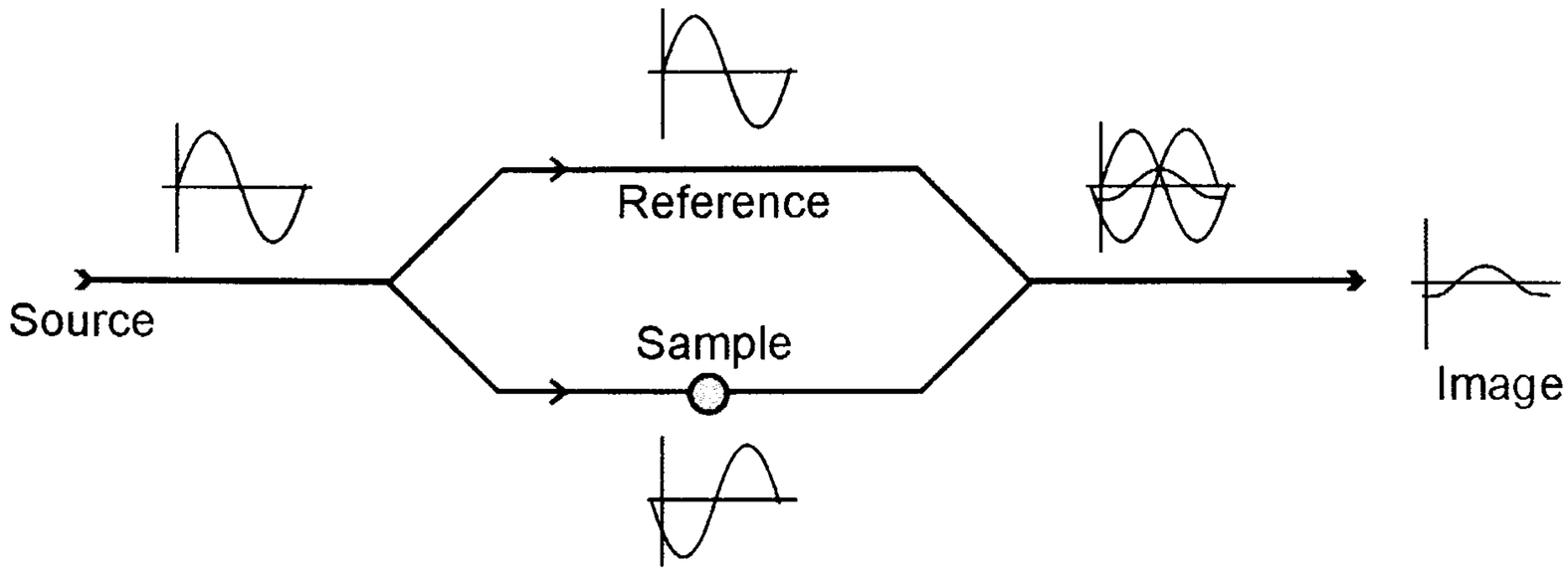

Fig. 1.1 Differential interference contrast effect.

A light beam ("source beam") is split into two beams so, that one beam passes through the specimen and the other ("reference beam") passes through the background. Subsequently the two beams are recombined and wave interference occurs resulting in the image.

The Smith and Francon type microscope used Wollaston prisms as light splitters/combiners, but the problem was that the combiner has to be placed at the back focal plane of the objective, which usually is inside the objective. Later, G. Nomarski modified the Wollaston prism, so that it can be placed outside the objective. In contradistinction to conventional phase contrast techniques, Nomarski DIC operates as a high-pass filter that emphasizes the edges, rather than adds 'halo' around them, making the lateral resolution higher. However, since DIC uses optical path differences to generate the image a three-dimensional illusion appears which does not correspond to the geometry of the object.

Although these methods have greatly improved conventional light microscopy, the use of lenses introduces diffraction effects and sets a theoretical limitation on the resolution of the light microscopy technique equal to $\lambda/2$. This limitation appears because after interaction with an object, electromagnetic waves diffract into propagating waves, those special wave length $> \lambda/2$, and evanescent waves, the wave length of which is $< \lambda/2$. Unfortunately, the evanescent waves, those are capable of carrying the information about sub-wavelength features of the sample, are confined to the sub-wavelength distance from the sample which is called 'near-field' (Fig. 1.2). So, classical optics that uses only the propagating waves, therefore named 'far-field', cannot image sub-wavelength objects.

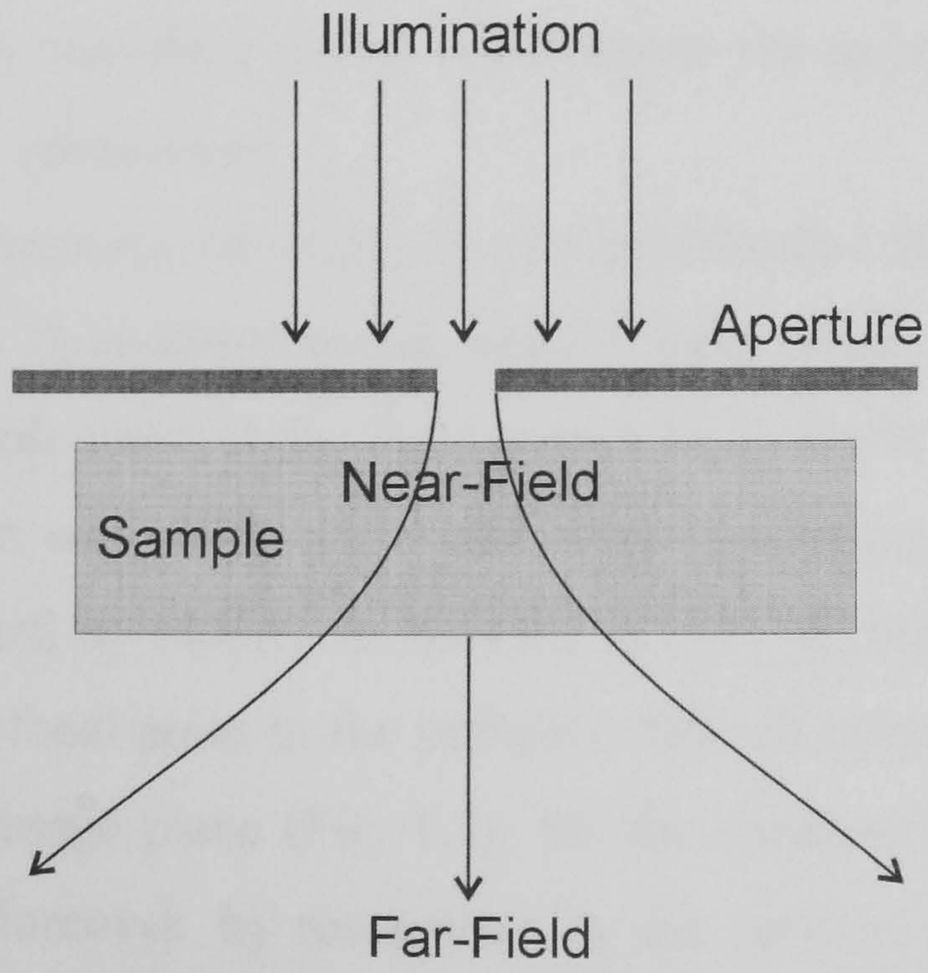

Fig. 1.2 Near-field effect.

A specimen is illuminated through a sub-wavelength sized aperture whilst kept the within the near-field regime of the source, so light does not have the opportunity to diffract before it interacts with the sample. The resolution of the system is determined by the aperture diameter.

On the other hand, there is a remarkable property of sub-wavelength sized objects in their ability to convert evanescent field to evanescent and propagating field. Thus, if such a sub-wavelength object could be placed into an evanescent field the converted propagating field that carries that objects properties can be imaged by conventional far-field light microscopy.

In 1928 the potential of operating a microscope in a near-field regime was discussed by Synge (Synge, 1928). The operational principle is based on illuminating a sample through a sub-wavelength sized aperture while scanning the specimen at a near-field distance from the light source. However, it took a long time until the technology for scanning was developed and the first scanning near-field optical microscope (SNOM) was built by Ash and Nichols (Ash and Nichols, 1972). Ash and Nicolas demonstrated a 'super-resolution' scanning microscope based on microwaves and obtained a resolution approaching $\lambda/60$. Twelve years later Pohl and co-workers (Pohl et al., 1984) achieved lateral resolution of the order of $\lambda/20$ with visible light by a system based on the scanning tunnelling microscope (discussed later in this chapter).

A major disadvantage of SNOM is the necessity of the precise positioning of the evanescent field source in relation to a sample. This requires combination with one of the scanning probe microscopy (SPM) techniques if the imaging of a three-dimensional surface is needed. So, SNOM itself cannot be utilized for imaging sub-wavelength features of a sample unless the sample is extremely flat (which is an ideal case). Also, the short distance at which near-field effects occur makes the technique 'short-sighted' compared to classical light microscopy.

Resolving three-dimensional structures is very problematic in light microscopy in general. In the case of a three-dimensional sample light passes through the whole sample thickness, as a result most of the light cannot be in focus resulting in a fuzzy lateral image. This problem was overcome by the confocal imaging technique proposed by Nipkow and implemented by Minsky in Harvard in 1957. In this technique the light from above and below the focal point in the sample is filtered out by a pinhole aperture that is placed in front of image plane (Fig. 1.3). So, the resulting image has the same focus as in the sample. Moreover, by reconstructing the sections (images acquired at different focal planes) of the same sample it is possible to create three-dimensional

images and estimate the height of objects. However, in this case the vertical resolution is limited to the height of the confocal volume, which depends on the size of the pinhole (1 – 100 μm) and usually is in the order of micrometers. To reduce the height of the confocal volume by reducing of the pinhole size in order to achieve higher vertical resolution is problematic due to the following reason. Only light that passes through the pinhole aperture could be seen in the final image.

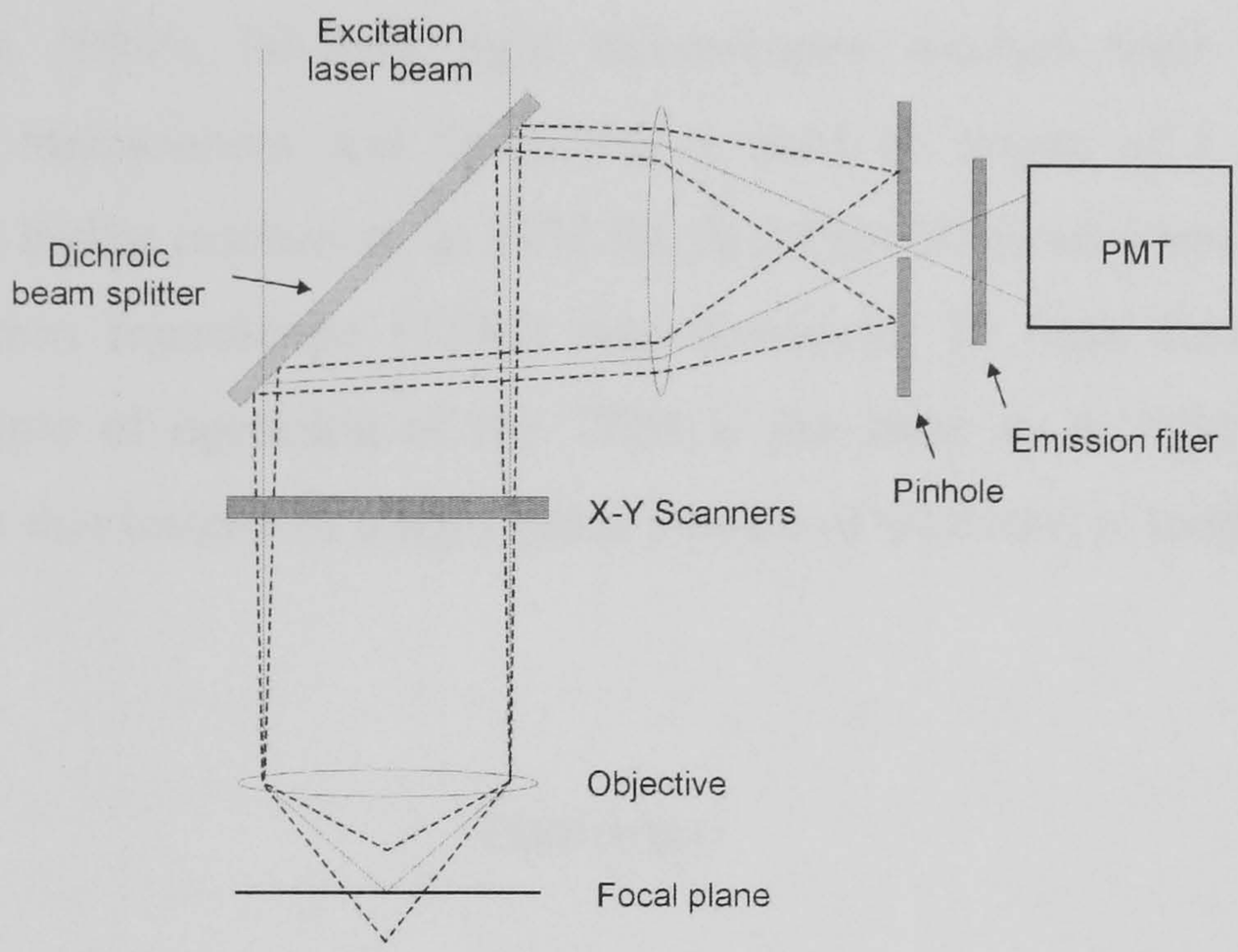

Fig. 1.3 Scanning laser confocal microscope schematic diagram.
A confocal "pinhole" situated in front of the image plane acts as a spatial filter and allows only the in-focus portion of the light to be imaged.

Usually, the standard pinhole reduces the amount of light up to 90-95% making high intensity illumination of the sample necessary. So, further reduction of the pinhole size requires much higher intensity illumination. To provide such high-power illumination a laser technique is used. Since the confocal technique has found wide application in imaging with the use of fluorescent probe labelling, where monochromatic light is required, laser technology was also found to be convenient because it produces light at very specific wavelengths. The illumination of the sample with high-intensity light causes another problem associated with the larger amount of free radicals that are produced in the process of fluorescence. The influence of these radicals on live samples is still not well characterized, however much evidence shows that it is detrimental.

To summarize it is important to note that beside the limitations of optical microscopy the light has unique properties including: non-perturbative penetration into

biological samples, and alteration according to the characteristics of the sample. These properties can be successfully used when combining variations of the optical microscopy technique with other microscopy techniques.

1.3 Transmission Electron Microscopy

In the early 1930's far-field light microscopes reached their limitation in resolution of 0.2 micrometers and there was a need to invent of a new type of microscopy with a higher resolution. In 1931 the first type of electron microscope – the transmission electron microscope (TEM) was developed by Max Knoll and Ernst Ruska. The principle of operation of the TEM is the same as in light transmission microscopy except that instead of a light beam a beam of electrons is used to image the sample (Fig. 1.4).

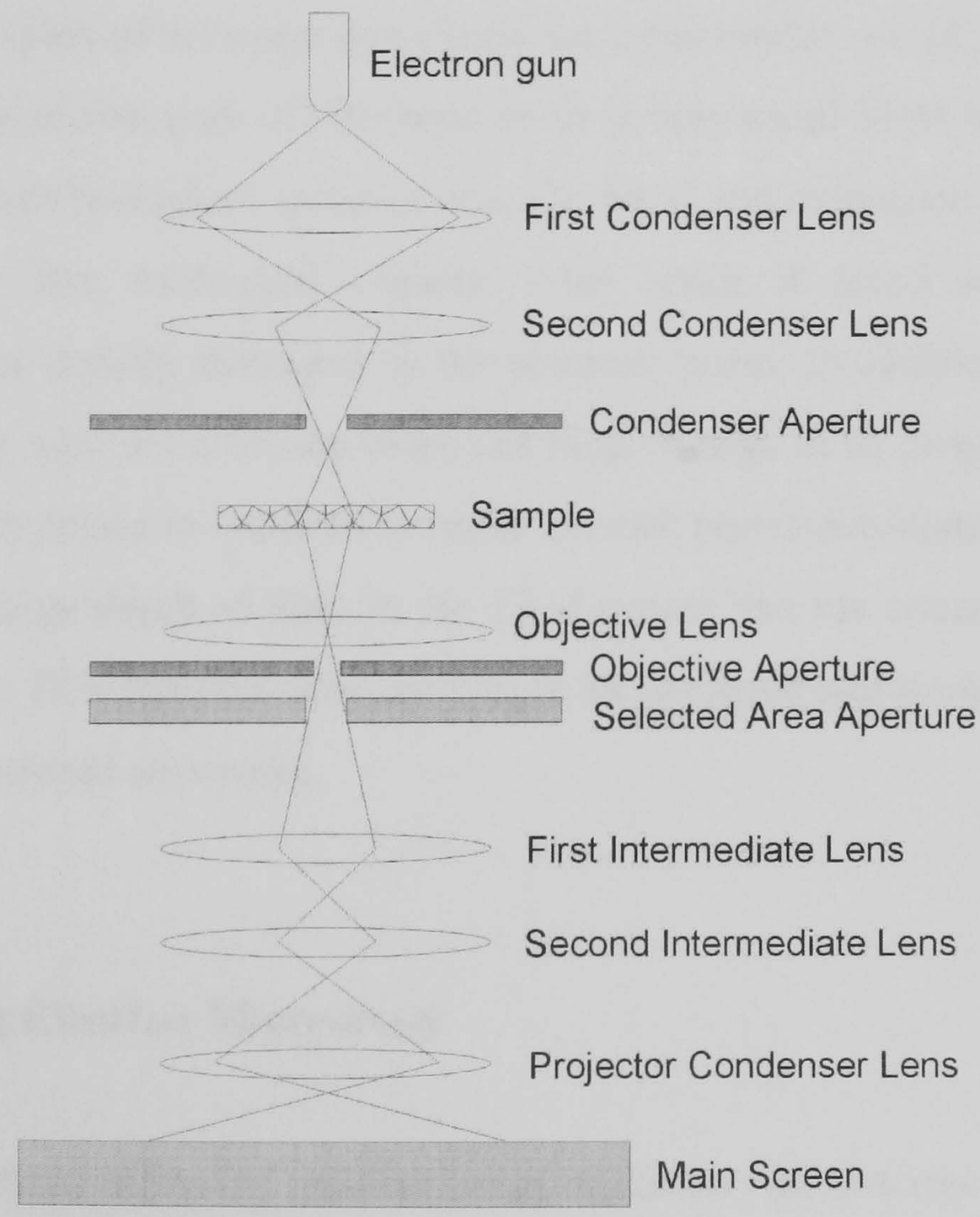

Fig. 1.4 Transmission electron microscope schematic diagram.
A beam of electrons is focused on the specimen. Electrons transmitted through the sample are projected onto a phosphor screen resulting the final image.

An electron gun is used to produce a beam of monochromatic electrons. This beam is focused to a thin coherent beam by two condenser lenses. The condenser lens is a magnetic lens made of a circular electro-magnetic cable, which projects a precise circular magnetic field in a specified region. This field focuses the electron beam in a similar manner to the optical lens that focuses light, and has the same parameters and errors. The condenser aperture is used to separate high angle electrons that are far from the optical axis. The sample is located behind the condenser aperture. When the electron beam hits the sample some of the electrons are scattered while others are transmitted. The transmitted electrons are focused by the objective lens into an intermediate image. The objective aperture is then used to block high angle diffracted electrons. Thereafter, the intermediate image is passed through intermediate and projector lenses to be enlarged. Eventually, it strikes the phosphor screen and a light image is generated. The darker areas of the image are those areas of the sample that are thicker or denser, thus transmitting fewer electrons.

Although the resolution of TEM is much higher than that of any optical microscope the principles of its operation limits the applicability of TEM to biological samples. Since the mean free path of electrons in air is very small TEM has to operate in high vacuum. Therefore biological samples must be fixed and dehydrated. This makes it impossible to study live biological objects. Also, even if fixed and dehydrated, biological samples are rapidly damaged by the electron beam. In addition, the densities of biological samples, such as cells, are often not high enough to be properly imaged, so the use of high-density labels is required in order to mark particular features.

The relatively large depth of field in the TEM means that the entire specimen is in focus simultaneously. This requires thin samples to be prepared and makes it impossible to image three-dimensional structures.

1.4 Scanning Electron Microscopy

In 1938 the first scanning transmission electron microscope (STEM) was described by M. von Ardenne (von Ardenne, 1938). His microscope used a scanning electron beam driven by electromagnetic coils and collected the electrons passing through the thin sample for imaging. Later, in 1942, this scanning technique was utilized and the first true scanning electron microscope (SEM) was developed

(Zworykin et al., 1942). The major difference of Zworykin's microscope compared to STEM was the use of secondary electron emissions for generating the image. Subsequently the SEM instrumentation was improved by many different scientists until in 1965 the first commercial microscope become available from Cambridge Scientific Instruments.

Similar to the transmission electron microscope the SEM cannot image live biological samples. Furthermore, sample preparation requires not only fixation and dehydration but also coating with a thin layer of conductive material in order to reflect the electron beam and produce secondary electrons. The advantage of the SEM is the ability to image three-dimensional surfaces. However, the image in this case is not topographical, it is rather a 'mirage' produced by the scattered electron beam. The true sizes in such an image cannot be measured; they can only be estimated by comparison with defined size objects. The estimation must be made on the understanding of perspective view aberrations.

1.4.1 Environmental Scanning Electron Microscopy

With the lapse of time the major disadvantage of the SEM, which is the high vacuum, was overcome and the first commercial Environmental Scanning Electron Microscope was announced by Danilatos in the 1993 (Danilatos, 1993). In an ESEM sample preparation is unnecessary, and they can be imaged in their 'natural' state, even when the samples contain water.

There are two major differences between the SEM and ESEM. The ESEM uses a differential pumping system that enables the electron gun and upper parts of the column to be held at high vacuum (10-7 torr), whilst the level of vacuum becomes progressively lower further down the column. The column is divided by pressure limiting apertures that allow the electron beam to pass through, but minimize the leakage of gases between zones pumped at different rates. Therefore, within the specimen chamber, pressures of up to 20 torr can be maintained. Hydrated specimens can be stabilized by means of careful control of sample temperature and chamber pressure, in order to achieve a saturated vapour pressure of water. The presence of water vapour causes some scattering of the primary electron beam, but is still low enough to prevent multiple scattering and the probe does not broaden.

The second distinctive feature of the ESEM is the gaseous secondary electron detector (GSED), which replaces solid-state backscattered electron detectors used in conventional SEM. The GSED detects the secondary electrons by using the gas between itself and the sample that amplifies the signal generated by secondary electrons. The amplification of secondary electrons arises via a gas cascade, initiated as the emitted secondary electrons collide with and ionise gas molecules on their way to the positively biased detector. Further electrons are produced as a result, and these will also undergo ionising collisions, thus propagating the cascade and amplifying the signal.

Although the ESEM provides the very conditions suitable for observing of organic/biological specimens in conditions close to their natural state, care is needed in order to avoid damage to the sample by the irradiating electron beam. In addition, the presence of saturated water vapour only is not enough to provide physiological conditions for live cells since they have to be fully immersed in medium. Such conditions can also be achieved, however, in this case the cell surface topography will be 'hidden' by the surface of the medium. This is because the secondary electrons are generated by inelastic collisions of a primary beam electron in the vicinity of the sample surface, which is within a region extending a few nanometres below the surface of the sample (in our case water) termed the `escape region'. Thus, the medium surface will be imaged.

1.5 Scanning Probe Microscopy Techniques

Scanning probe methods of investigating surfaces use a completely different approach compared to electron microscopy. For surface analysis, a probe is brought into close proximity to the sample surface until an interaction between the tip and the sample occurs. A property of the interaction is used as a signal for a feedback circuit that keeps this signal constant. Raster scanning of the probe over the surface then gives a contour map of the constant interaction, and changing the interaction generally leads to changes in the surface contours obtained. An alternative method of investigating the sample surface is to maintain a raster scan at a fixed distance between the probe and the sample, which results in a plot of the interaction.

A common feature of all SPMs is that the probe-sample spacing (*s*) is kept less than the characteristic distance (λ) of the particular interaction being studied. As well as high resolution, and the ability to obtain a three-dimensional picture, SPM has another advantage with regard to the imaging of biological samples over scanning electron microscopy: the possibility to scan in liquid under normal/atmospheric pressure. This enables the study of live objects.

1.5.1 Scanning Tunnelling Microscopy

The scanning tunnelling microscope (STM) was developed by Binning and Rother in 1981 at the IBM research centre in Zurich (Binning et al., 1982). The highest resolution of any SPM was obtained with a STM. STM was the first scanning probe technique to record an atomic resolution an image, the Silicon (1,1,1) surface was obtained in 1983 (Binning et al., 1983;Binning and Rohrer, 1987).

The STM set-up consists of scanning a metal tip over the surface at a constant tunnel current as shown in Fig. 1.5. The displacement of the metal tip is given by the voltage (V_p), which is a feedback function of the tunnel current (I_t) at a constant tunneling voltage (V_t) calculated by the control unit (*CU*) and applied to the three-dimensional (*x, y, z*) piezo-stage. This yields a topographic picture of the surface, which is shown as the dashed line (Fig. 1.5). The very high *z* resolution of STM rests on the strong dependence of the tunnel current on the distance (that is, resistance) between the two tunnel electrodes, i.e., the metal tip and the scanned surface.

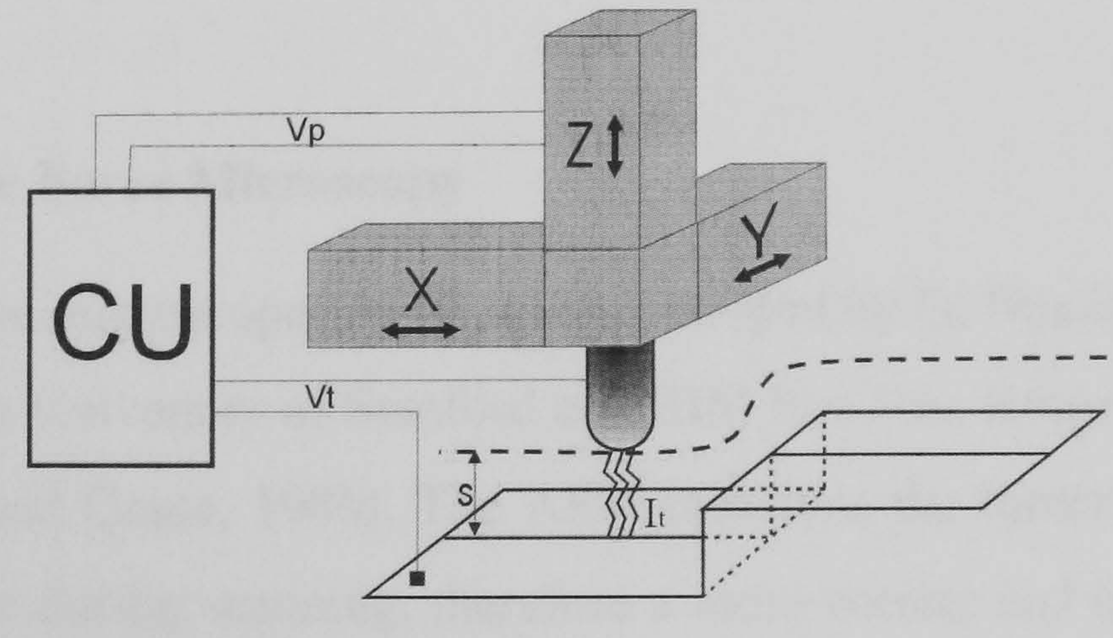

Fig. 1.5 Scanning tunneling microscope schematic diagram.
The piezodrivers X, Y and Z scan the metal tip over the surface. The control unit (*CU*) applies the appropriate voltage (*Vp*) to the piezodrive Z for constant tunnel current (I_t) at constant tunnel voltage (V_t). For constant work function the voltages applied to the piezodrivers yield the topography profile of the surface at the constant distance (*s*).

To obtain a high resolution, however, the distance between tip and sample must remain stable during the scan. Very stringent anti-vibration measures are required for atomic resolution imaging, because the stability must be at least six orders of magnitude smaller than typical floor vibration amplitudes (0.1 – 1.0μm). The use of very short probe tips also helps to suppress vibration.

The lateral resolution of STM is determined by the radius of the probe tip. There are some techniques, which allow the production of fine scanning tips, such that mono-atomic steps could be resolved within 10 Å resolution.

STM is a typical near-field method with sub-atomic resolution, which is beyond the wavelength of the electrons, which tunnel between the probe and sample.

The ability of STM to resolve surfaces with atomic resolution makes it applicable to a wide range of experiments. For example, it is possible to precisely position the scanning tip over a pre-scanned surface; thus, local experiments and manipulation with single atoms can be performed (Marti et al., 1987).

More recently, STM has been successfully used to image different conductive materials in vacuum or air and for a range of temperatures (4 – 10000K). This has given STM some use for studying biological materials in their native environment. However, most biological samples are not sufficiently conducting for STM imaging, so they have to be coated with a layer of conductive material, and this kills the sample. Even if the biological sample is fixed and coated, the resolution of an image obtained by STM is still reduced by the nature of the coating procedure, and the topography of the grain in the metallic surface.

1.5.2 Atomic Force Microscopy

The atomic force microscope (AFM) was developed by G. Binnig, C.F. Quate and Ch. Gerber in 1984 in University of Stanford and IBM San Jose Research Laboratory in California (Binning and Quate, 1986). The AFM measures the forces that act between the tip and the sample during scanning, therefore a more correct and common name for the technique is scanning force microscopy (SFM). However, historically the first SFM was capable of measuring atomic forces and subsequently a whole class of microscopes have inherited this name. One of the major advantages of AFM compared to STM is

that AFM can cope with non-conductive surfaces, so might be applied to a much wider range of samples.

The principles of AFM operation are similar to STM, but instead of measuring tunnelling current the forces of the tip-sample interactions are measured. The first AFM set-up consisted of ordinary STM, where between the sample and measuring tip (field-emission electrode) a cantilever with a diamond tip was placed (Fig. 1.6). The AFM sample was attached to a three-dimensional piezo-stage, and both, the cantilever and the tunnelling tip, were mounted on piezoelectric elements as well. There were four measuring modes possible on that system.

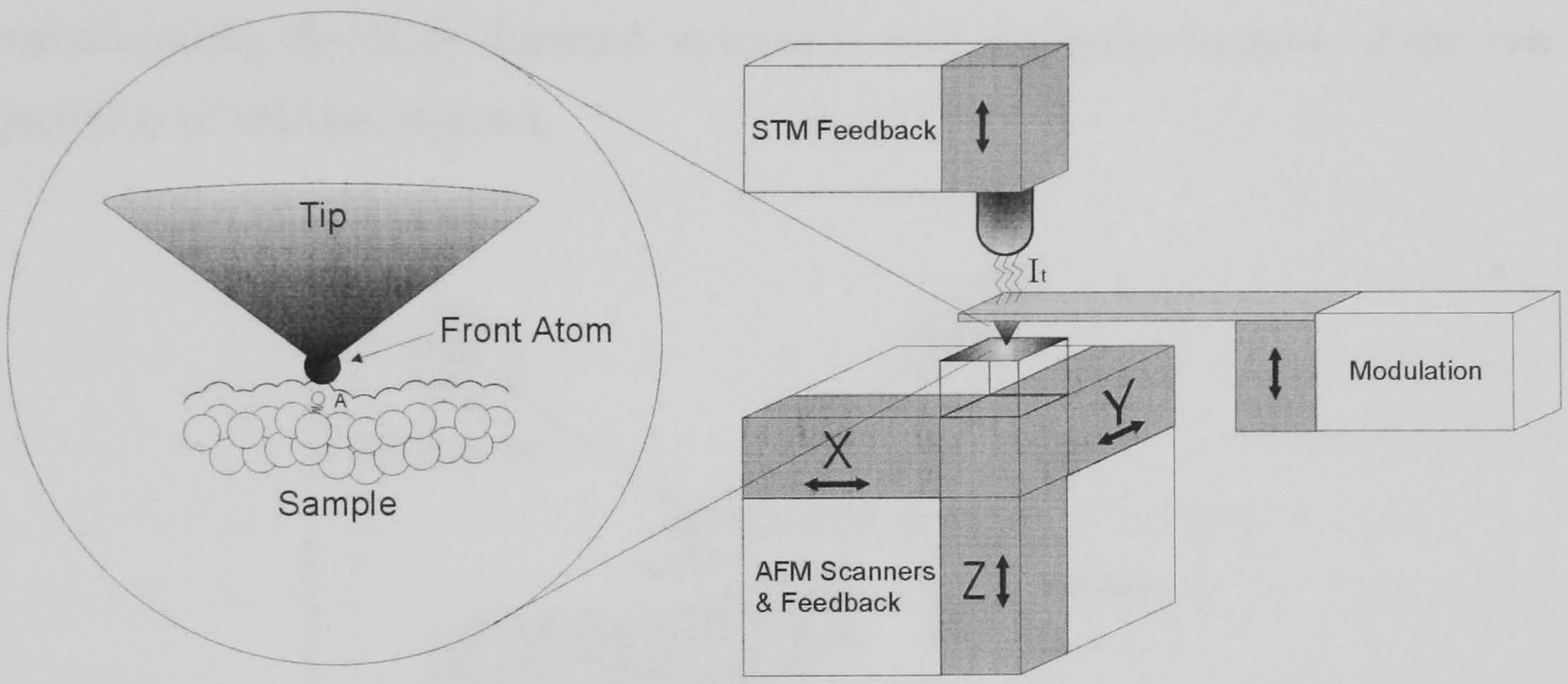

Fig. 1.6 Schematic diagram of the atomic force microscope with tunneling current control. The STM and AFM piezodrivers are facing each other, sandwiching the diamond tip that is glued to the lever. During the scan the tip follows the contour of the sample, in one case to keep the tunnel current constant (STM) and in the other to maintain constant force between the tip and the sample (AFM, sample, and tip either insulating or conducting).

In the first mode the sample is modulated in the *z* direction producing AFM-tip – sample force changes which deflect the cantilever holding the stylus. In turn, this modulates the tunnelling current, which is a signal for the AFM-feedback circuit used to maintain the AFM-tip – sample force at a constant level.

In the second and third modes the cantilever is driven at it's resonant frequency in the *z* direction. The force between sample and stylus changes the resonant frequency of the lever. This changes both the amplitude and phase of the tunnelling current, which can be used as a signal for the feedback control.

In the fourth mode the feedback circuit of the STM-tip was connected to the AFM cantilever, and the system maintained the tunnelling gap at a constant level by changing the force on the stylus.

With time the system was improved, and a laser beam reflected off a mirror mounted on the back of the cantilever was used for deflection detection (Meyer and Amer, 1988) (Fig. 1.7). The reflected beam reaches a photodiode, which consists of four photoactive segments separated by a gap of order of 10 μm. The set-up was tuned so that the laser spot falls equally on each segment of photodiode when the cantilever is in its equilibrium position. When the cantilever bends as a result of stylus – sample interaction forces, the laser spot moves towards one or other segments of the photodiode producing the current changes which are used as a feedback control signal to maintain a constant force on the stylus. However, the cantilevers have to be flexible enough to measure low forces, and have a high resonant frequency at the same time. In addition to that, manufacturing the sharp diamond styluses is very expensive because of the low reproducibility of uniform styluses.

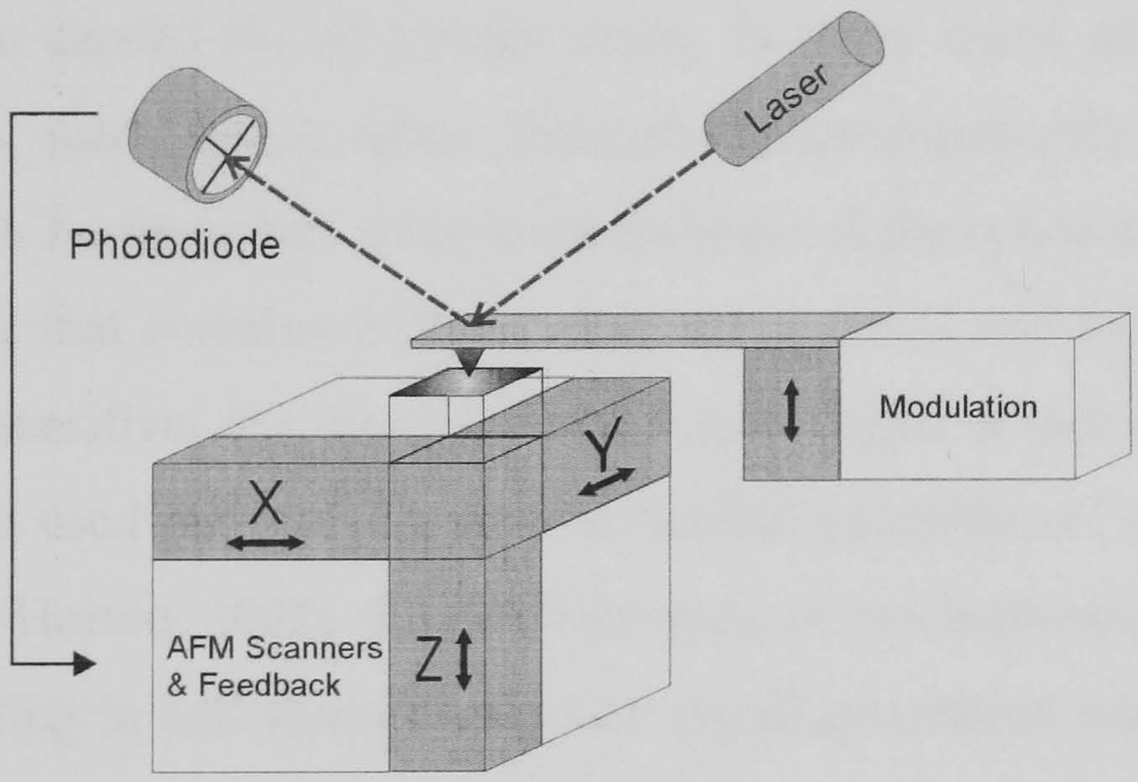

Fig. 1.7 Atomic force microscope schematic diagram.
The piezodrivers X, Y and Z scan the sample while the diamond tip follows the contour of the sample deflecting the lever. The deflection of the lever tilts the reflection of the laser beam that is detected by the photodiode. The photodiode provides the feedback signal to control the position of the Z piezodrive to maintain constant force between the tip and the sample.

Since the first paper about atomic-resolution imaging using AFM was published (Albrecht and Quate, 1987) this technique became widely applied for a variety of experiments such as friction measurements (Radmacher et al., 1992) and imaging of organic non-conductive materials. More recently, AFM has been used for studying unfolding proteins (Carrion-Vazquez et al., 1999), cellular mechanotransduction (Lehenkari et al., 2000) and the observation of DNA condensation (Golan et al., 1999). However, as mentioned above, AFM measures the tip – sample interaction force, hence, reflects local mechanical properties of a sample. As a result, the resolving of soft

samples, for example, cell membranes formed by lipid bilayer, the use of AFM is a very complicated task.

Despite of the high resolution of AFM, a number of difficulties in using this technique for imaging living cells were reported by different groups (You and Yu, 1999). Among the technical limitations, such as poor vertical range and lack of optical interface, that were overcome by Lehenkari and colleagues (Lehenkari et al., 2000), fundamental problems exist. One of the problems appears to be deterioration of the quality of AFM images with time. This is mainly due to the adhesion of metabolic molecules and cellular secretion that are always present on the extra-cellular part of the membrane, to the AFM scanning tip. Also, the cantilever loading force is often deforming or even destructive for the cell membrane. It is not surprising that fine membrane structures, such as microvilli, have not been properly resolved by AFM to date (Braet et al., 1998;Lesniewska et al., 1998). And yet, most of the AFM studies of living cells have been carried out in contact mode. In many cases when imaging the surface of living cells, scans reveal, rather, intracellular structures such as cytoskeleton (Sinniah et al., 2002a). Furthermore, since the membrane of the cell is a multifunctional and dynamic structure that contains different types of channels and receptors, some of which are mechano-sensitive, the applied force could trigger a cell response. Thus, although AFM can be used for studying the mechanical properties of cells (Charras et al., 2001;Charras and Horton, 2002), the AFM imaging of mechano-sensitive cells with rapid responses resulting in cell shape changes or signal generation would appear very problematic.

The adhesion of the molecules to the scanning tip, and the cell membrane deformation, can be greatly reduced by lowering the loading force of the cantilever down to 1-10 pN. However, operating the AFM in this range represents technical challenge (Le Grimellec et al., 1998). The problem of loading can be partially overcome by introduction of tapping mode that utilizes the vibration of the cantilever at a high frequency when 'soft' cell membrane behaves as 'hard' material (Putman et al., 1994). Unfortunately, the application of tapping mode in liquid is limited by the low resonant frequency of the cantilever and complex image contrast mechanism in this environment (Schäffer et al., 2002).

To summarise this scanning probe microscopy overview it is important to note that AFM became one of the most commonly used types of scanning probe microscopy

for imaging of living cells. This very powerful technique has already produced important knowledge in biological fields and still has a great potential.

1.6 Conclusions

It is not surprising that every type of microscopy described above has its own unique advantages and limitations in terms of studying living cells. Therefore, utilising only the advantages in one instrument is logical. Unfortunately, so far the development of an entirely new process of imaging that could satisfy all the requirements for living cell experiments is not yet known. However, there may be a possibility to develop a multifunctional instrument, on the basis of the one most suitable microscopy technique, that could incorporate major capabilities of other microscopy methods. The microscopy that can be used as a basis for such a multifunctional instrument should meet following requirements:

- allow absolutely-intact imaging
- operate in physiological (or close to) environments e.g. in physiological solution, under normal pressure, at physiological temperature
- be capable of nanometer resolution
- require minimum sample preparation
- to be compatible with other microscopy types and measuring techniques.

Achievement of first two requirements could enable long-term experiments during which cell behaviour over time can be studied. The compatibility could allow the exploitation of the advantages of other microscopy techniques and methods related to them.

The microscopy that complies with all the requirements above was developed in 1989 and the next chapter is dedicated to it. This microscopy was chosen as the basis for the development of a multifunctional instrument, which is described in this thesis.

Chapter 2 Scanning Ion Conductance Microscopy technique

2.1 Introduction

The Scanning Ion Conductance Microscope (SICM) was originally developed and described by P.K. Hansma and co-authors (Hansma et al., 1989). SICM belongs to a wide family of scanning probe microscopes, and it was specially designed for the scanning of soft non-conductive materials at sub-micrometer resolution that are bathed in electrolyte solution. Also, in order to achieve higher contrast imaging, SICM was used in combination with tapping mode atomic force microscopy (Proksch et al., 1996). However, for a long time this technique was limited to imaging of flat polymeric films. In 1997 significant improvements to SICM have been made by Y. E. Korchev et. al to allow the imaging of live cells without making direct contact with the sample surface (Korchev et al., 1997a). Since then, SICM has been used for investigating of biological samples, such as cells and tissues in vitro (Korchev et al., 1997b;Korchev et al., 2000a).

2.2 Principle of operation

The SICM consists of a glass micropipette probe filled with electrolyte lowered into a bath of electrolyte (Fig. 2.1) toward an insulating, for ions, surface of the sample. As the tip of the micropipette approaches the sample, the ion conductance reduces because the gap that ions can flow through is decreased. Changes of the ion current (I_{ion}) are monitored by a control unit (CU), and are used as a feedback input signal (V_p) to keep the distance between electrode tip and sample constant by applying corresponding voltages to the Z-piezo drive during the scanning procedure. Therefore, the path of the tip follows the topography of the surface. This mode of operation is known as constant conductance mode.

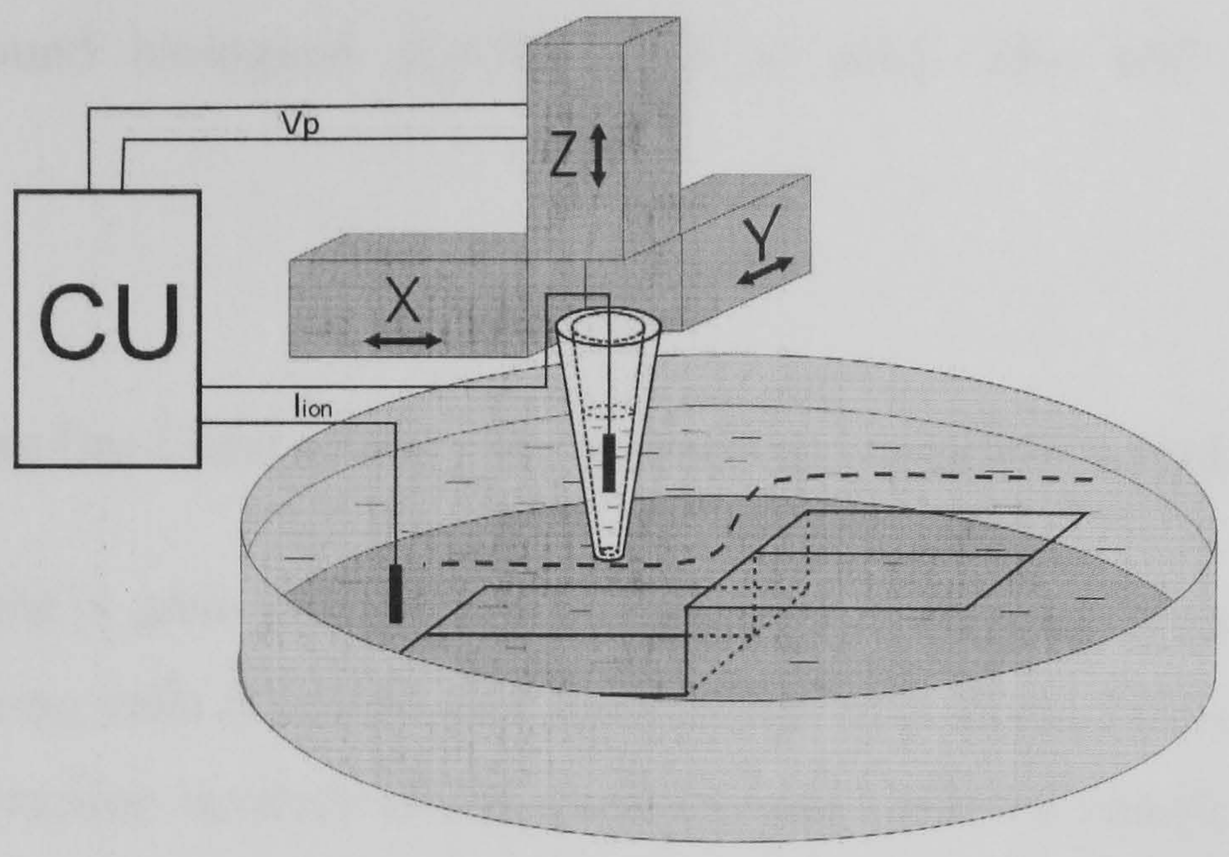

Fig. 2.1 Scanning ion conductance microscope schematic diagram.
The piezodrivers X, Y and Z scan the micropipette over the sample surface. The control unit (*CU*) applies the appropriate voltage (*Vp*) to the piezodrive Z for constant ion current (I_{ion}) through the tip of the micropipette.

To investigate spatial changes in the local conductivity the constant height mode can be used. In this mode of operation the micropipette scans at a constant height over the sample surface while obtaining ion current changes. However, this mode is suitable for relatively flat surfaces only and cannot be used for biological samples, which often vary of the order of tens of microns in height.

In theory, the lateral resolution of SICM is determined by the inner diameter (ID) of the scanning pipette if the noise of the ion conductance signal could be reduced to less than 1%. The ID of micropipettes which Hansma et. al. used in his first publication varied from 0.05 to 0.1 μm. These micropipettes were pulled from glass capillaries with ID of 0.75 mm and outer diameter (OD) of 1.5 mm using Brown-Flaming puller. Hansma et. al. found that in practice they resolved features a few times smaller than the ID of the micropipette, and there was a compromise between averaging the signal for a long time to reduce noise, and obtaining entire images in reasonable time.

In order to achieve higher lateral resolution the ID of micropipettes can be reduced down to 10 nm. However, a number of problems arise because of this small size. Firstly, the smaller micropipettes are very fragile and often break during the scan. Fortunately, this can be overcome using shorter taper pipettes, or pipettes made from quartz or aluminosilicate glass capillaries. Secondly, the higher resistances of smaller pipettes become a problem when scanning live cells in their growth medias, because of the low ion currents. Concentrated solutions cannot be used in order to increase conductivity since it might affect cells. Increasing the voltage applied to the electrodes leads to static charging of the micropipette that, in turn, attracts small particles, that are

always present around biological samples such as cells. This will cause pipette blockage.

2.3 Scanning Ion Conductance Microscopy of biological samples

Nowadays there is great interest in applying SPM techniques to study biological samples, such as living cells (Hansma and Hoh, 1994;Prater et al., 1991). However, in most cases, the interaction between the microscope probe and the sample deforms and often damages them (chapter 1). Since the first attempts to use AFM for imaging living cells, further improvements have been made to reduce applied force, for example, application of "tapping in liquid" mode of operation (Putman et al., 1994), in order to adapt AFM for cell biology (Lehenkari et al., 2000;Schneider et al., 2000). Even so, the nature of the AFM technique, which means direct contact with the sample, is a major disadvantage preventing its wide usage for investigation of living cell properties, because the properties of interaction forces between the probe and the sample are not fully understood.

As already mentioned above, Y. Korchev (Korchev et al., 1997a) developed a SICM that, in contrast to AFM, is capable of scanning any sample bathed in electrolyte without making direct contact. As a result, this instrument is suitable for studying both the topography and certain functional properties of the surface of living cells.

The principle of operation is similar to SICM developed by Hansma and co-workers (Hansma et al., 1989). The ion current (I) through the pipette is strongly dependent on the position of the tip relative to the sample, so provides the feedback signal, which controls the vertical position of the probe. This ion current is determined by the overall resistance (R) of the tip (Fig. 2.2), which is a combination of the micropipette resistance (R_p) and access resistance (R_{Ac}) of the micropipette's aperture:

$$R = R_p + R_{Ac} \tag{2.1}$$

The pipette resistance can be easily calculated from the resistance of the electrolyte inside the tip of the pipette. The pipette tip's shape is assumed, for simplicity, to be the shape of a right cone, with a base radius of the radius of the glass capillary from which the pipette was pulled, and an aperture radius (r) of the pipette

opening. The height of the cone is considered to be that of the micropipette tip filled with electrolyte.

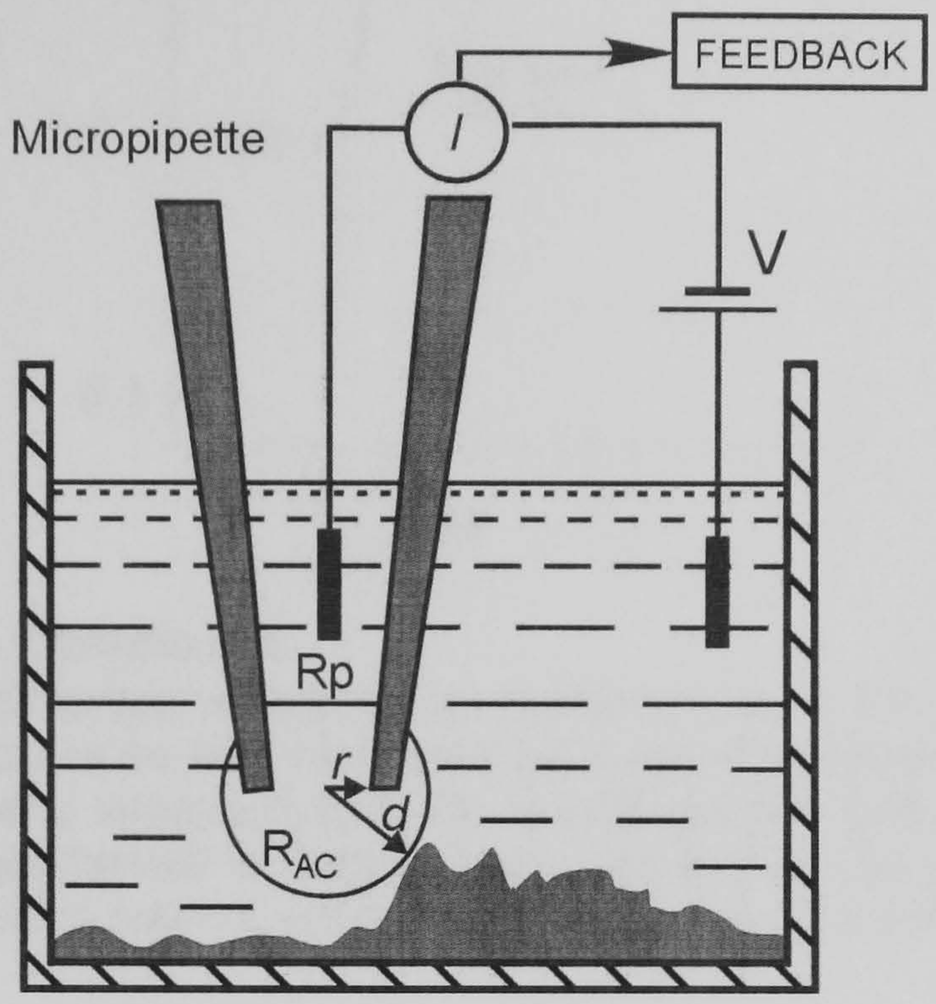

Fig. 2.2 Principle of SICM operation.
The position of the micropipette tip relative to the sample surface strongly influences the access resistance (R_{AC}) and, consequently, the ion current (I) flowing through the pipette. The current value at a distance (d) that exceeds the radius (r) can be used to control the vertical position of the tip to sense the neighbouring structures that are higher than the vertical probe/sample separation distance. During the scan, the tip of the pipette, with its 'spherical current sensor' of radius d, 'rolls' over the surface structures without damaging it.

Access resistance can be defined as a function of probe – sample separation and it depends on electrochemical properties of both media and the sample. Naturally, the ion current flowing through the pipette depends on the voltage (V) applied to the electrodes, and is therefore, given by:

$$I_{DC} = \frac{V}{(R_p + R_{Ac})} \tag{2.2}$$

In theory, it is possible to model the current function assuming that the tip is approaching a flat, nonconductive surface. The theoretical curve of the current as a function of tip/sample separation (d) and actual approaching characteristic are shown in Fig. 2.3.

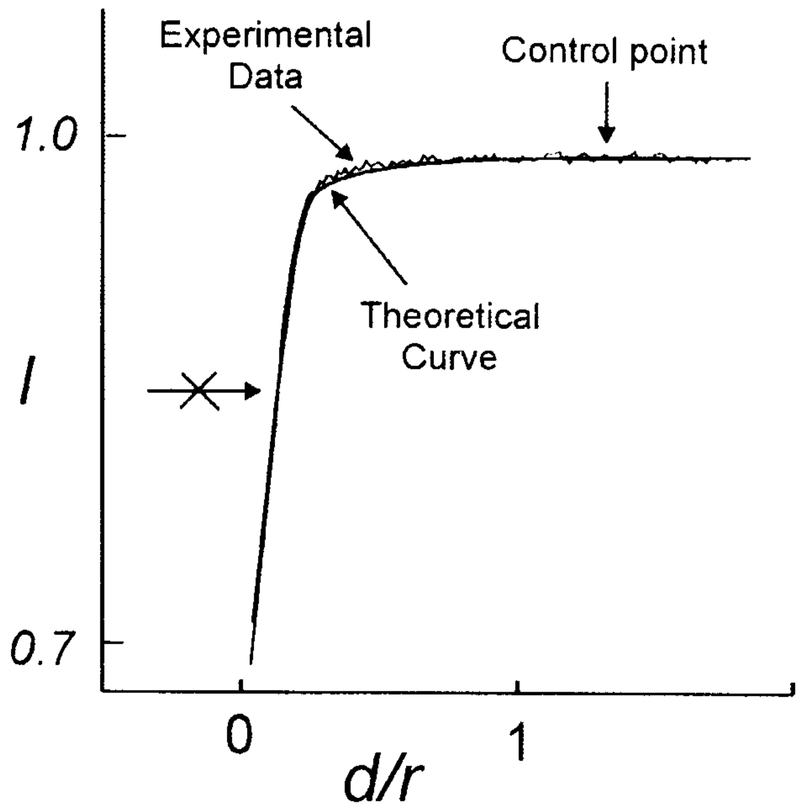

Fig. 2.3 SICM approach characteristic.
Comparison of expected and actual values of ion current (*I*) as a function of the tip/sample separation (*d*). The theoretical curve was calculated for a simplified model of a truncated cone-shaped tip of known geometry approaching a flat, nonconductive surface. The experimental data show the approach characteristic of a tip of similar geometry. The vertical arrow indicates the value of the current (control point) used for the scanning protocol in the feedback control circuit.

As can be seen, experimental data match with the theoretical curve. The vertical axis represents normalized current (I/I_{max}, where I_{max} is the maximum current recorded when the micropipette probe is far away from the sample) and the horizontal axis is the tip/sample separation distance expressed in *r*.

The region of the curve marked with a crossed arrow is where the position of the tip relative to the local sample surface strongly influences the measured ion current. Choosing the set-point for a feedback loop of constant conductance scanning from this region will affect the vertical position of the tip with maximum efficiency (i.e. a small change in distance is easy to detect). However, in this case, if the tip/sample separation is smaller than the size of neighbouring structures, and lateral sensitivity is very limited. During a scan with this set-point, the probe may directly contact a raised part of the specimen without reducing the ion current, hence damaging itself and/or the sample. On the other hand, choosing as the set-point a value of ion current observed at a distance *d* greater than *r*, more on the plateau of the curve, produces a sensitive 'sphere' around the micropipette tip, which is capable of "sensing" obstacles from the side (Fig. 2.2). This approach enables the micropipette to move at a determined distance above the surface without damaging either tip or sample.

2.4 Applications of Scanning Ion Conductance Microscopy

Despite the fact that SICM was introduced many years ago it is still not commonly used. However, the power and beauty of this technique is in its multifunctionality. In addition to such classical applications of SICM as the imaging of live cells (Korchev et al., 1997b;Korchev et al., 1997a), it can also be used for a variety of high-technological in vitro experiments. Some examples of such applications are presented below.

2.4.1 Cell volume measurement

The idea of cell volume measurement is simple and based on the nature of the SICM image generation, which is common for all SPM systems. Topography imaging involves raster scanning, so an image consists of a limited number of points where each point presents a sample height (Z_{xy}) at x and y coordinate, which is in our case the cell height. Before estimating the cell volume, the vertical position (Z_{ref}) of the probe tip on the substrate has to be measured in order to calculate absolute cell height by subtracting Z_{ref} from the measured height Z_{xy}. Assuming that the basal cell membrane has a close contact with the substrate the volume of the cell (V_{Cell}) can be estimated as:

$$V_{Cell} = \sum_{y=1}^{m} \sum_{x=1}^{n} Z(x, y) \tag{2.3}$$

Where n and m are the number of scan points per line and the number of lines per image respectively, $Z(x, y)$ is the cell height at each raster scan point.

It is possible to measure cell volume by SICM with a 2.5×10^{-5} μm^3 resolution (Korchev et al., 2000a).

2.4.2 Functional localization of a single active ion channel

Localization of single active channels on the membrane of a living cell is another good example of SICM's multifunctionality, as illustrated in (Korchev et al., 2000b). An important aspect of the SICM is that it uses a micropipette as the sensing probe. This

means it can also deliver ions, agonists or other agents to the membrane during the scan in a very precise way. Combining this technique with a traditional whole-cell patch-clamp configuration for a second electrode it is possible to record single channel currents in the patch-clamp pipette while the scanning micropipette brings particular ions to the place where the channels are localised (Fig. 2.4). This configuration requires conditions where the outside medium is free from the ions that are carriers.

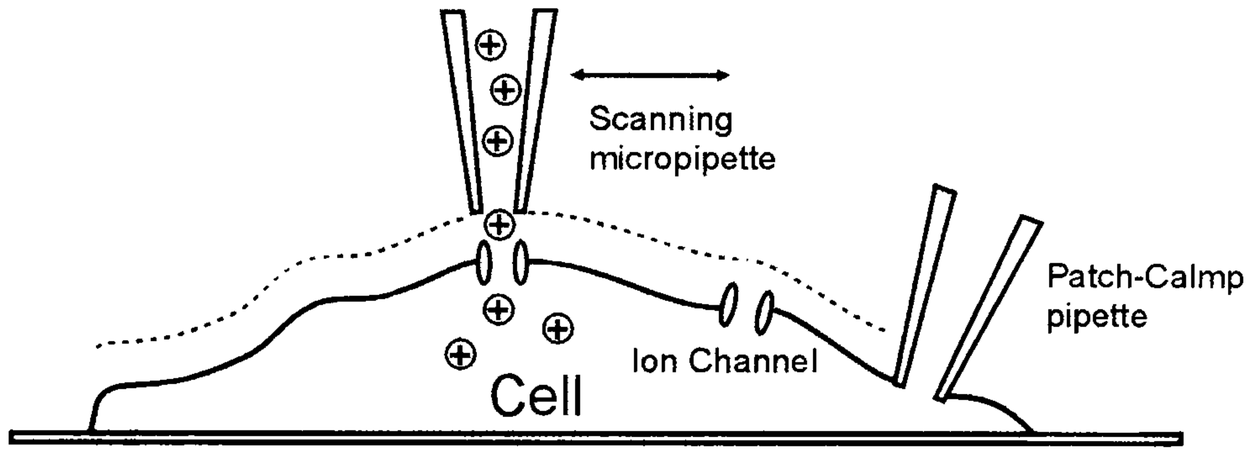

Fig. 2.4 Functional localization of single active ion channels with SICM.
Diagram of the sensing mechanism of the combined SICM/whole-cell voltage-clamp technique. The scanning micropipette provides local application of ions to the cell surface/ion channel during the scan while the patch-clamp micropipette records the cellular electrical response.

Collecting two images simultaneously i.e. both the topography and the 'ion current' image, the distribution of the channels on the cell surface structures can be seen: that is, it is possible to map ion channels.

2.4.3 Combination of SICM and Scanning Confocal Microscopy

The SICM is able to obtain topographical information of the surface, so it is possible to investigate only the processes that take place on the cell membrane. However, many, and maybe the most important structures and mechanisms of the operation are hidden inside the cell, which SICM cannot probe. However, there are other methods of visualizing intracellular components available such as scanning confocal microscopy (SCM). For example, the cytoskeleton can be stained and imaged by SCM. Also, the changes of the intracellular concentration of particular particles, say (Ca^{2+}) or protons (H^{+}), can be measured with the help of fluorescence molecular probes.

With the aim of combining SICM with scanning confocal microscopy, the following modifications were introduced to the SICM optical system. The excitation light source is provided by a laser diode. The optical recording system consisted of an inverted microscope equipped with oil-immersion objective, an epi-fluorescent filter

block, and a photomultiplier with a pinhole. The schematic diagram of the setup is shown in Fig. 2.5.

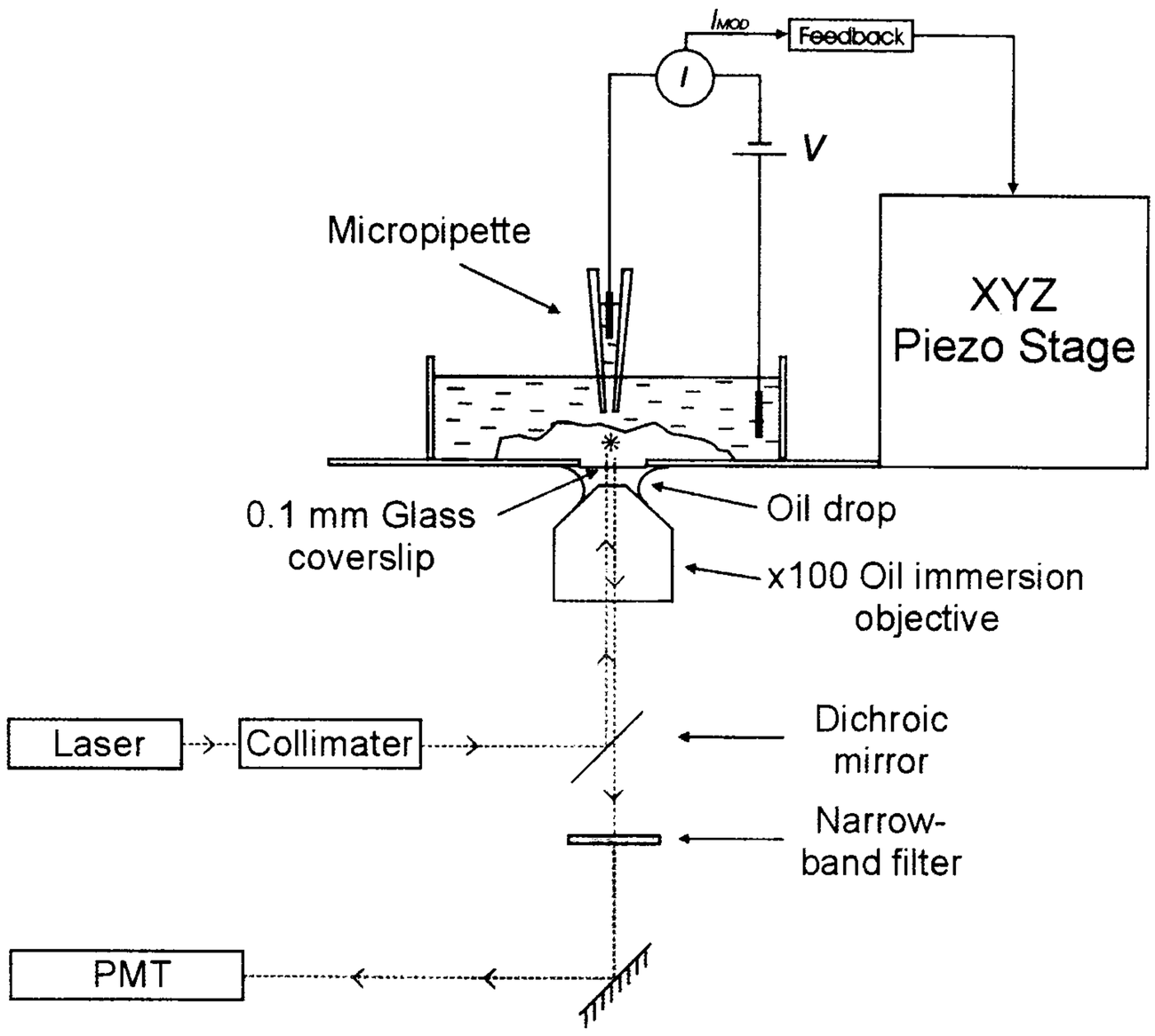

Fig. 2.5 Schematic diagram of the combination of SICM and SCM.
In this combined technique the sample is moved up and down during scanning to maintain a constant distance between the pipette and the cell surface. The position of the pipette and objective stays fixed. This means that during scanning the fluorescence is recorded from the cell membrane just under the micropipette tip.

To acquire an image, the system can be operated in two possible modes. The first mode does not involve SICM feedback control and slices like a conventional scanning confocal microscope. Driving the piezo stage in different directions different pictures can be acquired. For example, vertical (*xz/yz*) or lateral (*xy*) slices can be scanned with subsequent three-dimensional reconstruction. This mode can be used for the scanning of static structures where the sample does not move out of the focal plane. This mode of operation was used to verify the SICM method of volume measurement (Korchev et al., 2000a).

The second mode is what we call surface- confocal mode of operation, and is performed with the use of SICM feedback control to follow the topography of the sample surface. In this mode the SICM probe, the focus of the objective and the position of the laser beam are co localized at the same point. During scanning the SICM moves the sample, keeping the objective constantly focused on the SICM probe tip i.e. on the sample surface. As a result, the fluorescent signal right from or just under the cell membrane can be acquired. For example, such mode can be used for action potential

detection using voltage sensitive dyes. In addition, adjusting the focus above, or, more relevant, under the cell membrane other important information, like calcium release during contraction (Shevchuk et al., 2001), can be obtained. The more detailed use of surface confocal measurement will be described later in this thesis.

2.4.4 Combination of SICM with Scanning Near-Field Optical Microscopy

SICM can also be combined with Scanning Near-Field Optical Microscopy (SNOM) (Korchev et al., 2000c). The following modifications were made to conventional SICM in order to implement SNOM within one system.

Continuous wave laser light was coupled via a multi mode optical fibre into the micropipette. In order to confine light to the aperture, 100-150 nm of aluminium was sputtered onto the walls of the micropipette. Thus, a high-intensity, sub-wavelength dimensions near-field source of light was achieved. The schematic diagram of the hybrid SICM-SNOM apparatus is shown in Fig. 2.6. The rest of the setup is similar to that in Fig. 2.5.

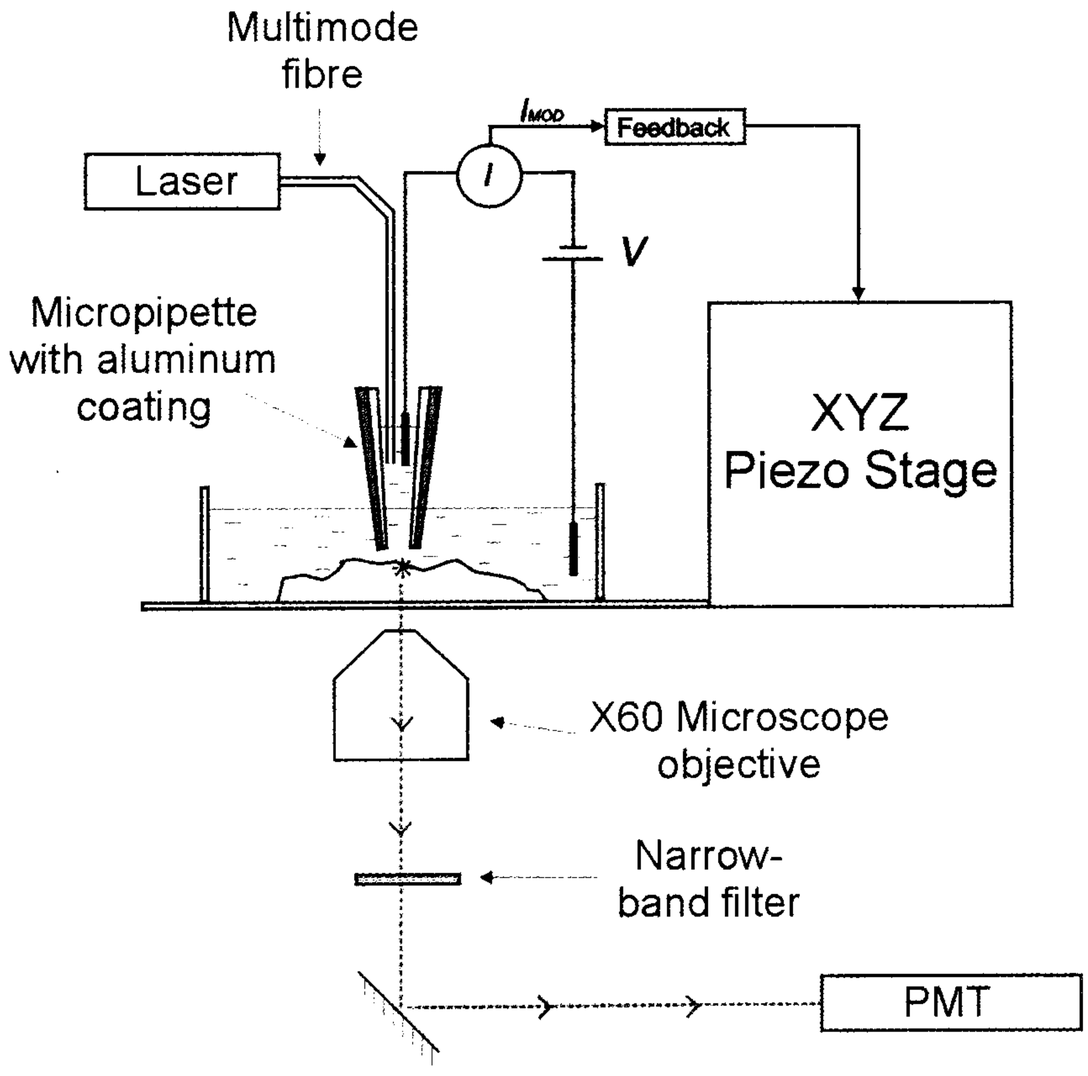

Fig. 2.6 Schematic diagram of the combination of SICM and SNOM.
In this combined technique the sample is moved up and down during scanning to maintain a constant distance between the pipette and the cell surface. The position of the pipette and objective stays fixed. This means that during scanning the scattered laser light is recorded from the cell membrane just under the micropipette tip.

As a result, an optical picture from the surface collected by the SNOM may present important information in addition to topography.

2.5 Conclusions

As can be seen, the SICM technique complies with most of the major requirements outlined in the first chapter and:

- allows non-invasive imaging
- operates in physiological environment e.g. in liquids, under normal pressure, at physiological temperature
- is capable of close to nanometer resolution
- requires minimum sample preparation
- is compatible with other microscopy types and measuring techniques.

These features make SICM attractive for studying of the functional properties of living cells in vitro and was, for this reasons, chosen as the basis for the development of a multifunctional instrument.

Chapter 3 Development of a Scanning Ion Conductance Microscope (Part I)

3.1 Introduction

As no commercial version of the SICM is available on the market to date, the microscope setup has to be described in full. This chapter is dedicated to one of two SICMs that I designed during my PhD study and used for biological experiments. Both SICMs that I built are based on the prototype that was described in the previous chapter.

The aim of this description is to provide as much information as possible to enable someone to assemble a similar microscope. Among the principles of development of the SICM brands and models of particular components that were used will be given in this chapter. However, any other similar equipment can be used for assembling the microscope.

3.2 SICM Architecture

The SICM setup consists of a number of units that are linked and communicate with each other. The diagram in Fig. 3.1 illustrates the common principle of the microscope operation.

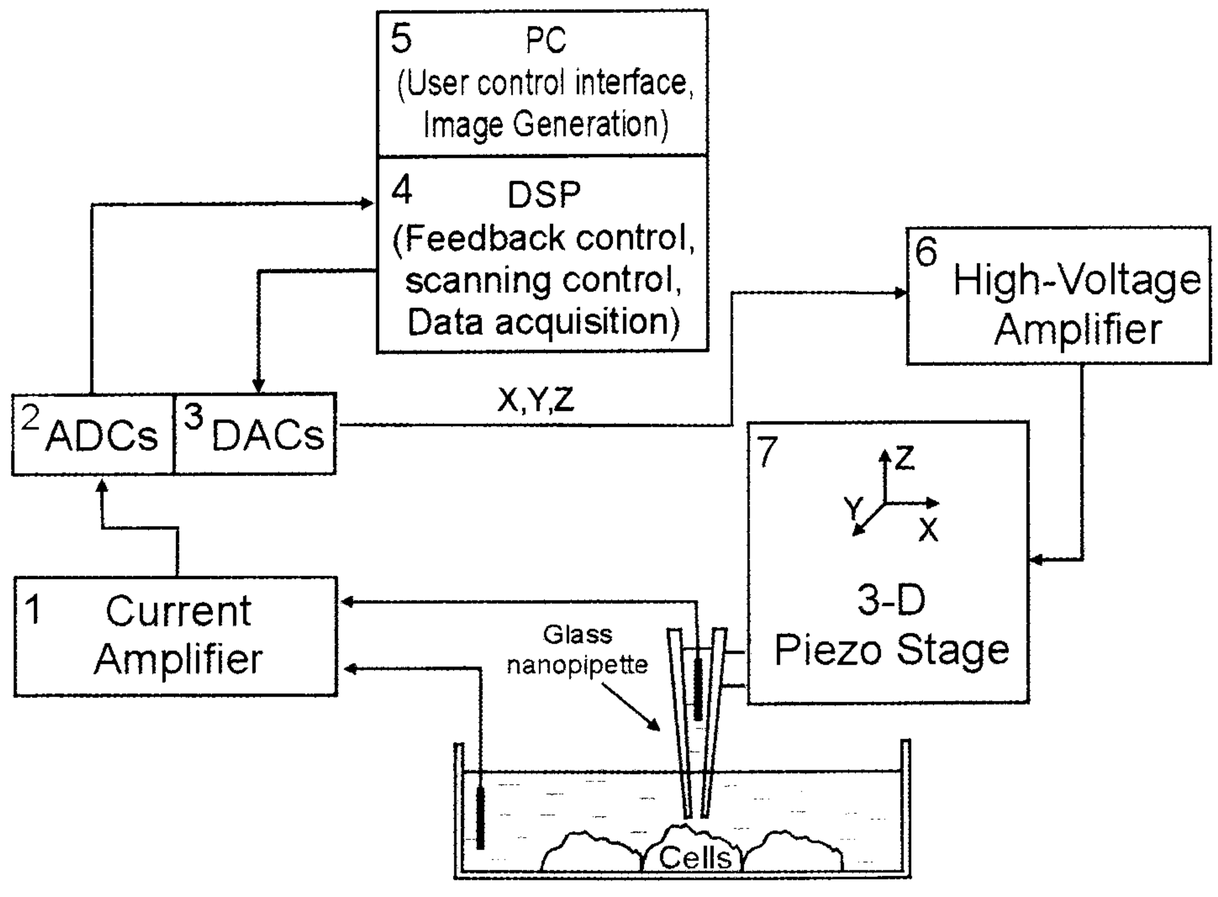

Fig. 3.1 Schematic diagram of SICM architecture.

The ion current that flows through the tip of the nanopipette is measured by the current amplifier (1). The value of the ion current depends on the position of the pipette relative to the sample. This dependency is described in the previous chapter (Fig. 1.5 and 1.6). The amplified ion current is digitised by the analog to digital converter (2) and fed into the Digital Signal Processor (DSP) (4). The DSP calculates the feedback correction signal for Z-position of the scanning pipette using the digitised ion current as an input signal. Simultaneously, the DSP generates two signals for the *x* and *y*-axes to perform raster scanning of the pipette over the sample surface. The *X, Y* and *Z* signals are then converted to analog form by the digital to analog converter (DAC) (3), amplified by the high-voltage amplifier (6) and fed into the three-dimensional piezo translation stage (7) to drive the position of the pipette. All these three signals (*X, Y* and *Z*) are transmitting to the PC (5) during scanning which generates topographical image of the scanned surface. It is also possible to record the ion current itself in relation to the *XY*-coordinates during scanning – this is known as the error signal. The error image provides additional information about the sample and enables one to estimate the efficiency of the feedback control. Also, the error image, together with the approach characteristic data, can be used for topographical image correction.

In the following paragraphs each component of the SICM will be described in detail, and some advice on how to choose, assemble and use the parts will be given.

3.3 Current Amplifier

The current amplifier was specially designed to measure the ion current through the tip of the micropipette and is based on two amplifiers: a high-impedance operational amplifier OPA129 (Burr Brown International, USA) and an instrumentation amplifier AD623ARM/BR (Analog Devices Inc. USA). The schematic diagram of the circuit is shown in Fig. 3.2.

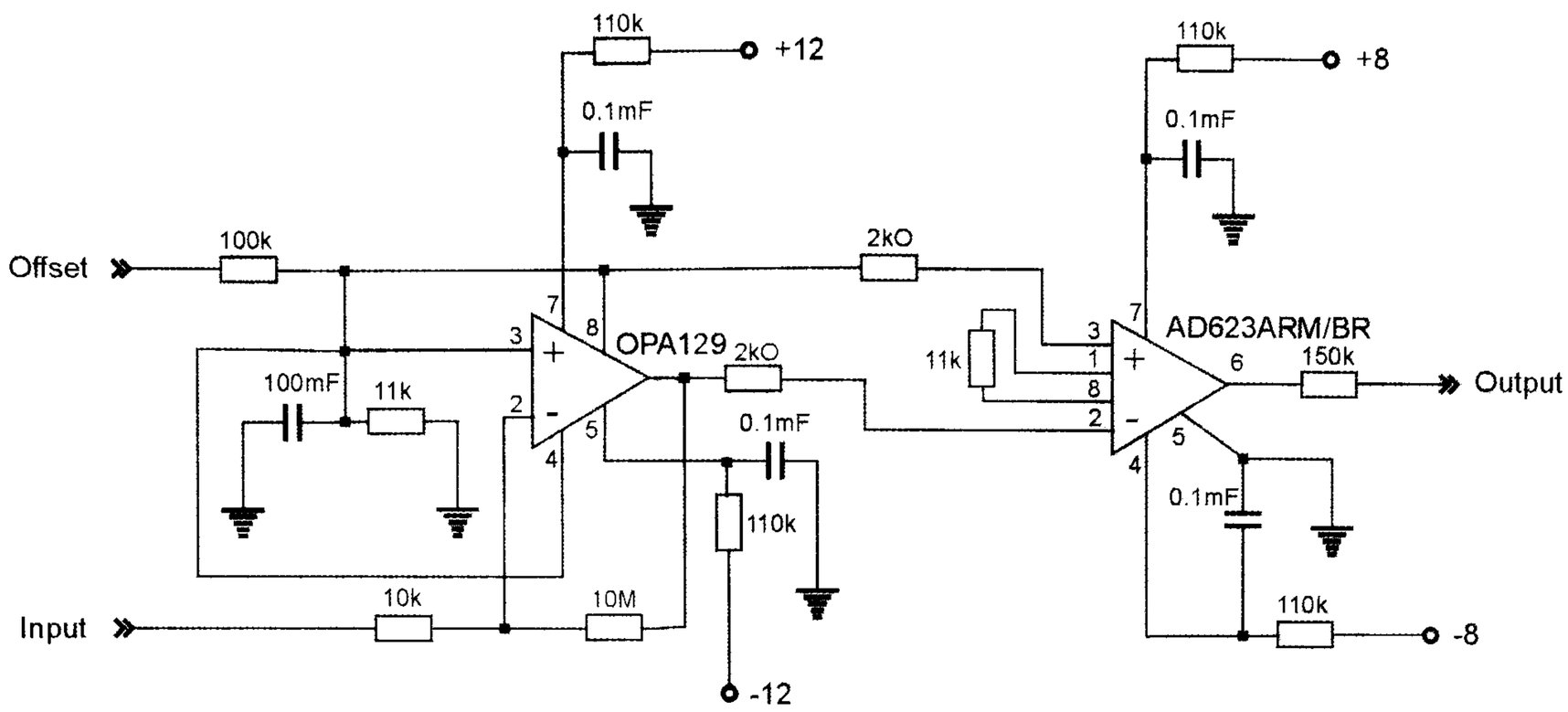

Fig. 3.2 Schematic diagram of the SICM current amplifier electrical circuit.

Depending on the system configuration the amplifier's input might be changed with the reference signal in order to achieve a better signal/noise ratio. In normal situations the input of the amplifier should be connected to the measuring electrode, and the reference connected to the ground electrode. However, the high voltages used to drive the piezo stage can cause noise on the measuring electrode inside the micropipette. If this is the case, changing the measuring and reference electrode places may reduce the noise.

3.4 Control/data acquisition system

The control/data acquisition hardware and software are produced by East Coast Scientific (Cambridge, UK). The electronics comprise a set of four stand-along digital-to-analog and three analog-to-digital converters (both 16-bit resolution) and the EISA Digital Signal Processor (DSP) card (DSP32C PC, Loughborough Sound Images plc, Loughborough, UK). The DSP card functions as a 'front-end' controller and provides digital feedback, scan control and data acquisition. The PC provides the user control interface, automated image generation, and analysis.

3.5 Positioning system

Three-dimensional and high-precision movement of the probe over the sample or sample relative to the probe is achieved by the piezo-translation stages (Tritor 100,

Piezosystem Jena, Germany), on which both the SICM probe and the sample are mounted (Fig. 3.3). The stage has a range of 100 μm in the *x, y* and *z* directions, thus the scanning of relatively large areas of biological samples is possible. As the piezo driver, a high-voltage amplifier with a high current output (System ENV 150/40, Piezosystem Jena, Germany) is used.

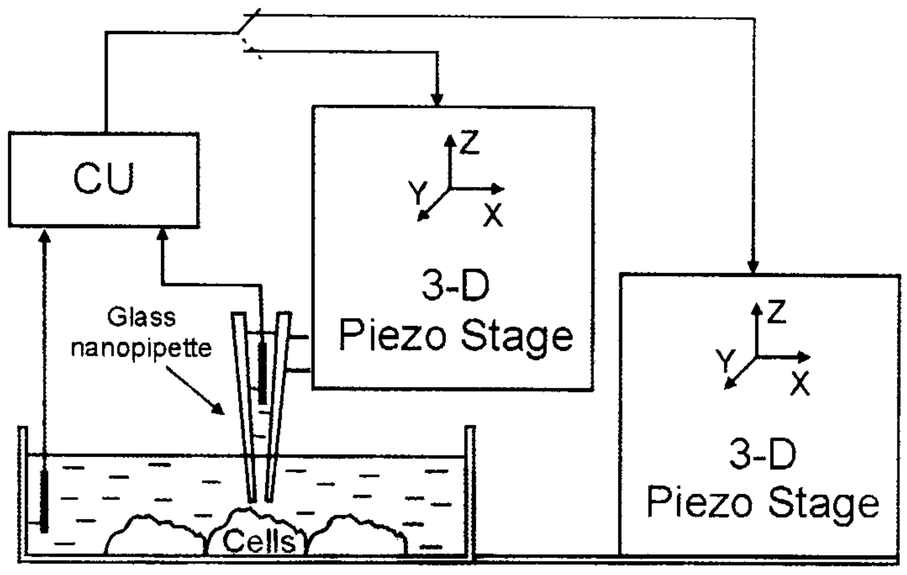

Fig. 3.3 SICM positioning system schematic diagram.
Both, the micropipette and the sample can be mounted on dedicated piezodrivers that brings additional flexibility, which is important, especially when combining SICM with other microscopy techniques.

These piezo stages can move the probe with nanometre precision when operated under resonant frequency (550 Hz for Tritor 100). In order to achieve reasonably fast scanning maintaining higher resonant frequency is preferable. However, it is well known that resonant frequency decreases dramatically with the loading, for example with 90 g of additional load the resonant frequency falls down to 340 Hz (for Tritor 100), so the clamp for a micropipette holder and the holder for a sample have to be made from lightweight material.

Although the range of the piezo stage is large compared to AFM, coarse three-dimensional adjustment should be implemented to make the approaching procedure more flexible. To achieve such adjustment, the piezo stage was mounted on two mechanical micromanipulators with 8 mm working distances (OptoSigma Corporation, USA). Used as a couple they allow us to move a probe laterally. These micromanipulators were screwed onto the microscope's adjustable platform (Modular Focusing Unit) that moves in the *z* direction and is driven by coarse and fine screws. The possibility of lateral tuning of the probe plays an important role when the tip – laser beam co-localization is necessary for the experiments described later.

3.6 Optical system

Since all components such as piezo stages and micromanipulators have small dimensions (45x45x40 mm for 3-D piezo translation stage) the scanning head of the microscope can designed to be compact, similar to those of the AFM or STM. However, SICM is mainly developed for scanning biological samples, so the optical control is necessary for rapid and pre-focused approach, and the combination with other microscopy techniques. In order to meet this requirement the scanning head was placed on an inverted optical microscope Diaphot 200 or TE Eclipse (Nikon Corporation, Tokyo, Japan). The laterally movable table of the microscope provides useful rough adjustment of the sample in the horizontal plane to select the place of interest. In addition, this model can be equipped with a number of optical ports, that can be used for various optical signal registration and recording when combining SICM with scanning confocal microscopy.

In the case of combination of the SICM and SCM the excitation light source was provided by a LCS-DTL-364 laser diode (473 nm wavelength, Laser Compact, Moscow, Russia) or a GPNT-02 laser diode (532-nm wavelength, Lasertechnik, Bremen, Germany). The inverted optical microscope was equipped with an oil-immersion objective l00X 1.3 NA. It is important to note that due to short working distance of the high-resolution objectives (for example, the working distances (WD) of the objective we used is 0.14 mm) structures higher than 0.14 mm could not be resolved. It is clear that, even the base of the conventional 35 mm diameter petri-dish is unusable, because it is 1.0 mm thick. In this case 0.08 mm thick glass cover slips as a sample substrate were used.

The emitted light of the fluorescent probe is filtered with particular narrow band filter, mounted in an epi-fluorescent filter block, to cut off all unwanted frequencies, such as autofluorescence; and collected by a photomultiplier with a pinhole (D-104–814, Photon Technology International, Surbiton, England).

Also, a video camera (JVC TK-1280E, Victor Company, Japan) and a monitor were used to simplify the process of bringing the micropipette to the control point and provide safe laser tuning.

Although the design of the SICM on the base of the optical microscope simplifies the approach procedure, this way of assembly introduces additional mechanical vibrations associated with a ‘long arm’ on which the probe is mounted in relation to the

sample. In addition, the use of an optical microscope makes the setup too bulky to be easily covered with a vibration isolating case. Therefore, for high-resolution imaging more compact design would be preferable. To reduce vibrations, the SICM was built on MICRO-g vibration isolation table (63-500 series, Technical Manufacturing Corporation, Peabody, MA, USA). The more detailed description of the mechanical and electrical noise isolation measures is given appendix.

3.7 Micropipettes and electrodes

The micropipette probe is one of the most crucial parts of the SICM experiments, since the diameter of the micropipette's opening defines the lateral resolution of the scan.

The ideal micropipette has to have a "short" taper in order to have a "low" resistance and a "high" stiffness, and a "small" diameter of opening. Low resistance provides higher signal to noise ratio and high stiffness results in less vibrations.

The diameter of the micropipette's opening and final taper length depends on the pulling procedure and the glass that capillaries are made from.

Micropipettes in our experiments were prepared from borosilicate glass, quartz capillaries (Intracell Ltd, UK) or aluminosilicate glass capillaries (Harvard Apparatus, UK) capillary outer diameter is 1.00 mm and inner diameter is 0.58 mm with an inner filament. For micropipette fabricating a CO_2 laser powered pipette puller P-2000 (Sutter Instrument Co, USA.) was used. The tip size of the pipettes was 200 nm approximately. They were pulled according to the instruction manual (1993). A typical example of a pipette similar to that was used is shown in Fig. 3.4 (*A* and *B*).

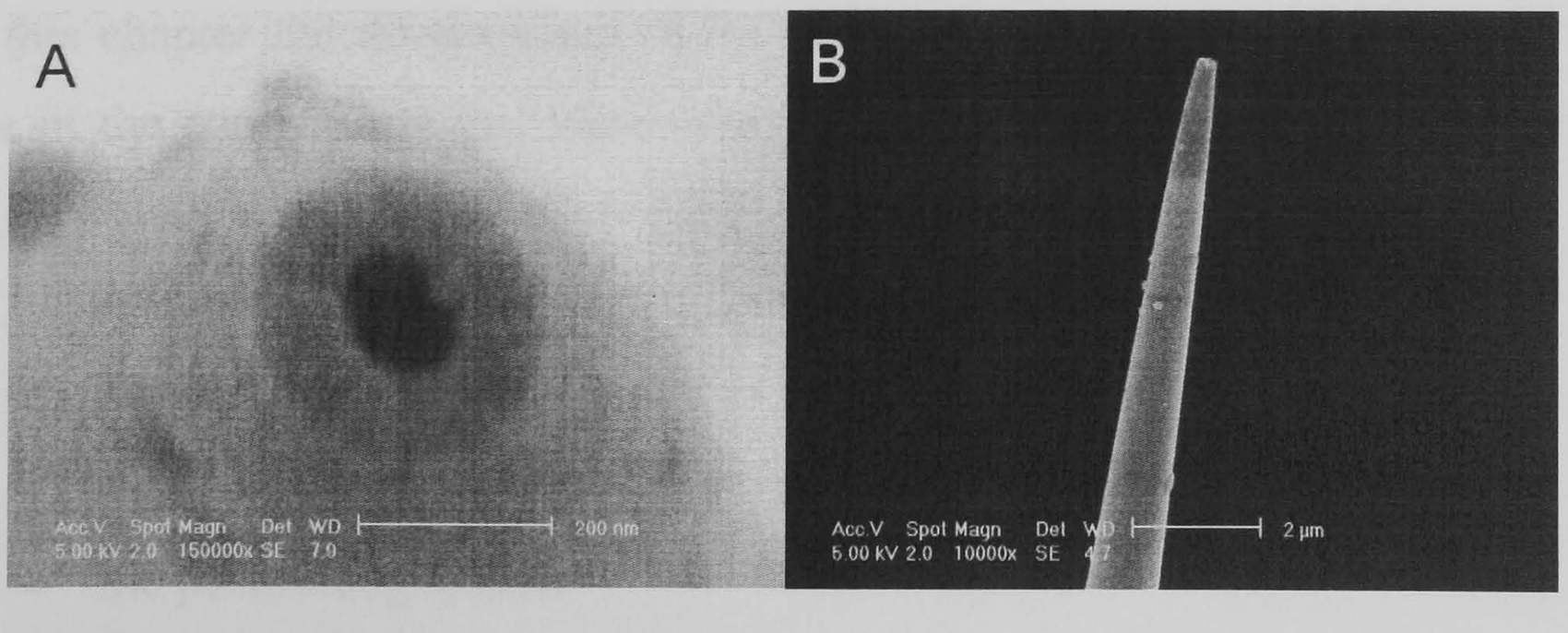

Fig. 3.4 SEM images of typical scanning micropipettes.

Different models of micropipette pullers are extensively used in biological research of cells, and all of them relate closely to Brown and Flaming design. In brief, the pulling process based on heating a small volume of the glass capillary which is held under tension by the two pulling holders. The small volume of heat is achieved by a local application of laser beam or coil shape heater (filament). As the temperature increases the glass starts to melt and the tension stretches the capillary. When the velocity of stretching reaches a certain specified value a stronger stretching force is applied to the holders. During this stretching, the laser is turned off, after which the glass cools. When the temperature of the capillary falls below melting point the applied tension fractures the glass to leave a flat end face of the micropipette.

Micropipettes were held in E-Series micropipette holders (Warner Instrument Co., USA.) with a side port, which was used for pressure application. A special clamp was designed, and mounted directly on the piezo stage for fixation of the micropipette holder.

In order to provide electrical connection similar to those used in an electrophysiological patch-clamp procedures, Ag/AgCl electrodes are used in our system. E200 Ag/AgCl pellet electrodes (Warner Instrument Co., USA.) are used as a reference electrode. The measuring electrode is made by chloriding silver wire by electrolysis dissociation in 0.1M KCl with 9V DC for 1.5 – 2 hours.

3.8 Summary

In this chapter the development of the SICM setup has been described with the examples of the components that were used. In particular, advice on how to chose or design:

- the current amplifier
- the control/acquisition system
- the positioning system
- the optical system

- the micropipettes and electrodes

was given. This chapter also described the common principles of the SICM architecture and operation.

Chapter 4 Improvements of Scanning Ion Conductance Microscope control

4.1 Introduction

This chapter is focused on the two major modifications that have been made to the original SICM with the aim to improve the reliability of the system and to increase its functionality.

The approach characteristic of the SICM was analysed and its non-linear behaviour was corrected by the introduction of additional coefficient. This correction allowed more accurate imaging and simplified the procedure of scanning parameters adjustment.

The DC current that is used by the SICM as a feedback signal has considered to be not stable enough, so a distance-modulated control was developed. The implementation of the distance-modulated control made the SICM control robust enabling long-term imaging. Subsequently, the existing control software was modified and the scanning procedure was automated.

4.2 Non-linearity correction

Classical integral feedback control was implemented in the original program to achieve a constant distance between the probe and the sample. An integral controller has an output u proportional to the integral of its input e, that is:

$$u = K_1 \int e(t)dt \tag{4.1}$$

where K_I is proportionality constant and e is an error signal that in our case is determined as:

$$e = V_{ADC} - SP \tag{4.2}$$

where V_{ADC} is the voltage read from the ADC that presents the position of the piezo stage e.g. probe position, and *SP* is a set point (DiStefano et al., 1990) that in our case determines probe – sample separation.

As can be seen from Fig. 2.3 the ion current function of the distance between the tip and the sample is not linear (inset in Fig. 4.1), so the error signal *e* behaves differently when approaching to or retracting from the surface. For example, if the tip is at a distance of one radius of the aperture from the sample, and suddenly some feature on the surface appears on the scanning path, the ion current decreases dramatically. In turn, the feedback retracts the probe from the sample producing the 'rising surface' on the topography image, but then it has to re-approach the surface in order to follow the surface. However, if the tip is at a distance from the sample that is more than one radius, the ion current reaches a plateau and the error signal stays approximately constant. As a result, the probe moves towards the surface with a constant speed, which might be not fast enough. Schematically this is shown in Fig. 4.1 *A*.

Increasing the K_1 coefficient (Eqn. (4.1)) can force the system to move the probe more rapidly down to the surface on the second slope, but on the other hand it causes overshoot on the first slope, as in Fig. 4.1 *B*.

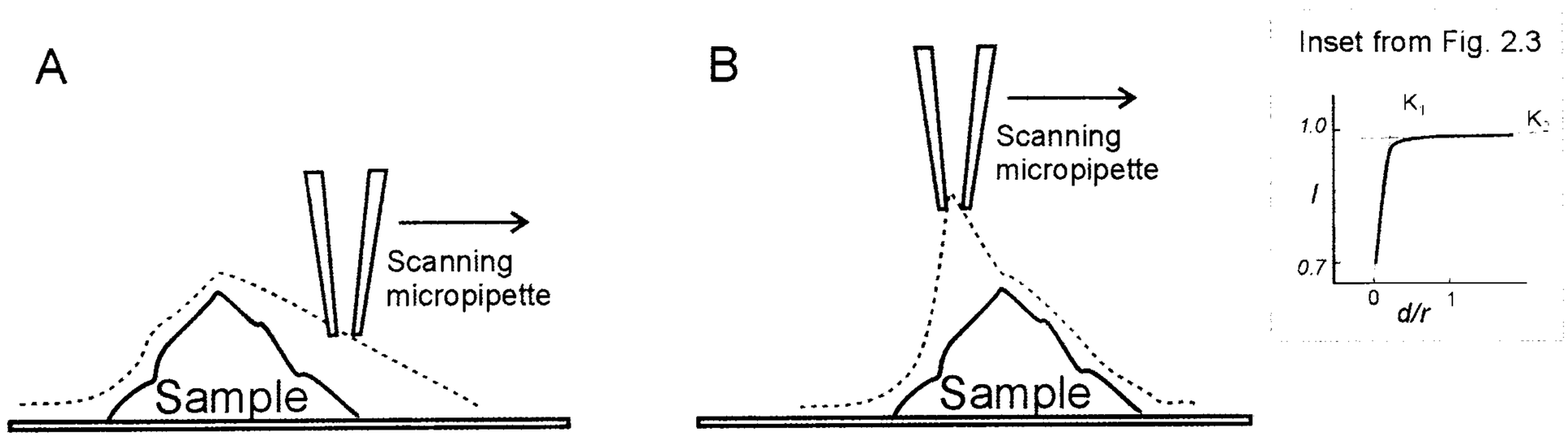

Fig. 4.1 Artefacts caused by non-linear approach characteristic.
(*A*) The value of the feedback control gain (K_1) can be optimal to correctly follow the front slope of the sample, but insufficient to trace the rear slope. Higher values of gain can lead to overcompensated reaction when scanning the front slope (*B*). Inset shows the SICM approach characteristic and two proposed coefficients (K_1 and K_2) that can be used when scanning at different values of ion current.

Therefore, we concluded that using only one coefficient K_1 could cause an artefact. Although this artefact could be avoided by slowing the scanning speed to allow the probe to better follow the sample surface, such a reduction in scanning speed is not always acceptable.

In order to improve the quality of the feedback control the following modifications to the software (East Coast Scientific, Cambridge, UK) have been made according to the DSP32C manual (1995).

Ideally, the an array of coefficients should be calculated for a particular approaching characteristic, however it is complicated to modify the existing scanning software to implement such an algorithm. Alternatively, for simplicity the approach characteristic (Fig. 4.1, inset) can be approximated to two linear dependencies. Therefore, we coupled a second coefficient K_2, to K_1, and the output function u derived as:

$$u = \begin{cases} K_1 K_2 \int e(t)dt; e \le 0 \\ K_1 \dfrac{1}{K_2} \int e(t)dt; e > 0 \end{cases} \tag{4.3}$$

Depending on the sample, coefficient K_2 can be set to a value that makes the probe follow both slopes equally as shown in Fig. 4.2.

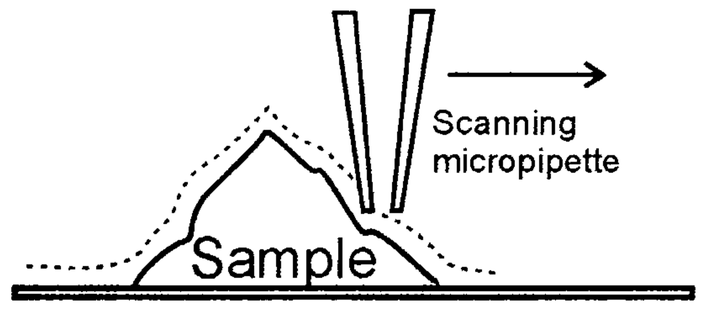

Fig. 4.2 Corrected non-linearity artefact.
Schematic diagram shows the scanning micropipette following the front and rear slopes equally.

Although, with the implementation of the additional coefficient K_2 the overall number of control parameters become higher, the procedure for setting up the values of the parameters that are needed to correct artefacts of control and reproduce topography more accurately become easier. In practice we found that in most cases in order to achieve the correct topography for the majority of cell samples the coefficient K_2 has to be equal to 0.6.

4.3 Distance modulated control

The original SICM control described above uses DC ion current that flows through the tip of the micropipette as a feedback signal to control tip-sample separation during scanning. Unfortunately, the feedback signal can easily be affected by the drift of DC current, which can happen, for example as a result of solution conductivity change, or pipette partial blockage by contaminants that are always present in biological media. Such dependency makes it difficult to use the microscope for relatively long and/or complicated experiments, especially when changes of bathing medium osmolarity are necessary.

In order to make the SICM scanning procedure more reliable attempts were made to use alternative methods of micropipette – sample separation distance control. One of the methods involved a combination of SICM with scanning force microscopy (Mosbacher et al., 1996) and another method operated the SICM in a pulse-mode (Mann et al., 2002).

We have developed a distance-modulated protocol for scanning ion conductance microscopy to provide a robust and reliable distance control mechanism for imaging living cells (Shevchuk et al., 2001). Soon after a similar technique was independently proposed by Pastre and co-workers (Pastre et al., 2001).

This protocol allows us to modulate the ion current flowing through the microscope micropipette, and to use this ion current for feedback control of our microscope. The principle of the method is shown in Fig. 4.3.

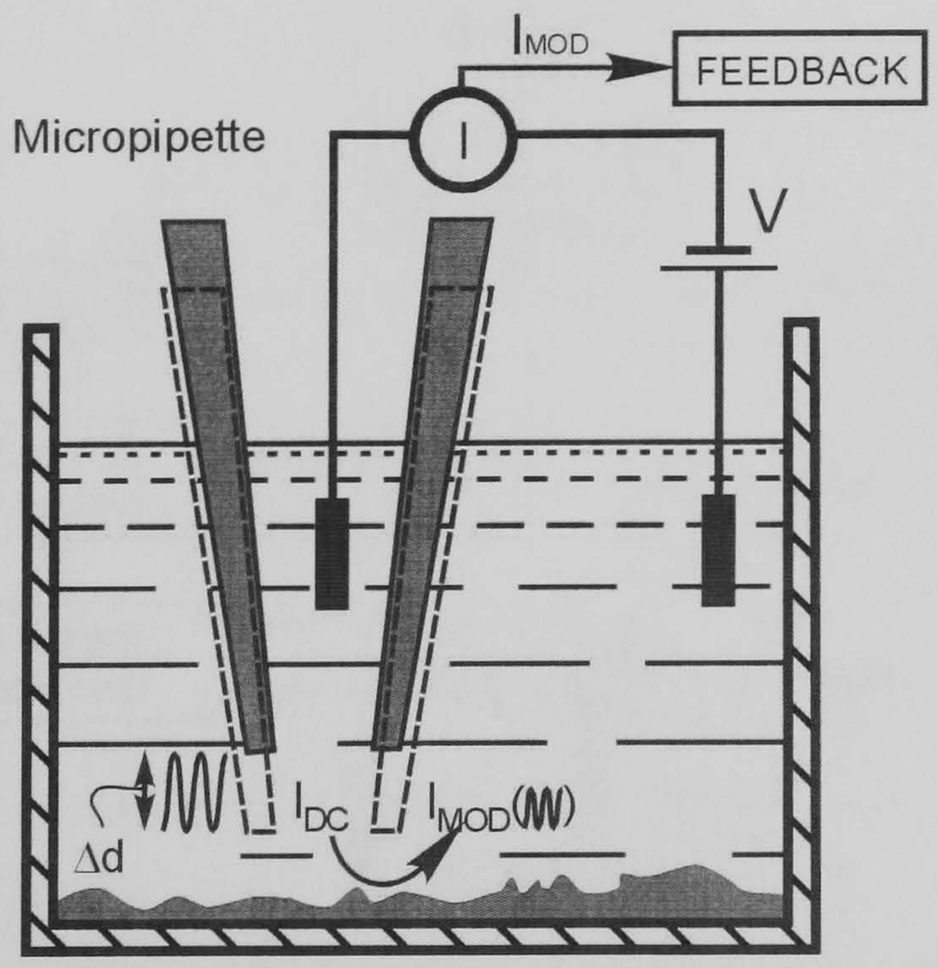

Fig. 4.3 Distance modulated control principle of operation.

In this method, the modulation of the micropipette-sample distance by Δd results in an additional component in micropipette current - modulated current (I_{MOD}), which is used for feedback control.

In the distance-modulated mode of the SICM operation, the movement of the microscope tip/sample (Δd) generates a modulated current (I_{MOD}) that is present in the overall current (I in Fig. 2.3). To perform distance modulation an AC voltage was applied to the piezo on which the sample or pipette was mounted. The frequency of modulation might vary from 100 to 10,000 Hz depending on the piezo loading. Piezo loading lowers the resonance frequency of the piezo and hence lowers the maximum modulation frequency possible. We operate close to this limit but we also selected modulation frequencies away from the noise in our system such as any harmonics of mains frequency. Typically, for a sample with an elaborate surface, we select a control point close to the radius of the pipette tip aperture, and the modulation distance is about 20 % of the radius.

The schematic diagram of the SICM with distance-modulated control is presented in Fig. 4.4. As can be seen, general arrangement remains similar to previously described (see paragraph 3.2).

The modulated ion current (Fig. 4.3) is measured by a current amplifier (1) and then fed into a lock-in amplifier (8) (SR830 DSP, Stanford Research Systems, Sunnyvale, CA). The same lock-in amplifier serves as a functional generator and supplies sinusoidal signal to modulate the micropipette.

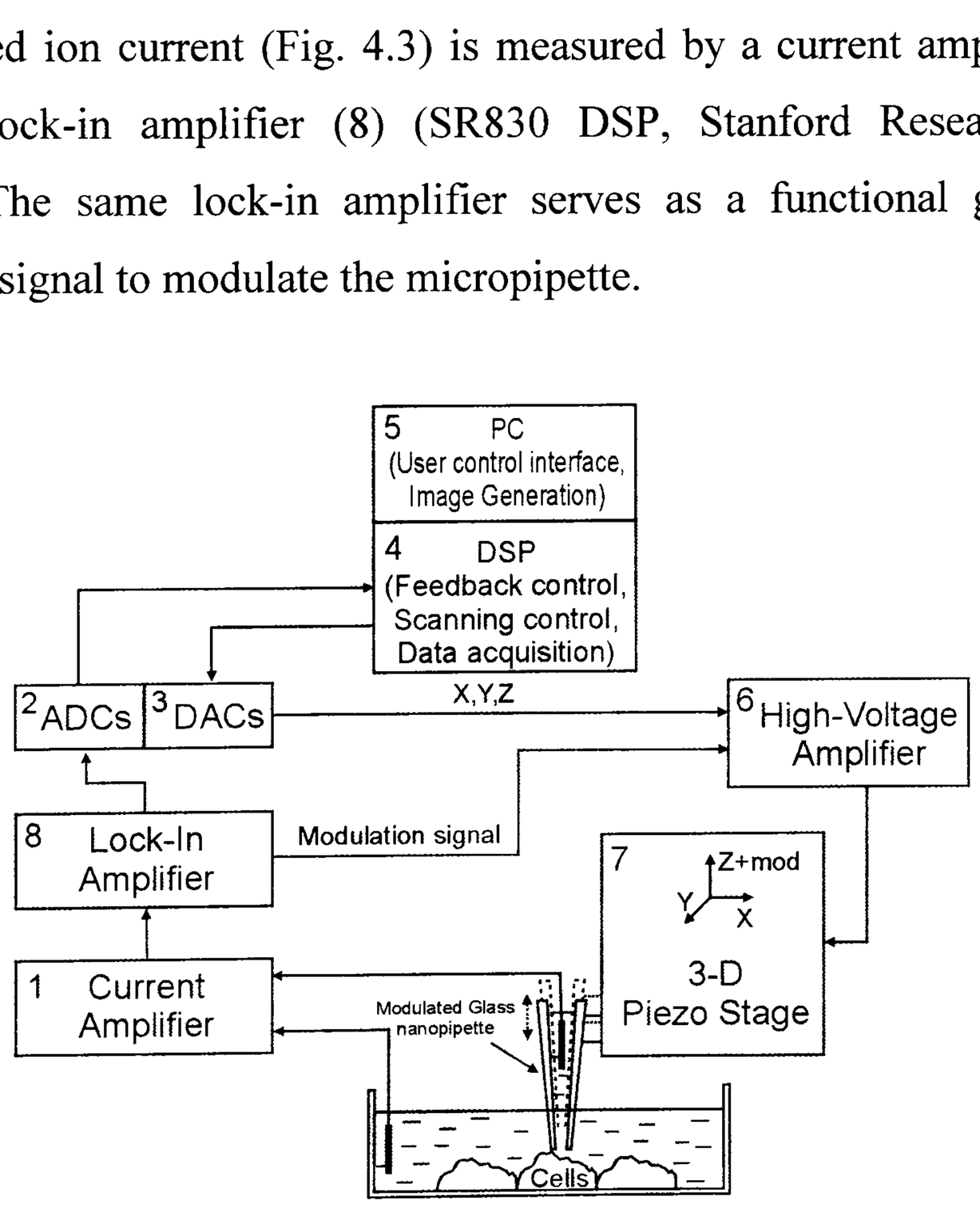

Fig. 4.4 Schematic diagram of the SICM setup with distance modulated control.

The piezodrive (7) modulates the scanning micropipette generating modulated ion current that flows through the tip of the pipette. The ion current is measured by the current amplifier (1), then fed into the lock-in amplifier (8), digitised by the analog to digital converter (2) and processed by the Digital Signal Processor (DSP) (4). The DSP calculates the feedback correction signal for Z-position of the scanning pipette using the digitised ion current as an input signal. Simultaneously, the DSP generates two signals for the *x* and *y*-axes to perform raster scanning of the pipette over the sample surface and the modulation signal (sine wave). The *X, Y* and *Z* signals are then converted to analog form by the digital to analog converter (3), amplified by the high-voltage amplifier (6) and fed into the three-dimensional piezo translation stage (7) to drive the position and modulate the pipette. All these three signals (*X, Y* and *Z*) are transmitted to the PC (5) during scanning which generates topographical image of the scanned surface.

The lock-in amplifier uses a technique known as phase-sensitive detection to single out the component of the signal at a specific reference frequency and phase.

Experimentally it was found that the phase of the modulated ion current shifts unpredictably during the scanning although the phase of the modulation signal applied to the piezo actuator was stable. Unfortunately, we cannot explain the nature of this phenomenon.

The output signal of the phase sensitive detector (PSD) of the lock-in is given by:

$$Vpsd = 1/2 \cdot V_{SIG} \cdot V_L \cdot \sin(\omega_{SIG} \cdot t + \Theta_{SIG}) \cdot \sin(\omega_L \cdot t + \Theta_{REF}) \qquad (4.4)$$

where V_{SIG} and V_L are amplitudes, ω_{SIG} and ω_L are frequencies, and Θ_{SIG} and Θ_{REF} are phases of the input signal, which in our case is modulated ion current, and lock-in reference signal correspondingly, and t is time. In case if the frequencies of the lock-in reference and modulated ion current signals are equal and the PSD output is passed through a low pass filter, the expression can be simplified to:

$$Vpsd = 1/2 \cdot V_{SIG} \cdot V_L \cdot \cos(\Theta_{SIG} - \Theta_{REF}) \qquad (4.5)$$

However, as can be seen, not only do the frequencies have to be the same, the phase between the signals have not to change with time, otherwise $cos(\Theta_{SIG} - \Theta_{REF})$ will change and the output signal of the phase sensitive detector V_{psd} will not be a DC signal. In other words, the lock-in reference has to be locked to the modulated ion current reference.

If a lock-in amplifier has a second PSD the phase dependency can be eliminated by operating in magnitude (R) mode. In this case the second PSD multiplies the input

signal with the lock-in reference signal shifted by 90°, thus generate second output proportional to sine of phase difference. By computing magnitude *R* as:

$$R = 1/2 \cdot V_{SIG} \cdot V_L \cdot \sqrt{\cos^2(\Theta_{SIG} - \Theta_{REF}) + \sin^2(\Theta_{SIG} - \Theta_{REF})} \qquad (4.6)$$

the phase dependency can be removed. In this case lock-in measures the input signal amplitude at the reference frequency and does not depend upon the phase between reference and modulated ion current.

In our experiments lock-in amplifier *R* output signal provides an input signal for the feedback loop calculated by DSP (Fig. 4.4, component 4), which controls the vertical probe (sample) position during lateral scanning.

The approach characteristics shown in Fig. 4.5 illustrate the dependence of I_{MOD} current signal with the distance of the micropipette from the sample surface. In contrast to the I_{DC}, which is at maximum when the pipette is a long way from the surface (Fig. 4.5 *A*), I_{MOD} is only generated when the probe senses the sample, and increases dramatically as the probe approaches the surface (Fig. 4.5 *B*). I_{MOD} reaches a maximum value at the point when the pipette touches the surface.

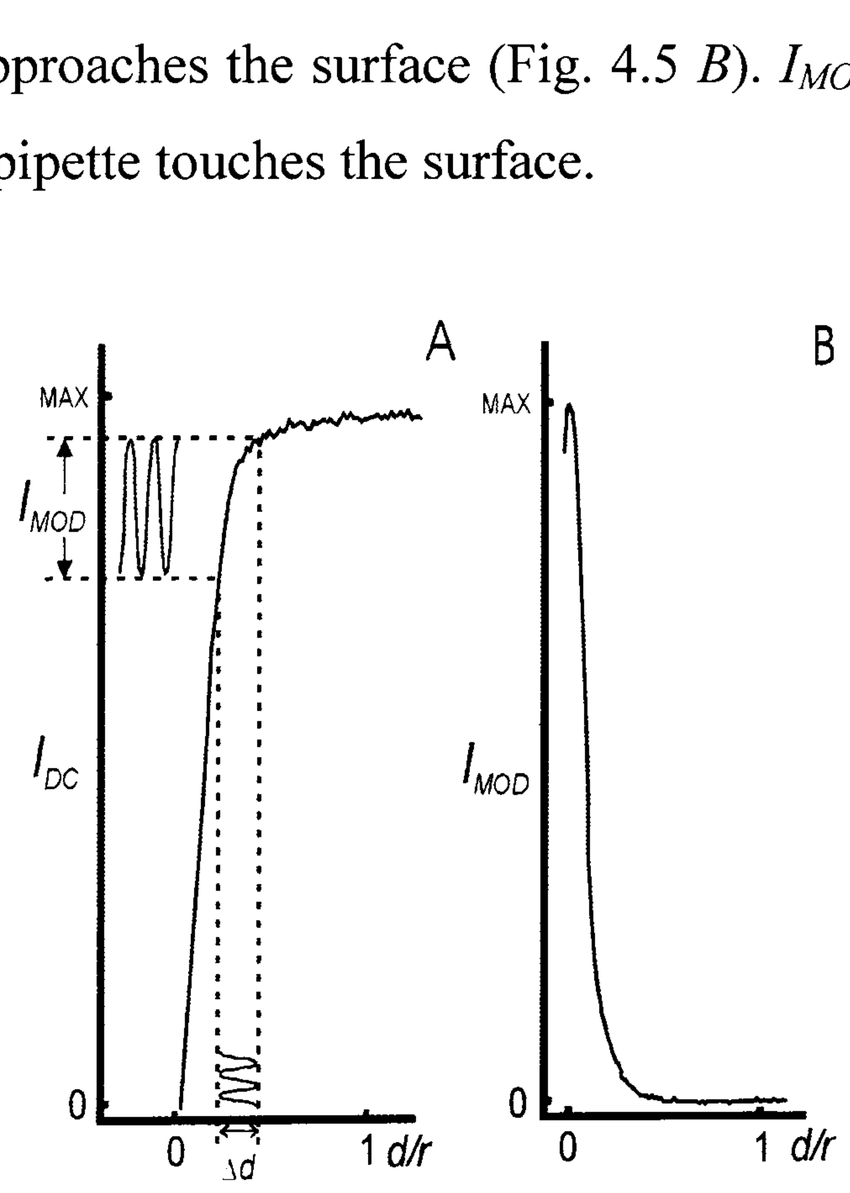

Fig. 4.5 Approach characteristic of the SICM with distance modulated control.
Experimental approach characteristics for I_{DC} and I_{MOD} showing the DC current modulation. Both approach characteristics (I_{MOD} and I_{DC} vs. *d*) were obtained on a flat plastic surface (bottom of a 35 mm petri dish) in phosphate-buffered saline, pH 7.4. I_{MAX} was 3.1 nA and 100 nm pipette tip radius (*r*) was used. (*A*) The modulation of DC current that is used for feedback control. The actual approach illustrates characteristically how the overall current, I_{DC}, varies with the distance between the sample and the micropipette, *d*. The DC current reaches the MAX point when the distance between the micropipette and a sample become greater or equal than the micropipette tip radius, *r*. Modulation of the sample-micropipette distance by Δd results in a modulated

current I_{MOD}. Note the size of I_{MOD} depends strongly on *d*. (*B*) Actual approach characteristics for I_{MOD}. Note the signal increases rapidly as the distance between the sample and micropipette becomes small.

Most successful scanning in non-modulated SICM can be achieved at the distance of around one micropipette tip radius from the sample surface which gives a range of set point current within 97% and 99,8% of I_{MAX} (micropipette tip current far from the surface) (Korchev et al., 1997a). This means that any changes in the value of the non-modulated current that exceeds 0.2 – 3% of I_{DC} will affect the feedback control, even making control impossible. In the distance-modulated mode of the SICM operation, the optimal scanning distance is also around one micropipette tip radius from the surface which gives a modulated current (I_{MOD}) that stays in the same optimal range of 0.2 – 3% of I_{DC}. In this case significant changes in the value of I_{DC}, even 100%, will induce a proportional change in I_{MOD} (from 1% to 2% of I_{DC}) still keeping I_{MOD} in the optimal range for the feedback control. This provides a robust feedback control that can tolerate significant changes in ion current due to DC drift or blockage of the pipette, changes in the ionic strength of the solution, or changes in the applied voltage. Distance modulation therefore makes the approach of the micropipette to the surface straightforward and allows one to perform complicated physiological experiments that require alteration of ionic strength of the media. With our modulated protocol we have been able to continuously scan living cells for more than 24 hours and to change ionic strength of the media by up to 4 times during the scanning process without loss of feedback control.

4.4 Continuous imaging

Biological experiments often require continuous observations during which all stages of particular process can be imaged. With the implementation of the distance modulated control such experiments become possible. In order to handle relatively long experiments, the original program has been modified. The modifications allow topological changes to be automatically monitored, processed and saved as a sequence of images during selected period of time. All other channels of the instrument that carry additional information such as error signal (current), reverse topography, fluorescent signal etc. can be also processed in parallel.

4.5 Summary

In this chapter the weaknesses of the SICM principle of operation were analysed and the ideas on how to improve it were proposed. As a result, the following features were added to the SICM:

- non-linearity correction
- distance modulated control
- continuous imaging

All of the added features were found to be very effective. The non-linearity correction rectified the artefact related to the non-linear approach characteristics of SICM, and hence made it possible to scan a larger variety of samples.

The distance modulated control greatly improved reliability of the scanning procedure allowing long-term imaging under various physiological conditions. When long-term imaging became possible, the control software was then modified and the scanning procedure was automated.

The next chapter presents the set of experiments where the distance-modulated control was tested and the results achieved. In later chapters if this thesis it will be shown how other improvements of SICM improve imaging.

Chapter 5 Study of contracting cardiac myocyte

5.1 Introduction

Several aims were set when planning the study of cardiac myocytes and experiments with the SICM. The first was to test the distance modulated SICM control and estimate the level of its reliability in order to perform continuous real-time measurements in extreme conditions.

The second aim was to utilize the combination of SICM and scanning confocal microscopy to follow the local calcium changes just under the cell membrane of the cardiac myocyte during contraction.

5.2 Scanning over a contracting cardiac myocyte

To demonstrate the reliability of the distance modulated SICM control we have chosen to measure the dynamics of cardiac myocytes that undergo regular contractions, since this represents an extreme case of rapid cellular motion.

Firstly, the image under conditions of low calcium was taken to obtain a topographic image of the surface of quiescent cardiomyocyte (for cell preparation procedure see appendix). The topographic image of a small area of living cardiac myocyte taken using the distance modulation control is shown in Fig. 5.1. It clearly illustrates the Z-grooves the regions where the cardiomyocyte plasmalemma is anchored to an intracellular cytoskeleton to form grooves, and give cardiac myocytes a characteristic scalloped surface.

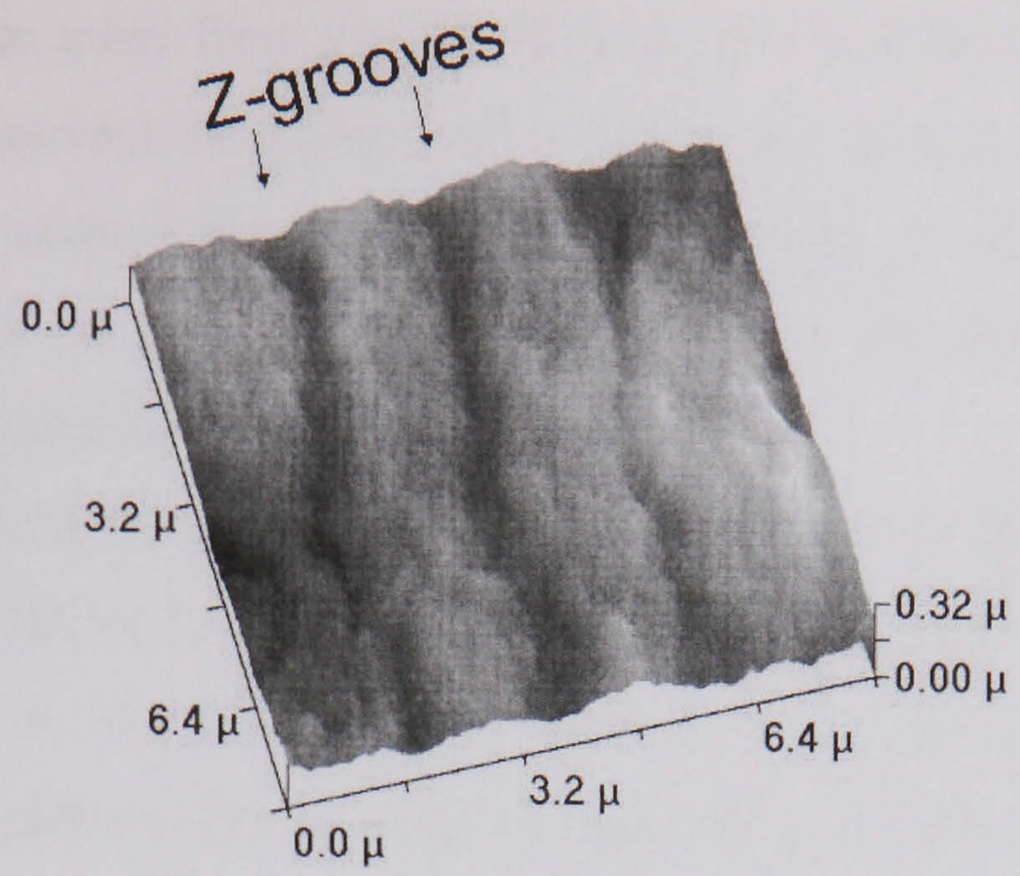

Fig. 5.1 SICM image of the cardiac myocyte under low calcium conditions.
A typical image of a quiescent cardiac myocyte obtained using distance-modulation control at 198 Hz frequency of modulation. The *Z*-grooves are marked on the image with the *arrows*.

At higher calcium concentration the cell undergoes spontaneous contractions. Fig. 5.2 shows a topographic image taken of a contracting cardiac myocyte using distance modulation control.

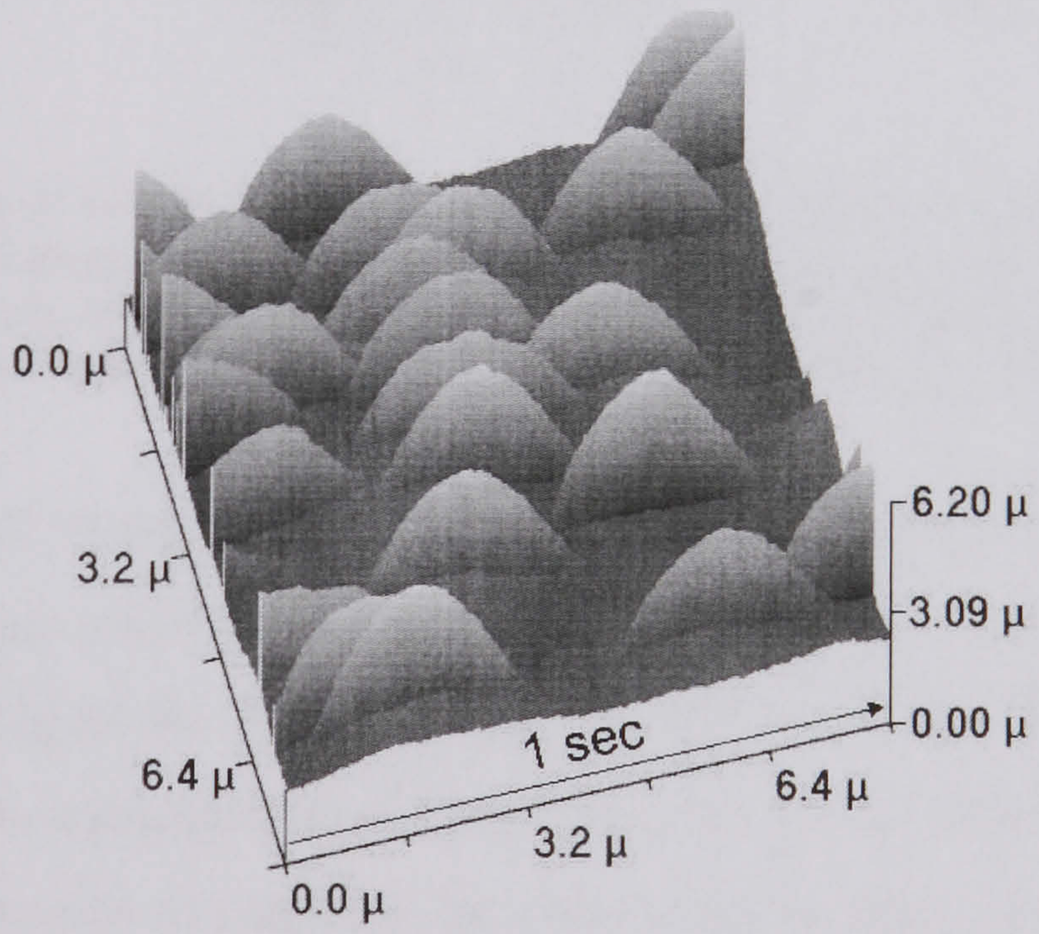

Fig. 5.2 SICM image of the cardiac myocyte under high calcium conditions.
An image of a similar cell under conditions of high calcium where the cell undergoes spontaneous contractions. Each peak on the cardiomyocyte surface was formed by the membrane rising. This was the result of a contraction during the line scan.

It can be seen from the figure that the extent of the vertical cell motion is up to 4 µm and most contractions are similar. The increase of the cell height of 4 µm during contraction within approximately 200ms, which is at a rate of rise of about 20 nm per

ms. The pipette is 75 nm away from the cell surface and the feedback control needs to operate within 4ms to prevent the pipette touching the cell surface during contraction. Since we can reliably control the probe over a contracting cell, it means that the feedback control works on a millisecond timescale and we can determine height changes with this time resolution.

In order to validate the method, we have also combined SICM with simultaneous optical measurements. SICM has been combined with Scanning Near Field Optical Microscope (Korchev et al., 2000c) (see section 2.4.4 Fig. 2.6 for details) to demonstrate that it is possible to image a contracting cardiac myocyte.

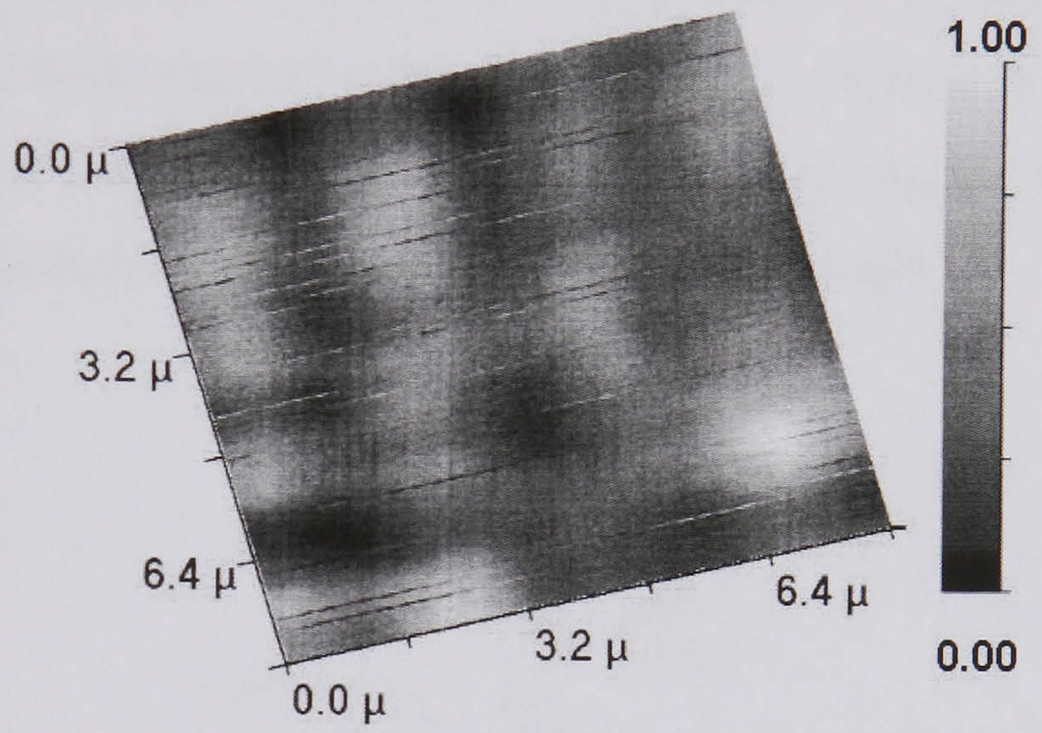

Fig. 5.3 SNOM image of the cardiac myocyte under high calcium conditions.
A SNOM image obtained simultaneously with the topographic image in (Fig. 5.2) using distance-modulation control. The dark regions are *Z*-lines that correspond to *Z*-grooves (Fig. 5.1, marked with *arrows*). The *gray scale bar* represents the optical signal in arbitrary units.

The SNOM optical image of a contracting cardiac myocyte taken simultaneously with SICM using distance-modulated control is shown in Fig. 5.3. The grey scale bar represents the optical signal in arbitrary units. As shown by the SNOM image, the position of Z-grooves on topographical picture (Fig. 5.1) closely matches the position of Z-bands, and the cell appears to return to the same position after contraction. The thin lines in the SNOM image are due to the change in the structure imaged under the pipette during the contraction. The large motions observed during contraction make the interpretation of the topographic image (Fig. 5.2) more complicated. However the contractions of the cardiac myocyte (the thin lines in Fig. 5.3) are clearly visible.

This experiment shows that the distance-modulated protocol is efficient enough to cope with scanning over a contracting cardiac myocyte and obtain a simultaneous optical image.

5.3 Simultaneous measurement of membrane dynamics and intra-cellular calcium

To measure the relationship between the local membrane motion and local calcium concentration SICM was combined with laser confocal microscopy (see paragraph 2.4.3 Fig. 2.5).

The schematic of this set-up is shown in Fig. 5.4. In these experiments the sample stage was moved up and down during scanning to maintain a constant distance between the pipette and the cell surface. The pipette, objective, and confocal volume stayed fixed. This means that, even during contraction, the fluorescence was recorded at the same distance below the cell membrane. The distance the stage was moved and the intensity of the fluo-3 fluorescence were simultaneously recorded.

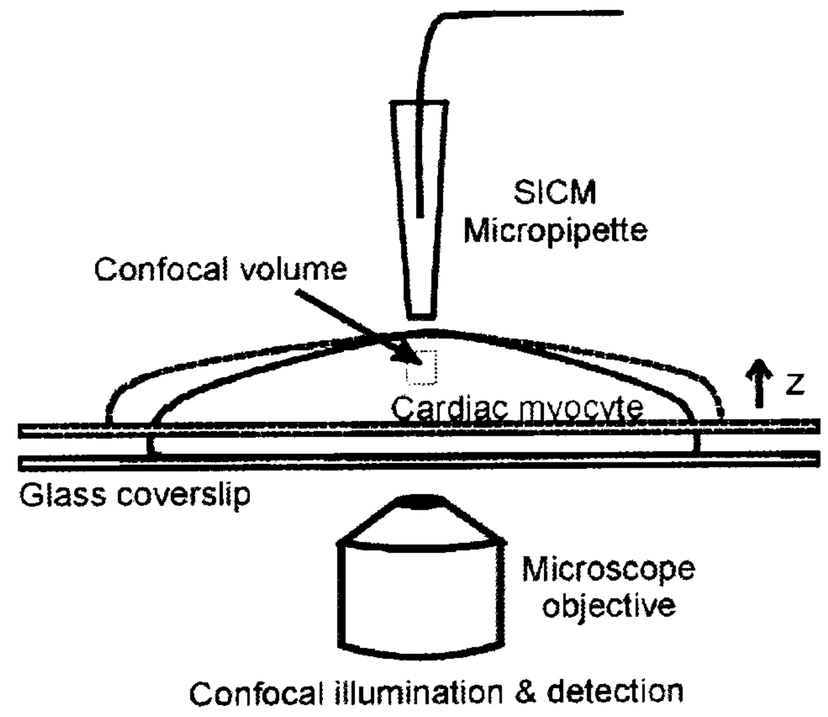

Fig. 5.4 Schematic diagram of simultaneous contraction amplitude and local calcium concentration recording.
When the cardiac myocyte contracts the feedback control moves the sample stage to maintain a constant distance between the micropipette and the cell surface. The confocal volume probed, therefore, remains at the same point below the cell surface.

The confocal volume was centred at the tip of the micropipette by focusing the laser onto a top surface of the coverslip and bringing the pipette into control above the surface. It was centred in the *xy* plane by filling the pipette with laser dye and adjusting the pipette position in the *xy* direction for maximum fluorescence. The position of the pipette was noted on the camera monitor and the pipette was then positioned so as to appear at this point on the monitor before any experiment. This was found to be a reproducible way to position the pipette, in the *xy* direction, in the laser focus. We

estimate that we probed a confocal volume approximately 500 nm in diameter and 2 μm in length centred at the tip of the pipette. This means that we probed the intracellular calcium within a μm of the cell membrane.

The relationship between the intracellular calcium concentration and whole cell contraction has previously been studied by optical methods (Cross et al., 2000;O'Rourke et al., 1990;Ozaki et al., 1999;Schneider et al., 1994). These methods are non-perturbative, and capable of following fast dynamics, but in general, the minimum size of motion detected is restricted to the diffraction limit for light. The results achieved with SICM can be compared with these optical measurements.

The results of the simultaneous measurement of the local membrane motion and relative calcium concentration just below the cell membrane at the centre of a contracting neonatal cardiac myocyte (for cell preparation procedure see appendix) are shown in Fig. 5.5.

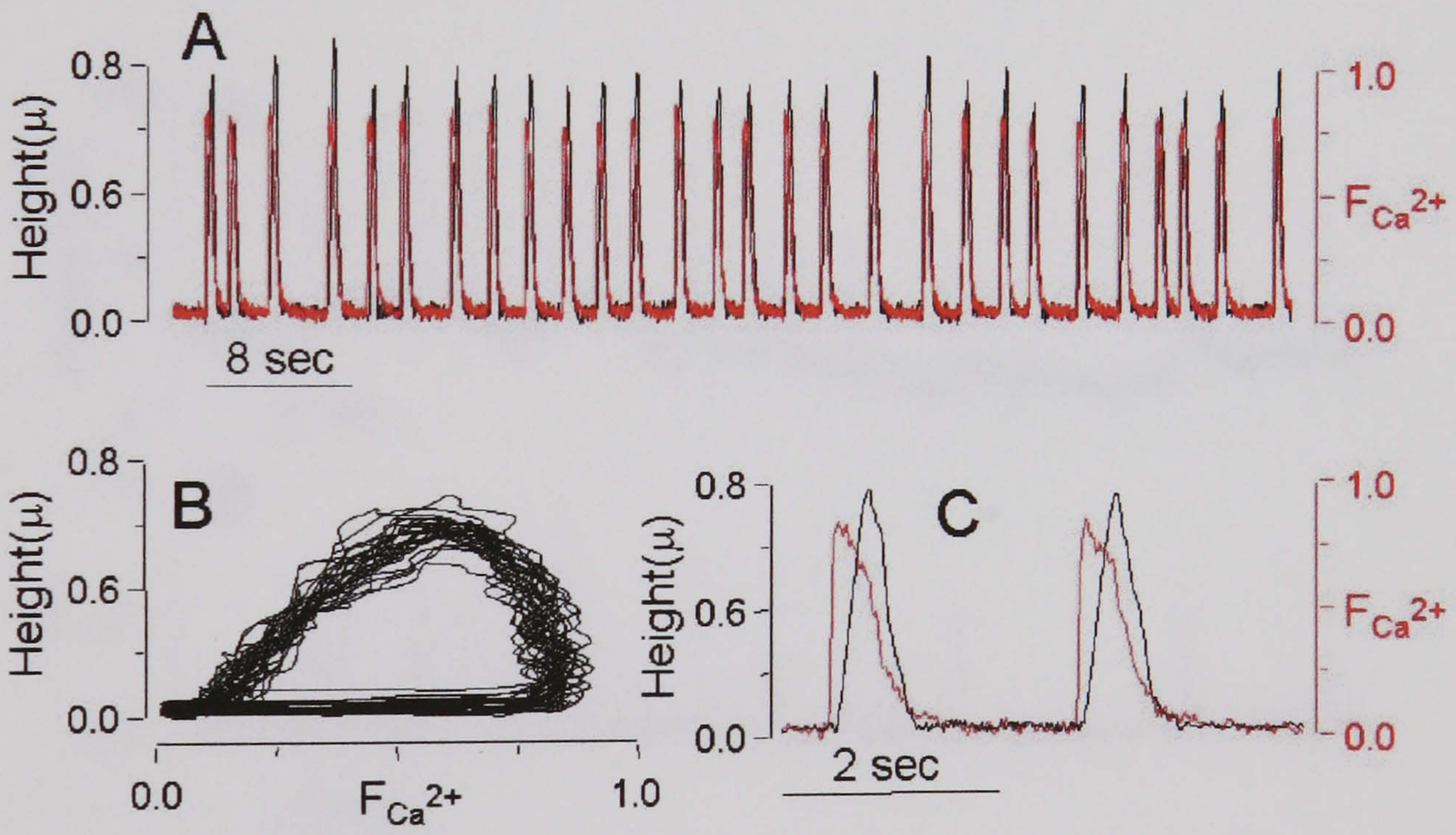

Fig. 5.5 Simultaneous high amplitude contraction and calcium dynamics recordings. (*A*) A simultaneous measurement of the position of the surface of 3-day-old cultured rat cardiac myocyte and the local relative calcium concentrations just below the cell surface. (*B*) A plot of cell height versus relative calcium concentration for all the contraction in (*A*). (*C*) A blow-up of two of the contractions in (*A*).

Note, the regular changes in calcium level, and resulting height changes (Fig. 5.5 *A* – traces superimposed). The rate is 35 beats per minute. Fig. 5.5 *B* is a phase plot and illustrates the variation in cell height with calcium level (Fig. 5.5 *B* is an overlay of all the contractions in Fig. 5.5 *A*). All the curves are very reproducible and correlate with each other. There is a mechanical diastole – the myocyte is relaxed, where there is a

rapid change in calcium but no contraction. This is followed by contraction of the cell and consequent change in cell height to reach the maximum height. The calcium then falls (some pumped out, some exchanged with sodium, most taken up by the sarcoplasmic reticulum) and following this the cell returns to its original height. Fig. 5.5 *C* shows two contractions on an expanded time base showing the rapid rise in intracellular calcium followed by changes in cell height. As expected, the calcium increases first, and is followed by the local motion. There is a delay of about 250 ms between the calcium and contraction peaks. The cell height changes show a symmetric shape indicating that the contraction and relaxation processes take approximately similar times. In contrast the calcium increase is much more rapid than the calcium decrease resulting in an asymmetric peak shape. This is similar to what has been observed on whole cell studies (Barrigon et al., 1996).

Fig. 5.6 shows the simultaneous height (panel *A*) and calcium (panel *B*) changes over a cell in a network of one day old cardiac myocytes.

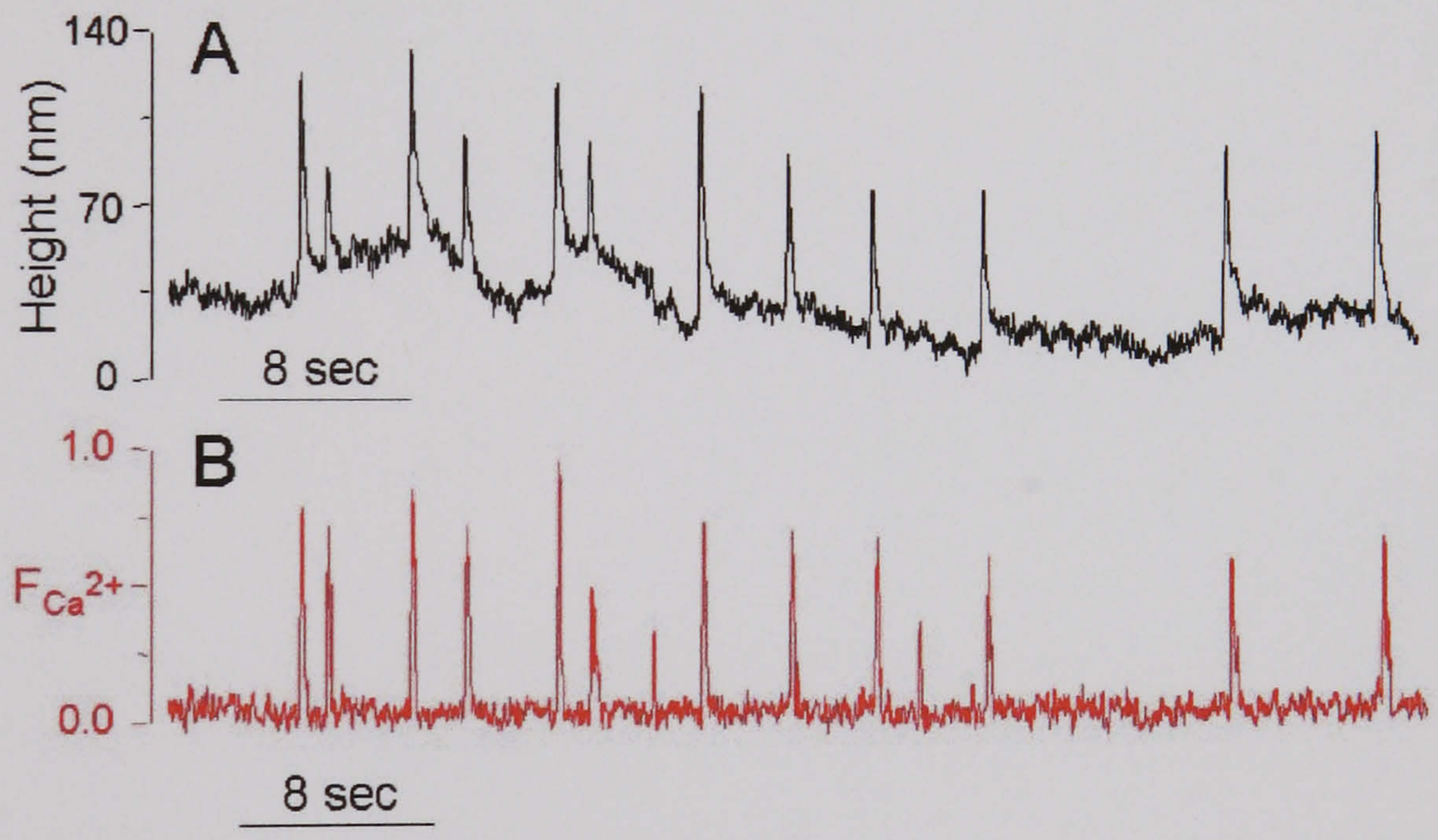

Fig. 5.6 Simultaneous low amplitude contraction and calcium dynamics recordings. The simultaneous measurement of the cell height (*A*) and relative calcium concentration (*B*) of 1-day-old cultured cardiac myocyte.

These show irregular and much smaller contractions compared to the mature adult cardiac myocytes but these nanometric motions are still detectable. There are also undulations of the cell height that do not correspond to any calcium changes. A control experiment over a glass surface with the same feedback parameters used for cell height measurements showed a constant value with less than 10 nm noise. This indicates that these undulations are real motions of the cell surface. Currently we do not know the

origin of these changes. These low-frequency motions may be undulations of the membrane as the result of osmoregulation and slow changes in cell volume, and further work is needed to understand this observation.

5.4 Conclusions

In principle, it would have been possible to perform these experiments using non-modulated current for feedback control. However, in practice, this is not a robust control mechanism be cause of DC drift.

SICM with distance modulated control in combination with other techniques open the possibility of performing new types of experiments on dynamic living cells because they provide a means to perform high-resolution topographic imaging and simultaneous measurement of the local concentration of many important cellular properties such as calcium, pH, and voltage.

Chapter 6 Bile acid taurocholate impairs rat cardiomyocyte function: a proposed mechanism for intra-uterine fetal death in obstetric cholestasis

6.1 Introduction

The implementation of the distance modulated control and the combination of the SICM and SCM methods made possible further detailed study of a potential mechanism(s) of intra-uterine fetal death in obstetric cholestasis (OC). The study was originally initiated by C. Williamson and J. Gorelik (Williamson et al., 2001).

Obstetric cholestasis is a liver disease of pregnancy that can cause fetal distress, spontaneous prematurity and unexplained intrauterine death (Fisk and Storey, 1988;Reid et al., 1976;Reyes, 1982;Rioseco et al., 1994). OC is characterized by maternal pruritus (itchiness) and abnormal liver function tests, including raised serum primary bile acids which can increase 100-fold and return to normal within one week of delivery of the baby (Bacq et al., 1995;Laatikainen and Ikonen, 1977;Laatikainen and Tulenheimo, 1984;Sjovall and Sjovall, 1966). Raised maternal bile acid levels have been shown to be associated with fetal distress (Laatikainen and Ikonen, 1977;Laatikainen and Tulenheimo, 1984), and it has been proposed that raised maternal and fetal bile acids are the cause of the fetal complications of OC (Bacq et al., 1995;Heikkinen et al., 1980;Laatikainen and Ikonen, 1977;Laatikainen, 1975).

It was not possible to investigate the effects of bile acids on the intact human fetal heart at a cellular level. Therefore, C. Williamson and J. Gorelik decided to use the closest available model of fetal myocardium at term: a primary culture of neonatal rat in which cells beat synchronously and develop pacemaker activity (for cell preparation procedure see appendix). Their study revealed that bile acid taurocholate impairs rat cardiomyocyte function. It was shown that the primary bile acid taurocholate (in concentrations of 0.3 and 3.0 mM) reversibly decreases the rate of contraction and the proportion of beating cells ($P < 0.001$) in cultures of neonatal cardiac myocytes. Also, confocal microscopy measurements indicated that taurocholate results in the loss of

integrity of synchronously beating network and alters calcium dynamics of cardiac myocytes.

C. Williamson and J. Gorelik hypothesized by that neonatal cardiomyocytes are more susceptible to the effects of bile acids than their adult counterparts, as mothers with OC have not been reported to develop dysrhythmias.

6.2 Changes in rat cardiomyocyte contraction induced by bile acid taurocholate

In the present study (Gorelik et al., 2002b) the effect of taurocholate on cultured cardiomyocytes was investigated further.

The isolated adult rat cardiomyocytes were used as the adult model to allow the comparison of the results obtained from both neonatal and adult cells. The effect of taurocholate on the contraction amplitude of adult rat cardiomyocytes was also investigated, so the results could be compared with the neonatal cells (for cell preparation procedure see appendix).

The maternal total bile acid concentration has been reported to be over 0.2 mM in some studies (Dixon et al., 2000;Shaw et al., 1982) but we decided to study a range of concentrations of taurocholate starting at 0.05 mM, as this corresponds to the level commonly found in the maternal serum. We also aimed to investigate in more detail the events that follow the addition of taurocholate to cells. The combination of SICM and SCM was used to analyse the different types of rhythm disturbance that were observed in a previous investigation (Williamson et al., 2001). This allowed us to measure simultaneously the rate, amplitude and rhythm of contractions and corresponding intracellular calcium changes.

A typical measurement of cell vertical displacement prior to the addition of taurocholate (TC) is shown in Fig. 6.1 (*A*).

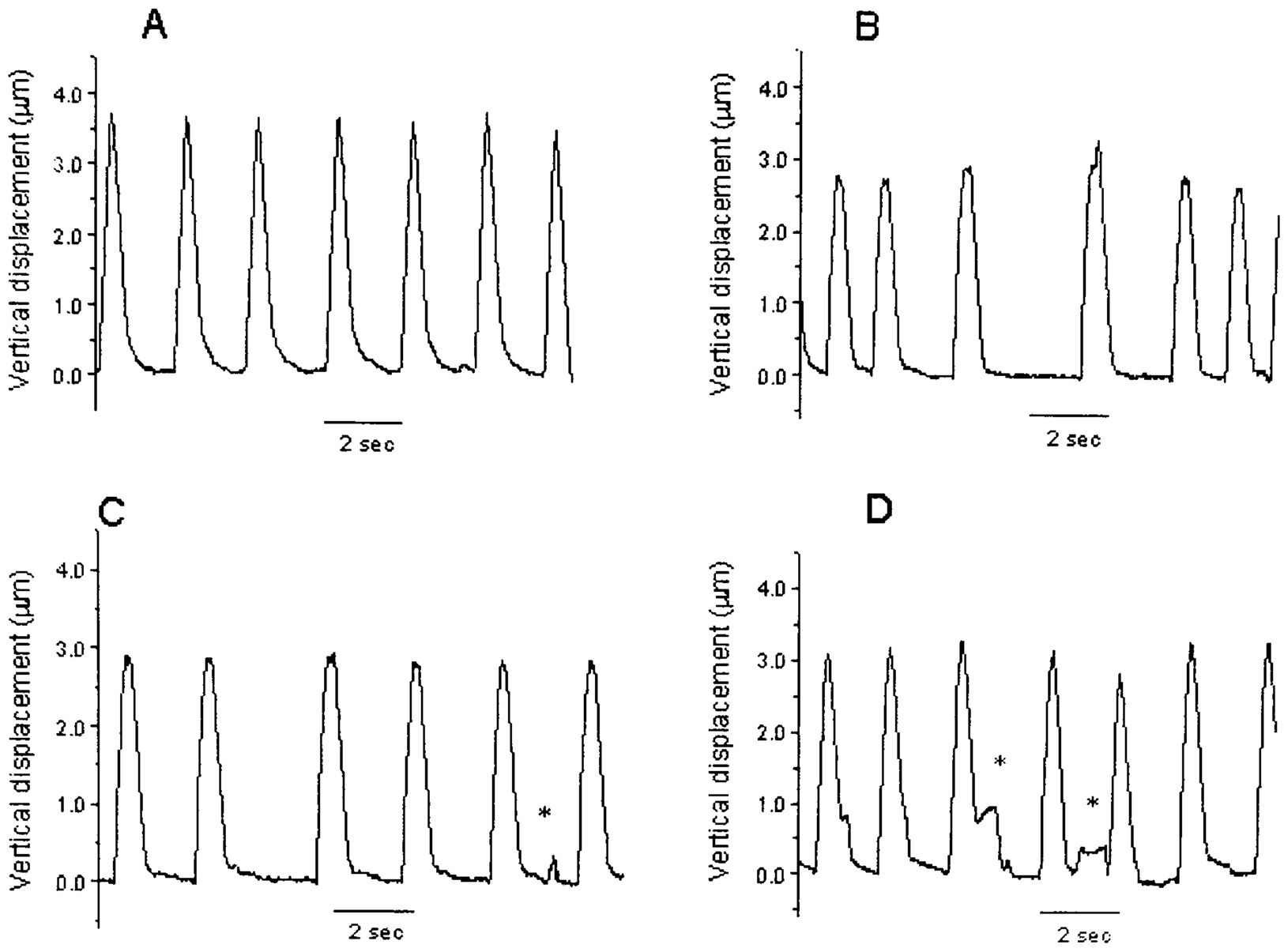

Fig. 6.1 Effect of 0.1 mM taurocholate on the contraction of an individual newborn rat cardiomyocyte in culture.
(*A*) Control; (*B, C* and *D*) examples of rhythm disruption; n=7 observations. Asterisks indicate displacements of small amplitude.

The cell is contracting rhythmically at a mean rate of contraction of 42 b.p.m., with an amplitude of 3.7 µm. Fig. 6.1 (*B*), (*C*) and (*D*) show examples of rhythm disturbances after applying 0.1 mM TC to newborn rat cardiomyocytes in culture and demonstrate an overall reduction in amplitude of contraction from 3.7 µm to 3 µm ± 0.4 µm. Fig. 6.1 (*B*) and (*C*) also reveal a slight reduction in the rate of contraction from 42 b.p.m. to 36 b.p.m. Additional displacements of small amplitude (0.25 – 0.5 µm) are seen in Fig. 6.1 (*C*) and (*D*) (marked by asterisks). This type of behaviour was observed in seven preparations.

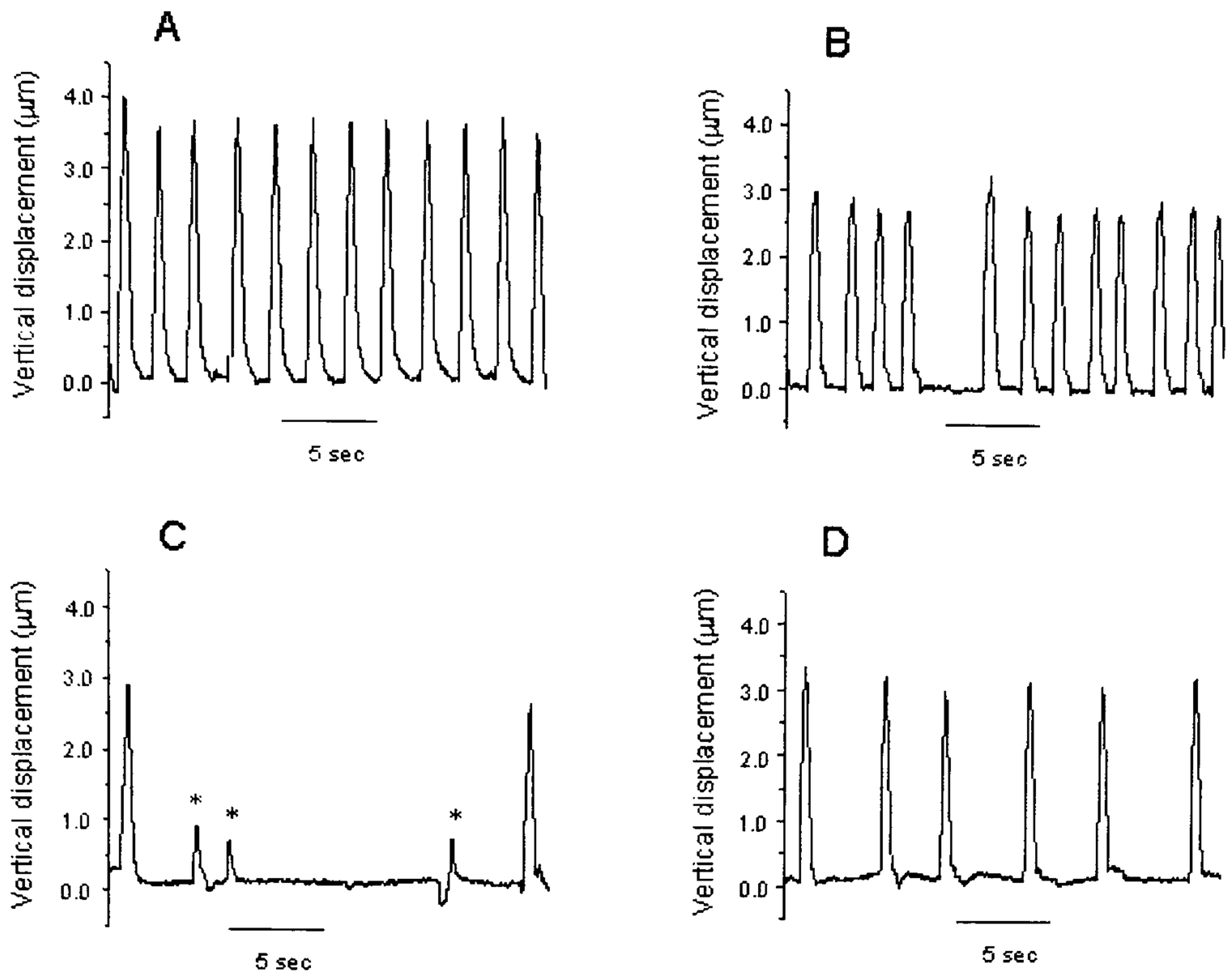

Fig. 6.2 Effect of 1 mM taurocholate, and of transfer to taurocholate-free medium, on the contraction of a newborn rat cardiomyocyte.
(*A*) Control; (*B*) 1 min and (*C*) 20 min after the addition of taurocholate to the culture medium; (*D*) 1 h after transfer to taurocholate-free medium; n=8 observations. Asterisks indicate displacements of small amplitude.

Fig. 6.2 and 6.3 illustrate the effect of 1 mM taurocholate on different individual cardiomyocytes with and without subsequent recovery. Control measurements are shown in panels (*A*) for both cases. Fig. 6.2 (*B*) and (*C*) demonstrates a reduction in the amplitude of contraction from 3.7 µm to 3.0 µm. Twenty minutes after addition of taurocholate the overall rate of contraction reduced by 58% from 36 b.p.m. to 15 b.p.m. However, a large number of these beats (Fig. 6.2 *C*) were small (0.5-0.75 µm, represented by asterisks). After recovery the rate of contraction was 18 b.p.m., slower than the rate before addition of taurocholate (Fig. 6.2 *D*).

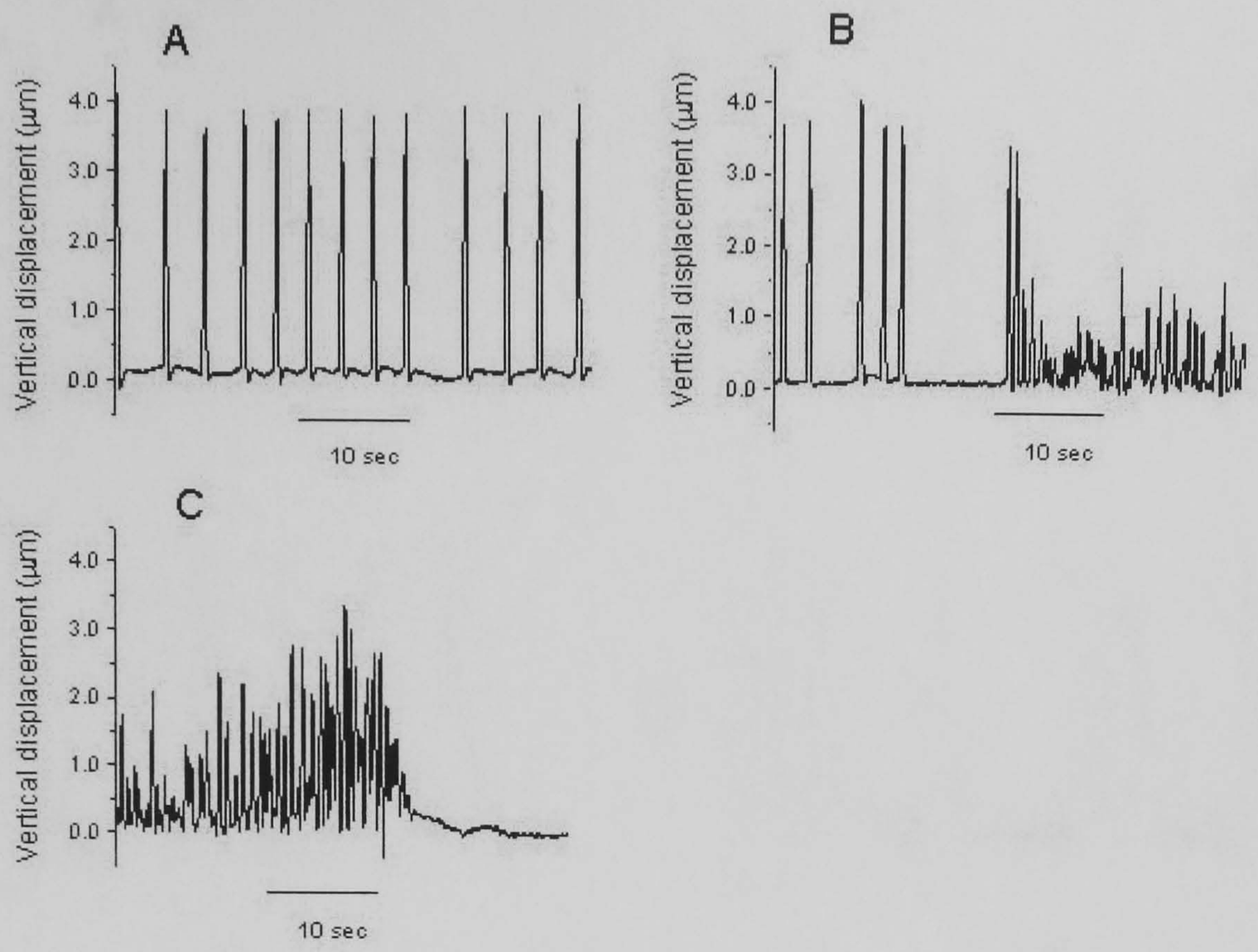

Fig. 6.3 Effect of 1 mM taurocholate on the contraction of a newborn rat cardiomyocyte. (*A*) Control; (*B*) 2 min and (*C*) 10 min after the addition of taurocholate to the culture medium; n=4 observations.

Fig. 6.3 illustrates the example when some cells did not recover after 1 mM taurocholate treatment. This cell initially contracted at a normal rate and rhythm with the amplitude of about 4 µm (Fig. 6.3 *A*). Two minutes later, after addition of taurocholate at 1.0 mM the overall rhythm was disturbed (Fig. 6.3 *B*) with subsequent deterioration into oscillations. Ten minutes after taurocholate (Fig. 6.3 *C*) these small oscillations ceased leaving a quiescent cell.

6.3 Changes in rat cardiomyocyte calcium dynamics induced by bile acid taurocholate

Neonatal cardiac myocyte membrane and calcium dynamics were measured as described in paragraph 5.3 (for cell preparation and loading procedure see appendix).

Fig. 6.4 (*A*) and 6.5 (*A*) present measurements of local motion (upper traces), and relative calcium concentration just below the cell membrane (lower traces) prior to the addition of taurocholate.

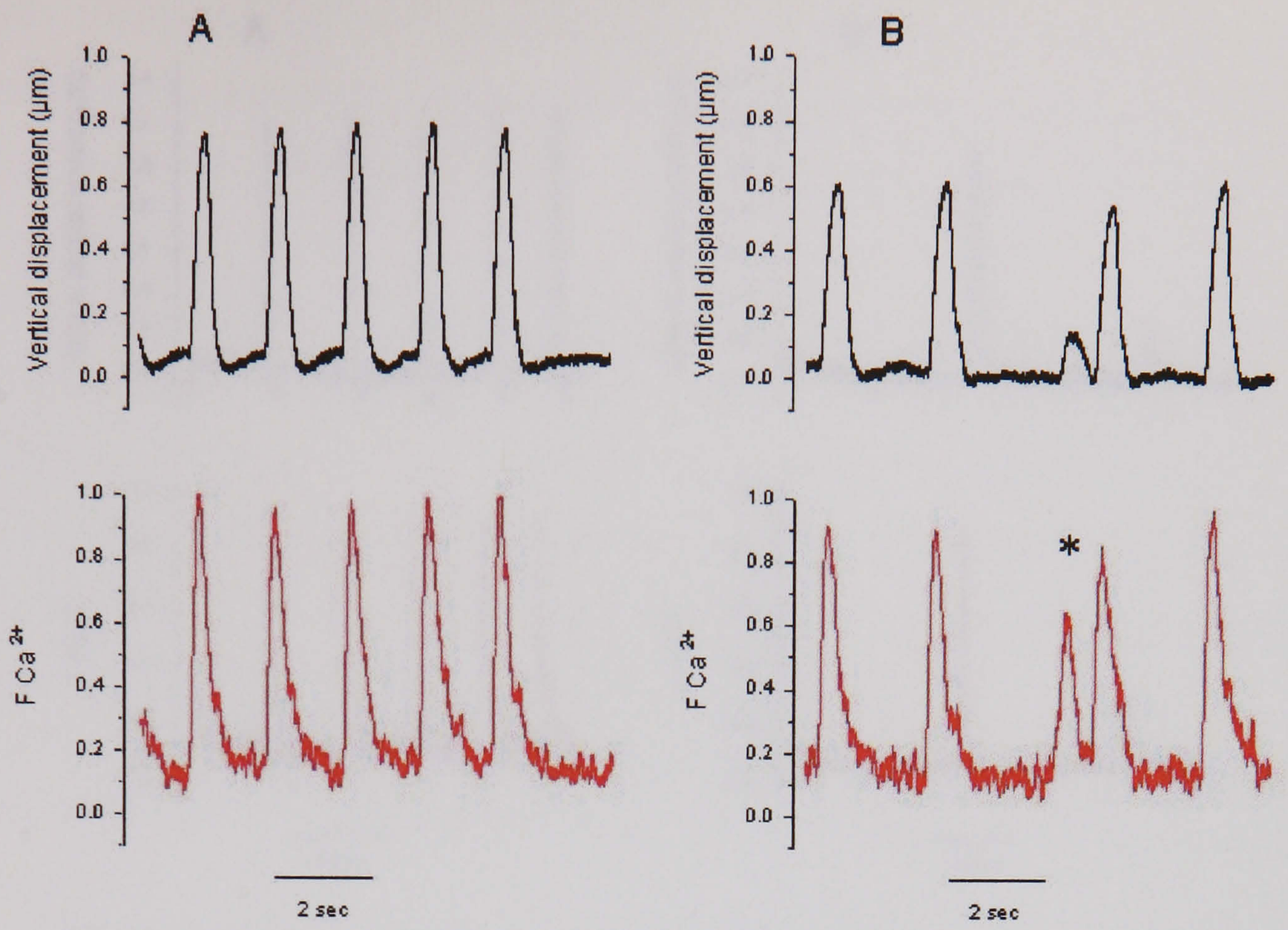

Fig. 6.4 Effect of 0.1 mM taurocholate on the contraction and calcium dynamic of an individual newborn rat cardiomyocyte in culture.
(*A*) Control; (*B*) 10 min after the addition of taurocholate to the culture medium.

Fig. 6.4 (*B*) and 6.5 (*B*) present mechanical movement and Ca^{2+} dynamics of cardiomyocyte after application of 0.1mM and 1 mM TC, respectively. As in the earlier records (Fig. 6.1, 6.2 and 6.3), rhythm is disrupted. The records showed that some beats have both a small calcium transient, and mechanical response.

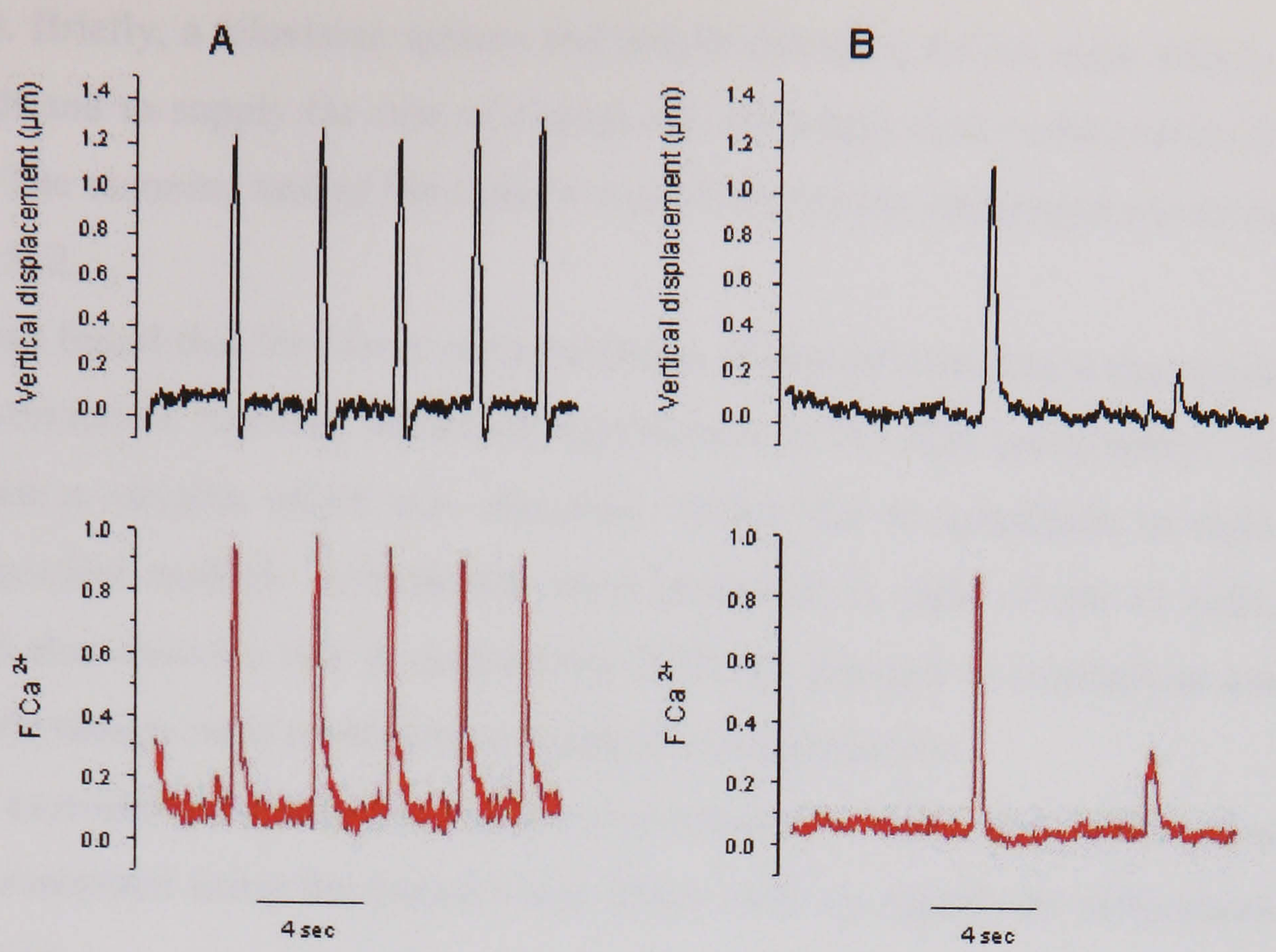

Fig. 6.5 Effect of 1 mM taurocholate on the contraction and calcium dynamic of a newborn rat cardiomyocyte.
(*A*) Control; (*B*) 20 min after the addition of taurocholate to the culture medium.

Our method of monitoring contraction using scanning ion-conductance microscopy permitted us to not only measure the rate of contraction, but also to monitor changes in amplitude (Shevchuk et al., 2001). At 0.1 mM taurocholate both rate and amplitude decreased. This dose of taurocholate caused additional displacements of small amplitude, which could not be seen with an optical microscope. However, this method cannot be used for measuring the contraction amplitude of adult cardiomyocytes where electrical stimulation is required, since the stimulation pulses affect SICM feedback control signal. So, the standard technique of contraction recording in isolated cells was used. The technique is described below.

Adult rat myocytes are rod-shaped structures that contract along their long axes; contraction amplitude can be expressed as percentage shortening with each beat. Myocytes in suspension were placed into a Perspex bath with a glass floor on the stage of an inverted microscope. After 5 min to allow settling, they were superfused with Krebs-Henseleit solution equilibrated with 95%O_2/5% CO_2 and maintained at 37 °C by a feedback system. Cells were electrically stimulated at 0.5 Hz using a bipolar pulse via platinum electrodes along the sides of the bath. Pulse width for each half of the stimulation was 0.1±0.5 ms. Continuous measurement of contraction amplitude and rates of shortening and relaxation were carried out as described previously (Harding et

al., 1988). Briefly, a television system and length detection device were used to display cell length and to supply the rate of change of cell length data continuously to a chart recorder. The scanning rate of the camera was 50 or 100 Hz and spatial resolution was 1 in 256 or 512.

It was found that the lower concentrations of taurocholate had a depressant effect on cell contraction, reaching statistical significance at 0.3 mM taurocholate. At 3 mM taurocholate a variable effect was observed, with a rise in amplitude in eight of the eleven myocytes studied. Arrhythmias were generated in eight of the 11 cells, six of which had also shown a rise in contraction. Both the changes in contraction amplitude and the arrhythmias were reversible on washout of taurocholate.

The taurocholate-induced reduction in contraction amplitude in adult and neonatal cells was compared using the paired *t* test. There were no significant differences at any concentration.

6.4 Discussion

Taurocholate causes reduced amplitude of contraction as well as dysrhythmias in both neonatal and adult cardiomyocytes. The reduction in amplitude of contraction was similar in adult and neonatal cardiomyocytes, although the threshold at which there was a significant alteration differed. Both adult and neonatal cardiomyocytes are susceptible to taurocholate-induced arrhythmia at the high taurocholate doses. If our hypothesis that bile acids cause intrauterine death in OC is correct, we would expect an age-related susceptibility to the effects of taurocholate in humans. In keeping with this, women with OC have not been reported to suffer from cardiac conduction abnormalities. In our study we have only compared the amplitude of contraction in adult and neonatal cardiomyocytes. It is possible that cardiomyocytes have different age-related susceptibilities to taurocholate-induced changes in other features of contraction. Also, the lack of reversibility of the changes seen in neonatal cells may have greater significance with regard to arrhythmogenesis *in vivo*.

The effect of taurocholate is dose dependent, and a higher concentration of 1 mM had a greater detrimental effect on contraction, including an arrhythmogenic effect. This study has demonstrated that taurocholate can have different effects on contraction in individual cells. While some cells become bradycardic and then recover, others can

develop a tachycardia and mechanical oscillations analogous to fibrillation, the cells going on to permanent asystole. This may partly explain the loss of synchronous contraction of the network of cardiomyocytes following culture with taurocholate, although studies of single cells, even when within the network, cannot fully explain the interaction between cells in a network.

The observed bradycardia suggests a slowing of diastolic depolarisation, and this would be in keeping with the observation that taurocholate slows the diastolic depolarisation in the sinoatrial node in rabbit by decreasing the slow inward Ca^{2+} current and the time dependent outward K^+ current (Kotake et al., 1989).

Arrhythmia is usually the result of re-entry mechanisms that require groups of cells, or is a consequence of membrane depolarisation in single cells. Our observation that taurocholate can produce arrhythmia in single myocytes (neonatal an adult) indicates membrane depolarisation. However, this is not easy to equate with the proposal that the bradycardia is caused by the effective opposite mechanism of slowing of diastolic depolarisation. However, taurocholate can produce membrane depolarisation in hepatocytes (Wehner, 1993), and this is caused by a change in Na^+ conductance, a different current to the diastolic depolarisation currents. We propose that the bile acid effect is caused by a different mechanism, and that the calcium changes may provide some clues. These may also explain the changes in contractility.

Our observations indicate that taurocholate affects calcium release from the sarcoplasmic reticulum (SR) in that both contractile function and calcium transients reduce in parallel, apart from the relationship deviating at low-amplitude contractions. The parallel reduction could be a direct effect of taurocholate on SR calcium dynamics, and altered SR calcium dynamics could also explain the small irregular calcium transients. These could be spontaneous releases of SR calcium, such as are found in adult rat ventricle (Fabiato, 1985). A requisite is often intracellular calcium overload, and we have shown that this is the case (Williamson et al., 2001). The mechanism for this type of SR release is calcium-induced calcium release, which is prominent in adult rats, but absent before birth. However, taurocholate may provide the stimulus for spontaneous calcium release, even in the absence of calcium overload. These calcium releases could also contribute to the arrhythmia by calcium-activated currents and/or Na^+/Ca^{2+} exchange.

6.5 Conclusions

In this study we have demonstrated that the bile acid taurocholate can cause different types of dysrhythmia in individual neonatal and adult rat cardiomyocytes. We have discussed the most likely mechanisms for the effects of taurocholate on membrane depolarisations, calcium dynamics and also on contraction in cardiomyocytes.

Our observations indicate that taurocholate may slow diastolic depolarisation, affect calcium release from the SR and that the alterations in contractile function parallel the effects of taurocholate on calcium transients.

Chapter 7 Scanning Patch-Clamp: new approach to ion channels studies

7.1 Introduction

Scanning patch-clamp technique (Gorelik et al., 2002a) is another powerful application of the SICM that has been developed in our laboratory to facilitate a single channel electrophysiological recordings from small cells and sub-micrometer cellular structures inaccessible by conventional patch-clam[methods. The scanning patch-clamp technique is based on the combination of Scanning Ion Conductance Microscopy and Patch-Clamp, both of which use a glass micropipette as a probe.

In this study we have shown how the ion channels in small cells and subcellular structures can be recorded and their distribution can be mapped. Based on our results we also have suggested a model of action potential propagation control in adult cardiac myocytes.

7.2 Ion channels in small cells and subcellular structures can be studied with Scanning Patch-Clamp

Many cellular functions such as growth, locomotion, secretion, contraction as well as cellular communication depend upon specialized membrane components - ion channels / receptors. Their functional characteristics and distribution play an important role in cell regulation and provide a precise, localized control over cell functions. A number of studies suggests that several types of ion channels are arranged in a specific pattern on the cell membrane, and this appears to have important functional implications (Alkondon M, 1996;Angelides, 1986;Banke et al., 1997;Cohen et al., 1991;Frosch and Dichter, 1992;Joe and Angelides, 1992;Karpen et al., 1992;Kinnamon et al., 1988;Tousson et al., 1989;Angelides, 1986;Banke et al., 1997;Alkondon M, 1996;Tousson et al., 1989;Frosch and Dichter, 1992;Kinnamon et al., 1988;Karpen et

al., 1992;Cohen et al., 1991). Thus, mapping of the ion channels on the surface of the cell is a key to understanding their function and interaction.

The spatial distribution of ion channels has been investigated mainly by microscopy-based techniques (Abrami et al., 1997;Alonso and Widmer, 1997;Grabner et al., 1998;Joe and Angelides, 1992). However, these techniques provide little information on the functional characteristics of ion channels. By contrast, the patch-clamp technique provides a method for the investigation of ion channel electrophysiological characteristics and hence function. The patch-clamp that was first described by Neher and Sakmann (Neher and Sakmann, 1976;Neher et al., 1978;Neher et al., 1978) and subsequently refined by Hamill (Hamill et al., 1981) has led to techniques for recording of ion channel current in cell-attached and excised membrane patches. Single channel recording has yielded information about unitary conductance and kinetic characteristics of ion channels and also facilitated the discovery of new classes of ion channels. Together with the method of whole-cell recording, patch clamp techniques have enabled the investigation of the physiological role of ionic channels in a large variety of cells and cellular organelles.

The principle of patch-clamp is to isolate a patch of a cell membrane electrically and to record current flowing through the patch (Fig. 7.1). This is achieved by bringing a fire-polished glass micropipette, which has been filled with a suitable electrolyte solution, to the surface of a cell and applying light suction until a high electrical resistance seal is formed. To date, conventional optical visualization is used to select a region for patch clamping and to manipulate a micropipette towards a selected region on the cell surface. However, the optical microscopy neither permits visualization of true membrane topography nor allows selection of small cellular structures (e.g. microvilli, transverse tubules of muscle cells) for patch clamp recording. Furthermore, the patch pipette's angled arrangement makes it extremely difficult to manipulate the pipette tip and cell in three-dimensional space keeping them in the focal axis at the same time.

The major principle of the operation of scanning patch-clamp is based on the idea that both independently developed techniques, SICM and patch-clamp, can use a glass micropipette as their probe. Moreover, the same micropipette probe can be used first to image the cell surface and to identify membrane structure of interest using SICM protocols, and then to record electrophysiological characteristics from a selected cellular structure using patch clamp procedures. The schematic diagram of the scanning patch clamp setup is presented in Fig. 7.1.

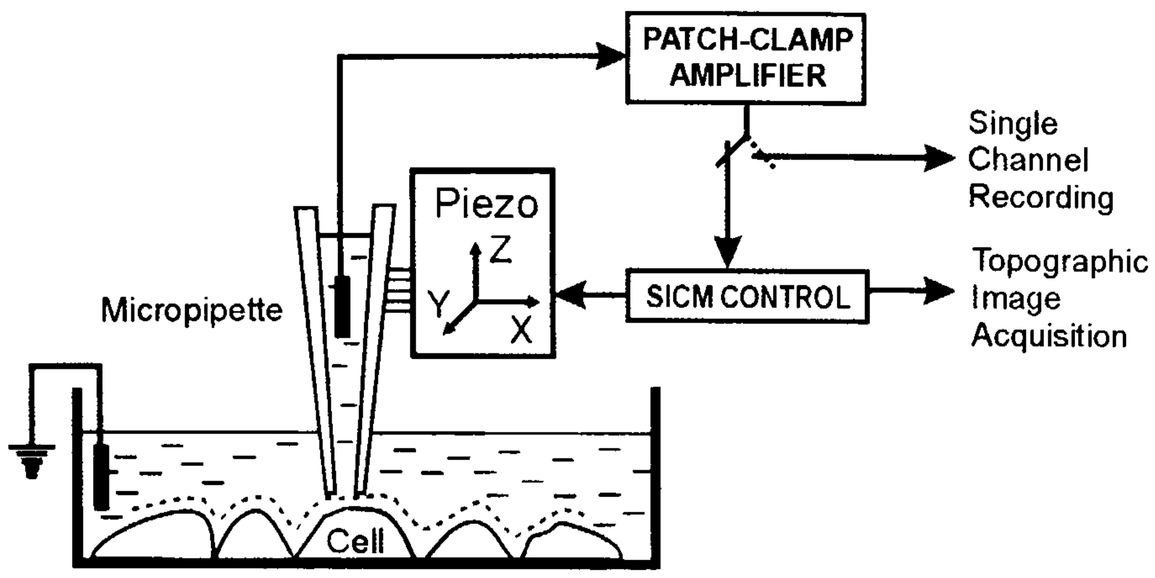

Fig. 7.1 Scanning Patch-Clamp schematic diagram.
The micropipette is mounted on a three-axis piezo actuator controlled by a computer. The ion current that flows through the pipette is measured by a patch-clamp amplifier, and it is used for the feedback control to keep a constant distance between the micropipette and the sample during scanning. Upon completion of the scanning procedure, computer control is used to position the micropipette at a place of interest based on the topographic image acquired, and finally the same patch-clamp amplifier is used for electrophysiological recording.

In order to perform patch-clamp recordings the home-built current amplifier of the SICM was replaced with a commercial patch-clamp amplifier (Axopatch 200B, Axon Instruments, Foster City, CA). This was the only modification made to the SICM system. In principle, it would have been possible to record ion channel currents by our home-built current amplifier, however commercial patch-clamp amplifier not only enables better quality recordings but is also supported by pClamp 8.0 software (Axon Instruments, Foster City, CA) which automates procedures of recording and analysis of the data.

In the scanning patch-clamp technique the micropipette is arranged vertically and manipulated by the SICM computer control (Fig. 7.2 *A*).

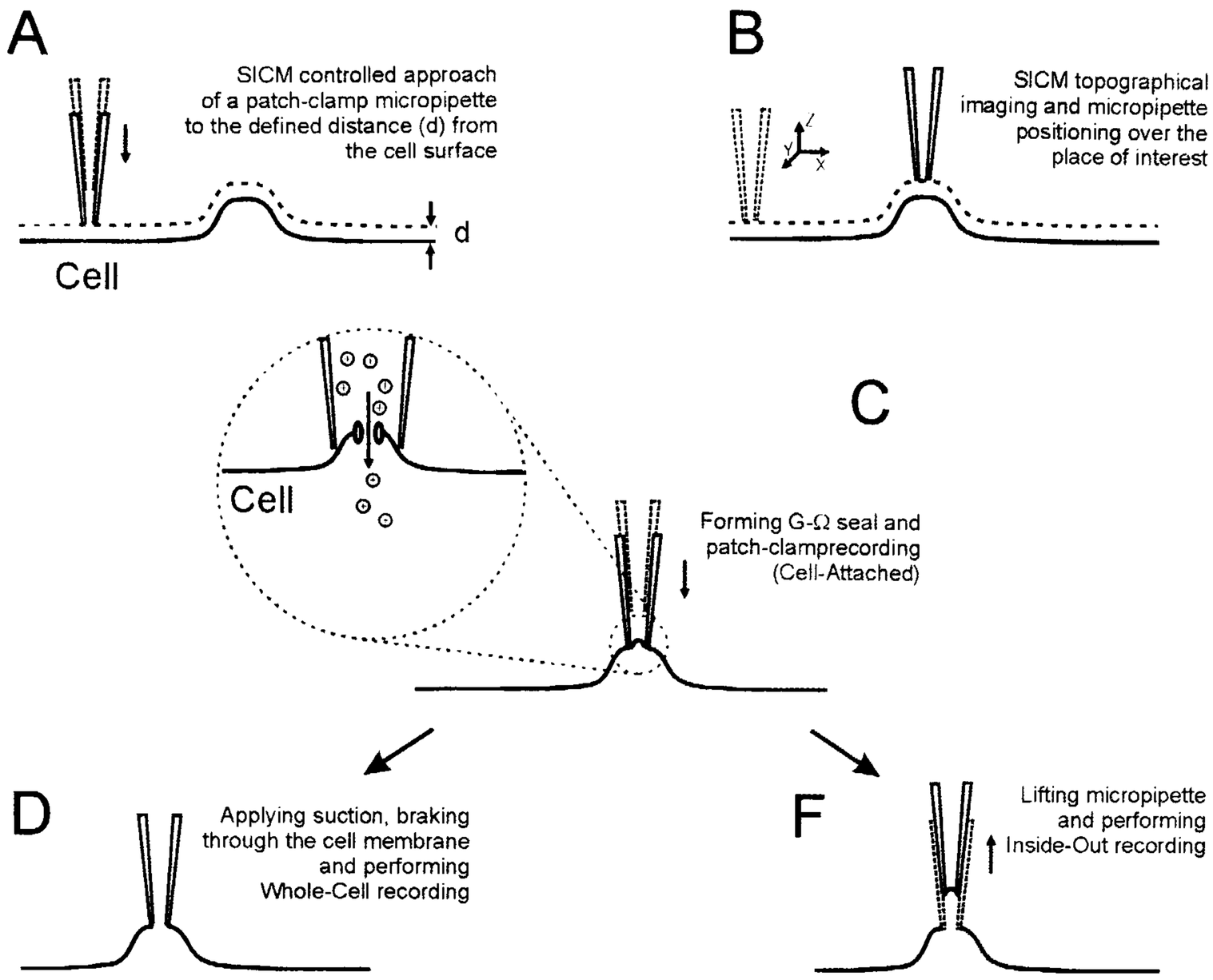

Fig. 7.2 Scanning Patch-Clamp algorithm.
(*A*) A micropipette approaches the cell surface and reaches a defined separation distance (*d*) whereupon the distance is kept constant by SICM feedback control. (*B*) The SICM scans this micropipette over the cell surface and positions it at a place of interest for patch-clamp recording. (*C*) The micropipette is lowered to form the giga-ohm seal for patch-clamp recording from the selected structure. (*D*) Negative pressure can be applied to break through the cell membrane and perform ion channel recording in whole-cell configuration. (*F*) Alternatively, the pipette can be lifted with the patch of the membrane attached for inside-out ion channel recording.

The feedback control is in operation while the pipette approaches the cell surface. As soon as the pipette reaches the distance *d* from the surface, the SICM feedback control maintains a constant tip - sample separation. This procedure makes the approach straightforward and safe, because the patch pipette never touches the cell membrane until the seal has to be formed. It is also important to note that optical control is not necessary for this approach. The SICM obtains the topographical image of the cell surface and positions the patch pipette over the selected place of interest according to the acquired image, where the ion channel recording has to be obtained (Fig. 7.2 *B*). At this point the feedback control is switched off, the pipette is lowered and suction applied, resulting in the formation of GΩ-seal (Fig. 7.2 *C*). Ion channel recording is then performed by conventional methods with all of the following configurations available: cell-attached, inside-out, whole-cell and/or outside-out mode (Fig. 7.2 *C, D* and *F*).

To explore the potential of the scanning patch-clamp technique we chose various experimental conditions and artificially divided them into three groups.

7.3 Ion channel recordings in small cells

In the first group we assessed how ion channel recording can be obtained from cells and structures that are small in size but still visible under a light microscope, such as spermatozoa and neuronal dendrites. As usual for patch-clamp, cells were optically selected in these experiments, so the vertical alignment of the pipette and feedback control were the only differences. The use of feedback control allowed us to approach the membrane surface in a controlled manner, therefore minimizing the risk of damaging the cell or breaking the tip.

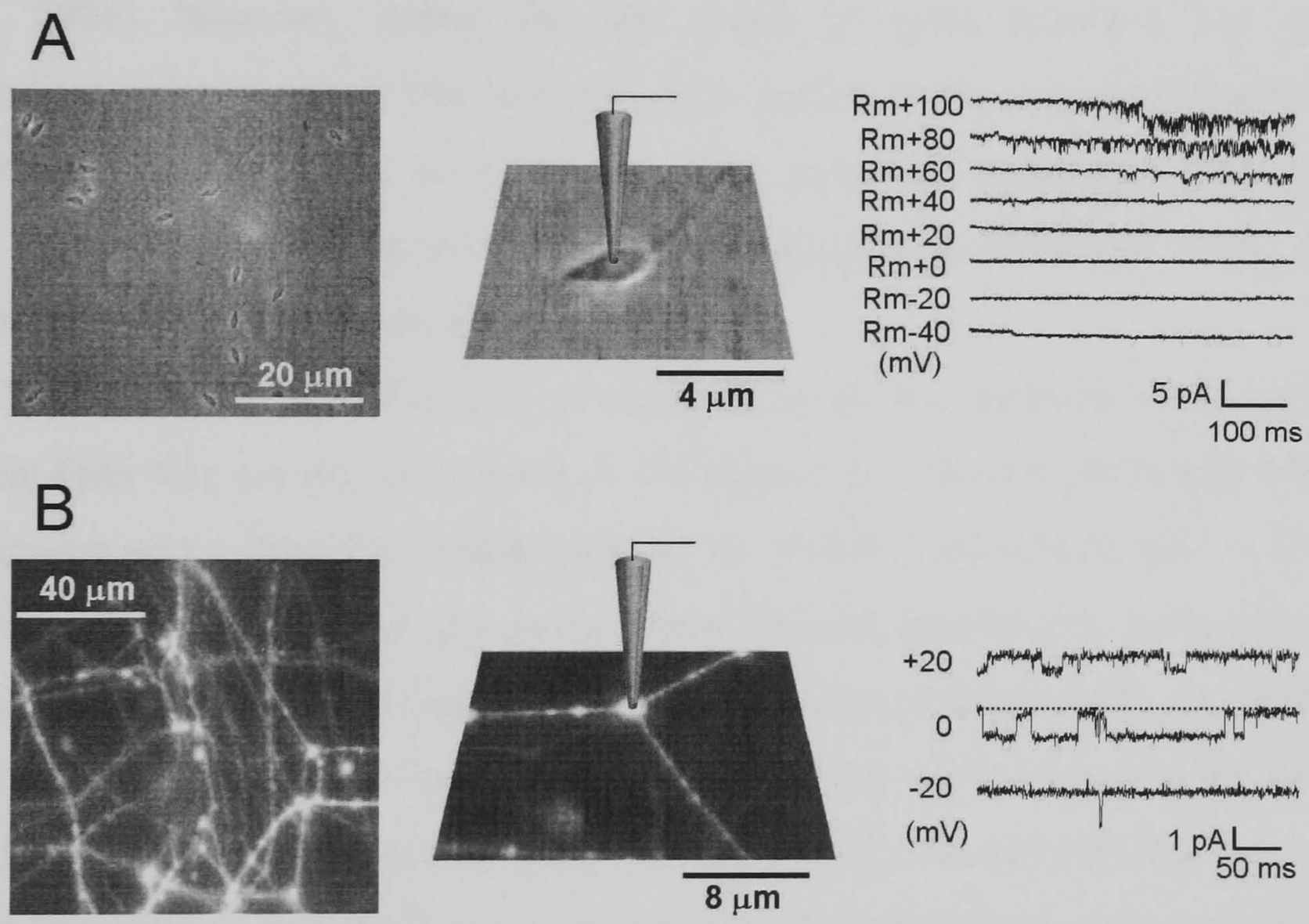

Fig. 7.3 Scanning Patch-Clamp ion channels recording from sperm cell and neuron.
(*A*) Ion channel recording from sea urchin spermatozoa: optical image of sea urchin sperm (*left*), a schematic of the pipette positioned over a sperm (*middle*), and a cell-attached current recording showing Ba^{2+} currents through Ca^{2+} channels (*right*). (*B*) Ion channel recording from a neurite varicosity structure: optical image of SCG neuritis loaded with a lipid-binding dye DiI (*left*), the pipette placed above the junction between neurites (*middle*), and a cell-attached recording of Ba^{2+} currents through Ca^{2+} channels (*right*).

Fig. 7.3 presents ion channel recordings from the sea urchin spermatozoa and from the fine neuronal processes. (*A*) Scanning patch-clamp recording from the sea urchin spermatozoa: optical image of sea urchin sperm (left). A schematic of the pipette positioned over a sperm (middle). Cell-attached current recording showing Ba^{2+} transients through Ca^{2+} channels (right). (*B*) Scanning patch-clamp recording from the

dendritic varicosity: optical image of superior cervical ganglion (SCG) cells loaded with a lipid-binding dye DiI (left). A schematic of the pipette placed above the junction between three dendrites (middle). Cell-attached Ba^{2+} current transients through Ca^{2+} channels (right).

Previous studies show that the direct electrophysiological characterization of the ion channels in sperm by conventional patch-clamp has been very difficult due to their small size. In order to make high-resistance seal formation possible sea urchin sperm were swollen, however the obtained cell-attached seals lasted only for a few minutes, making the characterization of ion channels still difficult(Sanchez et al., 2001). Alternatively, in mammals, spermatogenic cells, the progenitors of sperm which are larger, are being used to study sperm ion channels electrophysiologically (Munoz-Garay et al., 2001). However, during the last stages of spermatogenesis the type and localization of ion channels that will end up in mature sperm may significantly change (Serrano et al., 1999). Thus, the field needs new improved electrophysiological tools to define the molecular identity and mechanisms and modes of regulation of ion channels that participate in sperm physiology.

To circumvent this difficulty reconstitution of ion channels from sperm into artificial lipid bilayers was carried out. A multistate Ca^{2+} channel with a high main state conductance and voltage-dependent decaying to smaller conductance states was studied in planar bilayers containing sea urchin sperm plasma membranes. Unfortunately this type of reconstitution makes definition of channel orientation impossible (Lievano et al., 1990). Fig. 7.3 *A* shows the first direct recordings of a similar channel on the sperm cell from this species using our scanning patch-clamp set-up. The channel displays a similar voltage-dependence and multistate conductances as in the planar bilayer studies. This recording allows assignment of the polarity of the channel in sperm indicating that it opens at positive potentials and then relaxes to lower conductance states. This channel may participate in the uptake of Ca^{2+} required for the acrosome reaction (Lievano et al., 1990).

The probability of obtaining a seal on the cell body of sperm by the scanning patch-clamp is 0.45, that is 15 times higher than the probability in previous studies using conventional patch-clamp set up (Guerrero et al., 1987). The duration of cell-attached seals was approximately 20 minutes. Also, for the first time, we managed to obtain an ion channel recordings from sea urchin sperm in the inside-out configuration.

For many years, dendrites were presumed to be passive, cable-like structures in which the electrical signals of the dendrites spread to the soma by way of the well-described linear membrane properties of resistance and capacitance (Magee et al., 1998). A number of recent techniques, including high-speed fluorescence imaging and dendritic patch clamping, have provided new information and perspectives about the active properties of dendrites (Johnston et al., 1996). It is now clear that dendrites are anything but passive cables, and instead possess a rich variety of voltage-gated ion channels (Delmas et al., 2000). However, for technical reasons, most recordings are usually made on large processes e.g. dendrites of about 5μm (Delmas et al., 2000).

Using the scanning patch technique we observed the formation of focal swellings (varicosities) on the dendrites of SCG neurons. These varicosities (0.5-1 μm) were visible in a light microscope (Fig. 7.3 *B*, left and middle panel). It has been demonstrated in cultured neurons that hypoxia and glutamate excitotoxicity can mediate the formation of dendritic varicosities (Park et al., 1996). Fig. 7.3 B (*right panel*) demonstrates the 22 pS calcium channels measured from the dendritic varicosity of SCG neurons.

7.4 Ion channel recordings in sub-cellular structures

Another experimental group that is beyond the capabilities of conventional patch-clamp is presented by those cells (i) those vertical dimension is too small to be properly resolved and (ii) structures that are undetectable by light microscopy. Under these conditions the scanning patch-clamp was implemented fully in compliance with the algorithm described earlier in this paragraph. First, the SICM topographical image of the cell surface was acquired, and then the pipette was positioned to the selected region of interest according to coordinates selected from topographical image.

For example, in order to characterize the distribution of ion channels on dendritic processes of superior cervical ganglion cells we scanned and patched the flat membranous protrusion formed on a neuronal dendrite, which is approximately 100 nm in height. We found K^+ channels on the dendritic surface (Fig. 7.4 *A*). The probability of obtaining a seal on neuronal dendrites was 0.62.

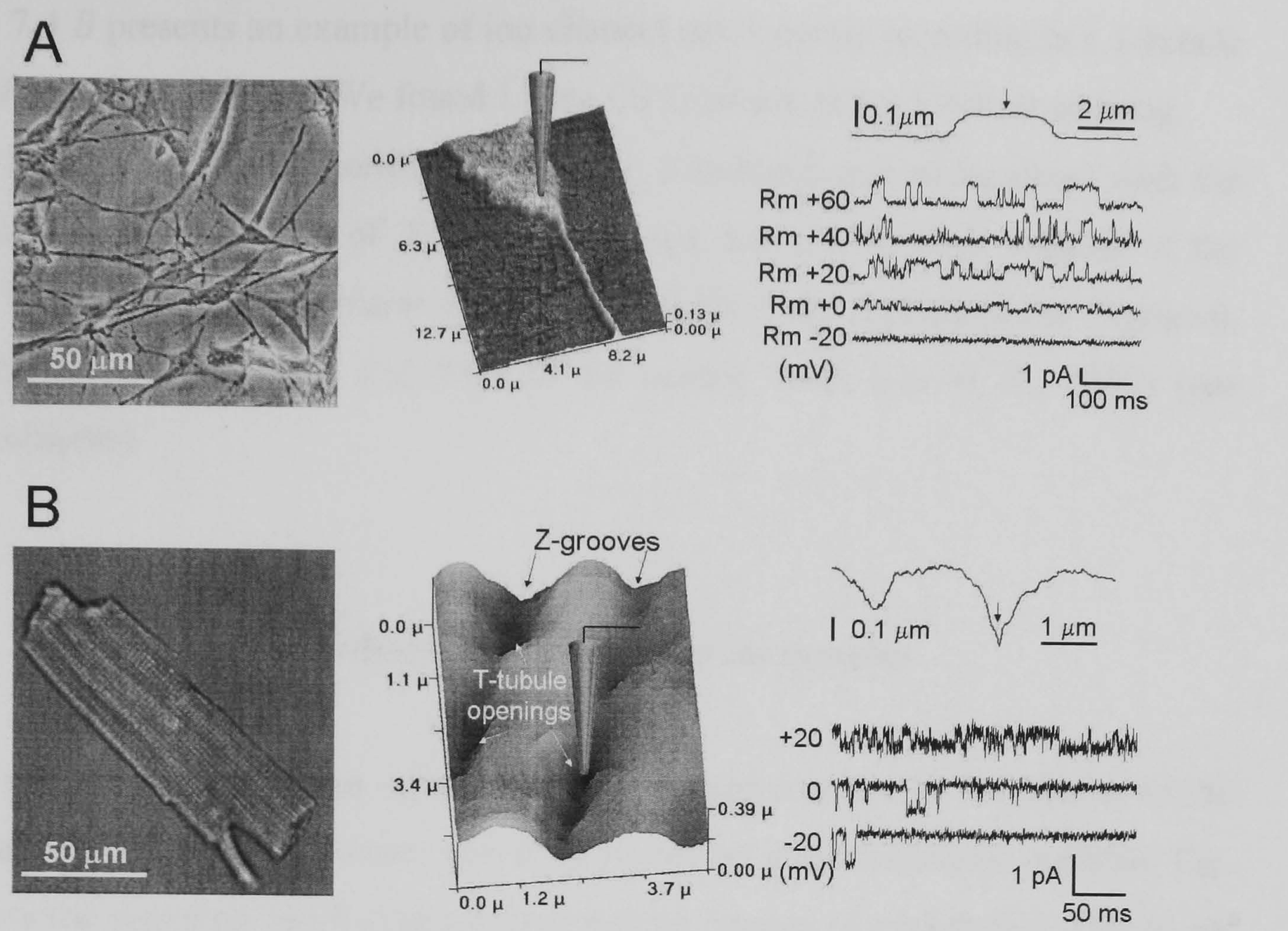

Fig. 7.4 Scanning Patch-Clamp ion channels recording from neuron and cardiac myocyte. (*A*) Ion channel recording from a fine neuronal process: optical image of SCG cells (*left*), SICM image of a flat membranous protrusion formed on an SCG neurite, which is approximately 100 nm in height (*middle*), and outward K^+ currents recorded in the cell-attached configuration (*right*; *inset* shows a profile of neurite process where the position of the pipette is marked by an *arrow*). (*B*) Ion channel recording from a T-tubule opening of a cardiac myocyte: optical image of adult rat cardiomyocyte (*left*), SICM image of a rat cardiomyocyte membrane, with Z-grooves, T-tubule opening, and characteristic sarcomere units marked (*middle*), and cell-attached Ba^{2+} currents through Ca^{2+} channel (*right*; *inset* shows profile of cardiac myocyte membrane where the pipette's position is marked by an *arrow*).

The transverse tubular system of cardiac muscle is a structure that allows rapid propagation of excitation into the cell interior (Cheng et al., 1994) where during the cardiac action potential, Ca^{2+} enters the cell through depolarisation-activated Ca^{2+} channels and triggers Ca^{2+} release from the sarcoplasmic reticulum. It has also been shown by immunofluorescence and immunoelectron microscopy that L-type Ca^{2+} channels and ryanodine receptors are co-distributed along the apposed membrane surfaces of the T-tubule and the sarcoplasmic reticulum, respectively (Carl et al., 1995;Sun et al., 1995).(Sun et al., 1995) However, no direct electrophysiological recordings of ion channels in transverse tubule opening regions have been made so far. This is mainly due to invisibility of transverse tubule openings under the light microscope. Certainly, it is not possible to position the patch-clamp pipette into these small openings and obtain ion channel recordings with conventional methods.

Fig. 7.4 *B* presents an example of ion channel patch-clamp recording in a T-tubule opening of a cardiac myocyte. We found L type Ca channels in the T-tubule opening.

We also showed that chloride channels are distributed and co-localized with the L-type calcium in the region of T-tubule openings, but not in other regions of the myocyte. The probability of obtaining a seal was 0.70 at the regions of the Z-groove, 0.59 at the T-tubule opening and 0.96 at the scallop crest (Gu et al., 2002) (see following chapter).

7.5 Ion channel recordings in non-transparent samples

Yet another group is when optical control is impossible due to the opacity of the investigated samples such as tissues and cells grown on non-transparent material. Fig. 7.5 presents the scanning patch-clamp topographical images of endothelial cells of rat aorta (*A*) and epithelial cells grown on opaque filter (*B*), with high pore density. Using these images the patch pipette can be easily positioned at the region of interest on the cell surface and then be used to obtain the GΩ-seal and ion channels recordings.

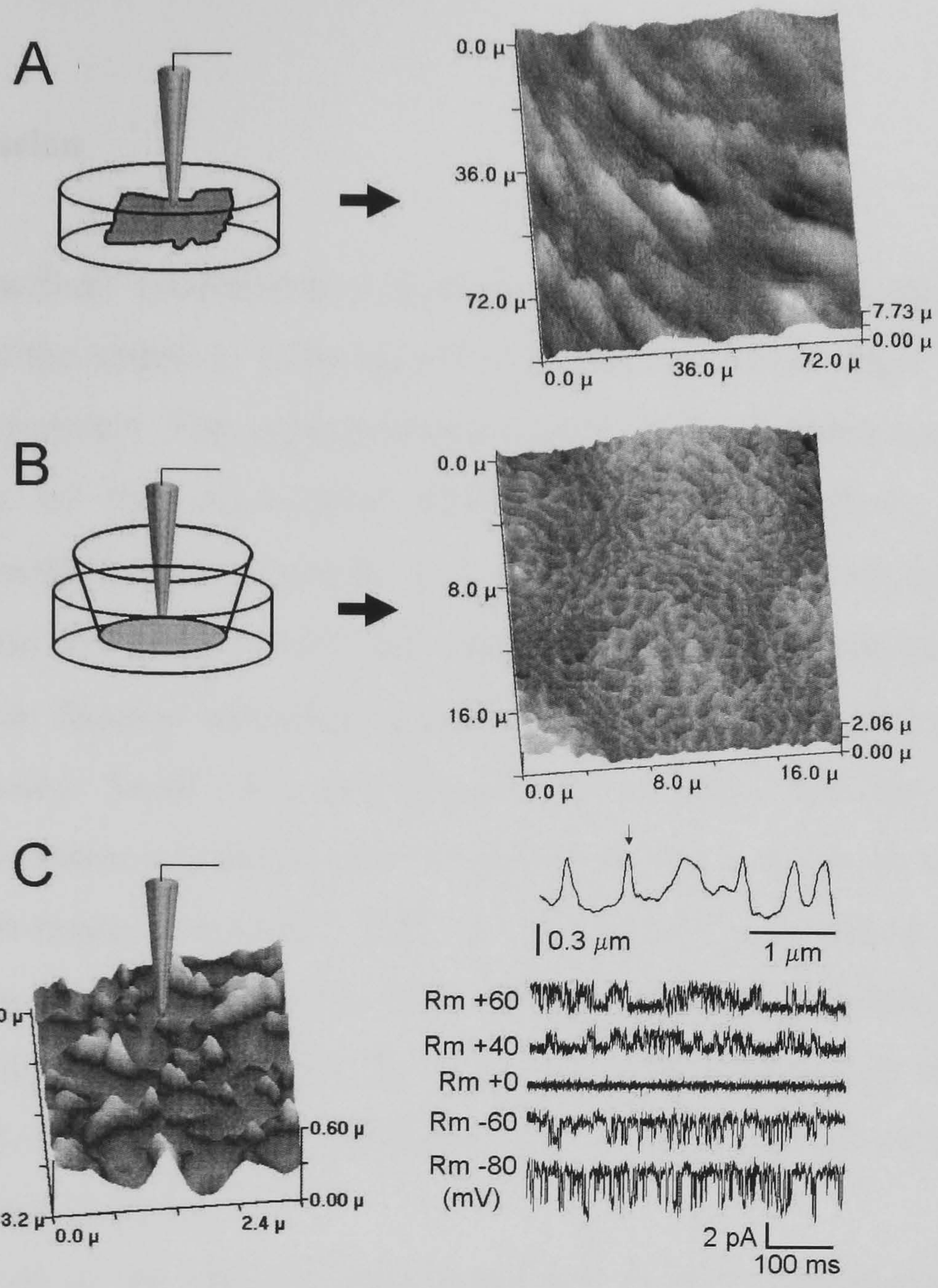

Fig. 7.5 Scanning Patch-Clamp ion channels recording from epithelial cells.
(*A*) Obtaining a SICM image of endothelial cells without optical control: schematic picture of a setup for scanning the inner surface of an opened-up rat aorta in a petri dish (*left*) and SICM image of endothelial cells of rat aorta (*right*). (*B*) Obtaining a topographic image from a nontransparent object: schematic picture of a set-up for scanning A6 epithelial cells on a non-transparent filter, which has a high pore density (*left*), and SICM image of a monolayer of A6 cells (*right*). The frame contains four epithelial cells and numerous microvilli are seen. (*C*) Ion channel recording on the top of a single microvillus: enlarged image of an A6 cell surface, where the pipette was placed on top of a microvillus (*left*) and K^+ channel currents recorded at the top of a microvillus in cell-attached configuration (*right*; *inset* shows the profile of several microvilli where the pipette's position is marked by an *arrow*).

Fig. 7.5 *C* shows a higher resolution image of a smaller area of the one presented in Fig. 7.4 *B* where the successful patch clamp current recording through the K^+ channel was performed from the top of the microvillus (right panel). Similar K^+ channels in A6 cells were previously described (Nilius et al., 1995). The probability of obtaining a seal by the scanning patch-clamp was 0.64 at the tip of the microvillus, and 0.72 between the microvilli. In our previous paper we showed Cl^- channels at the tip of the microvillus of aldosterone stimulated A6 cells. It was also suggested that other types of ion channels are associated with the tip of the microvillus of epithelial cells (Smith et al., 1997).

7.6 Discussion

From the described experiments it is clear that the scanning patch-clamp can significantly expand the variety of cells and cellular structures where single ion channel recording becomes possible. The implementation of the SICM feedback control allows precise positioning of the patch-clamp pipette, and further, allows us to use micropipettes of smaller sizes compared to conventional patch-clamp pipettes, and consequently enables formation of GΩ-seal on defined and chosen microareas of the membrane. All these features including topography imaging are computer-controlled and can be automated. Small cells and sub-cellular structures that are difficult to investigate with conventional methods, due to their small size, can now be studied with the scanning patch-clamp technique. This can be done by acquiring the SICM topographical image of the cell surface that visualizes cellular structures, therefore enables well determined positioning of the patch-clamp micropipette. In addition the system can be used as a conventional patch-clamp as it allows optical control and the use of different pipette diameters.

The applications of the scanning patch-clamp technique in studying ion channels are numerous. It can be applied to small cells like sperm and cell structures like microvilli. It can be used to study opaque cell samples such as tissues, brain slices, epithelial cultures, and hair cells. The spatial precision of the method allows for the localization of ion channels and the possibility of automation opens application in drug screening.

In the future, this technique could be also adapted to investigate and map the distribution of different types of ion channels such as ligand-gated or mechano-sensitive ion channels as the microscope nanopipette probe can be used to deliver defined chemicals, electrical or mechanical stimuli to narrowly defined areas on the cell surface.

7.7 Conclusions

We have developed the scanning patch-clamp technique and demonstrated that this approach can be used to make single-channel recordings from a large variety of preparations. Furthermore, the integration of patch-clamp with SICM enables single-

channel recording from specified location that makes possible electrophysiological studies of sub-cellular structures.

Chapter 8 Functional localization of calcium and chloride channels in the cardiomyocyte sarcolemma

8.1 Introduction

In cardiac myocytes, as in most excitable cells, action potential propagation depends essentially on the properties of ion channels that are functionally and spatially coupled.

In this study we decided to utilize the scanning patch-clamp technique to map these channels in the cardiomyocyte membrane. Because the patch is performed by a vertical approach controlling the pipette's distance electro-mechanically, we found that this method is more reliable than conventional patch-clamping and less prone to variation between experimenters.

Patches were performed equally probing three different regions of the cardiomyocyte sarcolemma; the T-tubule openings, Z-grooves, and scallop crests. The pipette was vertically lowered by piezo control until contact with the cell surface, usually after being moved down by one tip radius. In T-tubule regions of living cardiomyocytes, a downward movement of up to 2 µm was required. The probability of obtaining a seal varied at the different regions, but in general it was substantially higher compared to conventional patch-clamp. The high success rate for obtaining patches allowed the efficient accumulation of data points and statistical averaging of the channel distribution at distinct locations on the cell surface.

8.2 Mapping of calcium channels

We identified and mapped the distribution of L-type Ca^{2+} channels in rat cardiac myocytes. Fig. 8.1 *A* shows a representative topographic image of the cell surface.

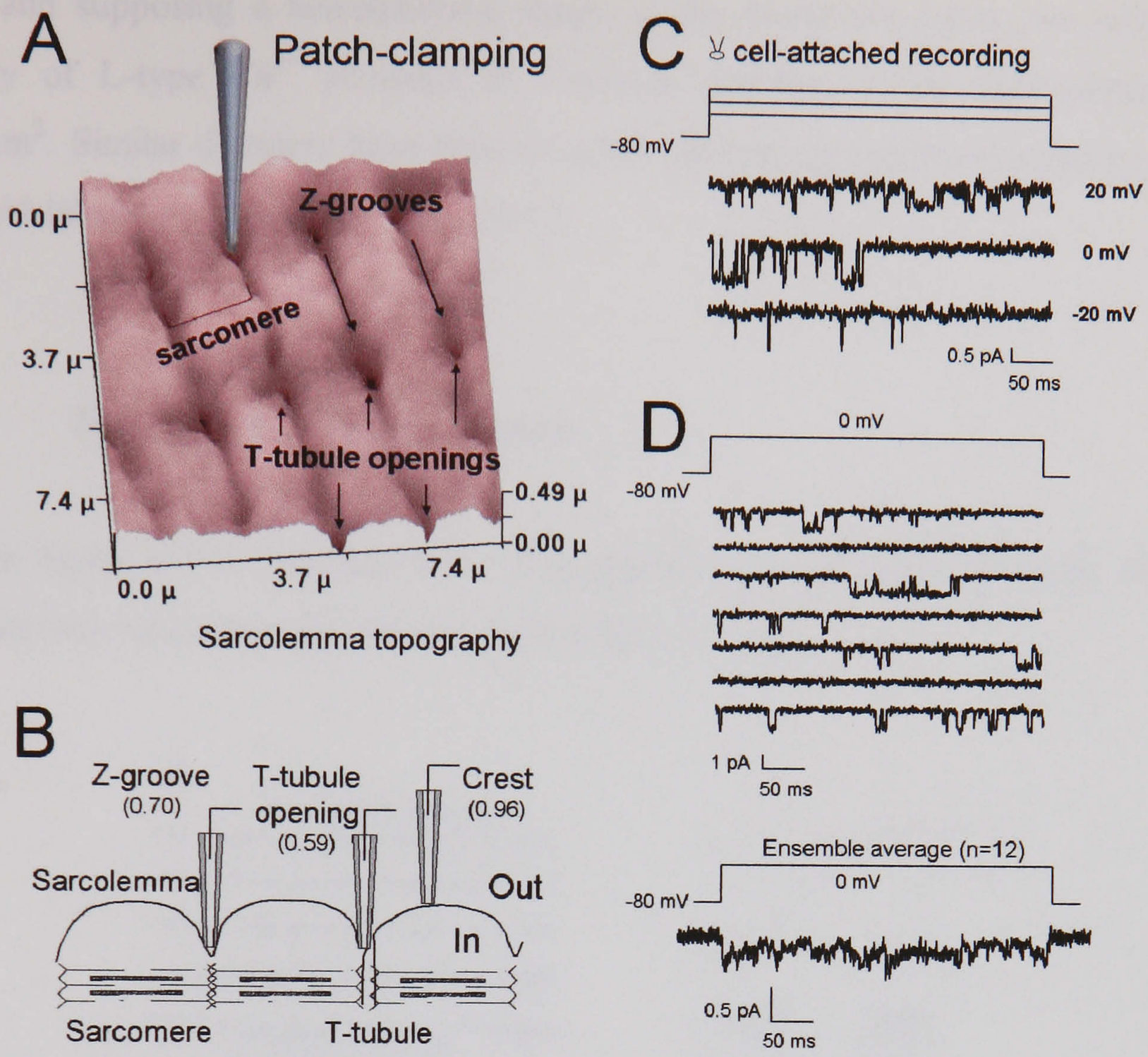

Fig. 8.1 Mapping of the Ca^{2+} channels in the cardiac myocyte with the Scanning Patch-Clamp.
(*A*) Typical experimental topographic image of a representative rat cardiomyocyte membrane. Z-grooves, T-tubule opening, and characteristic sarcomere units are marked. (*B*) Functional schematic of sarcomere units showing the position of the probed region (Z-groove, T-tubule opening and scallop crest). Probabilities of forming a G. seal as a function of surface position are shown in parenthesis. (*C*) Cell-attached Ba^{2+} current transients at voltages of +20, 0, –20 mV. (*D*) Several current transients elicited at 0 mV from one patch and ensemble average of 12 transients showing typical L-type inactivation kinetics.

The sarcomeres, openings of transverse tubules (T-tubules) and Z-grooves can be easily identified. Ca^{2+} currents in cell-attached configuration were detected only when the pipette was located in the T-tubule opening. Current traces shown in Fig. 8.1 *C* and current-voltage curves (not shown) are characteristic of L-type Ca^{2+} channels, which have been described previously in rat ventricular myocytes (Premkumar, 1999). Several single-channel Ca^{2+} currents of one patch are shown in Fig. 8.1 *D*, as well as the ensemble average, which identifies them as L-type. One out of every eight patches in the T-tubule openings exhibited L-type Ca^{2+} currents, and these were not found in any other probed regions of the cell (Fig. 8.1 *B*). Other studies suggest that L-type Ca^{2+} channels are distributed mainly in the membrane of the T-tubule system (Sun et al., 1995). Using the probability of obtaining a patch containing calcium channels (P=0.125) and estimating the membrane patch area (0.06 μm^2), based on the pipette

geometry and supposing a hemispherical shape of the membrane patch, we estimated the density of L-type Ca^{2+} channels at T-tubule openings to be approximately 2 channels/μm^2. Similar densities have been found in guinea pig cardiomyocytes by using immunogold-labeling (Gathercole et al., 2000).

8.3 Mapping of chloride channels

Three types of Cl^- currents were distinguished on the basis of single-channel conductance and rectification in cell-attached mode (Fig. 8.2).

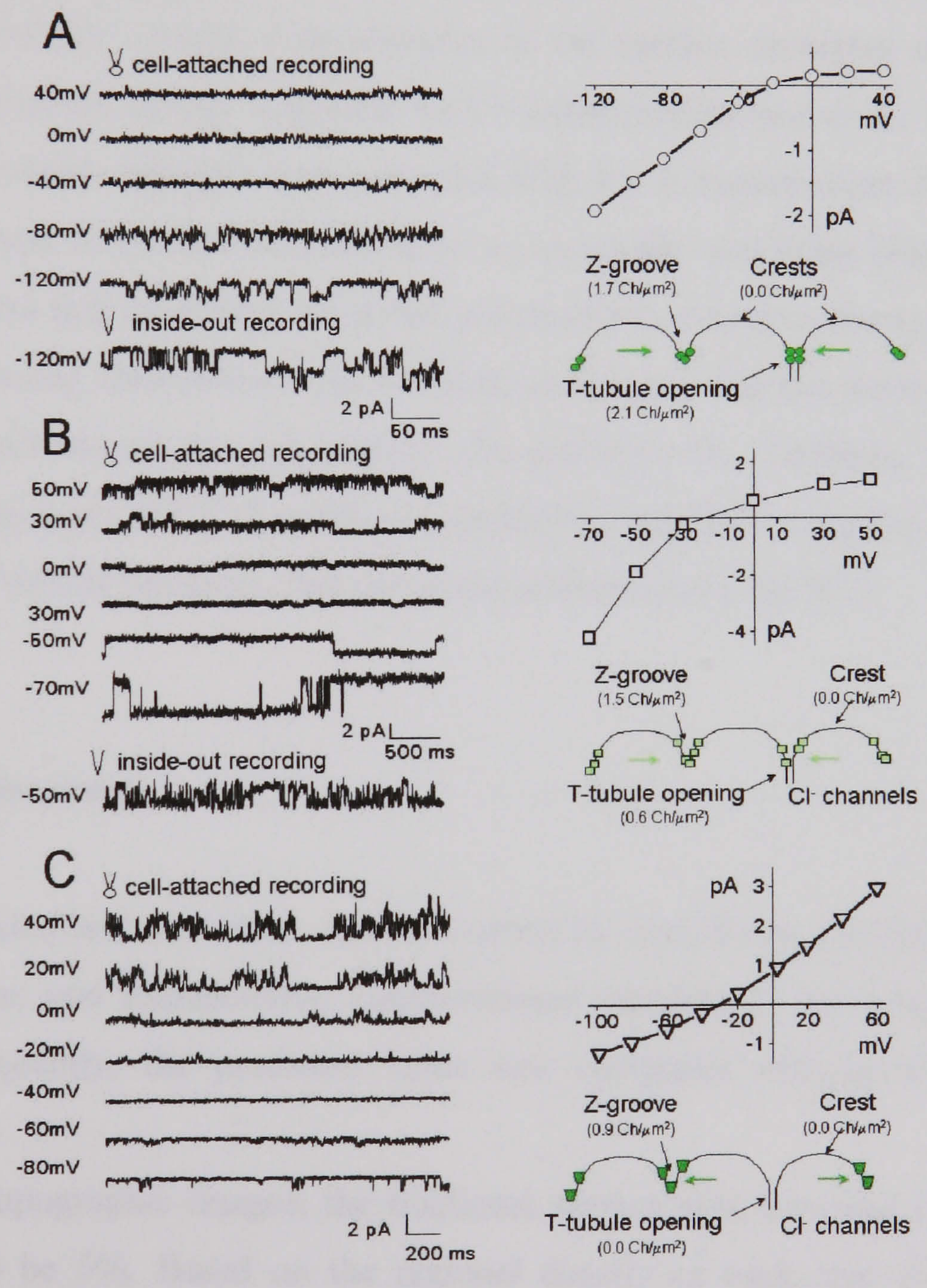

Fig. 8.2 Mapping of the Cl^- channels in the cardiac myocyte with the Scanning Patch-Clamp.
(*A*) A small-conductance inwardly rectifying channel (Cl_{SIR}). (*B*) A large-conductance inwardly rectifying channel (Cl_{LIR}). (*C*) An outwardly rectifying channel (Cl_{OR}). For each type of channel, a family of currents at different voltages (on the left side of the panels), current-voltage characteristics (on the top right side of the panels), and channel densities at different surface

positions (on the bottom right side of the panels) are shown. The mean reversal potential was –31.2 ± 2.4 mV (*n*=5) for (A); –31.8 ± 3.4 mV (*n*=5) for (B); and –33.5 ± 3.0 mV (*n*=4) for (C).

Channels were identified as Cl^- conductive from the reversal potential of the single-channel current-voltage relations. We also considered any K^+ currents that were blocked by TEA. Impermeable NMDG+ was the only cation present in the pipette. Two current types exhibited similar inward rectification and remained active after pulling the pipette off the cell to obtain the inside-out configuration. Channels of these subtypes may belong to the ClC family, because their current-voltage characteristics resembled those of ClC channels in other tissue or types of cardiomyocytes (Duan et al., 2000;Jentsch et al., 1999;Maduke et al., 2000). Expression of ClC-2 and ClC-3 channels in rat ventricle cells has been demonstrated previously (Britton et al., 2000), but the lack of information on ion current characteristics in rat cardiac myocytes did not allow definitive identification before. Typically for Cl^- channels (Saviane et al., 1999), clearly distinguishable current substates were observed (Fig. 8.2 *A*, bottom trace, Fig. 8.2 *B*, top trace). A third type of current was found to be outwardly rectifying (Fig. 8.2 *C*) and resembled currents that have been described previously in rabbit cardiomyocytes (Duan et al., 1997) by using conventional patch-clamp techniques. Patches were performed at three distinct positions on the cell surface: the scallop crest, Z-groove, and T-tubule opening. All three types of Cl^- channels are distributed only in the regions of Z-grooves and around the T-tubule openings, but not on the scallop crest (Fig. 8.2).

8.4 Discussion

We have calculated the whole-cell Cl^- current by considering channel densities at different positions and extrapolating single-channel currents to the total number of channels. Subsequently, the predicted value was compared with actual whole-cell currents.

From our topographic images, the fractional surface area occupied by Z-grooves was estimated to be 5%. Based on the regional density of each type of studied Cl^- channels, average channel density in sarcolemma was estimated to be 0.09 channels/μm^2 for a small-conductance inwardly rectifying Cl^- channel (Fig. 8.1 *A*), 0.06 channels/μm^2 for a large-conductance inwardly rectifying Cl^- channel (Fig. 8.1 *B*), and 0.03 channels/μm^2 for an outwardly rectifying channel (Fig. 8.2 *C*). Knowing that the

whole surface area of one cell is between 10,000 and 20,000 μm^2, the total number of each Cl^- channel type can be estimated. To simplify the calculation, the open probability is assumed to be 0.4 for all applied voltages. The value is based on our data (not shown) and that the open probability shows no strong voltage dependence. The estimated current-voltage relation for the whole-cell current is shown in Fig. 8.3 *A*.

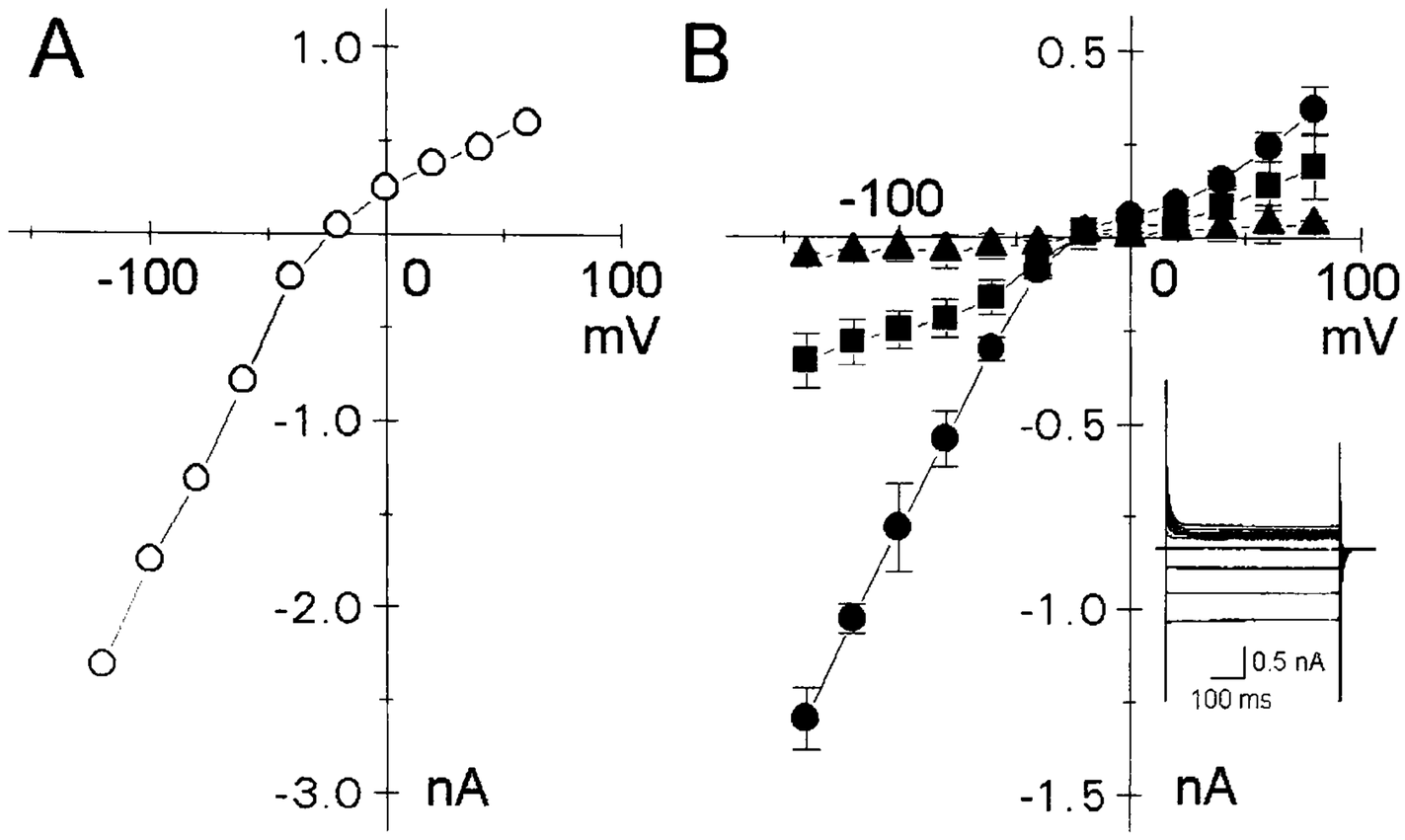

Fig. 8.3 Calculated and experimental current-voltage characteristics of whole-cell Cl^- current.
(*A*) Calculated whole-cell current extrapolated from single-channel currents. (*B*) Current-voltage characteristics of experimental whole-cell currents obtained from 22 cells (black circles). Currents were partially blocked by 300 µM of the Cl^- channel antagonist stilbene disulfonate (SITS) (black squares) (n = 12) and almost completely blocked by 1 mM Cd^{2+} (black triangles) (n=5). Currents were measured at plateau level. The inset figure shows a typical family of whole-cell currents.

The experimental whole-cell Cl^- current obtained from 22 cells (Fig. 8.3 *B*). The current is strongly inwardly rectified and sensitive to the Cl^- channel blockers SITS and Cd^{2+} (Maduke et al., 2000). The measured whole-cell current agrees well with predicted values but is proportionally lower at all voltages. This discrepancy is expected because our estimation did not take into account areas of low channel density, such as intercellular contacts and areas of discontinuous Z-grooves. Therefore, the measured whole-cell current is consistent with the number of Cl^- channels estimated from our recordings, and there is little contribution from other types of channels or undetected Cl^- channels.

Our results show that L-type Ca^{2+} channels are located only in the T-tubules and that Cl^- channels are predominantly clustered in the narrow regions of T-tubule openings and Z-grooves (Fig. 8.4). There are no channels detected on the scallop crest. To determine whether our failure to observe currents on the scallop crest regions of the

sarcolemma was an experimental artefact, we conducted a control experiment by inserting single α-toxin channels into these regions. We successfully recorded α-toxin induced ion currents (data not shown) after such insertions. This confirmed that ion channel currents could in fact be observed in the scallop crest region.

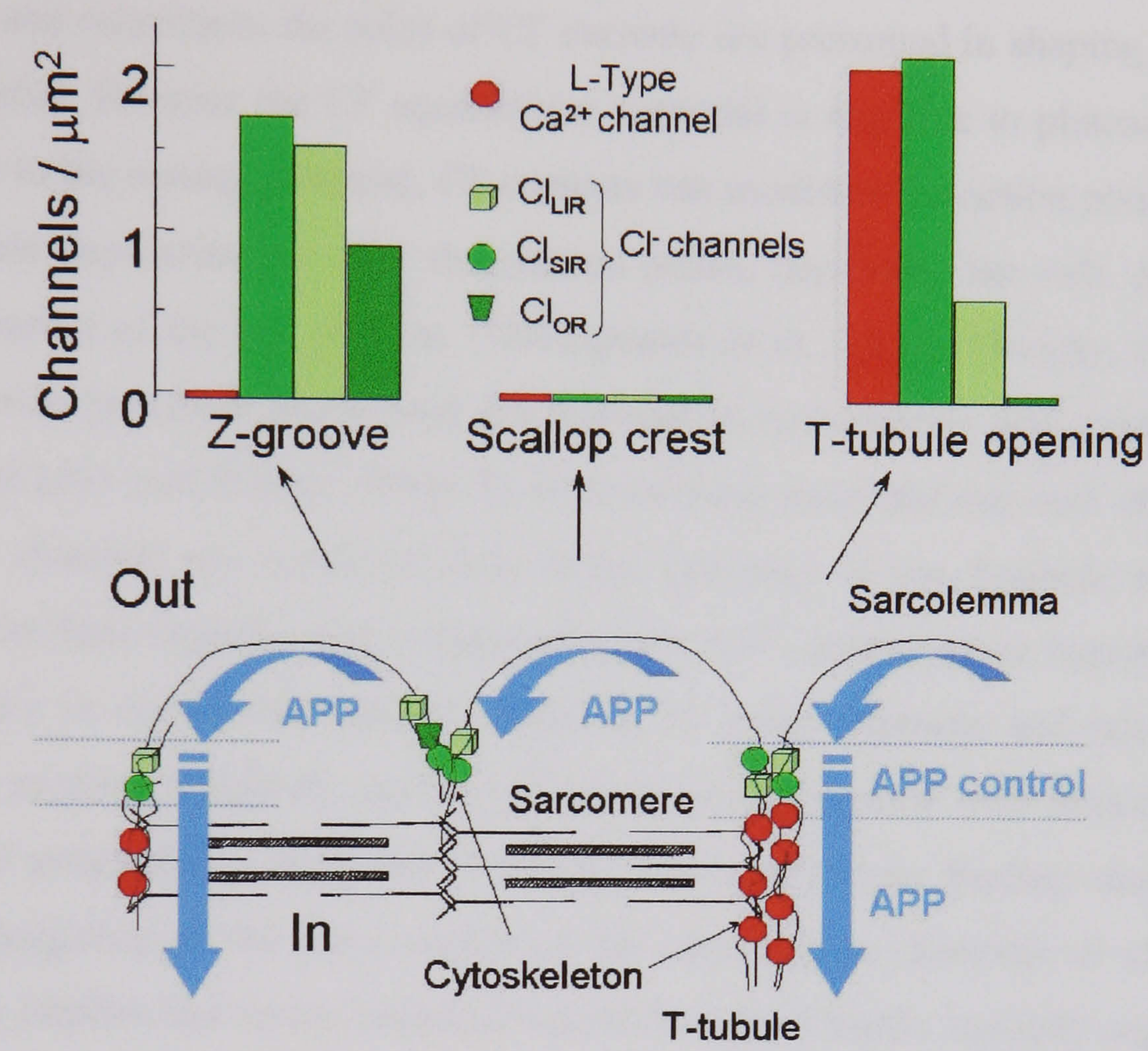

Fig. 8.4 Ca^{2+} and Cl^- channel distribution.
Variation of the density of Cl^- and L-type Ca^{2+} channels at different position and functional schematic of the sarcomeric unit showing clustering and co-localization of Cl^- and Ca^{2+} channels on the cell surface.

That the identified ion channels are confined to specific regions of the cardiomyocyte sarcolemma suggests that they are most likely anchored by the cytoskeleton. Published results also indicate a link between the F-actin cytoskeleton and L-type Ca^{2+} channels (Pascarel et al., 1999) and Cl^- channels (Ahmed et al., 2000;Haussler et al., 1994). Moreover, the channels are found in Z-grooves; that is, sarcolemma regions that strongly interact with the intracellular cytoskeleton. It is from these regions that the T-tubules emanate into the interior of the cell, forming the transverse tubular system of cardiac muscle. This system is a structure that allows rapid propagation of excitation into the cell interior (Cheng et al., 1994) where, during the cardiac action potential, Ca^{2+} enters the cell through depolarisation-activated Ca^{2+} channels and triggers Ca^{2+} release from the sarcoplasmic reticulum. Indeed, we found

that voltage-sensitive Ca^{2+} channels are distributed only in the T-tubular system but not in any other part of the cardiac myocyte sarcolemma. This finding strongly suggests that depolarisation-activated Ca^{2+} entry into the cell can exclusively occur at the T-tubule system of ventricular myocytes.

Although Ca^{2+} is considered the most essential ion in the process of heart cell contraction and relaxation, the roles of Cl^- currents are presumed in shaping the cardiac action potential. Because the Cl^- equilibrium potential is negative to plateau potentials and positive to the resting potential, Cl^- currents can modulate the action potential. They can accelerate depolarisation after the plateau phase, depolarise the cell, and prevent hyperpolarization of the cell (Sorota, 1999;Spencer et al., 2000). Thereby, Cl^- currents affect all action potential phases and are relevant in automaticity and mechanisms of arrhythmia (Curtis and Ridley, 1994). In view of these facts and our own observations that the Cl^- channels are localized only at the openings of the T-tubule system and colocalized in these regions with voltage-sensitive Ca^{2+} channels, we hypothesize that this proximity is crucial for electric coupling of these channels and necessary for providing a precise, localized, and as-yet-unrecognized control over action potential duration and propagation along the T-tubule system. Previous finding showed K_{ATP} channels aggregating in the same region of the sarcolemma (Korchev et al., 2000b). This strongly implies that action potential control is indeed highly spatially organized.

8.5 Conclusions

The spatial colocalization of Cl^-, Ca^{2+}, and K^+ ion channels in the region of sarcolemma at the entries of the T-tubular system can provide a new insight into functional, synergistic coupling between the channels. Further investigation of spatial distribution of other cardiac ion channels could elucidate the roles of spatial ion channel coupling in excitatory mechanisms and excitation-contraction coupling.

Chapter 9 Scanning Surface Confocal Microscopy for simultaneous topographical and fluorescence imaging

9.1 Introduction

The combination of SICM and scanning confocal microscopy described in paragraphs 2.4.3, 5.2.3 and 5.3.2, can provide valuable information about the cell membrane, not provided by other known techniques. This is especially when SICM is used in combination with confocal microscopy in "surface confocal" mode of operation. In this mode, simultaneous imaging of high-resolution topography and surface fluorescence of the cell membrane can be performed in a single scan. Therefore we called this technique scanning surface confocal microscopy (SSCM).

In this study (Gorelik et al., 2002c) we have chosen to use polyoma virus-like particles (VLPs) as a model system to validate our method and to gain insight into their mechanism of entry into cells. These particles enter cells by both receptor-dependent and independent routes, but only the former is productive for gene transfer (Krauzewicz et al., 2000b). Thus, the fate of the VLPs may be determined by their interaction with the cell membrane, making VLPs an ideal model to test the SSCM.

Crossing the cell membrane is the first critical event in achieving exogenous gene expression. Understanding the details of the passage of viruses, bacteria or other nanoparticles across this barrier is essential in developing drug or gene delivery systems. Most uptake is mediated by receptors that trigger internalisation, where the cell membrane invaginates to form a vesicle around the particle. The membrane-associated events involved, whether fusion (as in the case of enveloped viruses) or endo/phagocytosis (for nonenveloped viruses, bacteria, and most drug and gene delivery vectors), have largely been studied by electron microscopy, confocal microscopy, and by using reagents that block uptake pathways (Chimini and Chavrier, 2000;Godbey et al., 1999;Sieczkarski and Whittaker, 2002;Zabner et al., 1995). By using these techniques, the molecular mechanisms of endocytosis have been described in detail for viral infection, and attention is now focusing on the dynamics of the process (Bartlett and Samulski, 1998). Real-time, single particle tracing methods are being developed to

characterize viral infection pathways in living cells; however, details of movement across cellular membranes cannot be visualized because the membrane is not detectable optically (Seisenberger et al., 2001). As the dynamics of nanoparticle penetration of cellular membranes is a key element in their uptake and infectivity, there is a need to develop techniques that provide high-resolution measurements of this process as a function of time.

A number of methods have recently been developed to record surfaces at high resolution by using scanning probe microscopy techniques (paragraph 1.5). For example, by using scanning tunnelling microscopy and atomic force microscopy (AFM), atomic resolution is possible; however, as it has been shown (paragraph 1.5.2) their application in the field of biological sciences is limited, particularly when applied to live cells. Another method that has the potential to obtain both high-resolution topography and fluorescence images of the cell surface is scanning near-field optical microscopy (SNOM). This technique uses the force between the probe and the surface to control the distance between them, combined with a light from a sub-wavelength aperture to obtain simultaneous sub-diffraction limited optical or fluorescence images. Despite its potential, there have been few studies using SNOM on cells because of the difficulties in reliably regulating the distance control over the soft and responsive cell surface and operating in physiological buffers (de Lange et al., 2001).

In our study we have demonstrated that in contrast with other techniques the SSCM can successfully image VLPs adsorbed to the cell surface. The apparatus was sensitive enough to detect single VLPs and identify cell surface features corresponding to them from the topography scans. It has been shown that the SSCM not only produced fluorescence images similar to SCM but could also be used for imaging the process of VLPs interaction during their adsorption by living cells. These experiments demonstrate that SSCM can provide high resolution topographical and fluorescence data for following nanoparticle uptake in live cells.

9.2 Following virus-like particle entry into a cell by SSCM

To study the interaction of VLPs with the cell membrane, fluorescent Cy3-labeled VLPs were adsorbed to the surface of (see appendix for cell and VLP preparation) and imaged by using SSCM.

SSCM is based on a combination of SCM and SICM (see chapter 2). SICM is a scanning probe microscopy technique in which the ion current flowing into a nanopipette is used as a feedback signal to control the vertical (*z* axis) position of the cell relative to the pipette tip. As shown diagrammatically in Fig. 9.1 *A*, in SSCM the cell is moved up and down in the *z* direction while scanning in the *x* and *y* directions, so its surface is always the same distance from the nanopipette (typically, 25–75 nm). A laser is passed up a high numerical aperture objective so that it is focused just at the tip of the nanopipette (red asterisk), and a pinhole is positioned at the image plane so that the confocal volume follows the surface just below the pipette during scanning (red dashed line), similar to that described paragraph 5.2.3. Thus, a fluorescence image of the cell surface is obtained in a single scan (Fig. 9.1 *B*), as well as a simultaneously captured image of the cell topography. The superimposed fluorescence and topographical images of the cell surface (Fig. 9.1 *C*) show that the VLPs were scattered, apparently randomly, on or very close to the surface of the cell.

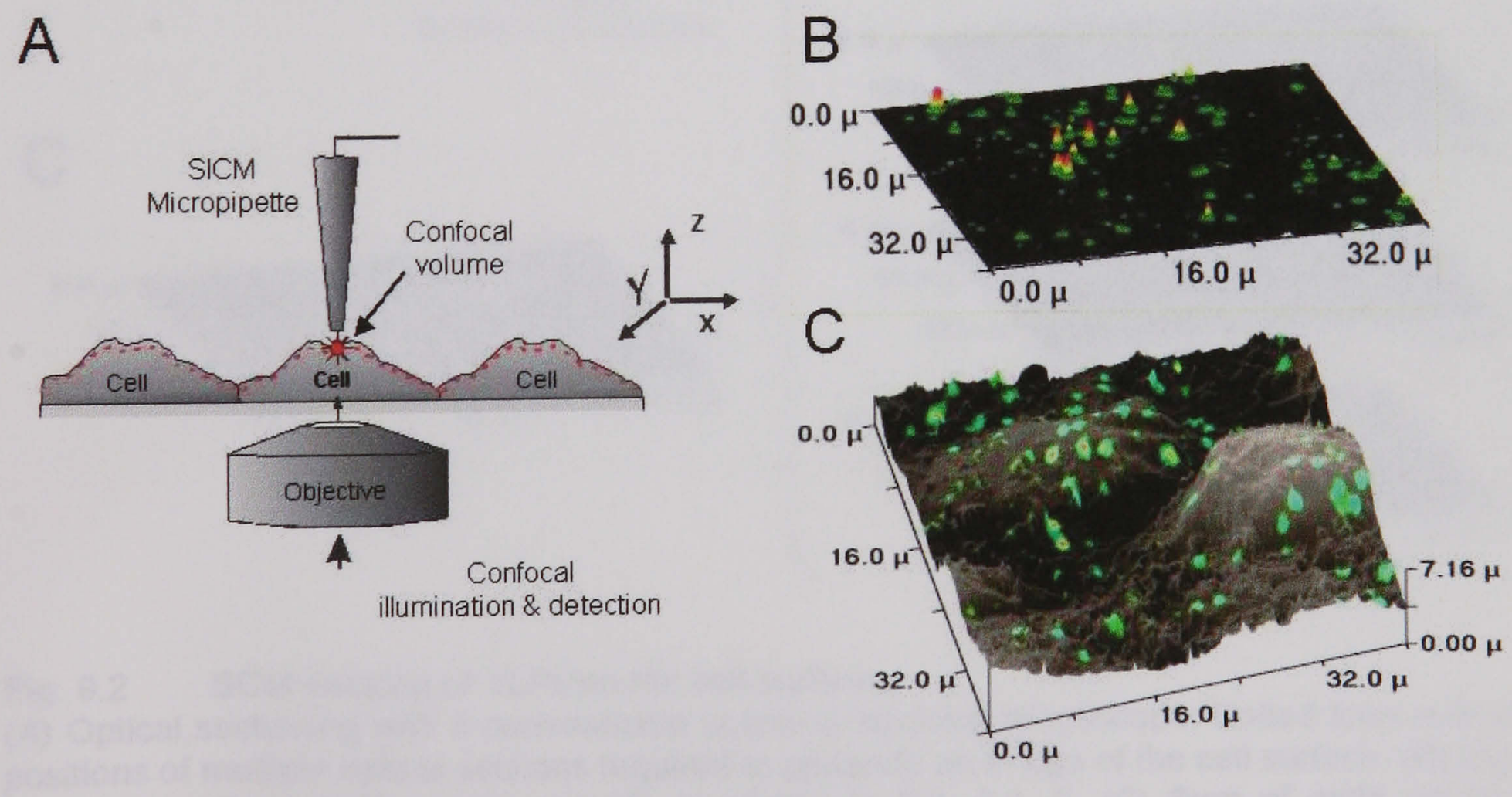

Fig. 9.1 SSCM imaging of VLPs on the cell surface.
(*A*) Optical and topographical contouring with an SSCM. The dotted line indicates the position of the optical image of the cell surface obtained in a single scan. (*B*) Single surface confocal microscopy scan projected on a flat surface. (*C*) Overlay of simultaneously obtained topographic and fluorescence images of fluorescent Cy3-labeled VLPs adsorbed to the surface of COS 7 cells.

By using conventional confocal microscopy, similar fluorescence data can be gathered, however because of the undulating surface of a cell, multiple scans are required to obtain the same amount of information (represented diagrammatically in Fig. 9.2 *A*). To compare the data gathered by each method, scanning of the same area (as in Fig. 9.1 *C*) by conventional confocal microscopy was carried out. In this case the same setup as for SSCM was used for imaging, but the feedback control of *z* position was switched off. The sample was scanning in *x*/*y* plane at a different heights The sum of eight scans (Fig. 9.2 *B*) resulted in image that is shown in Fig. 9.2 *C* which displayed spots of a similar number and intensity to the SSCM scan, demonstrating that a single SSCM scan generated data similar to the conventional confocal technique.

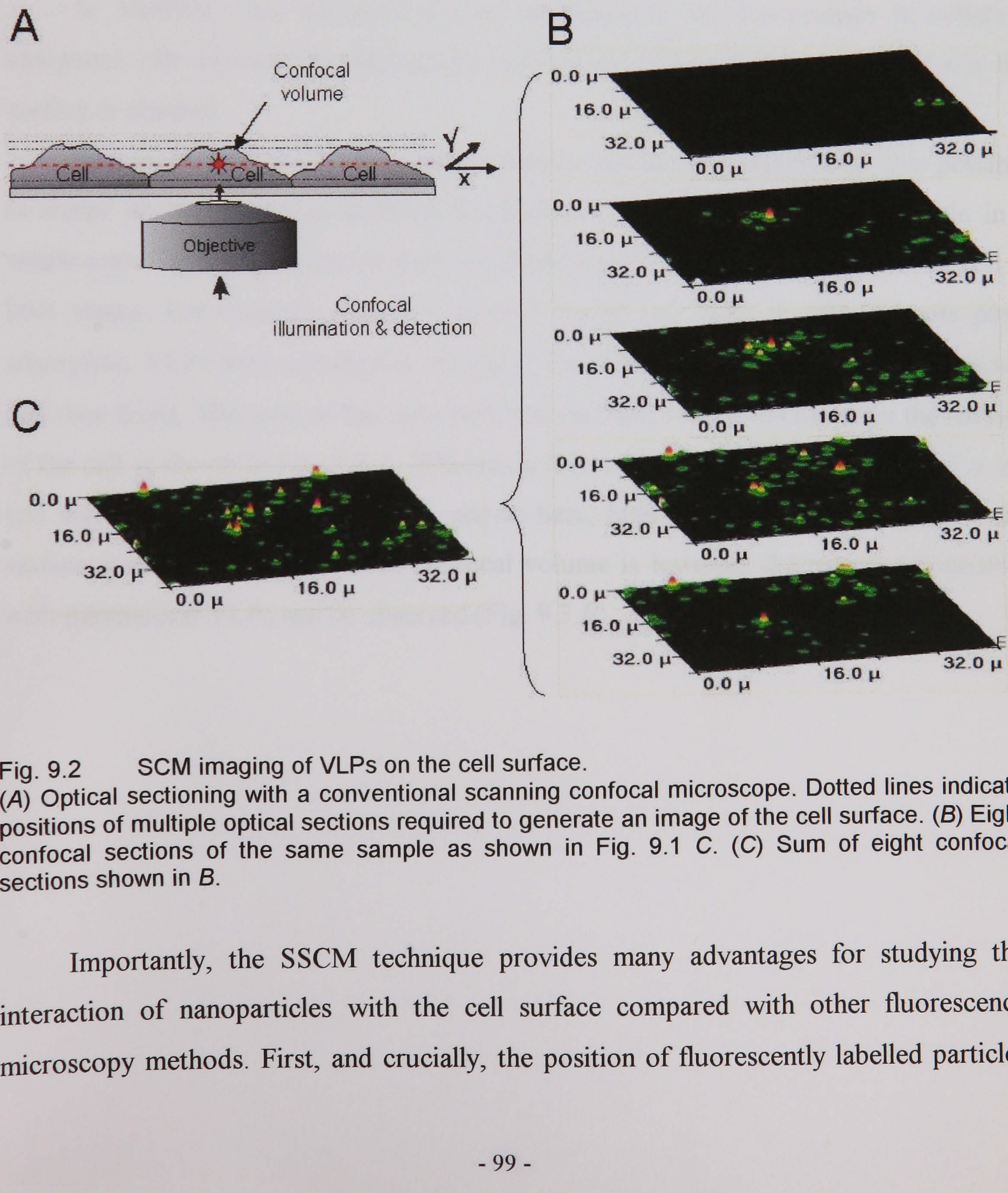

Fig. 9.2 SCM imaging of VLPs on the cell surface.
(*A*) Optical sectioning with a conventional scanning confocal microscope. Dotted lines indicate positions of multiple optical sections required to generate an image of the cell surface. (*B*) Eight confocal sections of the same sample as shown in Fig. 9.1 *C*. (*C*) Sum of eight confocal sections shown in *B*.

Importantly, the SSCM technique provides many advantages for studying the interaction of nanoparticles with the cell surface compared with other fluorescence microscopy methods. First, and crucially, the position of fluorescently labelled particles

can be related directly to the topography of the cell surface. Previously, this had only been possible in the context of markers such as plasma membrane proteins, cytoskeleton, or lipid dyes (Bkaily et al., 1999;Vanderplasschen and Smith, 1999). Such studies can result in artefacts if the markers change during the uptake process and, as the surface of most cells is dynamic, determining whether particles have passed through the membrane or have moved with the membrane as it undulates is extremely difficult.

It is also important to note that in contrast with conventional scanning confocal microscopy slicing in SSCM any point on the cell surface is only exposed to the laser once during the scan, equalizing photobleaching across the sample. Therefore, quantitative imaging of the fluorescent can be obtained which is impossible in case of slicing when some parts of the sample are photobleached before actually to be taken into measurement.

In addition, less background from intracellular autofluorescence is collected compared with similar data obtained by conventional confocal microscopy, as only the surface is scanned.

Moreover, by moving the confocal volume further from the pipette, it is possible to image inside the cell at different fixed distances from the cell surface, again in a single scan. This method can be used for following of VLPs internalisation into a cell at later stages. For example, Fig. 9.3 presents images of VLPs in cells 4 hours post-adsorption. VLPs were adsorbed to cells for 30 min at 4 °C, shifted to 37 °C for 4 hours and then fixed. The scan of the cells with the confocal volume focussed on the surface of the cell is shown in Fig. 9.3 *A*. Whereas at 0 hours VLPs can be seen scattered at the cell surface (Fig. 9.1 *C*) at 4 hours, shown here, little fluorescence is detected in the surface scan. However, when the confocal volume is lowered, fluorescence consistent with internalised VLPs can be observed (Fig. 9.3 *B*).

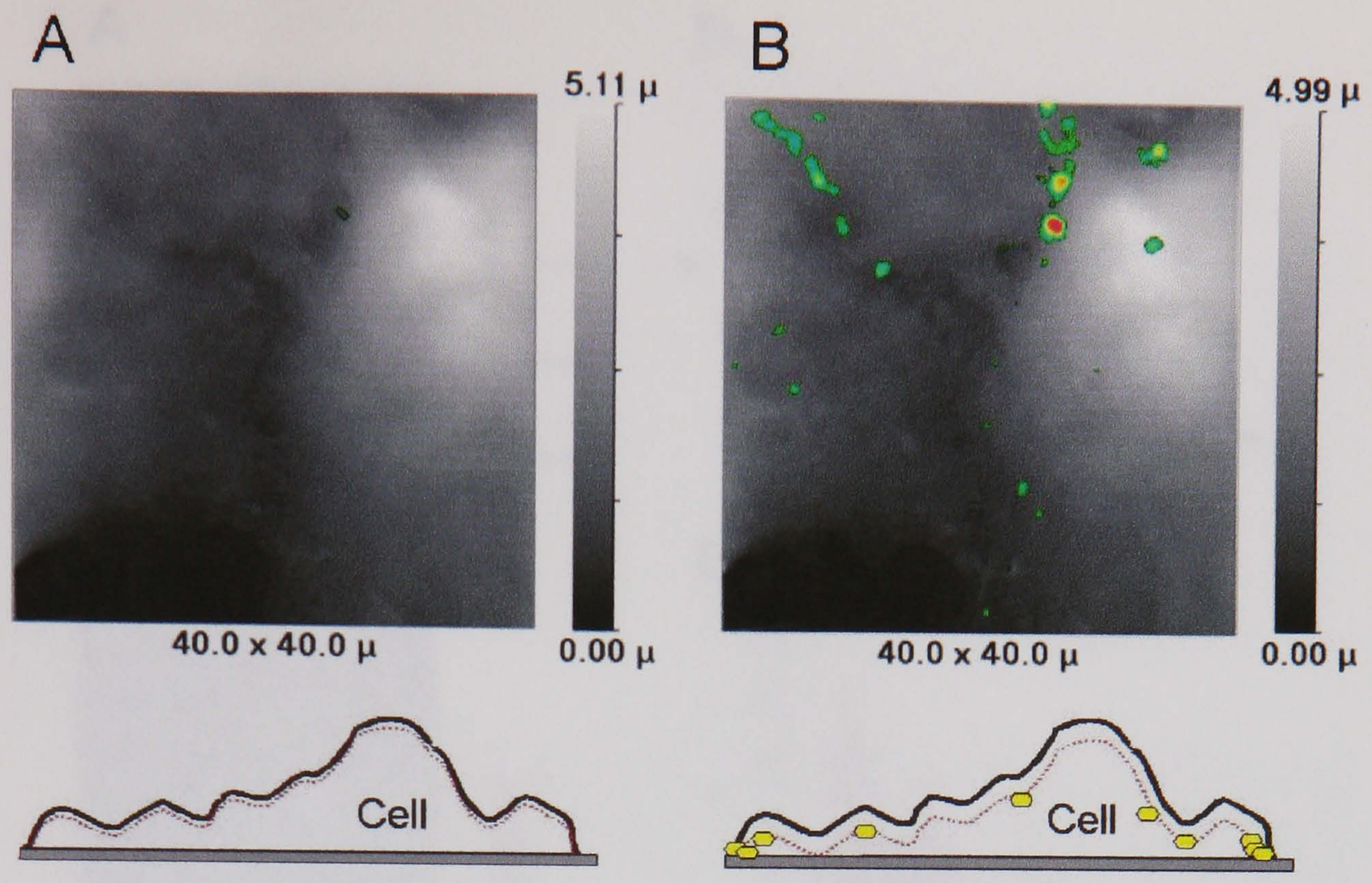

Fig. 9.3 SSCM imaging of VLPs inside the cell.
(*A*) A scan of the cells with the confocal volume focused on the surface of the cell. (*B*) A scan of the same cell with the confocal volume lowered by 1.5 µm below the cell surface. A schematic diagram indicating the path of the confocal volume is given below each image. VLP-related fluorescence is indicated by the yellow hexagons.

To determine whether SSCM would be sufficiently sensitive to track individual nanoparticles on the cell membrane, we first investigated whether single VLPs could be detected by fluorescence on a flat surface. The same preparation of fluorescent VLPs were analysed in parallel by AFM (on mica) and conventional SCM (on glass). By AFM, the preparation consisted predominantly of single or pairs of VLP, represented by 50-nm diameter spheres, loosely associated with strand-like structures presumed to be the plasmid DNA (examples are shown in Fig. 9.4 *A*).

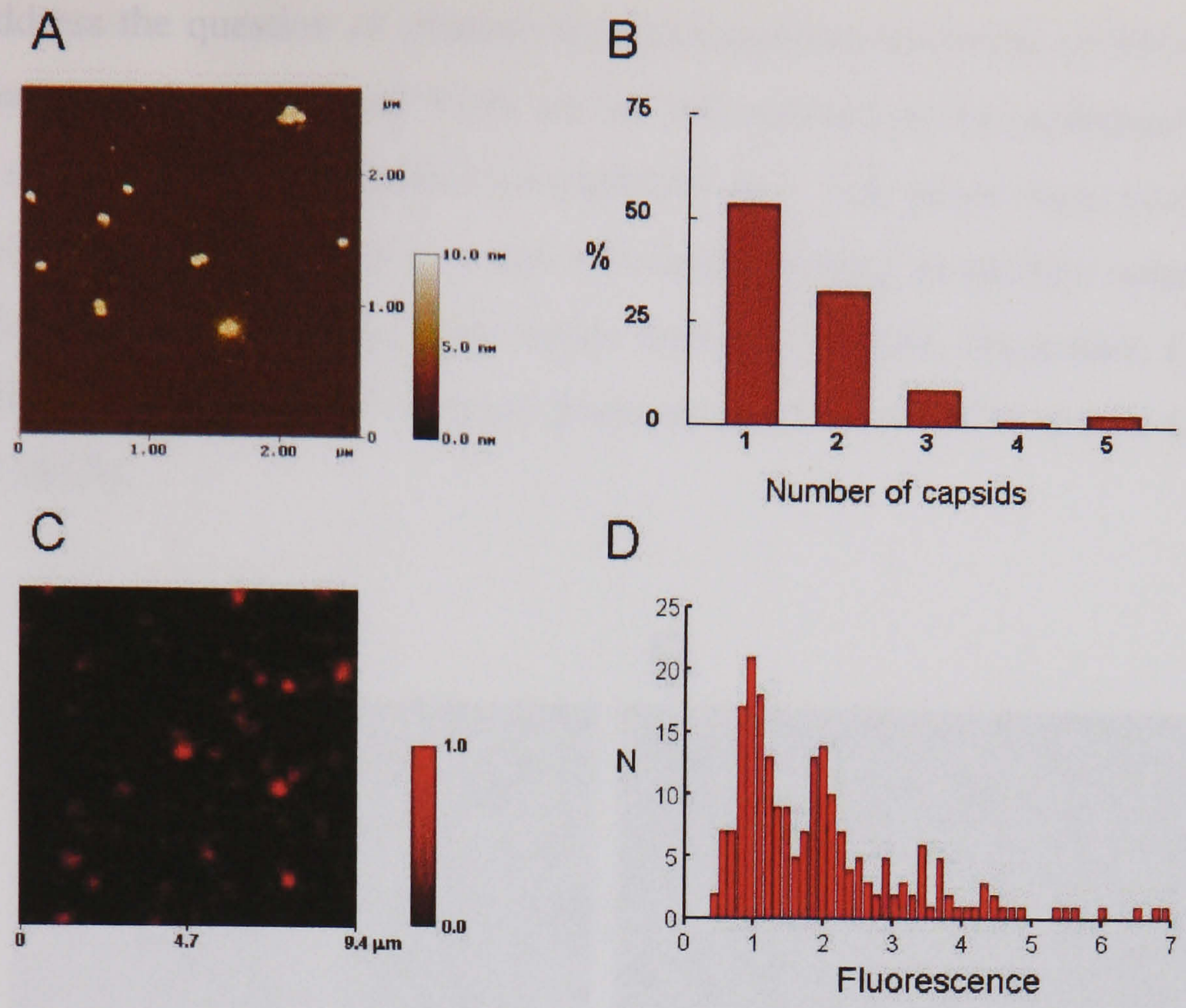

Fig. 9.4 AFM and SCM imaging of VLPs on mica (glass).
(*A*) An AFM image of typical preparation of fluorescent Cy3-labeled VLPs on mica. (*B*) Distribution of VLPs in aggregates based on the AFM measurements of 33 aggregates of VLPs. (*C*) A confocal fluorescence image of VLPs on glass. (*D*) Fluorescence intensity distribution of VLPs on glass calculated from confocal images.

The distribution of the number of VLPs associated in aggregates in a preparation calculated from the AFM image is presented in Fig. 9.4 *B*. Fig. 9.4 *C* shows the SCM image of the VLPs preparation on glass. Fluorescence intensities of the particles on glass, measured by confocal microscopy, were calculated per spot, and the distribution is shown in Fig. 9.4 *D*. The intensity distribution fell into two major peaks, one having twice the intensity of the other, corresponding to the distribution of single and paired VLPs and occasional larger groupings, determined by AFM (Fig. 9.4 *B*). Thus, the data are consistent with the smallest unit of fluorescence intensity corresponding to a single 50-nm VLP.

To address the question of whether the topographical resolution of SSCM would be sufficient to resolve individual VLPs on the cell membrane, we performed imaging of 50-100 nm pores in polyethylene terephthalate foil. The pores were produced by irradiation of the foil with heavy ions and subsequent etching in alkaline solution. The PET sample and its SEM image were kindly provided by GSI, Darmstadt, Germany. Fig. 9.5 *A* shows a topographical image of pores obtained by an SICM similar to the one adapted for SSCM.

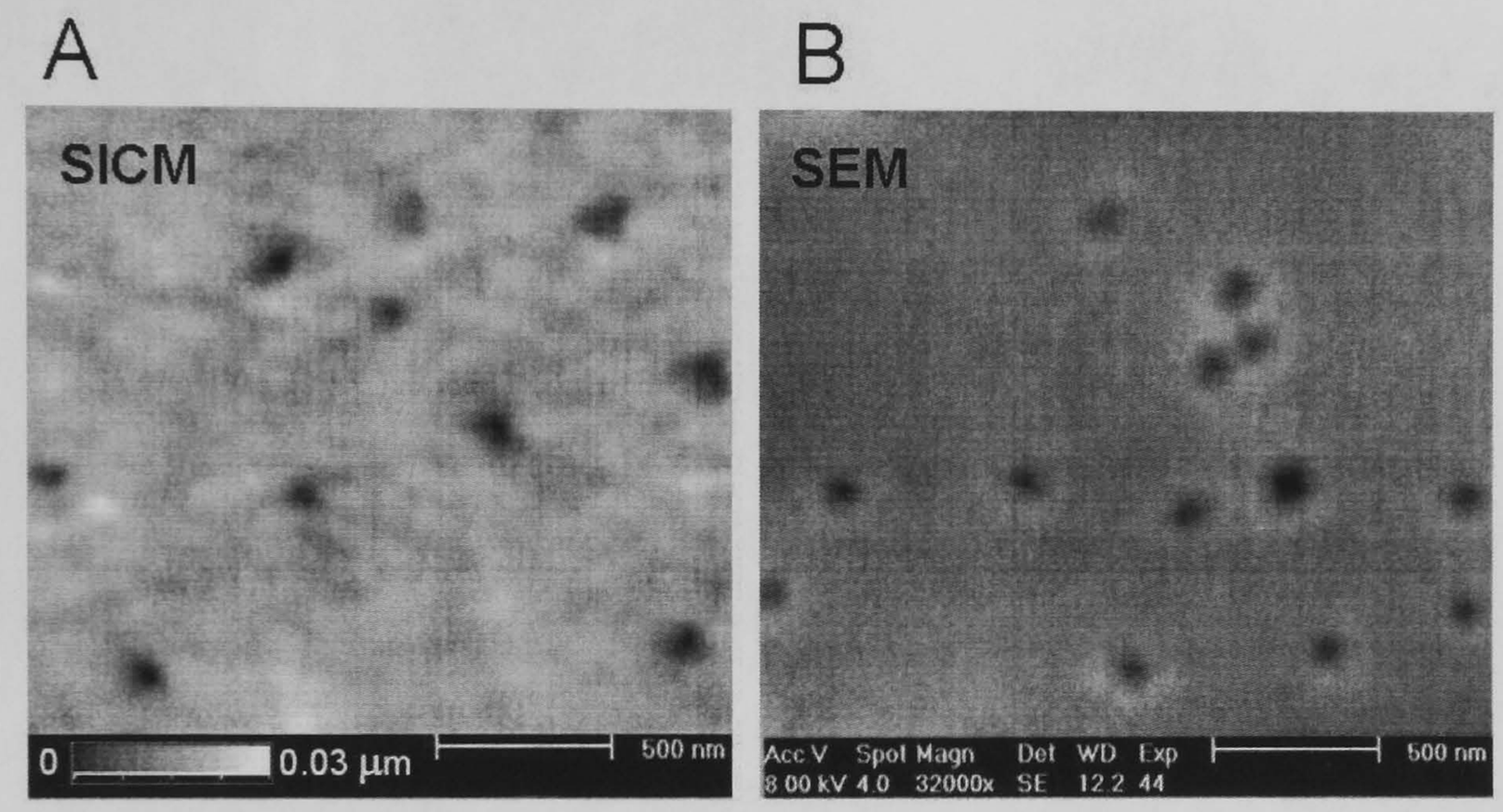

Fig. 9.5 SICM and SEM images of 59-100 nm pores in PET filter.
(*A*) A topographical image of the porous PET film obtained by an SICM. (*B*) An image of the same sample acquired by conventional scanning electron microscopy.

An image of the same sample acquired by conventional scanning electron microscopy is presented in Fig. 9.5 *B*. In both images, the pores appear to have similar dimensions, indicating that SICM resolution is sufficient to detect features on the cell surface in the 50-100 nm range and reflect their true size.

VLPs then were imaged on the surface of cells by using SSCM (Fig. 9.6). For this purpose the cells were fixed immediately after addition of VLPs to prevent VLP internalisation and also allow both re-imaging of the same region at increasing resolutions and quantitative analysis of the fluorescence. Images of the cell surface topography and fluorescence of the same area acquired simultaneously by SSCM are shown in Fig. 9.6 *A* and *B* correspondingly. Then, fluorescence intensity was measured for a random sample of ≈200 fluorescent spots and presented as a distribution in Fig. 9.6 *C*. Remarkably, the majority of the fluorescent objects had similar fluorescence intensities (Fig. 9.6 *C*, peak at 1 unit), a second smaller population had double the

intensity, and there were a few larger aggregates, producing a histogram very similar to that obtained for VLPs on glass (Fig. 9.4 *D*). Thus, we conclude that the smallest units of fluorescence we observe on the cell surface correspond to single VLPs.

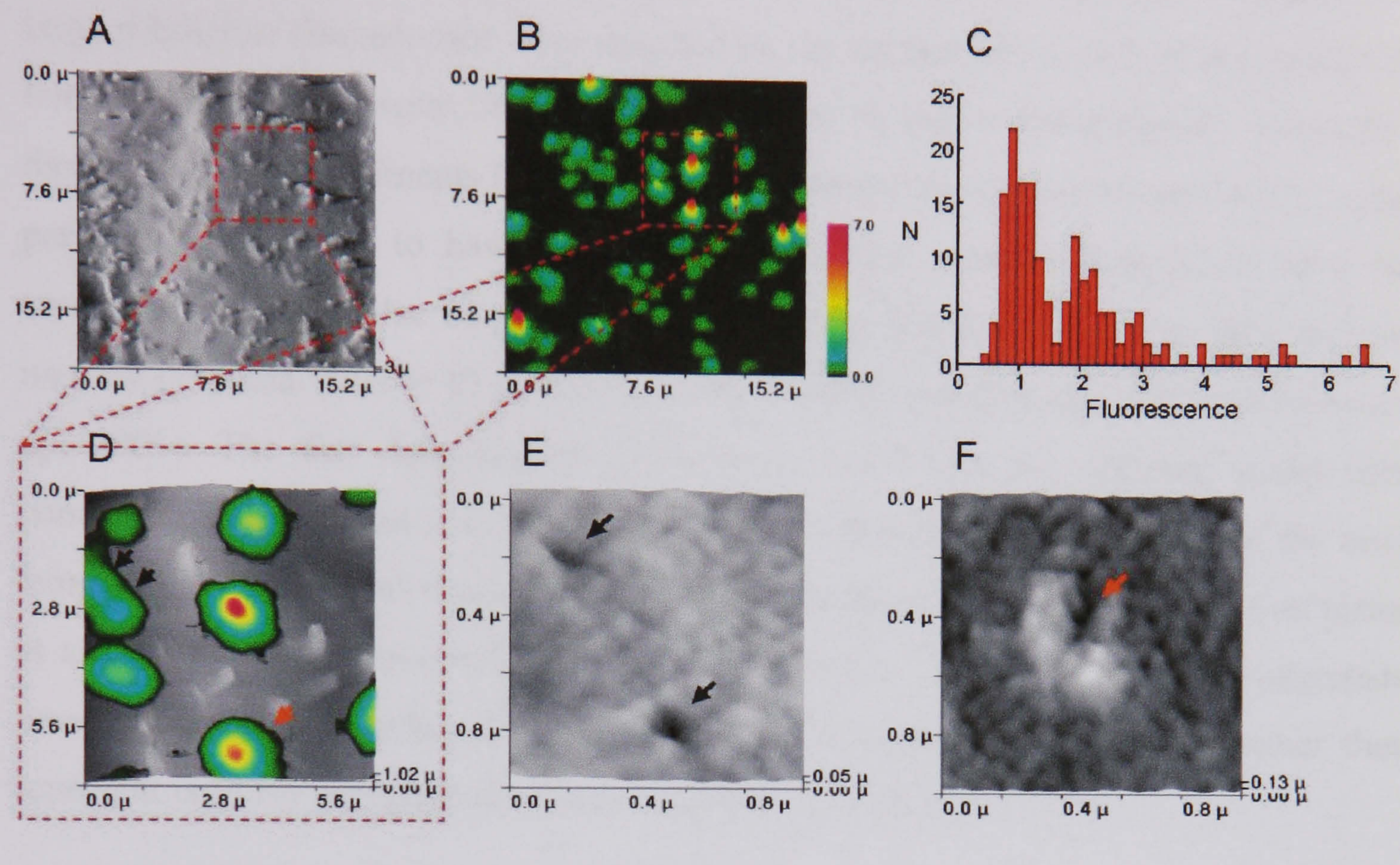

Fig. 9.6 SSCM imaging of single VPLs on the surface of the cell.
(*A*) A SICM topographic image of the cell surface. (*B*) A simultaneously obtained surface confocal fluorescence image of VLPs on the cell membrane. (*C*) Fluorescence intensity distribution of VLPs on the cell membrane obtained from surface confocal images. (*D*) A combination of SICM and surface confocal images of high resolution of the region marked with red box in *A* and *B*. (*E* and *F*) A zoomed topographic images acquired from the data gathered in the scan represented in *D* (regions containing VLPs are marked with arrows).

To track the process of VLP entry further we performed SSCM imaging of a smaller area of the cell surface at higher resolution. The superimposed fluorescence and topographical images of the cell surface area boxed in Fig. 9.6 *A* and *B* is presented in Fig. 9.6 *D*. Using this image as intermediate data for better targeting, guided by fluorescence we investigated two even smaller regions of the cell surface (marked with black and red arrows, Fig. 9.6 *D*). Zoomed topographic images of these regions are shown in Fig. 9.6 *E* and *F* where hollows in the surface no larger than 100 nm, corresponding to each VLP can be seen (marked with arrows, that ~~are~~ correspond to same positions shown in Fig. 9.6 *D*). The appearance of the holes recorded by SSCM for each structure was similar, confirming the size of the VLP-associated depressions to be within the 50–100 nm range.

As can be seen, single or small aggregates of VLPs are associated with the surface of the cell in an apparently random distribution. No tendency to associate with surface features such as microvilli was found (Fig. 9.6 *D*). Larger aggregates were not associated with the surface with any significant affinity: no topological structures or large patches of fluorescence were detected on the surface of the cells at low resolution, but some large fluorescent objects were dislodged by the scanning pipette. Although in these fixed-cell experiments (Fig. 9.2 and 9.6) adsorption was carried out at 0°C, single particles were found to have sunk into the surface, creating depressions of a size consistent with caveolae or pinocytic vesicles (Fig. 9.6 *E*), routes described as being used by polyoma virus or VLPs to enter cells (Griffith and Consigli, 1984;Richterova et al., 2001). The fact that apparent invagination of VLPs has occurred under these conditions suggests that it is possible that some internalisation may occur at the lower temperature. Similar internalisation events have been observed both by electron (Stang et al., 1997) and confocal microscopy (Pelkmans et al., 2001). Some small aggregates stood proud of the surface (Fig. 9.6 *F*), but it is currently not known whether these represent partially invaginated or superficially bound material.

9.3 Performing SSCM on live cells

As one of our major goals is to apply SSCM to studying particle uptake in cells with time, we tested whether recordings of fluorescent VLPs on the surface of live cells could be made. Large-scale scans of 40 x 40 μm were carried out (≈18 min per scan) to gain a global impression of the cell with regard to morphology and distribution of VLPs. Selected images of the topography with superimposed fluorescence measurements before and after adding VLPs are shown in Fig. 9.7.

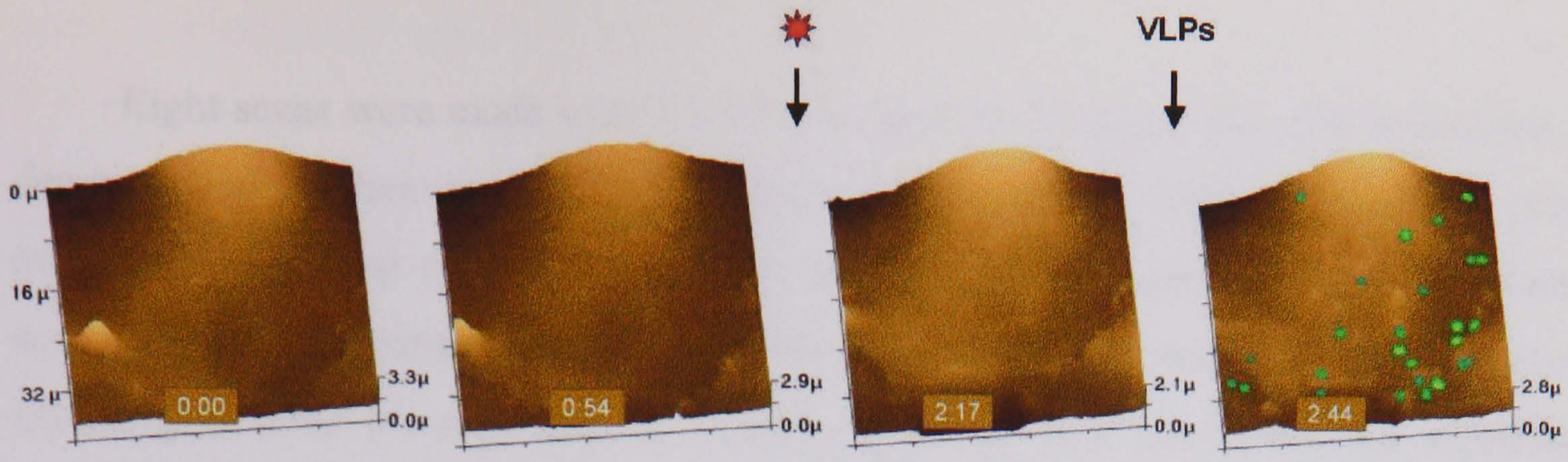

Fig. 9.7 SSCM imaging of VLPs on the surface of living cell.
Live COS 7 cells were sequentially scanned by SSCM approximately every 20 min for 4 h. Shown are topographical scans initiated at 0 min and 54 min and overlays of simultaneously obtained topographic and fluorescence scans at 2 h 17min, 2 h 44min, 3 h 2min, 3 h 20min, 3 h 37 min, and 3 h 55 min, respectively. Scanning for fluorescence was initiated at 2 h 17 min (red star); fluorescent VLPs were added at 2 h 40 min (VLPs). Fluorescence is represented as an intensity profile: black, lowest intensity; red, highest intensity. A slowly moving spot is clearly visible near the center of SSCM images at 3 h 2 min, 3 h 20 min, and 3 h 37 min (last remaining fluorescent spot in the image at 3 h 37 min).

Eight scans were made over 2 h 17 min. During this time, the cells were alive, as demonstrated by their morphology (flattened) and dynamic surface: microvilli (small projections scattered over the surface of the cell) formed and disappeared between scans, and a large feature (to the left of the images) could be seen migrating out of the frame (first three panels). At 2 h 17 min, the laser was turned on. No significant autofluorescence was observed on the surface. Fluorescent VLPs then were added to the surface of the cells and scanned at 2 h 44 min. VLPs bound to the cell surface, producing an image similar to that observed in fixed cells (compare with Fig. 9.1 C). By the next scan (3 h 2 min), the distribution of surface fluorescence had altered significantly. In the following image (3 h 20 min), much less surface fluorescence was observed, and by the last two scans, little remained (3 h 37 min and 3 h 55 min, respectively). At the end of the experiment, scanning by conventional confocal microscopy detected fluorescence within the cell. A slowly moving fluorescent spot that was still visible on the surface at 3 h 37 min, when all of the other fluorescence had gone, indicated that the disappearance of fluorescence was not solely caused by photobleaching.

9.4 Discussion

As can be seen, by using ion conductance to control the distance from the sample cells could be scanned repeatedly at high resolution over 4 h (Fig. 9.7). The SSCM imaging did not prevent internalisation of the VLPs, and uptake occurred over a time scale reported for this virus family (Pelkmans et al., 2001;Richterova et al., 2001).

However, to refine this technique for studying particle interactions with live cells, factors such as time resolution and photobleaching need to be considered. The scan rate used in these preliminary experiments was relatively slow (averaging 18 min), but it could be reduced to 30–50 sec by using a faster piezo (2–3 kHz resonant frequency) and by scanning a smaller area (7 x 7 μm, unpublished results). Thus, it would be feasible to use this technique for studying viral entry, where average internalisation rates are 5–30 min (Greber et al., 1993;Gromeier and Wetz, 1990;Sodeik et al., 1997). Also, because uptake of VLPs seems to be rapid or difficult to arrest with temperature, to assist real-time measurements, particles could be locally delivered to the cell surface with the

same, or a second, pipette, and then the entry process followed in a small area of the cell at high resolution.

Although it is possible to perform continuous topographic imaging, this is not possible for fluorescence imaging as, in common with most fluorescence methods, especially in live-cell fluorescence microscopy, photobleaching and photodamage limit the observation time. In our case, minimizing the cell exposure to the laser by scanning at a faster rate should extend the observation time. Furthermore, to follow a particle on the cell surface, it is not necessary to obtain a fluorescence image with every topographic image, allowing the cell exposure to the laser light to be reduced further. Once a particle has passed through the membrane, its physical interaction with the cell can no longer be observed by topographic imaging. However, by lowering the confocal volume in relation to the membrane, it is possible to obtain fluorescence images under the cell surface to follow subsequent steps. In this way, we were able to image VLPs internalised after 4 h (Fig. 9.3).

The live cell experiment demonstrated the dynamic nature of the interaction of VLPs with the cell surface. We observed large changes in the distribution of particles in the first 30 min after addition and, subsequently, loss of surface fluorescence, consistent with the particles being internalised.

By using this new surface-orientated approach, a number of cell plasma membrane phenomena can be addressed. For instance, the initial stages in virus, bacteria, gene delivery vehicle, or drug uptake may now be observed in relation to the actual membrane surface, allowing characterization of lateral movements and penetration of the membrane. Elucidation of their roles in uptake could be carried out by relating their position with fluorescently tagged cellular functions, such as receptors, lipids, or cytoskeleton. Further, apart from characterizing the basic process, it would be possible to identify new drug targets, test the ability of drugs to modulate uptake, or characterize uptake topography in a semi quantitative manner. These studies should provide real-time structural information only previously imaged statically by electron microscopy.

9.5 Conclusions

With SSCM, sensitive and quantitative imaging of fluorescence can be obtained in conjunction with topographic data gathering. This method will allow specific study of nanoparticles on the surface of cells and detailed characterization of their interactions with the plasma membrane. Thus, SSCM represents a valuable tool for understanding the earliest stages of particle uptake and will contribute to the development of new drugs and gene therapy vehicles in a range of clinical applications.

Chapter 10 Development of a Scanning Ion Conductance Microscope (Part II)

10.1 Introduction

The development of the second SICM and the new scanning control system that I have undertaken during my PhD study is presented in this chapter.

Chapters 5-9 described various studies that have been carried out with the SICM. As has been shown, most ~~of studies~~ experiments required specialized high-tech equipment and thereby, the SICM was often customized for a particular task. Such adaptation in many cases requires not only incorporation of additional hardware but also implementation of additional software functions. Our current SICM is equipped with commercial hardware and software, therefore not much can be changed in order to increase multifunctionality of the system at the present time.

Another limiting factor of the first instrument is the scan rate, which is about 20 minutes per image covering a 40 x 40 μm area. This fact has often been noted as a substantial drawback of SICM (e.g. by the reviewers of our papers). However, a comparison with the faster AFM scan rate is misleading, because AFM mainly applied to the scanning of much smaller areas, of much harder samples. When applied to live cell imaging in physiological conditions AFM shows a scan rate similar to that of SICM (Braet et al., 1998;Sinniah et al., 2002b).

The overall scan rate of the microscope is derived from the control hardware/software rate of operation and the speed of positioning system. Unfortunately, in our first setup both control and positioning systems were slow. With no capability to develop faster piezo positioning system ourselves, we have to wait for faster commercial actuators to become available. In contrast, we have capabilities to: (i) select new hardware on the basis of which the new SICM control can be built and (ii) develop new scanning control software that, together with the control hardware, will provide faster scanning rates.

Such a home-built SICM scanning system should also give us more flexibility in terms of modifications of the microscope to particular needs.

The SICM control system development process is fully described in Appendix (Paragraph 1).

10.2 SICM architecture

The general SICM architecture of the new instrument is similar to the one described in paragraph 4.3 (Fig. 4.4). Two major differences are a modulation-dedicated high-resonant frequency piezo actuator, and a new control system. Each of the new components will be described in detail later in this chapter. The schematic diagram of the newly developed SICM is presented in Fig. 10.1.

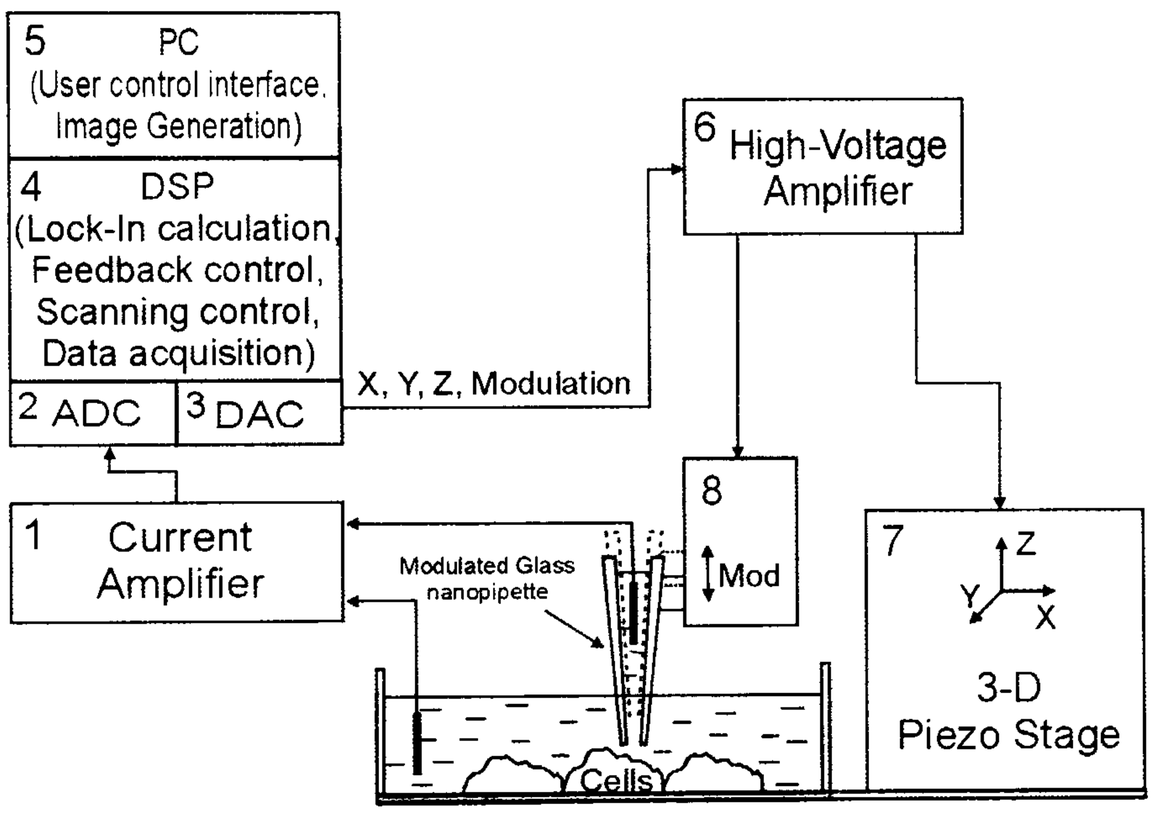

Fig. 10.1 SICM setup schematic diagram.

The modulated ion current (paragraph 4.3, Fig. 4.3) that flows through the tip of the nanopipette is measured by the current amplifier (1). The amplified ion current is digitised by the analog to digital converter (2) and fed into the digital signal processor (DSP) (4). The DSP calculates the lock-in and feedback correction signals using the digitised ion current as an input signal. Simultaneously, the same DSP generates two signals for *x* and *y*-axes to perform raster scanning of the sample/probe, and the modulation signal to vibrate the scanning pipette, which also serves as a reference signal for the lock-in measurements (paragraph 4.3). The *X, Y, Z* and *modulation* signals are then converted to analog form by the digital to analog converter (3) and amplified by the high-voltage amplifier (6). The scanning signals (*X, Y* and *Z*) are fed into the three-dimensional piezo translation stage (7) to drive the position of the sample/probe and the *modulation* signal is fed into the high-resonant frequency piezo (8). During imaging

digital scanning signals are also transmitted from the DSP (4) to the PC (5), which generates a topographical image of the scanned surface. PC also provides user control over the SICM.

10.3 Control hardware and software communications

The scanning control system operation starts with running of the host application on the main PC which establishes a connection with the DSP and uploads the DSP executable kernel into the M44 DSP board. The schematic diagram that represents hardware communication is presented in Fig. 10.2.

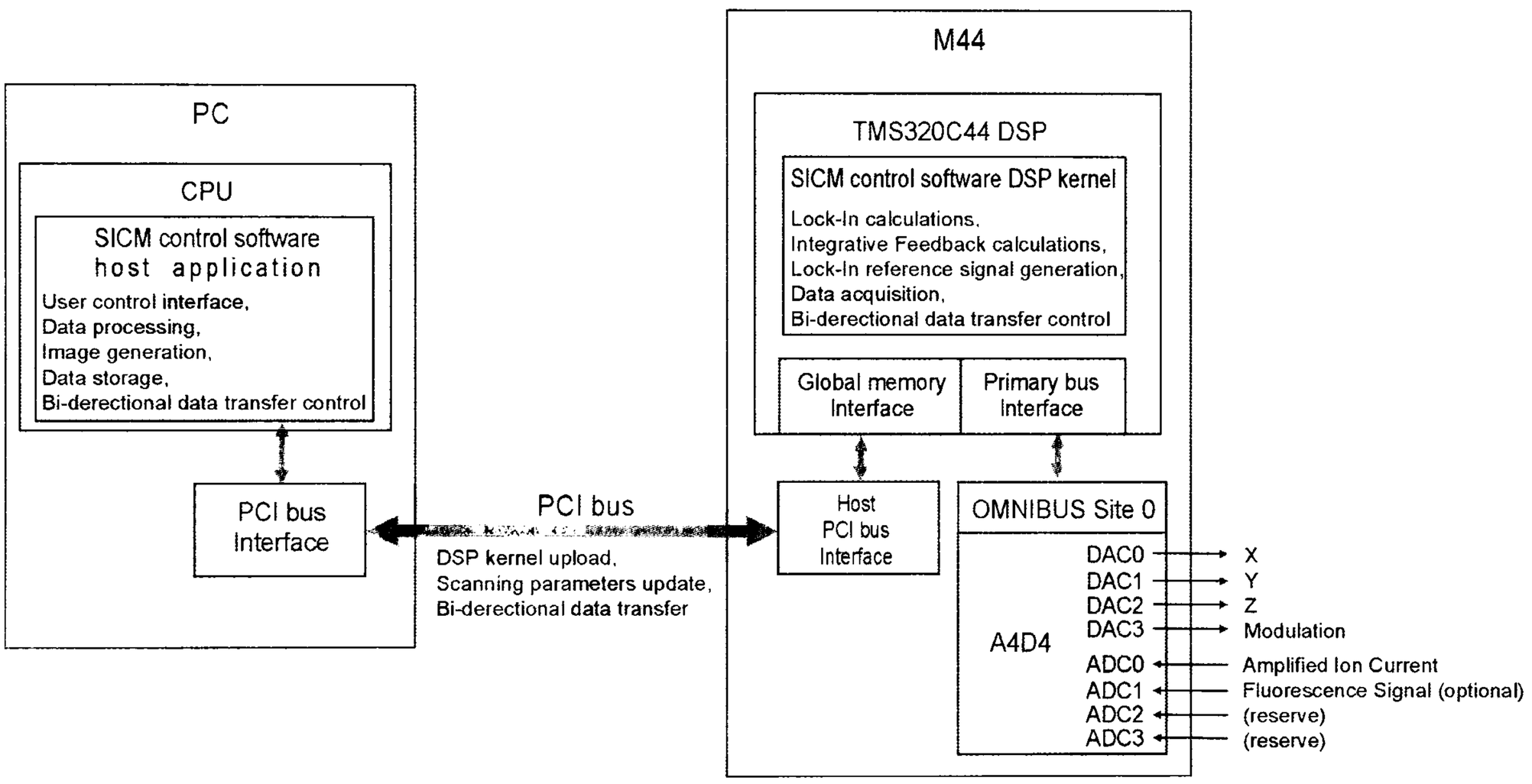

Fig. 10.2 SICM control system setup diagram.

When the DSP kernel is uploaded it starts the initialisation procedure as described in paragraph 10.5.2. Upon completion, the feedback control is in operation and running continuously, fully independently of any other procedures, until the program is stopped. In the next step, the host application program sends default scanning parameters to the DSP and waits for acknowledgement. When acknowledgement is received the control system is ready to start scanning. At this stage the user can change the scanning parameters such as *Scan Size, Scan Offset* and upload them to the DSP.

The triggering of the scanning procedure by the user on the host side results in the DSP kernel start scanning and collecting data. After the first line is completed the DSP

kernel makes the data available on the PCI bus for collection that, in turn, raises the interrupt in the host program, which executes the data processing procedure. While the data processing is in progress the DSP kernel positions the microscope probe at the beginning of the next line and waits for the signal from the host program to start. The host program process the data as described in paragraph 10.5.3.2 and updates the image with the new line. When update is completed the host program sends the message to the DSP kernel to start scanning the next line and scanning is repeated.

As soon as a number of collected lines is equal to a number of lines in the scan specified by the user the host program stops the scanning procedure, processes the image and saves the data (if the corresponding option is chosen). Meanwhile, the DSP kernel returns the scanning probe to its initial position.

If the *Repeat* scanning mode was chosen the scanning control software starts scanning the same area using the current scanning parameters. The repetitive scanning continues until stopped by the user.

In order to enable update of the scanning, control parameters such as *Gain, Proportional Gain, Set Point and Modulation Amplitude* at any stage of scanning, a special procedure was implemented. When the user changes any of the above parameters the host program sends the new value to the DSP, which updates the parameter in background mode, so that the feedback is not affected.

10.4 SICM control testing

Various testing procedures were undertaken at different stages of the SICM control system development.

Firstly, the integrative feedback control and the interface that allows feedback parameter adjustment were programmed.

Initial testing and tuning of the feedback was carried out using a physical model of a controlled device ("plant") represented by an RC-circuit where the disturbance signal was provided by a functional generator.

At the next stage, when the feedback control was considered to be correct, it was used for the SICM scanning. With this purpose the existing microscope (chapter 3) original feedback control (East Coast Scientific, Cambridge, UK) was replaced by

developed one. The rest of the system remains unchanged, so the topographical and current data were collected and visualized by East Coast Scientific control hardware and software as usual. Fig. 10.3 shows set of images acquired using the new feedback control as a part of the prototype microscope.

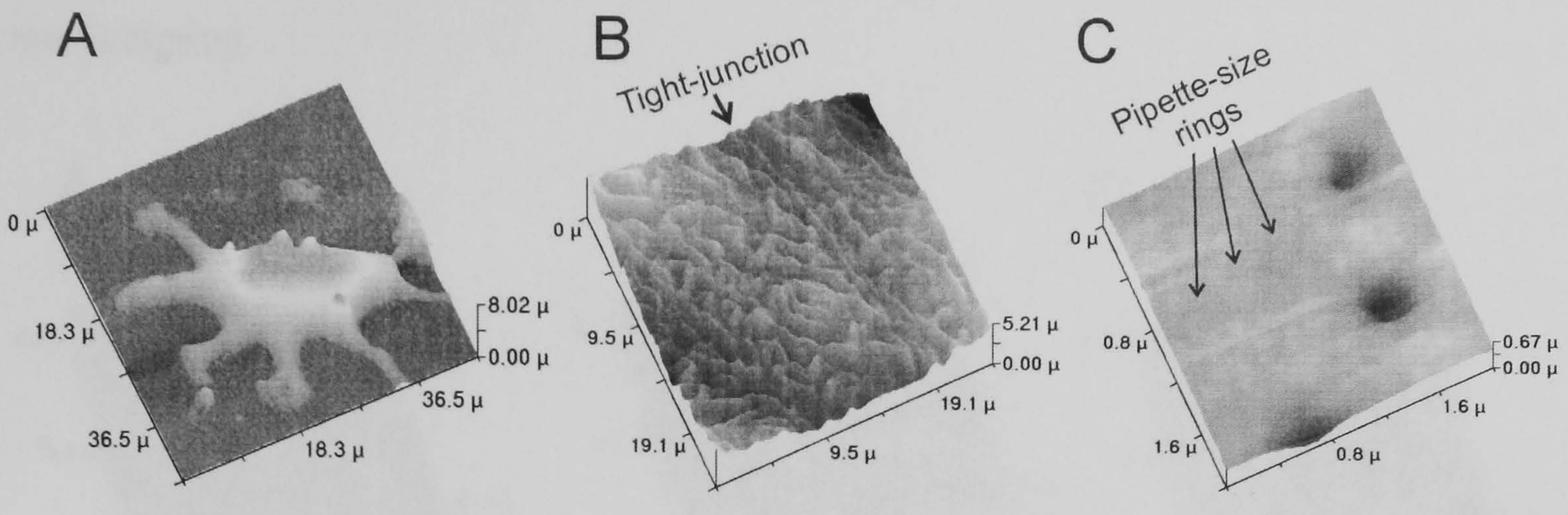

Fig. 10.3 New feedback control test images.
(*A*) A topographical SICM image of an osteoblast. (*B*) A topographical SICM image of *Xenopus* kidney epithelial A6 cells. (*C*) A topographical SICM image of an irradiated polyethylene terephthalate foil.

Fig. 10.3 *A* presents the topography of an osteoblast (cell sample was kindly provided by Prof. Dr. M.A. Horton) where the cell body and processes can be seen on the surface of glass. A topographical image of the surface of *Xenopus* kidney epithelial A6 cells is shown in Fig. 10.3 *B*. The image reveals microvilli (projections on the cell membrane) assembled in ridge-like structures and the tight-junction between two cells formed by two parallel rows of microvilli. Fig. 10.3 *C* shows ~200 nm nuclear pores in polyethylene terephthalate foil (similar to one that shown in paragraph 9.2). The pipette-sized rings that could be seen on the surface of the foil that are created by the scanning of hollows or holes whose dimensions are smaller than the size of the scanning pipette. These rings can be seen only if the surrounding area is flat and the noise is low. The size of the rings exactly matches the size of the scanning pipette.

As can be seen the new feedback can cope not only with a relatively large scanning area and large deviations in height, but is also sensitive enough to resolve sub-micron structures such as microvilli and 200 nm nuclear pores.

Secondly, the lock-in calculation was programmed and then tested by detecting the low amplitude (few mV) sinusoidal signal of various frequencies. The test showed that the lock-in can successfully extract and amplify the selected frequency. When a functional generator was added to the control software, the stand-alone lock-in amplifier

(SR830 DSP, Stanford Research Systems, Sunnyvale, CA) was also replaced and the control software was tested again by real scanning as a part of the prototype setup again.

The final stage of programming was to add the image generation procedures and user interface were added and the new control system was tested fully independently by real scanning.

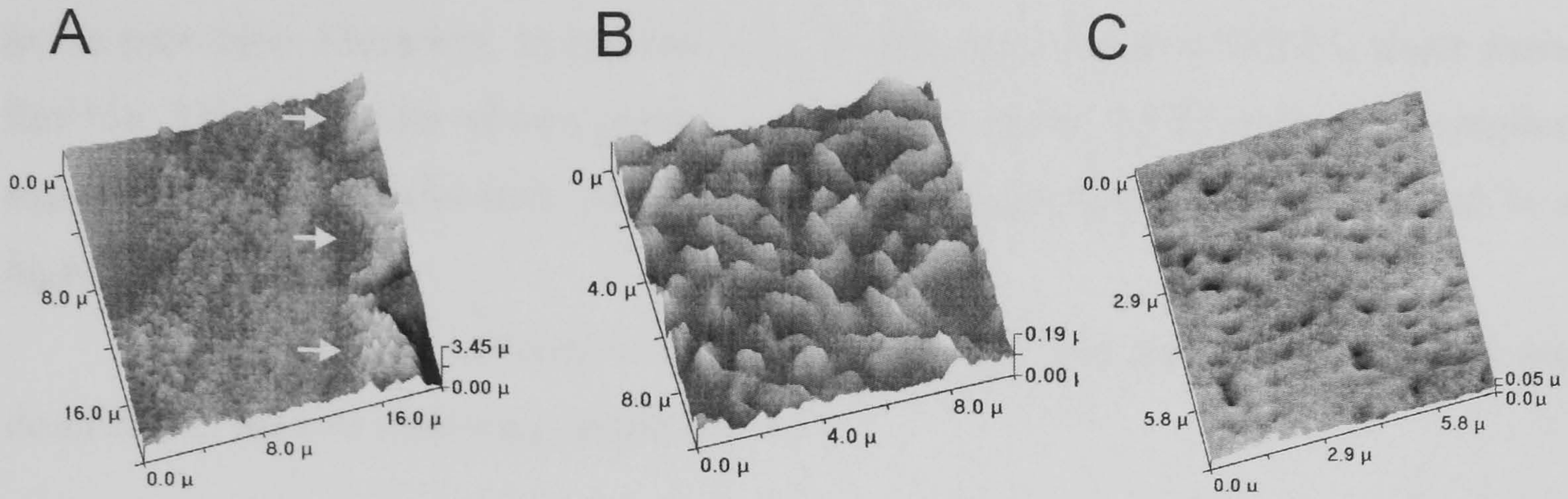

Fig. 10.4 New microscope control system test images.
(*A*) A topographical SICM image of stereocilias (marked with *arrows*) of sensory hair cells. (*B*) A topographical SICM image of *Xenopus* kidney epithelial A6 cell microvilli. (*C*) A topographical SICM image of an irradiated polyethylene terephthalate foil.

The image of stereocilias of sensory hair cells is presented in Fig. 10.4 *A* (arrows). Imaging of stereocilias presents a technical challenge for the SICM because of their large heights and the fact that they are perpendicular to the surface. Fig. 10.4 *B* and *C* show microvilli on the surface of *Xenopus* kidney epithelial A6 cells and pores in polyethylene terephthalate foil respectively, similar to those shown in Fig. 10.3 *B* and *C* but in different scale.

10.5 Summary

In this chapter the development and testing of the SICM has been described. The key difference of the new SICM setup is the specially designed control system. During the development of the SICM the following important tasks were addressed:

- selection of control system hardware
- development of control and data acquisition algorithms
- programming control and data acquisition algorithms

- testing the new SICM setup

On the basis of the results achieved during the testing of the SICM it has been considered that the selected scanning control system hardware is appropriate and capable of controlling the SICM.

The quality of the SICM images acquired during the testing clearly indicates that the developed SICM setup with the new control system can image the surfaces as well as the prototype. Moreover, in contrast with the prototype the new SICM is much more flexible. This flexibility allows greater functionality of the SICM and more complex experiments to be performed. Another major advantage that has been achieved is a higher scanning rate.

The experiments performed with the new SICM and the results achieved are described in the two following chapters.

Chapter 11 Real-time observation of cell surface structures assembly

11.1 Introduction

Although the dynamics of cell membranes and associated structures are vital for cell function, little is known due to lack of suitable methods. This chapter describes the direct real-time SICM observation of microvillar structures assembly in various living epithelial and non-epithelial cells.

Microvilli are projections from the surface of a cell that are supported by a central core of actin microfilaments and accessory actin-binding proteins (Bartles et al., 1998;Ezzell et al., 1989;Tilney and Mooseker, 1971). Although microvilli of various cell type have a similar structural organization, it has been shown that microvilli can play an important role in many cellular functions such as adhesion (Abitorabi et al., 1997), fusion (Wilson and Snell, 1998), transport (Lange, 2000), photoreception (Walz et al., 1995) and signalling (Foti et al., 2002).

One of the well-known functions of mivrovilli is cross-membrane transport in brush border cells, where microvilli are supposed to increase the absorptive surface area (Welling and Welling, 1975). These large specialized microvilli seem to be relatively stable throughout the life of the cell (Guild et al., 2002), although there are instances in which microvilli of intestinal cells can be dynamic. For example, Brunet et al showed that Ca^{2+} rise during rotavirus infection induces microvilli F-actin disassembly in intestinal epithelial cells (Brunet et al., 2000).

Other recent results also suggested that microvilli on different type of cells show dynamic behaviour as a response to physiological stimuli. For example, ATP depletion results in shortening or complete disappearance of microvilli (Golenhofen et al., 1995;Lange et al., 1989). Also, Reid et al showed that microvilli of diverse cell types elongate in culture in response to oxidative stress (Reid et al., 1997).

Relatively short (<500 nm) microvilli are observed on the surfaces of most cells, including fibroblasts, growing neurons, epithelial cells (DeRosier and Tilney, 2000;Bartles et al., 1998). It is suggested that these short microvilli may develop into

the larger microvillar structures like the intestinal microvilli or the stereocilia of hair cells of the mammalian inner ear (Chambers and Grey, 1979;Sobin and Anniko, 1984). However, in contrast with large specialized microvilli, almost nothing is known about stability of the shorter microvilli.

Originally, microvillar dynamic behaviour was suggested on the bases of their chemical structure (Hirokawa et al., 1982;Hirokawa et al., 1991). Later, in living cells a fluorescence photoactivation method was used to observe dynamical behaviour of actin filaments (Theriot and Mitchison, 1991;Theriot and Mitchison, 1992). In principle, this method could be implemented to study microvillar motility in live cells, however it can not provide precise measurement of dimensions, especially vertical, and requires staining that may alter cellular functionality.

In this study (Gorelik et al., 2003) for the first time we observed dynamics of single microvilli in living cells using the SICM technique. We studied such characteristics of microvillar dynamics as formation, retraction and lateral movement.

11.2 Measuring microvillar dynamics

To study microvilli dynamics we chose the A6 line of *xenopus* kidney epithelial cells which is widely used to investigate transport characteristics of epithelium (Kemendy et al., 1992). These cells form a monolayer with well-established tight junctions and microvilli (Candia et al., 1993). Previously, we showed that we can image microvilli in these cells by SICM under physiological conditions (Gu et al., 2002;Korchev et al., 2000a).

The SICM image of a monolayer of living A6 cells with well-developed tight junctions is presented in Fig. 11.1 *A*. Numerous microvillar structures can also be seen in Fig. 11.1 (*A* and *B*), These microvilli are supported by the bundles of actin filaments extending from the cortical cytoskeleton as shown in the SEM image (Fig. 11.1 *C*). The cell membrane was removed with mild detergent in order to reveal sub-membrane actin structures.

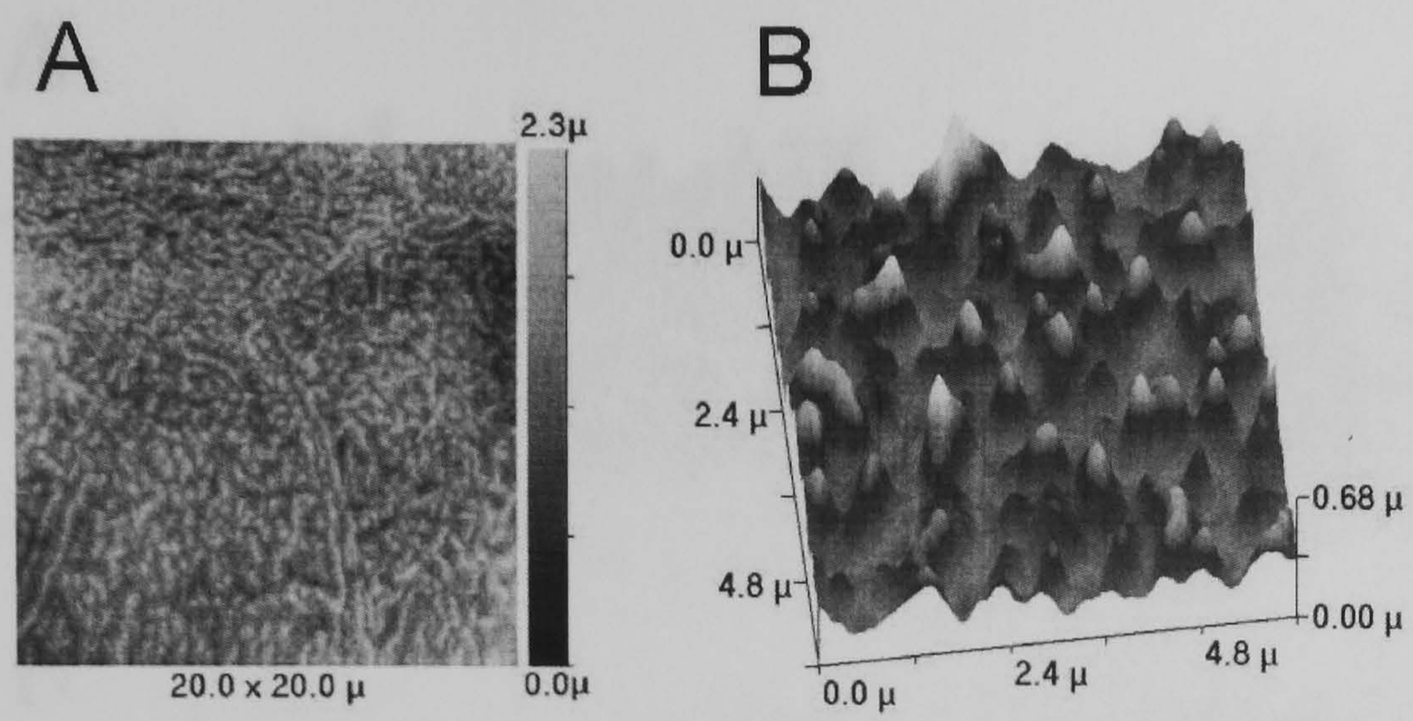

Fig. 11.1 SICM and SEM images of *xenopus* kidney epithelial A6 cell line.
(*A*) A topographical SICM image of cells with well formed microvilli. (*B*) 3-D representation of A6 cell microvilli. (*C*) A SEM image of A6 cell microvilli. To reveal the cortical cytoskeleton, the plasma membrane was removed by a mild detergent.

In order to measure the formation and retraction of a microvillus precisely we performed continuous imaging of the same area of an A6 cell at a rate of one frame per 50 sec. The total time of observation was approximately one hour. Fig. 11.2 presents a selection of images of the same area on the surface of a living A6 cell. Consecutive selected frames illustrate the dynamics of microvilli. With the exception of a few (marked white) all the microvilli underwent rearrangements, at any given time, some were forming on the surface (marked orange), while others were retracting (marked green).

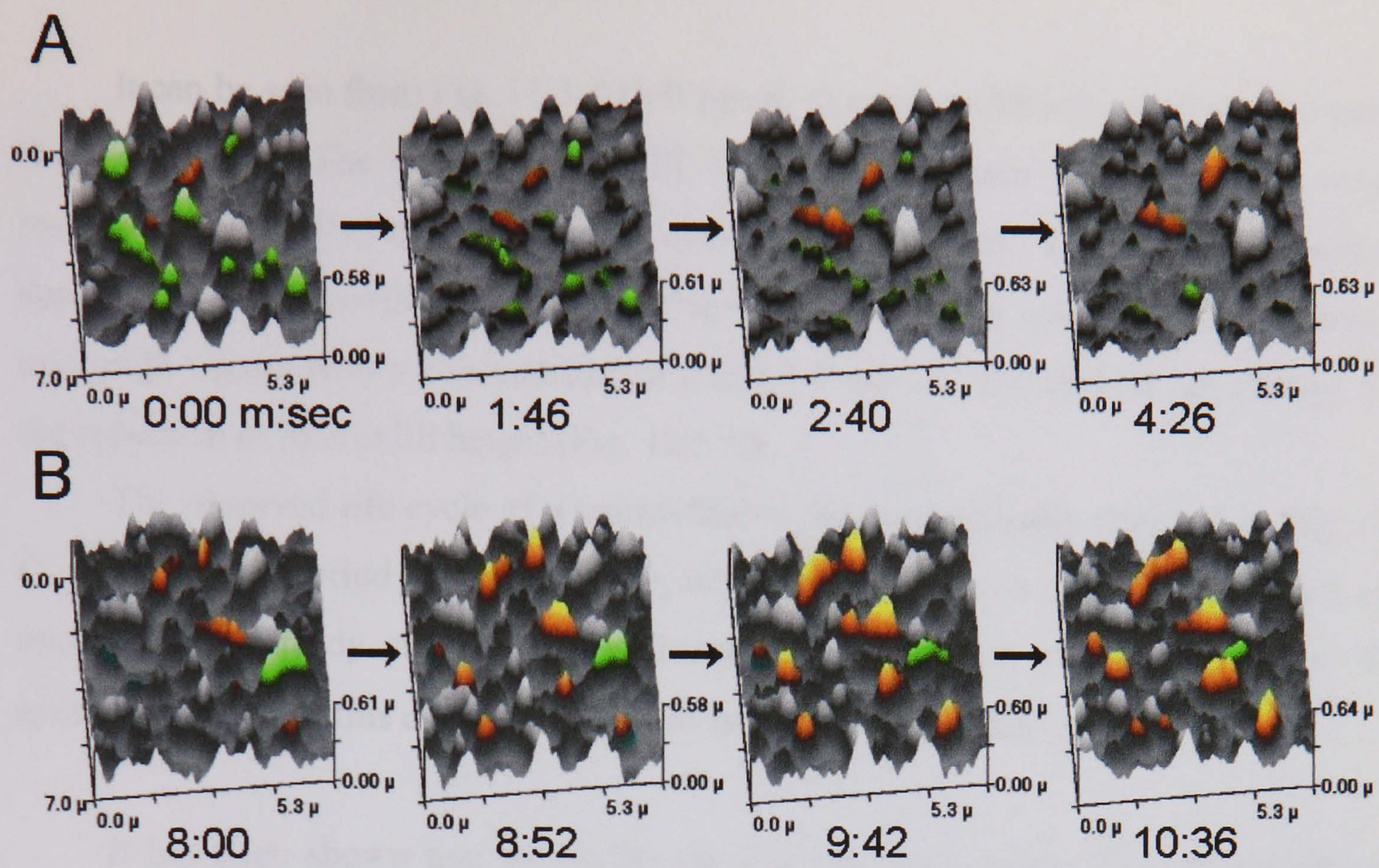

Fig. 11.2 High-resolution time-lapse imaging of microvilli.
Microvilli that are forming, retracting, or relatively "stable" are highlighted orange, green, and white, respectively. (*A*) Prevailing retraction of microvilli. (*B*) The same area at a later period of time, when the formation of microvilli prevails. Each image took 50 s to acquire. The complete sequence of images acquired in the experiment is presented as Movie 1, which is published (Gorelik et al., 2003) as supporting information on the PNAS web site, www.pnas.org.

Fig. 11.2 *A* (frames from 0:00 to 4:26 m:sec) represents the dynamics where the retraction of microvilli prevails. In contrast, the later frames taken from 8.00 to 10.36 (Fig. 11.2 *B*) depict the formation of microvilli. Therefore, during 200 sec separating the two sets of frames, the microvilli dynamics changed from retraction to formation.

Fig. 11.3 shows representative rates of single microvilli elongations.

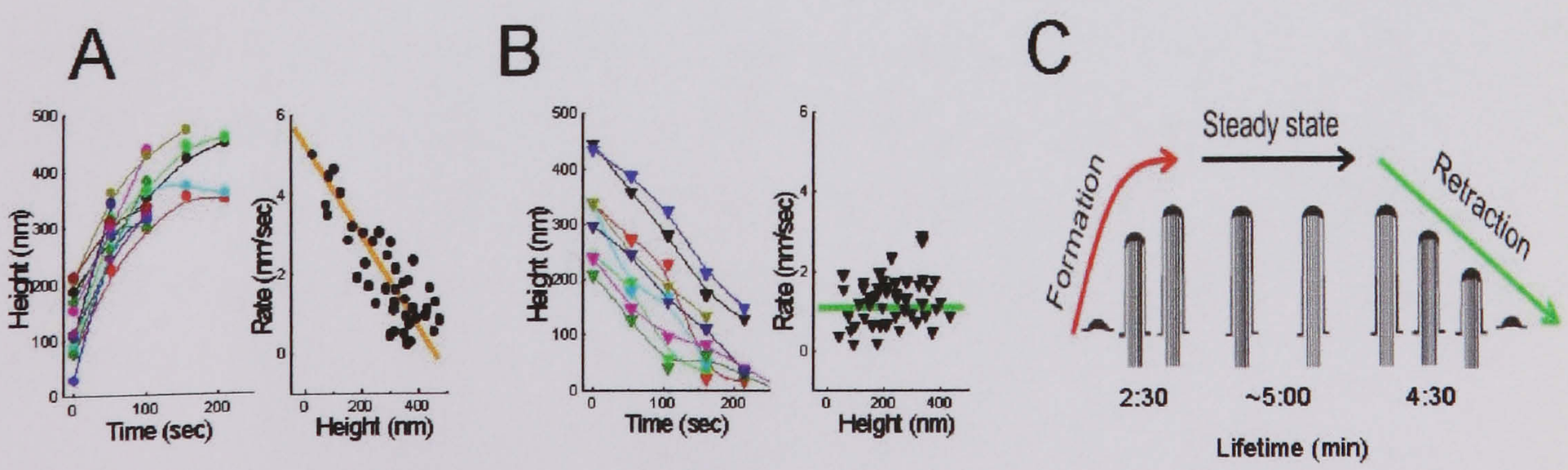

Fig. 11.3 Microvilli formation and retraction rates and schematic diagram of a life cycle.
(*A*) Heights of individual microvilli increase nonlinearly during their formation (*Left*). Height-dependent rate of microvilli formation (n = 566) (*Right*). (*B*) Individual microvilli undergo linear decrease in height during retraction (*Left*). Height-independent rate of microvilli retraction (n = 559) (*Right*). The experiment was performed at 27°C. (*E*) Schematic diagram of the life cycle of an individual microvillus: formation, steady state, and retraction.

It can be seen from Fig. 11.3 *A* (left panel) that microvilli initially form at a rate of about 5 nm/sec. The rate of microvilli formation decreases with increasing height, resulting, eventually, in cessation of microvilli elongation. The left panel presents dependence of microvilli formation rate versus its height. In contrast, the retraction of microvilli occurs with a constant rate of about 1.6 nm/sec, which does not change with the reduction of microvilli height (Fig. 11.3 *B*).

The observed life cycle of a microvillus is diagrammatically depicted in Fig. 11.3 *C*. After a short period of rapid growth, which characterizes a sudden appearance of a microvillus, a steady state ensues, followed by a retraction at a constant rate. The average duration of this cycle was found to be 12.1±5.6 minutes (n=244).

It has been shown that microvilli can fuse and form larger structures (DeRosier and Tilney, 2000). Following SICM observation we found that microvilli doublets and triplets form along one axis (Fig. 11.2 *B*, orange marked microvillus on the top of every image in sequence). The lateral movement of microvilli can also be seen from Fig. 11.2 *A*. The distance between two microvilli (marked white, first frame) increased (compare with last frame) giving the rate of lateral movement of approximately 3 nm/sec.

Formation of multiple aggregates of microvilli often led to ridge-like structures. Almost 50% of the cells in the monolayer had ridges rather than discrete microvilli (Fig. 11.4 *A*).

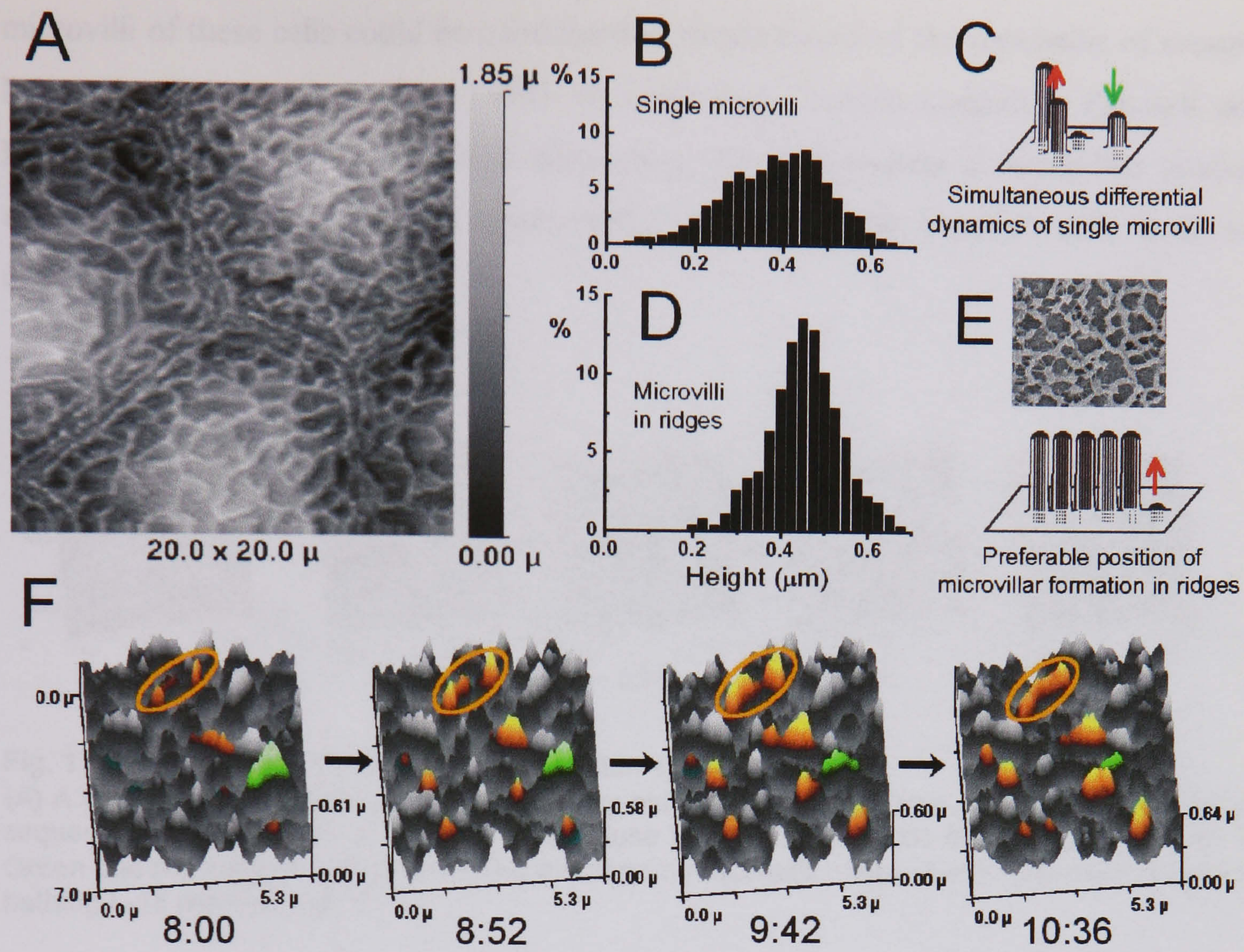

Fig. 11.4 Formation of ridge-like structures in epithelial cells. (*A*) A topographical SICM image of cells with well formed ridges. (*B*) The distribution of heights of single microvilli. (*C*) Schematic diagram of simultaneous formation and retraction of single neighboring microvilli. (*D*) The distribution of heights of microvilli in ridges. (*E*) A SEM image showing individual microvilli arranged into the ridges (*Upper*). Schematic diagram of sidewise formation of microvilli in ridges (*Lower*). (*F*) A sequence of topographical SICM images (from Fig. 11.2 *B*) shows formation of the ridge structure (marked with orange oval).

The assembly of a ridge starts from the formation of a new microvillus alongside an existing one. Then neighbouring microvilli appear aggregating into ridges (Fig. 11.4 *E* and *F*). Newly formed microvilli never aggregate together as a clump. They only associate laterally to form a ridge. Sometimes these ridges branched or angled at precisely 120-degrees. The ridges had a uniform height (within the boundaries of a normal distribution), whereas individual microvilli had a population of shorter microvilli (Fig. 11.4 *B, D*), which probably reflects their formation or retraction (Fig. 11.4 *C*).

To confirm that the observed microvilli dynamics is not a specific property of a cultured cell line but rather a wide-ranging cellular phenomenon, we studied the microvillar dynamics in different cell types (including human cells). One example is epithelial non-sensory cells of the mouse organ of Corti. The well-developed short

microvilli of these cells could be considered as predecessors of the stereocilia of sensory hair cells (Sobin and Anniko, 1984). In organotypic culture conditions (Russell and Richardson, 1987), these epithelial supporting cells still possess a microvillar coating albeit not as dense as *in vivo* (Furness et al., 1989). One type, Hensen's cells, is shown in Fig. 11.5 *A*.

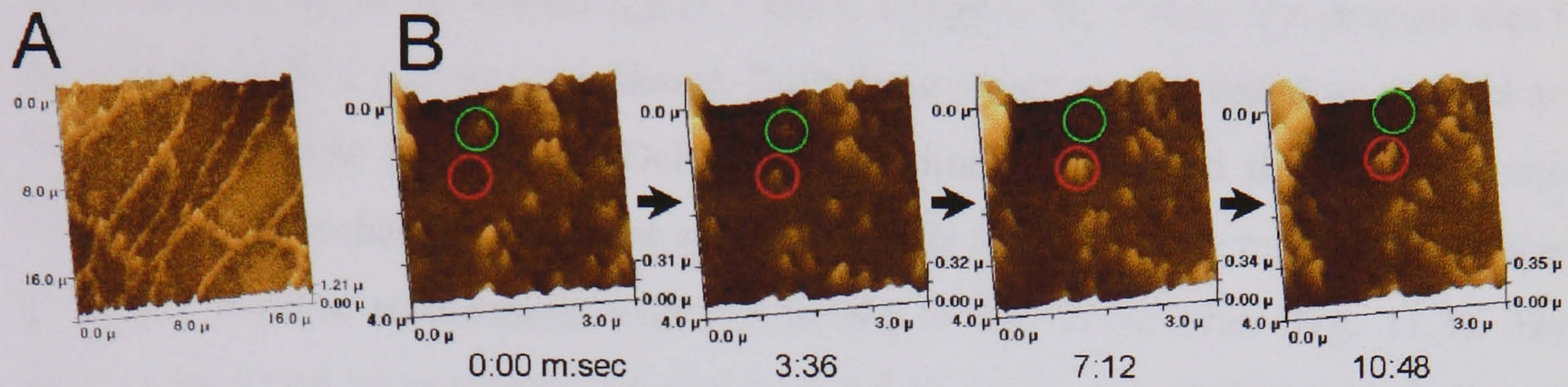

Fig. 11.5 Microvillar dynamics in mammalian epithelial cells.
(*A*) A SICM image of Hensen's cells in a 3-day-old organotypic cochlear culture. (*B*) Time-lapse sequence of four images of a smaller area close to the border of one of the cells shown in *A*. Green and red circles point to retracting and forming microvilli, respectively. Temperature of the bathing L-15 medium was 27°C.

Similar to A6 cells, time-lapse SICM observations revealed ongoing dynamics of microvilli on the surface of these Hensen's cells (Fig. 11.5 *B*). Remarkably, the rates of microvilli formation and retraction in these mammalian epithelial cells were similar to those of the Xenopus A6 cells. In the sequence of panels shown in Fig. 11.5 *B*, it took about three minutes for a microvillus to form, which is very close to the values measured for A6 cells (Fig. 11.3 *A*). Similar to A6 cells, retraction of microvilli was slower. Analogous microvillar dynamics was also observed in another type of epithelial supporting cells of the organ of Corti, outer phalangeal cells (data not shown). As expected, the larger microvillar structures, stereocilia of sensory hair cells, were substantially more stable showing no signs of dynamic changes of height or lateral arrangement within the accuracy of the SICM imaging technique (paragraph 10.7, Fig. 10.4 *A*).

In addition to our experiments, we performed time-lapse imaging of the surface of the following cell types: human colon cancer cells (CACO-2 line), murine melanocytes (melan-b line), breast cancer cell (T47D cell line), and fibroblasts (data not shown). In all these cells, we observed microvillar dynamics similar to those described above.

11.3 Discussion

We suggest that microvillar dynamics are likely to be a common phenomenon for short non-specialized microvilli irrespective of their cell origin.

Several features of these dynamics should be noted. Initial formation rate of individual microvilli is about 5 nm/s, which is very close to the rate of elongation of the fertilization cone in sea urchin egg (5.5 nm/s) (Begg et al., 1982). We propose that this is unlikely to be a simple coincidence. Both these structures are based on parallel actin fibres packed into the bundle (DeRosier and Tilney, 2000) and the measured initial formation rate probably reflects the speed of bundle assembly. The rate of growth shows a distinct inverse relationship with the height of the microvillus (Fig. 11.3). These observations can be explained bearing in mind that actin polymerisation is believed to occur close to the cell membrane, whereas actin depolymerisation happen on the opposite end of actin fibres. This inverse relationship would be expected if formation of the microvillus depends on simple diffusion of actin and actin-binding proteins to its tip. As the microvillus grows, the longer diffusion path leads to a decrease in the rate of actin bundle assembly. A microvillus stops growing when the rate of formation becomes equal to the rate of ongoing actin depolymerization. Such a dynamic steady-state equilibrium between actin bundle formation and actin depolymerisation was proposed to regulate the length of large microvillar structures like *Drosophila* bristles (Guild et al., 2002), brush border microvilli (Tyska and Mooseker, 2002) or stereocilia of hair cells (Schneider et al., 2002). In our experiments, microvilli after formation were in a steady state for approximately 5 minutes followed by retraction with a constant rate of 1.2 nm/s (Fig. 11.3), which is much slower than formation rate and is comparable to the rate of actin depolymerisation at 2 nm/s (Pollard et al., 2000). This suggests that, at least in the retraction phase, actin polymerisation is blocked and not involved in the control of the microvillar height. However, it is not clear what signals control retraction or growth of a microvillus. Presumably, this on/off signal has to operate locally since two neighbouring microvilli may exist in different phases of their life cycle (Fig. 11.4 *C*).

11.4 Conclusions

It has been proposed that microvilli serve as "the archetypal factory of an actin bundle" (DeRosier and Tilney, 2000) constantly providing a cell with organized bundle assemblies, which could be utilized by the cell to form larger specialized microvillar structures. Here we have shown that microvilli are constantly changing, which indeed implies ongoing assembly and disassembly or utilization of actin bundles. In fact, the dynamics of actin assembly in cortical cytoskeleton (Schafer et al., 1998) is strikingly similar to microvillar dynamics observed in our experiments. Moreover, microvillar dynamics also provide clusters of microvilli, which serve as crystallization points for more stable surface structures, where the microvillar steady state is prolonged. From the foregoing, we concluded that microvilli serve as elementary "building blocks" of the larger structures on the surface of the cell.

Chapter 12 SICM for controlled molecule deposition

12.1 Introduction

There is currently a great interest in controlled formation of micro and nanometer size patterns of biological molecules. This is due to the application of the molecular patterning in such techniques as bio-sensing, medical implants, and control of cell adhesion and growth (Chen et al., 1997;Dontha et al., 1997;Morgan et al., 1995;St John et al., 1997). The current methods of molecule deposition are based on microcontact printing (μCP), microfluidic devices (μFDs) of dip-pen nanolithography (DPN) (Bernard et al., 2001;Clark et al., 1990;Delamarche et al., 1997;Piner et al., 1999). Although μCP can provide sub-micrometer feature size, this technique has little control over the amount of material deposited. Using μFDs it is generally difficult to obtain feature sizes smaller than several micrometers because of difficulties in device fabrication and practical problems due to channel blocking during the microflow. Moreover, both, μCP and μFDs can be used for molecule deposition only on flat surfaces since they do not control for height of the substrate. Also, the pattern that has to be printed is determined by the master stamp or filling mask and cannot be easily changed if necessary. Theoretically, DPN, which is based on scanning probe microscopy principles, could provide the means for molecule deposition at nanometer scale with control of height deviations at the same time. Recently, DPN was reported for DNA and proteins (Lee et al., 2002;Wilson et al., 2001). However, the amount of "ink" the AFM scanning tip can carry is very limited. In addition, this technique has no "on/off" mechanism, which can control the deposition process: i.e. all the scanned area would be covered with deposited material. This can be overcome by scanning a substrate with different surface adsorption properties. In this case, ink from the tip will be transferred to the substrate according to the local absorption properties. However, this approach also allows predetermined pattern printing only.

In our study we utilized the unique capabilities of the SICM scanning probe, which is a glass micropipette, to act as a local reservoir of ink (Bruckbauer et al., 2002). Thus far, SICM has only been used to write micrometer-size copper structures onto conducting surfaces (Zhang et al., 1999). A closely related method, scanning

electrochemical microscopy, has also been used to pattern silver dots onto a gold substrate (Yatziv et al., 2002). We used the SICM probe to deliver small quantities of biotinylated and fluorophore-labeled DNA (Appendix, paragraph 7.4.3) to a surface where they are immobilized by biotinstreptavidin binding. The control over the amount of molecule delivery was achieved by an applied potential together with a variation in the time of deposition.

12.2 Printing with DNA using SICM

The potential applied to an electrode inside the micropipette and an electrode in the bath creates the electric field along the pipette axis that results in current. The number of molecules leaving and entering the tip depends on a combination of electroosmotic flow, electrophoresis, and dielectrophoresis, depending on the size, charge, and polarizability of the molecules. The flow of fluorophore-labeled singlestranded DNA (ssDNA) out of the nanopipette has been previously studied using single-molecule fluorescence measurements at the tip of the pipette (Ying et al., 2002). When the counter-electrode was at a negative potential relative to the pipette, there was negligible flow of DNA out of the tip. On application of a positive potential, DNA flow occurred, and the flux was linear with applied potential. This gave fine control of the rate of DNA delivery by controlling the applied potential over a voltage range from 0.2 to 1.0 V.

Unfortunately it is not possible to change the applied bias voltage or it's polarity in order to control molecule application during the scanning since it affects the SICM feedback control. So, the printing was performed at a constant positive voltage and the amount of deposited molecules was controlled by the time of deposition. With this purpose a special algorithm for molecule deposition was programmed.

The pattern that has to be printed is drawn fist as a greyscale bit-map image using any computer graphic software package. Then the SICM control software loads the image into the DSP, where the image is converted to an array of delays according to brightness so that the longest delay corresponds to a white colour, and black colour introduces zero delay. The dimensions of the array are equal to the number of pixels and lines in the SICM image to be scanned. During the scanning the control software uses a particular value from the array of delays that corresponds to a micropipette current

position. Therefore, the micropipette spends more time over some places than others. This results in different deposition times. Thus, different amounts of molecules can be attached to the surface of the substrate in different places.

The distance between the scanning micropipette and the substrate surface was controlled by the SICM feedback, as during the usual scanning procedure. Therefore, the separation gap was approximately equal to one pipette radius, that is ~ 100 nm.

After printing a pattern, the surface was retracted about 15 μm by the sample piezo stage so that the DNA leaving the tip diffuses into the bulk volume and dilutes rapidly.

The patterns of DNA molecules were inscribed on the surface of biotinstreptavidin home-coated glass (for coating procedure see Appendix, paragraph 7.4.4).

Fluorescence images of the printed patterns were acquired with a fluorescent microscope based on a Nikon TE Eclipse inverted microscope equipped with an oil immersion objective (100x, NA 1.30) and a high-sensitivity Charge Coupled Device (CCD) camera (PI-MAX 512RB, Princeton Instruments Inc., USA). Excitation source was provided by T-FL Epi-Fluorescence Attachment (Nikon Corporation, Tokyo, Japan) equipped with Xenon Lamp 100W (OSRAM: XBO100W OFR) and C-FL Epi-FL Filter Block N B-2A (Excitation filter N EX450-490, Dichroic mirror N DM505, Barrier Filter N BA520). General setup arrangement is similar to the one described in paragraph 2.4.3.

The optical resolution of the instrument was determined by imaging 200 nm fluorescent micro zspheres (Molecular Probes).

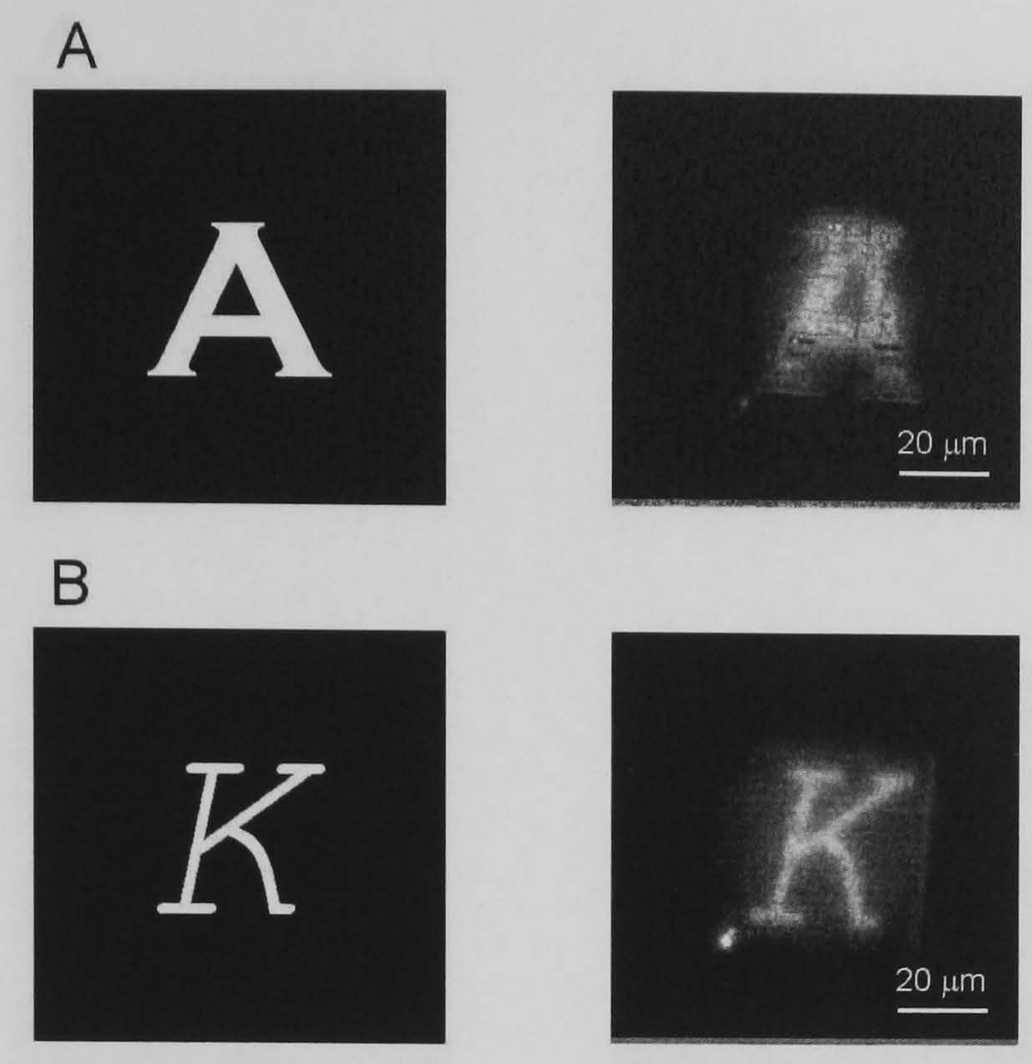

Fig. 12.1 Letters printed with fluorescently-labeled DNA molecules.
(*A*) An original bit-map image of the letter "**A**" (left panel) and a fluorescent image of the letter printed with fluorescently labelled DNA molecules (right panel). (*B*) An original bit-map image of letter the "*K*" (left panel) and a fluorescent image of the letter printed with fluorescently labelled DNA molecules (right panel). Both fluorescent images acquired with a CCD camera.

Fig. 12.1 shows letters printed by the SICM with fluorescently-labeled DNA molecules on the biotinstreptavidin-coated glass. The bit-map image of the letter "A" that has been loaded to the DSP as original data (left panel) and the printed image of the letter (right panel) are shown in Fig. 12.1 *A*. The bit-map image of the letter "K" and the letter itself printed in the same fashion is shown in Fig. 12.1 *B*.

To investigate the capabilities of the SICM to print more complex patterns we printed Imperial College London and Cambridge University crests (Fig. 12.2).

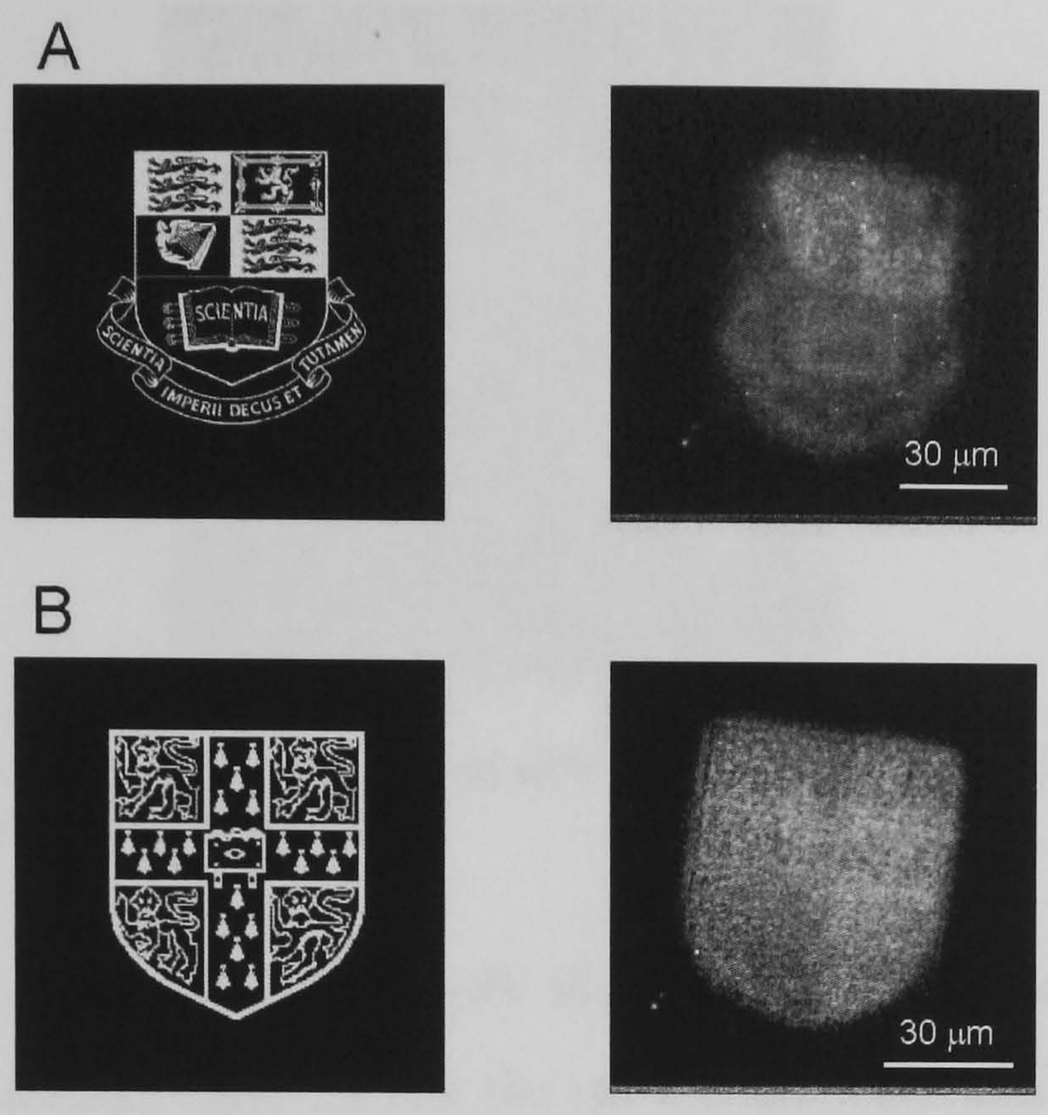

Fig. 12.2 Imperial College and Cambridge University crests printed with fluorescently-labeled DNA molecules.
(*A*) An original bit-map image of Imperial College crest (left panel) and a fluorescent image of the crest printed with fluorescently labelled DNA molecules (right panel). (*B*) An original bit-map image of Cambridge University crest (left panel) and a fluorescent image of the crest printed with fluorescently labelled DNA molecules (right panel). Both fluorescent images acquired with a CCD camera.

Fig. 12.2 *A* and *B* presents loaded bit-maps (left panels) and corresponding them printed (right panels) images Imperial College and Cambridge University crests accordingly.

Both sets of printed images, letters and crests, have a low resolution due to non-uniform molecular attachment to the substrate surface. The non-uniform molecular attachment can be seen especially well in Fig. 12.1 *A* (right panel). This non-uniform attachment was considered to be because of the not sufficient quality of biotinstreptavidin home-coating. However, when commercially-coated surface is used (Appendix, paragraph 7.4.4) prints of much higher resolution can be achieved.

Fig. 12.3 presents Cambridge University crest printed by the SICM on the commercial biotinstreptavidin coating.

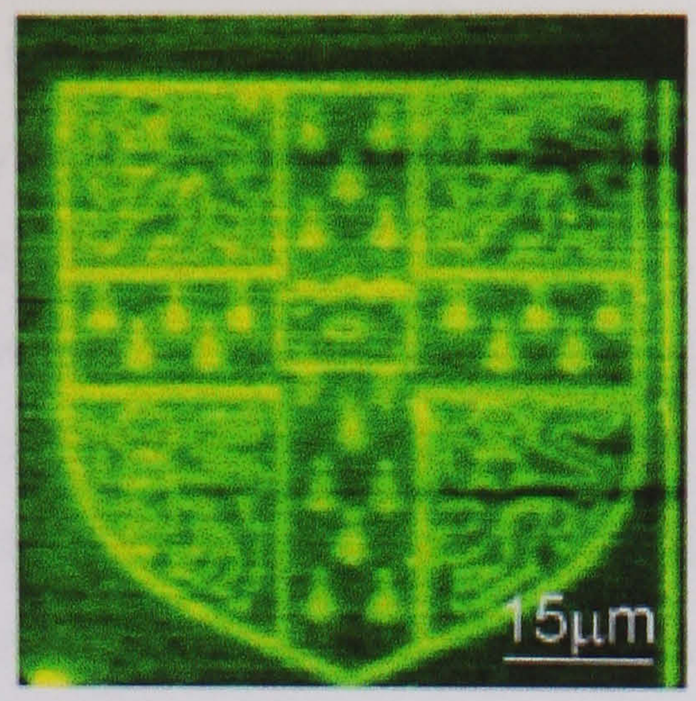

Fig. 12.3 Cambridge University crest printed with fluorescently-labelled DNA molecules. Image acquired with a confocal microscope.

This image was recorded under 5 µW illumination at 488 nm (Model 5400, Ion Laser Technology, Salt Lake City, UT) on the same instrument used for the writing. The fluorescence signal was detected using an oil-immersion objective (100x, NA 1.25) and a photomultiplier tube detector (Photon Technology Surbiton, UK). A dichroic beam splitter (Omega optical 505 DRLP), longpass filter (BA520, Nikon, Japan) and a 50 µm pinhole were used to separate the fluorescence signal and to reject background signal and laser scattering. The displacement of the piezo stage was calibrated using a hexagonal pattern formed by 2.9 µm beads and a micrometer scale bar (Pyser - SGI, Edenbridge, UK).

The optical resolution of the instrument was determined by imaging 200 nm fluorescent microspheres (Molecular Probes) and found to be the same as the resolution of the fluorescent microscope used in first set of experiments. However, in contrast with the first attempt where home-coated biotinstreptavidin surface was used, this image demonstrates higher resolution.

12.3 Discussion

Since the SICM molecule deposition method uses the micropipette as a delivery tool and operates in solution, the size of the printed feature should depend on the scanning micropipette diameter, the pipette – substrate surface separation distance, and the molecular diffusion rate.

The use of smaller size pipettes should increase the resolution in general, however it is associated with such problems as quality of the SICM scanning control (paragraph

2.2), and pipette blockage that provides restricts transport of molecules. The separation distance can be reduced by scanning at higher set points allowing higher concentration of molecules reach the substrate surface.

In a simple model, where the presence of the glass surface near the tip and the pipette wall thickness are neglected, the feature size can be estimated using the steady-state concentration profile derived for ultra-microelectrodes in the diffusion-limited case (Bond et al., 1988). The calculation for a pipette of 100 nm diameter held at 120 nm distance from the surface leads to a fwhm of 450 nm for the concentration profile. After deconvolution with the instrument function, the observed feature size is a factor of 1.6 larger in the case of DNA on streptavidin coated glass. This is in a good agreement with the experimental data (Bruckbauer et al., 2002).

Also, the lateral diffusion of the molecules on the substrate and the density of molecule binding sites should be considered when estimating the size of a printed feature. In order to prevent the consequent image blurring, fixation needs to be applied immediately after printing.

12.4 Conclusions

The SICM method of controlled molecule deposition offers advantage over previous methods. It can operate under physiological conditions so that it should be straightforwardly applicable to other biological molecules such as enzymes and antibodies. It allows fine control of the density of the deposited molecules on the surface potentially down to the single-molecule level, as single-molecule delivery from the nanopipette has already been demonstrated (Ying et al., 2002).

In comparison with other methods, the SICM molecular printing provides such important additional advantages as a large reservoir of ink and the possibility to print on 3D surfaces of most kinds of materials. Also, the easy and flexible master pattern generation procedure together with controlled molecular delivery can allow printing of complex patterns. Above all, subsequent assays can be performed on surface-attached molecules by local application of one or more reagents from the pipette.

Chapter 13 Summary and conclusions

The work discussed in this thesis describes the potential of SICM for biophysical and biomedical research. The results obtained clearly demonstrate the advantages of using SICM for biomedical studies over other scanning techniques.

The SICM vertical positioning control has been improved by the development of a distance modulated protocol enabling long term imaging and measurement of fast and slow membrane dynamics in living cells. This new robust SICM control system has also allowed the development of a wide range of new hybrid techniques summarized in Fig. 13.1.

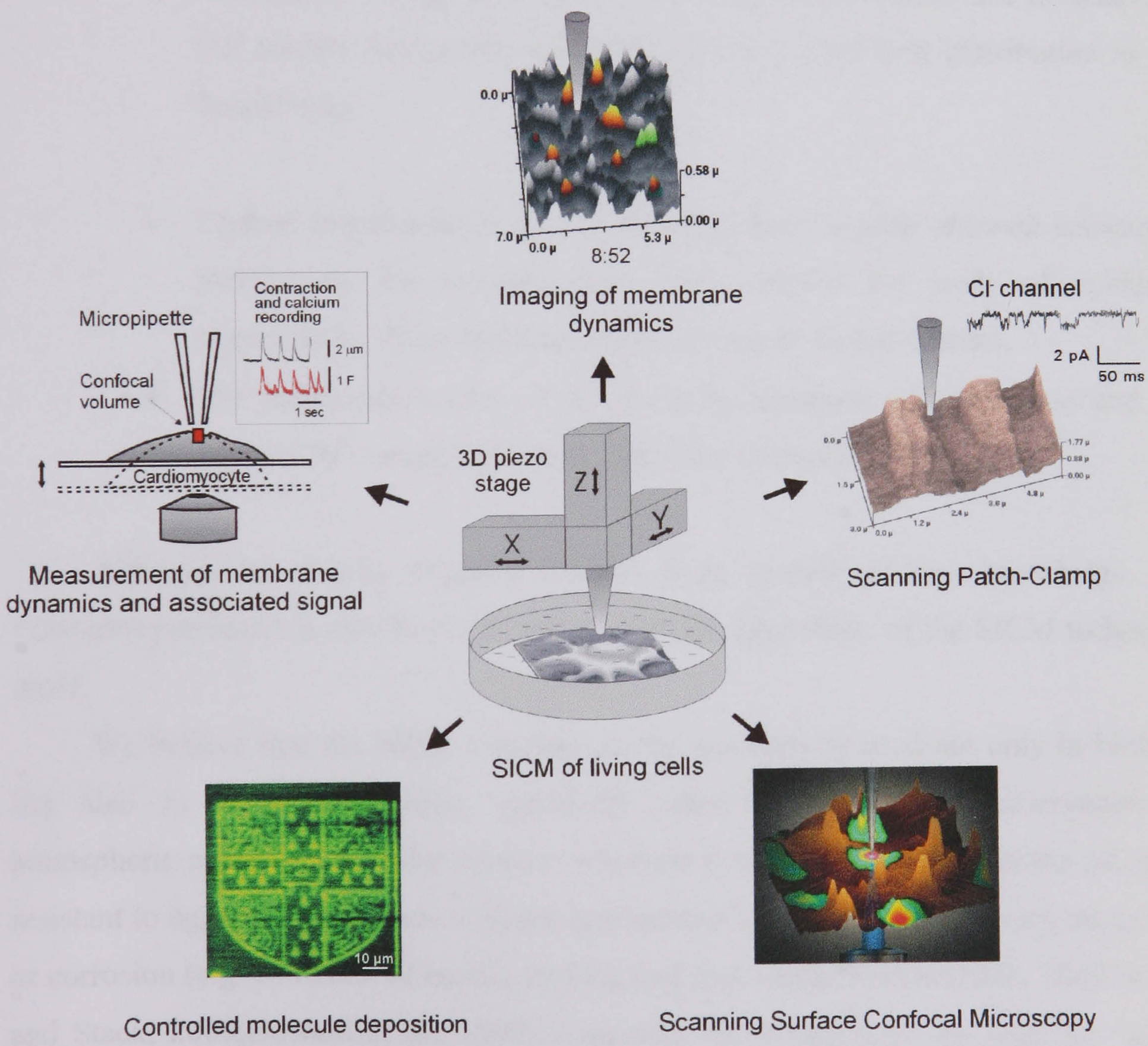

Fig. 13.1 SICM applications.

The scanning surface confocal microscopy and scanning patch-clamp were created by combining SICM with confocal microscopy and patch-clamp respectively.

The multifunctionality of SICM is briefly itemized:

- Scanning surface confocal microscopy was used to study abnormal cardiac myocyte contraction, and test potential anti-arrhythmic drugs.
- It was also used to image the interaction between fluorescently-labelled virus-like particles and the cell membrane, and follow the process of the viral internalisation.
- Scanning patch-clamp enabled recording of ion channels, for the first time ever, in small cells such as sperm, and subcellular structures such as epithelial microvilli and neural dendrites. In addition, it provided a means of mapping the ion channel distribution in the cell membrane in relation to cell surface topography and studying the role of their distribution in cell functioning.
- Further improvements of the SICM control system allowed substantial increase in the scanning rate. This enabled the study of epithelial microvilli by direct real-time measurement of their dynamics.
- The multifunctionality of the scanning technique was increased and the new SICM control facilitated controlled molecular deposition.

Although the results obtained in this study gained relevant knowledge, the examples presented in this thesis do not exploit all capabilities of the SICM technique itself.

We believe that the SICM imaging can be successfully used not only in biology but also in materials science, especially where high-resolution observation at atmospheric pressure and under aqueous solutions is needed. The fact that the SICM is resistant to aggressive mediums makes it applicable to real-time study of such processes as corrosion (e.g. corrosion of metal), etching and deposition (Lee and Shih, 2000;Wang and Stack, 2000;Howard et al., 1996). Currently, SEM and AFM are used for "post-mortem" imaging of the results of these processes, however in many cases samples reveal different properties depending on the environment and so in situ imaging would be much more powerful.

For example, with the purpose of study of polyethylene terephthalate foil etching we performed real-time imaging of this phenomenon. The etching was carried out in 3 molar KCl solution. The imaging revealed gradual conical pore appearance in the positions of the tracks left by heavy ions during irradiation (data not shown). Unfortunately, current resolution of SICM is not enough to visualize latent heavy ion tracks, but it is known that pores do not appear as a result of non-irradiated foil etching. Most importantly, SICM disclosed structures on the surface of PET foil undetectable by SEM and AFM (Milovanovic et al., 1997).

It has also been shown that SICM, in similar fashion to that used for controlled molecule deposition (see Chapter 12), can be used for electrochemical microprocess by metal deposition (Zhang et al., 1999). This method of nano-wire fabrication favourably compares with other methods such as nanolithography and electrodeposition (Lohau et al., 1998;Routkevitch et al., 1996). This spatial control over metal deposition means that SICM could be used for microcircuit printing.

Another potentially promising technique could be developed by combining SICM and scanning electrochemical microscopy (SECM) (Bard et al., 1989). Together with our robust SICM distance control, the SECM can provide localized measurements of specific chemicals at specified regions in close proximity to the live cell membrane or inanimate specimens.

On the basis of SICM, fully automated patch-clamp recording and microinjection systems can be developed. In these systems the same scanning micropipette can be used for electrophysiological recordings and microinjection of selected cells with genetic material or fluorescent probes. This will open up the possibility of reliably performing much more complex biological experiments on live cells.

It is important to note that all the applications of SICM would greatly benefit by the improvement of SICM topographical resolution and imaging speed.

Chapter 14 Suggestions for future work

14.1 Introduction

Future work will focus on following areas that are relevant to both SICM itself and SICM-combined techniques:

- improvement of the SICM topographic resolution
- increasing SICM scanning rate
- combination of the SICM with other techniques.

The improvement of the SICM topographic resolution at least five times should enable the visualization of many structures on the cell surface such as membrane domains, microvilli and caveolae, and open up the possibility of the direct observation of protein complexes in the cell membrane. Since this will be performed on live cells there will be no artefacts due to fixation, which plague in electron micrography of fixed cells. It should also enable us to follow changes in the cell surface at high resolution with time, before and after physiological stimuli.

Currently, a typical 80 μm x 80 μm scan takes up to 20 minutes. Improvement of the scan speed by at least an order of magnitude should enable observation of membrane and cytoskeleton dynamics and features on the cell surface that are washed out due to cell movement or diffusion.

This work would also have significant impact on all our other applications of SICM. It will enable us to increase the sensitivity in mapping the distribution of single ion channels, to perform higher resolution SNOM and patch clamp measurements. It would also enable us to perform nanowriting at higher resolution. In addition the instrument will have applications in the physical sciences for in situ imaging of solid-liquid interfaces and polymer surfaces.

On the basis of the high-resolution and fast SICM we will develop a fully automated scanning patch-clamp system. The automated scanning patch-clamp system should allow us to rapidly obtain a patch-clamp recording from any position on the cell membrane with high spatial resolution. Moreover, developing this methodology should

enable identification and patch clamping of small membrane structures such as fine neural dendrites, cellular microvilli, caveolae and transversal tubules of muscle cells. The technique will provide a direct and reliable way for patch clamping small cells or cells in tissue which is difficult to achieve with conventional methods.

14.2 Improvement of the SICM topographic resolution

The improvement of the topographic resolution of the SICM to better than 10 nm laterally and 2 nm vertically could be achieved by following measures:

- use of smaller diameter scanning pipettes
- topographical image deconvolution.

Since the small diameter pipette will be held much closer to the sample surface the SICM is much more sensitive to mechanical vibrations. Therefore, the use of the small diameter scanning pipettes will require better mechanical vibration isolation. Because of the smaller ion current that flows it will be necessary to build a better current amplifier with suitable filters to remove electrical noise. Also, the development of the high-resolution SICM will require a higher scanning rate because the sample drift becomes substantial in comparison with nm sized features.

14.2.1 Use of fine pipettes

It is possible to fabricate quartz pipettes down to 10 nm diameter (Brown and Flaming, 1986) that potentially could be used for SICM.

Although, the smaller micropipettes are very fragile it has been shown that the micropipettes with inner diameters down to 0.05 μm can be used for the SICM imaging (Hansma et al., 1989). Also, Hansma et. al. found that in practice they resolved features a few times smaller than the ID of the micropipette.

14.2.2 Deconvolution

In SICM the pipettes are pulled just before use by a pipette puller and the pipette characteristics are highly reproducible (Brown and Flaming, 1986). In addition the flow of ion current to the pipette is calculable. This enables the recorded image to be corrected for the size of the pipette to produce a higher resolution image. This principle is demonstrated in the proof-of-concept shown in Fig. 14.1:

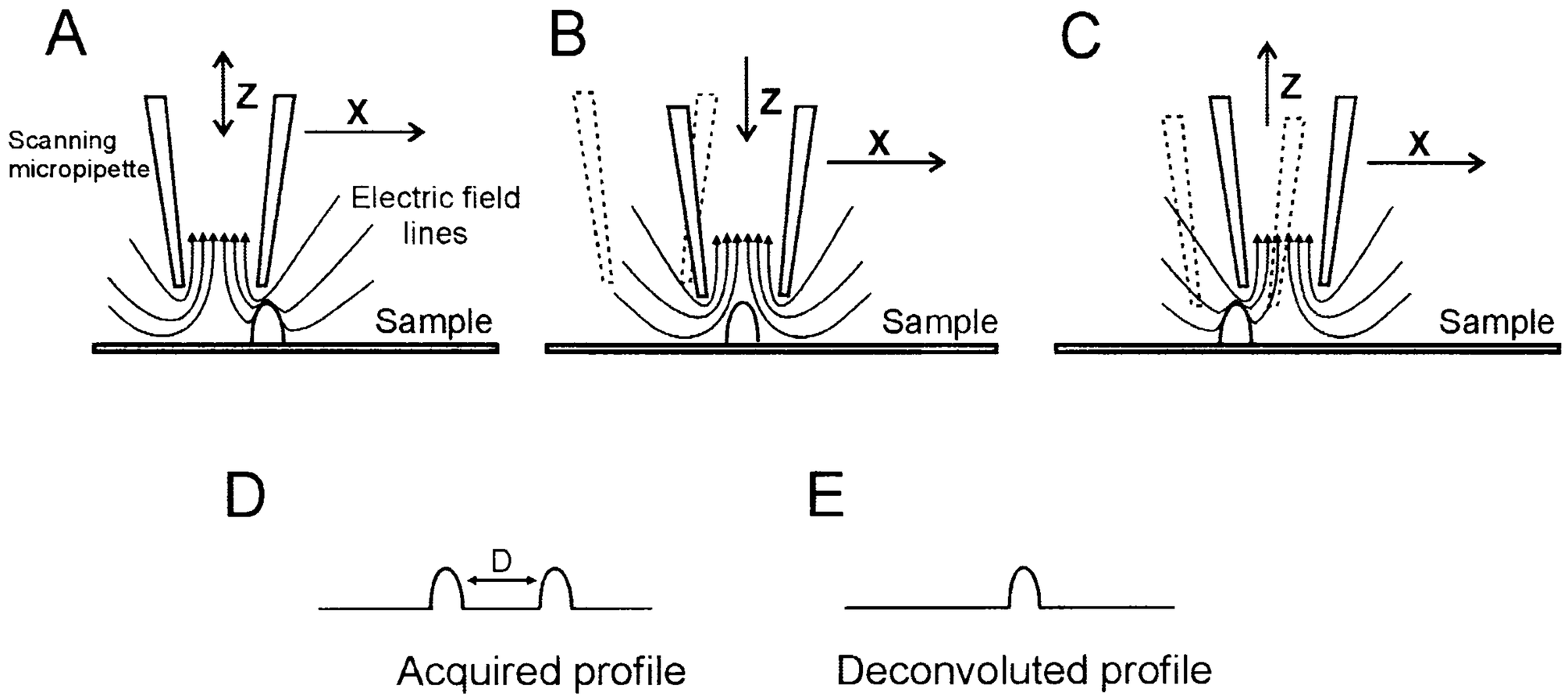

Fig. 14.1 Principle of deconvolution.

If the pipette scans over a small object, the object is very effective at blocking the ion current as the advancing wall of the pipette passes over it (Fig. 14.1, *A*). The ion current blockage results in the pipette rising, therefore a feature on the topographical profile that corresponds to the scanned object can be seen. However once the centre of the pipette is over the object there is little blocking of the ion current (Fig. 14.1, *B*). Thus a small object produces an apparent lowering in the topographic image. When the "second", trailing wall of the pipette reaches the object (Fig. 14.1, *C*) the ion current reduces again causing a second appearance of the feature on the profile (Fig. 14.1, *D*). Upon completion of the lateral scanning the profile features shown in Fig. 14.1 *D* appear as a ring on the topographic image. Similar rings were observed when imaging polyethylene terephthalate foil (shown earlier in Fig. 10.3 *C*).

These rings are effectively images of the scanning pipette tip. Each ring corresponds to a small object and the brightness of the ring depends on the object's size. If the image is deconvoluted to take account of the pipette size (Fig. 14.1, *D*) then the profile shown Fig. 14.1 *E* is obtained. The resolution is better than the pipette diameter

and is limited only by the thickness of the pipette wall. We intend to improve and develop this deconvolution method to process the images and hence obtain higher resolution images.

14.2.3 Compact design

The current instrument attaches the scanning head to the light post of the microscope and has micrometers to lower the pipette onto the sample and adjust its position in the x-y plane. This is subject to a vibration of about +/- 10 nm. To minimise vibration the SICM will be made more compact, similar to the design used for AFM. The scanning head will be also designed to be as small as possible with the current amplifier mounted directly on it to minimise vibrations. The head will either mount directly on a vibration isolation table or on the microscope stage. In addition an active vibration isolation table will be used to minimise coupling of external vibrations into the instrument.

14.2.4 Improved feedback

Since the dependence of the ion current with the distance from the sample is an analytical function it should be possible to use the difference in the ion current signal between the measured modulated signal and set-point to directly calculate the exact distance the pipette needs to move to maintain constant pipette-sample distance. At present this is only done using a linear function, so compromising the feedback. By using a programmable DSP board it should be possible to implement the optimum feedback and hence improve the topographic images.

14.3 Imaging speed

The imaging speed is currently limited by the rate of modulation (1000 Hz) of the pipette-sample distance. This is largely due to the size of the piezo used to mount the pipette since it has a low resonance frequency. The scanning head will be designed so

that a smaller piezo is used to mount the pipette so it can be modulated at much higher frequency, up to 5 kHz. This will improve our imaging rate by a factor of 25, and reduce the scan time to less than a minute for a complete image.

It is also possible to develop an algorithm that will allow us to scan rapidly over very convoluted cell surfaces with high resolution. Currently all SPM techniques are based on a raster scan where the probe is moved one step at a time, measuring the resulting differences in the interaction between the probe tip and the sample, and then readjusting its position. It takes a long time for the feedback to reach the set point if a large displacement in vertical direction is required (e.g. a steep cell wall or large cellular structure). It is proposed to firstly scan the cell surface at lower resolution and then use this topographical information to predict necessary feedback control for continuous imaging. This will allow us to move the probe rapidly along a very convoluted cellular surface. yet maintaining optimal feedback control.

Currently the raster scanning is performed so that only rectangular images can be acquired. It is not optimised for cellular imaging as cells can be of any shape but rectangular and scanning of empty regions could take extra time. The development of the software that will enable scanning of custom selected regions of the cell surface is required. The ability to obtain the image rapidly will allow both the following in real time of dynamic changes in membrane architecture, and also minimise experimental drift.

14.4 Automated Scanning Patch-Clamp

The automated scanning patch-clamp system will be built on the basis of the SICM similar to that described in chapter 7. The existing microscope control software will be modified to provide control over all automated scanning patch-clamp process.

In order to enable rapid scanning/patching pipette approach a coarse manual vertical manipulator will be replaced with computer-controlled DC motor with micrometer. The high-resolution and fast SICM described in the previous paragraph will be used for cell surface imaging.

The control software will be developed so that on completion of the scanning procedure, the computer will facilitate positioning of the micropipette at the place of interest according to the topographical or/and optical image acquired, and then run test

measurements to ensure accurate positioning. To minimize incorrect positioning problems associated with hysteresis, a piezo actuator with capacitive sensors will be used.

Once the pipette has been positioned over the place of interest, it will be lowered to make a cell membrane – pipette contact and an electronic valve will be opened to apply negative pressure to the pipette. The cell membrane – pipette contact will form the GΩ-seal. A patch clamp holder will be also re-designed to eliminate any pipette movement when suction is applied.

The final stage of the patch-clamping process is important since the cell or cell membrane can move, so implementation of software algorithm for accurate positioning and automated rapid formation of GΩ-seal is a necessity. As soon as GΩ-seal is formed the same patch-clamp amplifier will be used for patch-clamp recording.

In our on-going studies the automated scanning patch-clamp system will be used to probe:

- Ca^{2+} and K^{+} channels in sperm
- voltage dependant Ca^{2+} and K^{+}, and Ca^{2+} sensitive K^{+} channels in dendrites and dendritic synapses
- Na^{+}, K^{+} and Cl^{-} channels in the microvillus region of kidney epithelial cells.

Ion channels in these cell structures have not been previously directly studied due to the lack of suitable methods.

In summary, SICM has been demonstrated to be the premier scanning probe technique for live cell imaging. Further improvements in speed, resolution and automation will allow new details of cellular structure and function to be probed. This will make the method more universally available and applicable to a wide range of biological and biomedical problems.

Appendix

1. Development of SICM control system

Before developing each component of the SICM control in particular, the major control tasks have to be outlined. The SICM control should consist of:

- user control interface (general user control over the SICM)
- the SICM feedback control and scanning (maintaining all necessary calculations for constant probe-sample separation during the scanning and raster scanning procedure)
- data acquisition
- data processing, visualization and storage

The user control interface should provide a general control over the microscope such as starting and interrupting the scanning procedure, adjusting the scanning parameters, visualization, processing and saving of data. The control interface also has to be user-friendly.

The SICM feedback control should incorporate lock-in calculations, lock-in reference signal generation, feedback calculations and scanning signals generation.

The data acquisition should enable collection of such experimental data as topography, ion current and different signals from other selected channels such as fluorescence and reverse scan topography.

The data processing should include various fitting and filtering procedures that could be used for analysis of acquired data. Also the SICM control should provide possibilities for experimental and processed data preview and saving.

2. SICM control hardware

The performance of the microscope, its architectural flexibility, multifunctionality and simplicity of operation are greatly dependent on the control hardware. Therefore, choosing hardware for the SICM control is a very important process.

It has been shown in a previous paragraph that the SICM control system should serve many different functions simultaneously. Some of the control functions require analog signal acquisition and digitisation, when other functions need digital computations, data processing and storage, and user interface. In order to create the robust and stable SICM control system these tasks have to be divided into different groups and suitable hardware should be dedicated to each group independently. For instance, digital computations, data processing and the user interface can be better implemented on a personal computer, while data acquisition, pre-processing and scanning signal generation can be done on a digital signal processor board. Such a modular approach should allow proportional and hardware-orientated distribution of control tasks that is a key aspect of a reliable control system.

While the choice of a PC is straightforward, the selection of a DSP board is not as simple. Although, a wide variety of DSP boards and data acquisition systems is available on the market nowadays, there are only two major manufacturers of the digital signal processors. They are Texas Instruments Incorporation (Denver CO, USA) and National Instruments Corporation (Austin TX, USA). Both companies also provide complete solutions for data acquisition and processing. However, they are not always flexible enough to be used for the SICM control. In contrast, smaller manufacturers produce more flexible data acquisition and processing kits but which are still based on the powerful DSP processors from Texas and National Instruments.

The process of the DSP board choice in many cases is problematical (e.g. limited information provided by sales representatives coupled with difficulties to contact developers directly). Often, an evaluation period for the DSP board is required, because their real technical parameters do not match the provided description. In order to use the short evaluation time most efficiently, it is important to define the set of requirements with which the control system should comply.

The SICM control hardware should be capable providing:

- real-time digital feedback, including lock-in calculations
- lock-in reference signal generation
- real-time bi-directional data transfer between the PC and DSP
- in-the-fly feedback and scanning parameters adjustment.

Above all, the DSP board should have at least one input (via ADC) for amplified ion current measurement and five outputs for *X, Y, Z* and *modulation* signals and bias voltage generation (if used). In addition, all ADCs and DACs have to be DC coupled because DC signals are used to control piezo manipulators.

It is also important to take in to consideration the level of service and support provided by a company since it is often required on the early stages of development.

After considerable time and effort, excluding many DSP boards equipped with AD/DA converters with a long read/write delay (closed loop up to 1.5 ms) we finally settled on a M44 DSP board (Innovative Integration, USA). The M44 is a PCI bus-based board equipped with the TMS320C44 32-bit floating-point 60 MFLOPS digital signal processor (Texas Instruments Incorporation, Denver CO, USA) and dual OMNIBUS module I/O expansion sites. The M44 was equipped with an A4D4 instrumentation grade analog I/O module (optional, the number of modules can be extended to two in order to provide more input/output channels). The A4D4 is an analog I/O module capable of acquisition speeds up to 200 kHz based on four AD976A 16-bit ADCs, and four AD7846 16-bit DACs (Analog Devices Inc., Norwood MA, USA). The most important characteristic of the A4D4 analog I/O module for real-time feedback-control is settling time of the converters, which is 5 and 7 μs for ADC and DAC respectively. Having the DSP reading/writing time about 0.5 μs each we can expect approximately 13 μs delay that should allow "closed-loop sampling" at 76 kHz. Thus, according to Nyquist theorem the SICM feedback control on the basis of this hardware can be run at up to 38 kHz.

In order to provide communication between the DSP A/D converters and the high-voltage amplifier, a special interface module was designed. The interface module can be plugged in to the reserve slot of the high-voltage amplifier (System ENV 150/40, Piezosystem Jena, Germany) and splits the SICM control signals from 15-core cable into BNC connectors. The interface module also enables optional mixing the modulation and vertical positioning (*Z*) signals, and a voltmeter for input signal level monitoring.

3. SICM control software development

It has been shown in paragraphs 10.2 and 10.3 that in order to achieve reliable SICM control, two hardware platforms were dedicated to different control tasks. Therefore, the SICM control software also was separately developed for both platforms.

The control software consists of two parts. The first part is DSP executable kernel written in C++ and assembler language in C3x/C4x Code Composer Studio V. 4.10.36 (Texas Instruments Incorporated, Denver CO, USA). The kernel provides all the on-line calculations necessary to control the SICM: (i) lock-in calculations; (ii) reference signal generation; (iii) feedback and (vi) raster scanning. It also receives user-control signals from the main computer and passes them to the microscope, and transfers data acquired by the microscope to the PC so that the data may be subsequently processed, displayed and stored.

The host part provides user interface and control over the SICM and is written in Borland Delphi 5.0 (Inprise Corporation). This part also: handles data transfer between M44 and PC, displays, processes, as well as storing and opening the data acquired by the microscope.

Each part of the SICM control software is described in the following paragraphs.

3.1. Control software DSP kernel

The control software DSP kernel is downloaded into the DSP by the host application. When downloaded, it does the following initialisation procedures prior to operation:

- assigns default scanning parameters values
- initialises timers
- installs interrupts and assigns them to particular functions
- tunes DACs
- receives physical address of host buffer, number of dynamic memory access channel and data packet size
- receives scanning parameters

- initialises the PCI bus transfer
- generates the lock-in reference signal look-up table
- enables interrupts
- updates scanning parameters

The initialisation of the scanning parameters with the default values was done as a precautionary measure. These parameters are used in case the user starts scanning procedure without prior initialisation.

The initialisation of the timers sets the discretisation frequency (sampling rate).

There are two major interrupts in the program: the analog to digital conversion and scanning parameters update interrupt.

The analog to digital conversion interrupt is raised when a new set of data becomes available from the ADC. This interrupt triggers the procedure that calculates the lock-in and feedback signals, and initiates data transfer when the data is ready.

The scanning parameters update interrupt is raised if the user has changed any one of the scanning parameters in the host application program. This interrupt evokes a procedure that checks which parameter was updated, and assigns this value to real corresponding parameter in the DSP.

Tuning of DACs to one of the particular output gains (1,2,4 and 8) is necessary when working with different piezo actuators and/or at a different resolution. Setting the analog output gain to one of the mentioned values changes the output voltage range to ±10, ±5, ±2.5 or ±1.25V respectively. However, the digital to analog conversion procedure uses all available 12-bits regardless of the chosen output gain, so the precision of the positioning can be increased.

Host buffer physical address, dynamic memory access channel and data packet size are necessary for initialisation of the PCI bus transfer.

Scanning parameters such as scan size, number of points in line and lines in image, gain, set-point are necessary to perform the scanning, and there are obtainable from the host application program. All parameters will be described later in this chapter.

Initialisation of the PCI bus transfer sets bi-directional data transfer between PC and DSP using following parameters: the physical address of the host buffer, the dynamic memory access channel and the data packet size (all received from host application).

Generation of the lock-in reference signal look-up table will be described in following paragraph.

Enabling of the interrupts actually runs the program. Starting from this enabling the ADCs begin to digitise signals, and the moment the data is ready, the lock-in and feedback calculations occurs. Upon completion of the calculations the feedback correction signal is converted to an analog and one sent to the piezo actuator, and a position of the piezo actuator is written. When the number of acquired piezo actuator positions is equal to the number of points in a scan line these points are sent to the host program.

The lock-in, feedback, and data acquisition and transfer procedures are described in detail in following paragraphs.

During the operation, the control software DSP kernel updates the scanning parameters to enable a change of scan size, scan position, gain etc.

3.1.1. Lock-In calculations

The lock-in calculation procedure was programmed using principles similar to those described in paragraph 4.3.

It was shown that lock-in calculations require the reference signal to detect the frequency and the phase of the measured signal (equations 3.4 - 3.6). To remove a DC component of the input signal the signal is multiplied by the reference signal, which is a sine, and integrated for one period. However, it works only if the reference signal's positive and negative parts are symmetrical, otherwise the integral sum of values for the complete period does not equal to zero, and this causes an accumulation of error. This error affects the feedback signal resulting piezo actuator drift and false height measurements. Taking into account the high rate of the lock-in calculations a substantial error can accumulate very rapidly, even if the difference in positive and negative parts of the reference signal is negligible. Therefore, to generate the reference signal a look-up table of a sine wave is created by mirroring a half of period that allows an absolutely symmetrical table with zero period sum to be achieved.

When the DSP kernel is run it generates the reference signal at a specified frequency using the look-up table. Simultaneously, the program acquires the input

signal *Vin*, and the lock-in *X* and *Y* magnitudes can be calculated according to equations:

$$X = \sum_{i=1}^{period} x_i = \sum_{i=1}^{period} Vin_i \cdot Sin_{i+period/4} \tag{A.1}$$

$$Y = \sum_{i=1}^{period} y_i = \sum_{i=1}^{period} Vin_i \cdot Sin_i \tag{A.2}$$

where *period* is a number of points in the lock-in reference signal look-up table; Vin_i is a digitised value of the input signal (amplified ion current) in iteration *i*; Sin_i is a lock-in reference signal look-up table value that corresponds to iteration *i*. Cosine is calculated by shifting the sine look-up table by quarter of a period (*period/4*).

From the foregoing, *X* and *Y* values can be calculated only once a period. This makes lock-in, and therefore feedback, control rate low. In order to generate the lock-in solution in every single iteration, the *X* and *Y* magnitudes can be calculated as a continuously updated sum by adding new x_i and y_i components, and subtracting those calculated one period before ($x_{i\text{-}period}$ and $y_{i\text{-}period}$). For this purpose, in every iteration x_i and y_i values are saved in two additional arrays of the same dimension as a look-up table. Thus, *X* and *Y* magnitudes are calculated as:

$$X = X + x_i - x_{i-period} \tag{A.3}$$

where *X* magnitude is a constantly updated sum for a period; x_i is a value of sum component in iteration *i*; $x_{i\text{-}period}$ is a value of the same component of the sum for preceding period (iteration *i-period*). Similarly, *Y* magnitude is calculated.

In the next step of calculations the magnitude *R* is calculated as described in paragraph 4.3 (equation 4.6):

$$R = Gain_L \cdot \sqrt{X^2 + Y^2} \tag{A.4}$$

where $Gain_L$ is gain of lock-in. The magnitude *R* serves as an input signal for the feedback control calculated in the next step.

3.1.2. Feedback control

The feedback is calculated as described in paragraph 4.2 (equations 4.1 and 4.2). The error signal e_i in the current iteration i is derived as:

$$e_i = R - SP \tag{A.5}$$

where magnitude R is a solution of the lock-in calculations described in the previous paragraph and SP is a set point that is set up by the user in the host application program.

In the next step the integrated error signal E is calculated and saved for the next iteration:

$$E = E + e_i \tag{A.6}$$

and the feedback control output signal *Vout* calculated as:

$$Vout = \begin{cases} K_1 \cdot K_2 \cdot E; E \geq 0 \\ K_1 \cdot \dfrac{1}{K_2} \cdot E; E < 0 \end{cases} \tag{A.7}$$

where K_1 is the gain and K_2 is the proportional gain: both set up by the user in the host application program.

The same feedback control output signal *Vout* is a measured value of height (z direction) that can be taken into the final topographical image. To ensure a correct height measurement an additional parameter *CTRL O/S* was introduced. It defines the number of iterations the feedback loop is stabilised at each step before the actual measurement is taken into the topographical image.

3.1.3. Control signal generation, data acquisition and transfer

The control software DSP kernel handles the control signal generation and data acquisition at the sampling rate that is specified during the initialisation procedure described in paragraph 10.5.2. The generation of the signals includes their calculation (see previous paragraphs) and conversion into analog form by the A4D4 module.

The control signals are: *X*, *Y* and *Z* piezo actuator positioning signals and the *modulation* signal.

The vertical positioning (*Z*) and *modulation* signals are generated during each iteration of the feedback control loop. The lateral positioning signals (*X* and *Y*) represent the number of points in a line and a number of lines in an image and are generated only during the scanning procedure. The positioning signal *X* is generated after a new point has been taken into a line. The positioning signal *Y* is generated after a new line been taken into an image.

The number of points in a line and lines in an image, and modulation amplitude and frequency are all set in the host application program.

The control software DSP kernel acquires the amplified ion current by digitising the analog signal from the current amplifier. The value of the ion current is used in the feedback calculations as described in the two previous paragraphs. The scanning data is transmitted line by line from the DSP kernel via the PCI bus to the host application program where they are assembled into images. In parallel with the topographical data, the ion current measurement and signals from other additional ADC channels can be acquired, transmitted and assembled in images in similar fashion.

3.2. Control software host application

The control software host application provides general control over the SICM and handles the data processing and storage. The following procedures are performed by the host application:

- initialisation of the DSP board and uploading of the control software DSP kernel
- setting up the scanning parameters
- triggering, interruption and stopping the scanning procedure
- bi-directional data transfer

- data processing
- image(s) generation and storage

Initialisation of the DSP board and uploading of the control software DSP kernel executes automatically every time the host application is started.

Setting up the scanning parameters; triggering, interruption and stopping the scanning procedure is described in following paragraph.

Bi-directional data transfer, data processing, image(s) generation and storage are controlled by the host application automatically during the scanning procedure. Also, storage can be handled manually by user if necessary.

3.2.1. User interface

The host application allows the user to set up the following parameters that are necessary for the scanning procedure, and defines the way in which probe moves over the sample surface:

- scan size
- scan offset
- number of points in a line
- number of lines in an image
- number of control points
- topographical and/or current image generation
- number of additional channels to acquire
- single or repetitive scanning
- file name
- file sequence number
- piezo range

These parameters can only be adjusted while scanning is not in progress.

The size of the scan is determined by *X* and *Y* dimensions in microns (μμ.μμ) that allows scanning of any rectangular-shape area up to 99.99 × 99.99 μm^2.

The scan offset (*X* and *Y*) moves the probe/sample in *x* and *y* directions to define the start coordinate of the next scan in microns (μμ.μμ).

The range of the scan size and offset are dependent on each other so that sum of corresponding values (*Size X + X Offset*, and *Size Y + Y Offset*) cannot exceed the piezo scan range. If the user tries to enter a number that is larger than the piezo scan range an error message will be shown and the value will not be accepted.

The number of points in a line determines the number of points recorded in *x*-direction and can be set from 64 to 1024. The number of lines in an image is similar to the number of points but for *y*-direction.

The number of control points (*CTRL O/S*) is the number of oversamples on image point that are not taken into an image (see paragraph 10.5.2.2).

The user can decide what information to acquire during the scanning. It can be topography, ion current and two additional channels tuned to record fluorescence or other signals.

The SICM can be run in a single or repetitive mode of operation. In the single mode, the program stops after each scanned image and has data has to be saved manually. The repetitive scanning enables continuous imaging of the same region and automated processing and storage of images.

The file name prefix e.g. CELL and starting number [0..99] e.g. 7 should be set for image saving. Images will be automatically saved as:

CELL_7t.img – where "t" corresponds to topography,

The ion current image will carry the letter "c" and fluorescence image the letter "f" accordingly. Image number increments automatically.

The piezo range is presented by the *X, Y* and *Z* values that correspond to the piezo actuator scanning range and have to be set accordingly in order to ensure correct calculations.

In addition to the parameters described above, the user can set the scanning control parameters that can be adjusted on-the fly during the scanning procedure. The parameters are:

- gain
- proportional gain
- set point
- modulation amplitude
- modulation frequency

Gain is the numerical gain of the feedback loop (paragraph 10.5.2.2). Since the feedback algorithm contains an integrator element, changing the gain is inversely proportional to changing the time constant of the integrator. The appropriate value of this constant will depend on the gain of the current amplifier, gain of the piezoelectric amplifier, and the *z*-dimensions of the scanned sample.

Proportional gain and set point are described in paragraphs 4.2 and 10.5.2.2.

Modulation amplitude and *frequency* are described in paragraph 4.3.

3.2.2. Data processing, image generation and storage

During the scanning procedure the host application receives scanned data from the DSP kernel line by line and assembles it in a two dimensional image. The topographical height is presented in a grey scale pallet so, that higher region appears lighter in the image. In parallel, the host program draws a line profile in the separate window to help the user visualizing the scanned surface.

Certainly, 256 grey scale colours are not enough to represent 16-bit ADCs resolution used to measure the position of the piezo, so the data has to be rescaled accordingly. Otherwise, large deviations in height will cause saturation and appear as a white (256) or a black colour (0) in the image. In order to visualize the whole profile of the scanned surface, every line is scaled down to 256 points before it is shown. However, small features will disappear from the image after scaling because they too small to be represented if the gross deviations in height are large. This is always the case when scanning on the slope. To correct the slope, a line fit procedure can be used

that normalizes each line individually. Although this option gives the greatest contrast, it must be realised that the height scale is now artificial. Each line will have a different height calibration, making a single *z*-measurement meaningless.

The same procedures apply to the topographical line profile. The host program also calculates peak-to-peak value and displays it together with the topographical line profile. This value is calculated after the line fit procedure and allows us to estimate the size of a scanned object itself without taking in to account the slope.

Upon completion of the scanning the image may appear as lines with different intensities. This is mainly due to the hysteresis of the piezo actuators that cause different vertical positioning from line to line. In order to rectify the introduction of stripes a de-stripe procedure is implemented that moves each scanned line up or down so that its mean is nearer to zero. Each line may be moved a different amount, so the absolute *z* measurement is meaningless.

Although the scanned data are processed allowing better visualizing they are stored in unprocessed 16-bit format, so true values of height can be read. If necessary, the line fit and de-stripe procedures can be used later on again at the stage of data analysis.

4. Cell preparation

4.1. Rat cardiac myocytes

4.1.1. Neonatal rat cardiac myocytes

Ventricular myocytes were isolated from the hearts of 1-2 day-old rats (Iwaki et al., 1990). Cells were kept in a DMEM medium (Gibco) with 15% fetal calf serum (Gibco), 1% streptomycin, 1% penicillin (Gibco), 1% NEAA (Gibco). 100mkg/ml G418 geniticin (Gibco) was added for inhibiting of fibroblast growth. Cells were maintained at 37^0C, in an atmosphere of humidified air plus 5% CO_2. Cells were used 1 - 3 days after plating. Myocytes were cultured on 0.1 mm glass coverslips. Cells were kindly provided by Peter H. Sugden, National Heart and Lung institute, Division of Medicine, Imperial College London.

4.1.2. Adult rat cardiac myocytes

Cardiac myocytes from adult rats were isolated by digestion of intact perfused ventricle (Harding et al., 1988) and kindly provided by Prof. S. Harding. Male Sprague-Dawley rats were heparinised, killed by cervical dislocation and the heart was rapidly excised and placed in ice-cold Krebs-Henseleit (KH) solution of composition (mM): NaCl 119, KCl 4.7, $MgSO_4$ 0.94, KH_2PO_4 1.2, $NaHCO_3$ 25, glucose 11.5, $CaCl_2$ 1 and equilibrated to pH 7.4 with 95% O_2 / 5% CO_2. A Langendorff perfusion method was used and the heart stabilised for 5 min with KH solution. A further 5 min perfusion was carried out with a low calcium solution of composition (mM): NaCl 120, KCl 5.4, $MgSO_4$ 5, pyruvate 5, glucose 20, taurine 20, HEPES 10 and nitrilotriacetic acid (NTA) 5, with a pH of 6.95 and calcium added to give a final concentration of 12-14 mmol/L as measured with a calcium electrode. This solution was equilibrated with 100% O_2. A solution similar to the low calcium one but with no NTA, 200 µmol/L added Ca^{2+} and collagenase (1mg/ml) and hyaluronidase (0.6mg/ml) was perfused through the heart for 10 min. The two ventricles were then separated, keeping the interventricular septum with the left ventricle, and the right ventricle discarded. After chopping with scissors, the pieces were shaken at 35°C under 100% O_2 for 5 min with the same enzyme-containing solution, strained through gauze of mesh size 300 µm and incubated for a further 5 min with enzyme. The supernatant was centrifuged at 400*g* for 1 min at room temperature. Cells were washed and resuspended in the low calcium solution, with no NTA and Ca^{2+} at a concentration of 200 µmol/L (ES). Patch-clamp experiments were started after cells ceased to contract due to depolarization by high $[K^+]_{Bath}$

4.1.3. Loading of rat cardiac myocytes with fluorescent probes

The cardiomyocytes were loaded with the visible wavelength fluo-3 Ca^{2+} indicator by cell incubation with the esterified derivative of 5µM Fluo-3 AM (fluo-3 acetoxymethyl, Molecular probes) in a medium containing a mixture of part Leibovitz's L-15 (Gibco) and part HBSS buffer (Gibco) at room temperature for 15 min. Cells were re-washed five times with the medium, followed by a postincubation period of 20 min

to allow for complete intracellular dye cleavage (Lopez et al., 1995;Williams et al., 1992).

4.2. Sperm cells

Strogylocentrotus purpuratus or *Lytechinus pictus* sea urchins were obtained from Pacific Bio-Marine Laboratories (Long Beach, CA, USA). Spermatozoa were obtained by intracoelomic injection of 0.5 M KCl into sea urchins and collected with a Pasteur pipette directly from the gonopores (Lee and Garbers, 1986). The cell suspension was kept on ice in physiological bath solution composed of (mM) NaCl 486, KCl 10, $MgCl_2$ 25, $CaCl_2$ 10, HEPES 10, pH=8. Cells were pre-treated with 0.01mg/ml trypsin (Sigma) solution for 10 minutes in ice and plated on poly-L-lysine-treated dishes in a physiological bath solution (mentioned above). Pipette backfill solution contained (mM) $BaCl_2$ 300, HEPES 10, pH =8.0.

4.3. Rat superior cervical ganglion neurons

Superior cervical ganglion cells were cultured from 17 day old rats using previously described methods (Dunn, 1994). Briefly, ganglia were dissociated with collagenase followed by trypsin, and were cultured in L-15 medium supplemented with 10% fetal calf serum and 50 ng/ml neural growth factor. To investigate the calcium channels, the bath solution was composed of (mM) KCl 120, $MgCl_2$ 3, EGTA 5, glucose 11, HEPES 10, adjusted to pH 7.4 with KOH and the pipette solution contained $BaCl_2$ 90, HEPES 10, tetraethylammonium-Cl (TEA-Cl) 10, 4-aminopyridine (4-AP) 3, adjusted to pH 7.4 with tetraethylammonium-OH (TEA-OH) as described previously (Delmas et al., 2000). In several experiments we loaded cells by DiI as previously described (Hasbani et al., 2001).

4.4. Xenopus kidney epithelial cells

A single A6 cell line was kindly provided by Dr DeSmet. All experiments were carried out between 127-134 passages. Cells were cultured as described previously (Sariban-Sohraby et al., 1984) on high pore density membrane filters (Falcon, Bedford, MA). Cells were grown and kept in a 1:1 mixture of modified Ham's F-12 medium and Leibovitz's L-15 medium, modified to contain 105 mM NaCl and 25mM $NaHCO_3$. The mixture was supplemented with 10% fetal calf serum, 200µg/ml streptomycin, 200 units/ml penicillin. Cells were maintained at 28°C in an atmosphere of humidified air plus 1% CO_2. Cells were passaged and used between days 4 and 5 when they were 90-95% confluent. Single channel recordings were performed using a bath solution and pipette backfill solution both composed of (in mM) NaCl 140, KCl 5, $MgCl_2$ 0.8, $CaCl_2$ 1.2 and HEPES 10 (pH=7.4).

4.5. Rat aorta

Samples of aorta obtained form male Sprague-Dawley rats (200 to 300g) were kindly provided by Sussan Nourshargh (Imperial College, London). The aorta was mounted in a Petri dish and imaged in Leibovitz's L-15 medium.

4.6. Monkey COS 7 cells

Monkey COS 7 cells were routinely maintained at 37°C in 5% CO2, using DMEM (GIBCO_BRL) containing 5% (vol/vol) FCS (Helena Biosciences, Sunderland, Tyne and Wear, U.K.; ref. 17).

For experiments with fixed cells, COS 7 cells (5 x 10^4 cells per well) were plated on 13-mm glass coverslips in 24-well plates, incubated overnight at 37°C in DMEM containing 5% (vol/vol) FCS and then incubated for 30 min at 0°C with VLPs in 400 _l of DMEM containing 20 mM Hepes, pH 7.5, 0.5% BSA (0.25 µg of plasmid DNA per well). Cells then were washed with DMEM at 0°C, incubated at 37°C in DMEM containing 5% (vol/vol) FCS and harvested, 0 or 4 h posttransfection, by fixing for 15 min in PBS containing 3.7% (vol/vol) formaldehyde and 250 mM sucrose. Coverslips then were assembled for SSCM.

For live imaging, cells were plated and grown as above and then transferred to Leibowitz medium without phenol red (L15, GIBCO_BRL). Coverslips were mounted on a support Petri dish, and scanning was carried out at room temperature in L15. VLPs (0.25 μg of plasmid DNA) in 40 μl of L15 were added to the cells for 30 sec, the cells were washed twice in excess media, and scanning was resumed.

4.7. Organotypic cultures of the organ of Corti

The cultures were prepared by Corné J. Kros, Guy P. Richardson (School of Biological Sciences, University of Sussex) from cochleas of three-day-old mouse pups (Swiss CD-1, Charles River, UK) according to the procedure described previously (Russell and Richardson, 1987) with some modifications. Briefly, strips of the organ of Corti were carefully microdissected and placed in Leibowitz cell culture medium, L-15 (Gibco). Reissner's membrane and tectorial membrane were removed with fine forceps. Apical turn, middle turn, and apical half of the basal turn of the organ of Corti were separated, transferred to the DMEM/F12 medium supplemented with 7% fetal bovine serum (Gibco), and adhered to the bottom of the petri dish coated with CellTak (Collaborative BioMedical Products). Cultures were maintained at 37°C and 5% CO_2 for 1-5 days before use. Immediately before the experiment, the medium was changed to L-15.

5. Other preparations

5.1. Plasmid DNA

The plasmid DNA used in all SSCM experiments was pCIKLuxOE, based on pCIKLux (Gill et al., 2001), and contained the simian virus 40 origin of replication and enhancer region from nucleotides 5,176 to 268 (N. Krauzewicz, unpublished data).

5.2. Polyoma capsid-like particles

Capsid-like particles were purified by sucrose and CsCl gradient centrifugation from Hi5 insect cells infected with recombinant baculovirus, as described (Krauzewicz et al., 2000a), and resuspended in sterile 20 mM Hepes, pH 7.5 at 3–6 mg_ml. Capsid-like particles were covalently labeled with Cy3 by using the FluoroLink Cy3 monofunctional dye (Amersham Pharmacia). Cy3-labeled capsid-like particles were incubated with Qiagen-purified, supercoiled plasmid DNA at a molar ratio of 5:1 to produce VLPs, as described (Krauzewicz et al., 2000a).

5.3. Biotinylated and fluorophore-labeled DNA

The single stranded DNA sample was synthesized by Cruachem (Glasgow, UK) and was HPLC purified. The sequence of the DNA is 5'-CTATGCAGCCATTGTAGTCC-3'. The 3' end was modified by Rhodamine Green (Molecular Probes, Leiden, The Netherlands). For the writing experiment, the 5' end was modified with biotin. The concentration of the dye-labeled DNA was determined by UV-Vis absorption at 260 nm, and the absorption at 504 nm was used as an internal reference. The pipet was filled with 100 nM DNA in phosphate buffer solution (PBS, 10 mM phosphate, 137 mM NaCl).

5.4. Glass surfaces

Glass-bottomed dishes (WillCo, Wells B.V., The Netherlands) were coated with 1 mg/ml biotin-BSA overnight by adding of 200-400 µl of biotin to the dish. Then biotin-BSA solution was removed and dish cleaned with milliq water, and dried with N_2. When dried, 200-400 µl of 100 µg/ml streptavidin was added to the dish for 30-60 minutes. After removing excess streptavidin the dish was gently rinsed with milliq water again.

For high-quality experiments glass-bottomed dishes (WillCo, Wells B.V., The Netherlands) were coated with streptavidin by BioTeZ Berlin-Buch GmbH, Germany. The biotin binding capacity of these coatings was 280 fmol/mm^2 (68 pg/mm^2).

Reference list

1. Instruction manual, Model P-2000 Micropipette Puller. Sutter Instrument Company 7. 1993.
Ref Type: Serial (Book,Monograph)

2. DSP32C Digital Signal Processor with External memory interface. AT&T Microelectronics, Data Sheet . 6-1-1995.
Ref Type: Serial (Book,Monograph)

3. Abitorabi,M.A., R.K.Pachynski, R.E.Ferrando, M.Tidswell, and D.J.Erle. 1997. Presentation of integrins on leukocyte microvilli: a role for the extracellular domain in determining membrane localization. *J Cell Biol.* 139:563-571.

4. Abrami,L., R.Gobin, V.Berthonaud, H.L.Thanh, J.Chevalier, P.Ripoche, and J.M.Verbavatz. 1997. Localization of the FA-CHIP water channel in frog urinary bladder. *Eur. J. Cell Biol.* 73:215-221.

5. Ahmed,N., M.Ramjeesingh, S.Wong, A.Varga, E.Garami, and C.E.Bear. 2000. Chloride channel activity of ClC-2 is modified by the actin cytoskeleton. *Biochem. J.* 352 Pt 3:789-794.

6. Albrecht,T.R. and C.F.Quate. 1987. Atomic resolution imaging of a nonconductor by atomic force microscopy. *J. Appl. Phys.* 62:2599-2602.

7. Alkondon M,P.E.A.E. 1996. Mapping the location of functional nicotinic and gamma-aminobutyric acidA
receptors on hippocampal neurons. *J Pharmacol Exp Ther* 279:1491-1506.

8. Alonso,G. and H.Widmer. 1997. Clustering of KV4.2 potassium channels in postsynaptic membrane of rat supraoptic neurons: an ultrastructural study. *Neuroscience* 77:617-621.

9. Angelides,K.J. 1986. Fluorescently labelled Na+ channels are localized and immobilized to synapses of innervated muscle fibres. *Nature* 321:63-66.

10. Ash,E.A. and G.Nichols. 1972. *Nature* 237:510.

11. Bacq,Y., A.Myara, M.C.Brechot, C.Hamon, E.Studer, F.Trivin, and E.H.Metman. 1995. Serum conjugated bile acid profile during intrahepatic cholestasis of pregnancy. *J Hepatol* 22:66-70.

12. Banke,T.G., A.Schousboe, and D.S.Pickering. 1997. Comparison of the agonist binding site of homomeric, heteromeric, and chimeric GluR1(o) and GluR3(o) AMPA receptors. *J. Neurosci. Res.* 49:176-185.

13. Bard,A.J., F.F.Fan, J.Kwak, and O.Lev. 1989. Scanning Electrochemical Microscopy. Introduction and Principles. *Anal. Chem.* 61:132-138.

14. Barrigon,S., S.Y.Wang, X.Ji, and G.A.Langer. 1996. Characterization of the calcium overload in cultured neonatal rat cardiomyocytes under metabolic inhibition. *J Mol Cell Cardiol* 28:1329-1337.

15. Bartles,J.R., L.Zheng, A.Li, A.Wierda, and B.Chen. 1998. Small espin: a third actin-bundling protein and potential forked protein ortholog in brush border microvilli. *J Cell Biol.* 143:107-119.

16. Bartlett,J.S. and R.J.Samulski. 1998. Fluorescent viral vectors: a new technique for the pharmacological analysis of gene therapy. *Nat Med* 4:635-637.

17. Begg,D.A., L.I.Rebhun, and H.Hyatt. 1982. Structural organization of actin in the sea urchin egg cortex: microvillar elongation in the absence of actin filament bundle formation. *J Cell Biol* 93:24-32.

18. Bernard,A., B.Michel, and E.Delamarche. 2001. Micromosaic immunoassays. *Anal. Chem.* 73:8-12.

19. Binning,G. and C.F.Quate. 1986. Atomic Force Microscope. *Phys. Rev. Lett.* 56:930-933.

20. Binning,G. and H.Rohrer. 1987. Scanning tunneling microscopy—from birth to adolescence. *Rev. Mod. Phys.* 59:615-625.

21. Binning,G., H.Rohrer, Ch.Gerber, and E.Weibel. 1982. Surface Studies by Scanning Tunneling Microscopy. *Phys. Rev. Lett.* 49:57-61.

22. Binning,G., H.Rohrer, Ch.Gerber, and E.Weibel. 1983. 7 x 7 Reconstruction on Si(111) Resolved in Real Space. *Phys. Rev. Lett.* 50:120-123.

23. Bkaily,G., D.Jacques, and P.Pothier. 1999. Use of confocal microscopy to investigate cell structure and function. *Methods Enzymol.* 307:119-135.

24. Bond,A.M., K.B.Oldham, and C.G.Zoski. 1988. Theory of electrochemical processes at an inlaid disc microelectrode under steady-state conditions. *J. Electroanal. Chem.* 245:74-104.

25. Braet,F., C.Seynaeve, R.De Zanger, and E.Wisse. 1998. Imaging surface and submembranous structures with the atomic force microscope: a study on living cancer cells, fibroblasts and macrophages. *J. Microsc.* 190 (Pt 3):328-338.

26. Britton,F.C., W.J.Hatton, C.F.Rossow, D.Duan, J.R.Hume, and B.Horowitz. 2000. Molecular distribution of volume-regulated chloride channels (ClC-2 and ClC-3) in cardiac tissues. *Am. J. Physiol Heart Circ. Physiol* 279:H2225-H2233.

27. Brown, K. T. and Flaming, D. G. Advanced Micropipette Techniques for Cell Physiology. 1986. Wiley, New York.
Ref Type: Catalog

28. Bruckbauer,A., L.Ying, A.M.Rothery, D.Zhou, A.I.Shevchuk, C.Abell, Y.E.Korchev, and D.Klenerman. 2002. Writing with DNA and protein using a nanopipet for controlled delivery. *J. Am. Chem. Soc.* 124:8810-8811.

29. Brunet,J.P., N.Jourdan, J.Cotte-Laffitte, C.Linxe, M.Geniteau-Legendre, A.Servin, and A.M.Quero. 2000. Rotavirus infection induces cytoskeleton disorganization in human intestinal epithelial cells: implication of an increase in intracellular calcium concentration. *J Virol.* 74:10801-10806.

30. Candia,O., A.J.Mia, and T.Yorio. 1993. Influence of filter supports on transport characteristics of cultured A6 kidney cells. *Am J Physiol* 265:C1479-C1488.

31. Carl,S.L., K.Felix, A.H.Caswell, N.R.Brandt, W.J.Ball, Jr., P.L.Vaghy, G.Meissner, and D.G.Ferguson. 1995. Immunolocalization of sarcolemmal dihydropyridine receptor and sarcoplasmic reticular triadin and ryanodine receptor in rabbit ventricle and atrium. *J Cell Biol* 129:672-682.

32. Carrion-Vazquez,M., A.F.Oberhauser, S.B.Fowler, P.E.Marszalek, S.E.Broedel, J.Clarke, and J.M.Fernandez. 1999. Mechanical and chemical unfolding of a single protein: a comparison. *Proc Natl Acad Sci U S A* 96:3694-3699.

33. Chambers,C. and R.D.Grey. 1979. Development of the structural components of the brush border in absorptive cells of the chick intestine. *Cell Tissue Res* 204:387-405.

34. Charras,G.T. and M.A.Horton. 2002. Single cell mechanotransduction and its modulation analyzed by atomic force microscope indentation. *Biophys. J* 82:2970-2981.

35. Charras,G.T., P.P.Lehenkari, and M.A.Horton. 2001. Atomic force microscopy can be used to mechanically stimulate osteoblasts and evaluate cellular strain distributions. *Ultramicroscopy* 86:85-95.

36. Chen,C.S., M.Mrksich, S.Huang, G.M.Whitesides, and D.E.Ingber. 1997. Geometric control of cell life and death. *Science* 276:1425-1428.

37. Cheng,H., M.B.Cannell, and W.J.Lederer. 1994. Propagation of excitation-contraction coupling into ventricular myocytes. *Pflugers Arch.* 428:415-417.

38. Chimini,G. and P.Chavrier. 2000. Function of Rho family proteins in actin dynamics during phagocytosis and engulfment. *Nat. Cell Biol* 2:E191-E196.

39. Clark,P., P.Connolly, A.S.Curtis, J.A.Dow, and C.D.Wilkinson. 1990. Topographical control of cell behaviour: II. Multiple grooved substrata. *Development* 108:635-644.

40. Cohen,M.W., O.T.Jones, and K.J.Angelides. 1991. Distribution of Ca2+ channels on frog motor nerve terminals revealed by fluorescent omega-conotoxin. *J. Neurosci.* 11:1032-1039.

41. Cross,K.M., L.M.Dahm, and C.W.Bowers. 2000. Simultaneous measures of contraction and intracellular calcium in single, cultured smooth muscle cells. *In Vitro Cell Dev Biol Anim* 36:50-57.

42. Curtis,M.J. and P.D.Ridley. 1994. Anions, membrane resistance and ventricular fibrillation. *J. Basic Clin. Physiol Pharmacol.* 5:19-26.

43. Danilatos,G.D. 1993. Introduction to the ESEM instrument. *Microsc. Res. Tech.* 25:354-361.

44. de Lange,F., A.Cambi, R.Huijbens, B.de Bakker, W.Rensen, M.Garcia-Parajo, N.van Hulst, and C.G.Figdor. 2001. Cell biology beyond the diffraction limit: near-field scanning optical microscopy. *J Cell Sci* 114:4153-4160.

45. Delamarche,E., A.Bernard, H.Schmid, B.Michel, and H.Biebuyck. 1997. Patterned delivery of immunoglobulins to surfaces using microfluidic networks. *Science* 276:779-781.

46. Delmas,P., F.C.Abogadie, N.J.Buckley, and D.A.Brown. 2000. Calcium channel gating and modulation by transmitters depend on cellular compartmentalization. *Nat Neurosci.* 3:670-678.

47. DeRosier,D.J. and L.G.Tilney. 2000. F-actin bundles are derivatives of microvilli: What does this tell us about how bundles might form? *J Cell Biol* 148:1-6.

48. DiStefano, J. J., Stubberud, A. R., and Williams, I. J. Theory and problems of feedback and control systems. Schaum's outline series, McGreaw-Hill Inc. 2. 1990.
Ref Type: Serial (Book,Monograph)

49. Dixon,P.H., N.Weerasekera, K.J.Linton, O.Donaldson, J.Chambers, E.Egginton, J.Weaver, C.Nelson-Piercy, M.de Swiet, G.Warnes, E.Elias, C.F.Higgins, D.G.Johnston, M.I.McCarthy, and C.Williamson. 2000. Heterozygous MDR3 missense mutation associated with intrahepatic cholestasis of pregnancy: evidence for a defect in protein trafficking. *Hum Mol Genet* 9:1209-1217.

50. Dontha,N., W.B.Nowall, and W.G.Kuhr. 1997. Generation of biotin/avidin/enzyme nanostructures with maskless photolithography. *Anal. Chem.* 69:2619-2625.

51. Duan,D., J.R.Hume, and S.Nattel. 1997. Evidence that outwardly rectifying Cl- channels underlie volume- regulated Cl- currents in heart. *Circ. Res.* 80:103-113.

52. Duan,D., L.Ye, F.Britton, B.Horowitz, and J.R.Hume. 2000. A novel anionic inward rectifier in native cardiac myocytes. *Circ. Res.* 86:E63-E71.

53. Dunn,P.M. 1994. Dequalinium, a selective blocker of the slow afterhyperpolarization in rat sympathetic neurones in culture. *Eur. J. Pharmacol.* 252:189-194.

54. Ezzell,R.M., M.M.Chafel, and P.T.Matsudaira. 1989. Differential localization of villin and fimbrin during development of the mouse visceral endoderm and intestinal epithelium. *Development* 106:407-419.

55. Fabiato,A. 1985. Spontaneous versus triggered contractions of "calcium-tolerant" cardiac cells from the adult rat ventricle. *Basic Res. Cardiol.* 80 Suppl 2:83-87.

56. Fisk,N.M. and G.N.Storey. 1988. Fetal outcome in obstetric cholestasis. *Br J Obstet Gynaecol* 95:1137-1143.

57. Foti,M., M.A.Phelouzat, A.Holm, B.J.Rasmusson, and J.L.Carpentier. 2002. p56Lck anchors CD4 to distinct microdomains on microvilli. *Proc. Natl. Acad. Sci. U. S. A* 99:2008-2013.

58. Frosch,M.P. and M.A.Dichter. 1992. Non-uniform distribution of GABA activated chloride channels in cultured cortical neurons. *Neurosci. Lett.* 138:59-62.

59. Furness,D.N., G.P.Richardson, and I.J.Russell. 1989. Stereociliary bundle morphology in organotypic cultures of the mouse cochlea. *Hear. Res* 38:95-109.

60. Gathercole,D.V., D.J.Colling, J.N.Skepper, Y.Takagishi, A.J.Levi, and N.J.Severs. 2000. Immunogold-labeled L-type calcium channels are clustered in the surface plasma membrane overlying junctional sarcoplasmic reticulum in guinea- pig myocytes-implications for excitation-contraction coupling in cardiac muscle. *J. Mol. Cell Cardiol.* 32:1981-1994.

61. Gill,D.R., S.E.Smyth, C.A.Goddard, I.A.Pringle, C.F.Higgins, W.H.Colledge, and S.C.Hyde. 2001. Increased persistence of lung gene expression using plasmids containing the ubiquitin C or elongation factor 1alpha promoter. *Gene Ther* 8:1539-1546.

62. Godbey,W.T., K.K.Wu, and A.G.Mikos. 1999. Tracking the intracellular path of poly(ethylenimine)/DNA complexes for gene delivery. *Proc. Natl. Acad. Sci. U. S. A* 96:5177-5181.

63. Golan,R., L.I.Pietrasanta, W.Hsieh, and H.G.Hansma. 1999. DNA toroids: stages in condensation. *Biochemistry* 38:14069-14076.

64. Golenhofen,N., R.B.Doctor, R.Bacallao, and L.J.Mandel. 1995. Actin and villin compartmentation during ATP depletion and recovery in renal cultured cells. *Kidney Int.* 48:1837-1845.

65. Gorelik,J., Y.Gu, H.A.Spohr, A.I.Shevchuk, M.J.Lab, S.E.Harding, C.R.Edwards, M.Whitaker, G.W.Moss, D.C.Benton, D.Sanchez, A.Darszon, I.Vodyanoy, D.Klenerman, and Y.E.Korchev. 2002a. Ion channels in small cells and subcellular structures can be studied with a smart patch-clamp system. *Biophys. J.* 83:3296-3303.

66. Gorelik,J., S.E.Harding, A.I.Shevchuk, D.Koralage, M.Lab, M.de Swiet, Y.Korchev, and C.Williamson. 2002b. Taurocholate induces changes in rat cardiomyocyte contraction and calcium dynamics. *Clin. Sci. (Lond)* 103:191-200.

67. Gorelik,J., A.Shevchuk, M.Ramalho, M.Elliott, C.Lei, C.F.Higgins, M.J.Lab, D.Klenerman, N.Krauzewicz, and Y.Korchev. 2002c. Scanning surface confocal microscopy for simultaneous topographical and fluorescence imaging: application to single virus-like particle entry into a cell. *Proc. Natl. Acad. Sci. U. S. A* 99:16018-16023.

68. Gorelik,J., A.I.Shevchuk, G.I.Frolenkov, I.A.Diakonov, M.J.Lab, C.J.Kros, G.P.Richardson, I.Vodyanoy, C.R.Edwards, D.Klenerman, and Y.E.Korchev. 2003. Dynamic assembly of surface structures in living cells. *Proc. Natl. Acad. Sci. U. S. A.*

69. Grabner,M., R.T.Dirksen, and K.G.Beam. 1998. Tagging with green fluorescent protein reveals a distinct subcellular distribution of L-type and non-L-type Ca2+ channels expressed in dysgenic myotubes. *Proc. Natl. Acad. Sci. U. S. A* 95:1903-1908.

70. Greber,U.F., M.Willetts, P.Webster, and A.Helenius. 1993. Stepwise dismantling of adenovirus 2 during entry into cells. *Cell* 75:477-486.

71. Griffith,G.R. and R.A.Consigli. 1984. Isolation and characterization of monopinocytotic vesicles containing polyomavirus from the cytoplasm of infected mouse kidney cells. *J Virol.* 50:77-85.

72. Gromeier,M. and K.Wetz. 1990. Kinetics of poliovirus uncoating in HeLa cells in a nonacidic environment. *J Virol.* 64:3590-3597.

73. Gu,Y., J.Gorelik, H.A.Spohr, A.Shevchuk, M.J.Lab, S.E.Harding, I.Vodyanoy, D.Klenerman, and Y.E.Korchev. 2002. High-resolution scanning patch-clamp: new insights into cell function. *FASEB J* 16:748-750.

74. Guerrero,A., J.A.Sanchez, and A.Darszon. 1987. Single-channel activity in sea urchin sperm revealed by the patch-clamp technique. *FEBS Lett.* 220:295-298.

75. Guild,G.M., P.S.Connelly, K.A.Vranich, M.K.Shaw, and L.G.Tilney. 2002. Actin filament turnover removes bundles from Drosophila bristle cells. *J Cell Sci.* 115:641-653.

76. Hamill,O.P., A.Marty, E.Neher, B.Sakmann, and F.J.Sigworth. 1981. Improved patch-clamp techniques for high-resolution current recording from cells and cell-free membrane patches. *Pflugers Arch.* 391:85-100.

77. Hansma,H.G. and J.H.Hoh. 1994. Biomolecular imaging with the atomic force microscope. *Annu. Rev. Biophys Biomol. Struct* 23:115-139.

78. Hansma,P.K., B.Drake, O.Marti, S.A.Gould, and C.B.Prater. 1989. The scanning ion-conductance microscope. *Science* 243:641-643.

79. Harding,S.E., G.Vescovo, M.Kirby, S.M.Jones, J.Gurden, and P.A.Poole-Wilson. 1988. Contractile responses of isolated adult rat and rabbit cardiac myocytes to isoproterenol and calcium. *J Mol Cell Cardiol* 20:635-647.

80. Hasbani,M.J., M.L.Schlief, D.A.Fisher, and M.P.Goldberg. 2001. Dendritic spines lost during glutamate receptor activation reemerge at original sites of synaptic contact. *J Neurosci.* 21:2393-2403.

81. Haussler,U., M.Rivet-Bastide, C.Fahlke, D.Muller, E.Zachar, and R.Rudel. 1994. Role of the cytoskeleton in the regulation of Cl- channels in human embryonic skeletal muscle cells. *Pflugers Arch.* 428:323-330.

82. Heikkinen,J., O.Maentausta, R.Tuimala, P.Ylostalo, and O.Janne. 1980. Amniotic fluid bile acids in normal and pathologic pregnancy. *Obstet Gynecol* 56:60-64.

83. Hirokawa,N., R.Sato-Yoshitake, N.Kobayashi, K.K.Pfister, G.S.Bloom, and S.T.Brady. 1991. Kinesin associates with anterogradely transported membranous organelles in vivo. *J Cell Biol* 114:295-302.

84. Hirokawa,N., L.G.Tilney, K.Fujiwara, and J.E.Heuser. 1982. Organization of actin, myosin, and intermediate filaments in the brush border of intestinal epithelial cells. *J Cell Biol* 94:425-443.

85. Howard,A.J., R.R.Rye, and J.E.Houston. 1996. Nanomechanical basis for imaging soft materials with tapping mode atomic force microscopy. *Journal of Applied Physics* 79:1885-1890.

86. Iwaki,K., V.P.Sukhatme, H.E.Shubeita, and K.R.Chien. 1990. Alpha- and beta-adrenergic stimulation induces distinct patterns of immediate early gene expression in neonatal rat myocardial cells. fos/jun expression is associated with sarcomere assembly; Egr-1 induction is primarily an alpha 1-mediated response. *J Biol Chem* 265:13809-13817.

87. Jentsch,T.J., T.Friedrich, A.Schriever, and H.Yamada. 1999. The CLC chloride channel family. *Pflugers Arch.* 437:783-795.

88. Joe,E.H. and K.Angelides. 1992. Clustering of voltage-dependent sodium channels on axons depends on Schwann cell contact. *Nature* 356:333-335.

89. Johnston,D., J.C.Magee, C.M.Colbert, and B.R.Cristie. 1996. Active properties of neuronal dendrites. *Annu Rev Neurosci.* 19:165-186.

90. Karpen,J.W., D.A.Loney, and D.A.Baylor. 1992. Cyclic GMP-activated channels of salamander retinal rods: spatial distribution and variation of responsiveness. *J. Physiol (Lond)* 448:257-274.

91. Kemendy,A.E., T.R.Kleyman, and D.C.Eaton. 1992. Aldosterone alters the open probability of amiloride-blockable sodium channels in A6 epithelia. *Am J Physiol* 263:C825-C837.

92. Kinnamon,S.C., V.E.Dionne, and K.G.Beam. 1988. Apical localization of K+ channels in taste cells provides the basis for sour taste transduction. *Proc. Natl. Acad. Sci. U. S. A* 85:7023-7027.

93. Korchev,Y.E., C.L.Bashford, M.Milovanovic, I.Vodyanoy, and M.J.Lab. 1997a. Scanning ion conductance microscopy of living cells. *Biophys J* 73:653-658.

94. Korchev,Y.E., J.Gorelik, M.J.Lab, E.V.Sviderskaya, C.L.Johnston, C.R.Coombes, I.Vodyanoy, and C.R.Edwards. 2000a. Cell volume measurement using scanning ion conductance microscopy. *Biophys J* 78:451-457.

95. Korchev,Y.E., M.Milovanovic, C.L.Bashford, D.C.Bennett, E.V.Sviderskaya, I.Vodyanoy, and M.J.Lab. 1997b. Specialized scanning ion-conductance microscope for imaging of living cells. *J Microsc* 188 (Pt 1):17-23.

96. Korchev,Y.E., Y.A.Negulyaev, C.R.Edwards, I.Vodyanoy, and M.J.Lab. 2000b. Functional localization of single active ion channels on the surface of a living cell. *Nat. Cell Biol* 2:616-619.

97. Korchev,Y.E., M.Raval, M.J.Lab, J.Gorelik, C.R.Edwards, T.Rayment, and D.Klenerman. 2000c. Hybrid scanning ion conductance and scanning near-field optical microscopy for the study of living cells. *Biophys J* 78:2675-2679.

98. Kotake,H., T.Itoh, M.Watanabe, I.Hisatome, J.Hasegawa, and H.Mashiba. 1989. Effect of bile acid on electrophysiological properties of rabbit sino- atrial node in vitro. *Br. J. Pharmacol.* 98:357-360.

99. Krauzewicz,N., C.Cox, E.Soeda, B.Clark, S.Rayner, and B.E.Griffin. 2000a. Sustained ex vivo and in vivo transfer of a reporter gene using polyoma virus pseudocapsids. *Gene Ther* 7:1094-1102.

100. Krauzewicz,N., J.Stokrova, C.Jenkins, M.Elliott, C.F.Higgins, and B.E.Griffin. 2000b. Virus-like gene transfer into cells mediated by polyoma virus pseudocapsids. *Gene Ther* 7:2122-2131.

101. Laatikainen,T. and E.Ikonen. 1977. Serum bile acids in cholestasis of pregnancy. *Obstet Gynecol* 50:313-318.

102. Laatikainen,T. and A.Tulenheimo. 1984. Maternal serum bile acid levels and fetal distress in cholestasis of pregnancy. *Int J Gynaecol Obstet* 22:91-94.

103. Laatikainen,T.J. 1975. Fetal bile acid levels in pregnancies complicated by maternal intrahepatic cholestasis. *Am J Obstet Gynecol* 122:852-856.

104. Lange,K. 2000. Microvillar ion channels: cytoskeletal modulation of ion fluxes. *J Theor Biol* 206:561-584.

105. Lange,K., U.Brandt, K.Keller, and B.Zimmermann. 1989. Endogenous regulation of 2-deoxyglucose uptake in C6 glioma cells correlates with cytoskeleton-mediated changes of surface morphology. *J Cell Physiol* 140:29-43.

106. Le Grimellec,C., E.Lesniewska, M.C.Giocondi, E.Finot, V.Vie, and J.P.Goudonnet. 1998. Imaging of the surface of living cells by low-force contact-mode atomic force microscopy. *Biophys. J.* 75:695-703.

107. Lee,C.K. and H.C.Shih. 2000. The abrasive corrosion behavior of plasma-nitrided alloy steels in chloride environments. *Journal of Materials Science* 35:2361-2369.

108. Lee,H.C. and D.L.Garbers. 1986. Modulation of the voltage-sensitive Na+/H+ exchange in sea urchin spermatozoa through membrane potential changes induced by the egg peptide speract. *J Biol Chem* 261:16026-16032.

109. Lee,K.B., S.J.Park, C.A.Mirkin, J.C.Smith, and M.Mrksich. 2002. Protein nanoarrays generated by dip-pen nanolithography. *Science* 295:1702-1705.

110. Lehenkari,P.P., G.T.Charras, A.Nykanen, and M.A.Horton. 2000. Adapting atomic force microscopy for cell biology. *Ultramicroscopy* 82:289-295.

111. Lesniewska,E., M.C.Giocondi, V.Vie, E.Finot, J.P.Goudonnet, and C.Le Grimellec. 1998. Atomic force microscopy of renal cells: limits and prospects. *Kidney Int. Suppl* 65:S42-S48.

112. Lievano,A., E.C.Vega-SaenzdeMiera, and A.Darszon. 1990. Ca2+ channels from the sea urchin sperm plasma membrane. *J Gen Physiol* 95:273-296.

113. Lohau,J., S.Friedrichowski, G.Dumpich, and E.F.Wassermann. 1998. Electron-beam lithography with metal colloids: Direct writing of metallic nanostructures. *J. Vac. Sci. Technol. B* 16:77-79.

114. Lopez,J.R., A.Jovanovic, and A.Terzic. 1995. Spontaneous calcium waves without contraction in cardiac myocytes. *Biochem Biophys Res Commun* 214:781-787.

115. Maduke,M., C.Miller, and J.A.Mindell. 2000. A decade of CLC chloride channels: structure, mechanism, and many unsettled questions. *Annu. Rev. Biophys. Biomol. Struct.* 29:411-438.

116. Magee,J., D.Hoffman, C.Colbert, and D.Johnston. 1998. Electrical and calcium signaling in dendrites of hippocampal pyramidal neurons. *Annu. Rev. Physiol* 60:327-346.

117. Mann,S.A., G.Hoffmann, A.Hengstenberg, W.Schuhmann, and I.D.Dietzel. 2002. Pulse-mode scanning ion conductance microscopy--a method to investigate cultured hippocampal cells. *J Neurosci. Methods* 116:113-117.

118. Marti,O., B.Drake, and P.K.Hansma. 1987. Atomic force microscopy of liquid-covered surfaces: Atomic resolution images. *Appl. Phys. Lett.* 51:484-486.

119. Meyer,G. and N.M.Amer. 1988. Novel optical approach to atomic force microscopy. *Appl. Phys. Lett.* 53:1045-1047.

120. Milovanovic,M., Y.Korchev, M.Lab, and C.L.Bashford. 1997. Scanning Probe Microscopy of soft samples: comparison of AFM with SICM. *Biophys J* 72:212.

121. Morgan,H., D.J.Pritchard, and J.M.Cooper. 1995. Photo-patterning of sensor surfaces with biomolecular structures: characterisation using AFM and fluorescence microscopy. *Biosens. Bioelectron.* 10:841-846.

122. Mosbacher,J., W.Haberle, and J.K.H.Horber. 1996. Studying membranes with scanning force microscopy and patchclamp technique. *J. Vac. Sci. Technol. B* 14:1449-1452.

123. Munoz-Garay,C., J.L.Vega-Beltran, R.Delgado, P.Labarca, R.Felix, and A.Darszon. 2001. Inwardly rectifying K(+) channels in spermatogenic cells: functional expression and implication in sperm capacitation. *Dev Biol* 234:261-274.

124. Neher,E. and B.Sakmann. 1976. Single-channel currents recorded from membrane of denervated frog muscle fibres. *Nature* 260:799-802.

125. Neher,E., B.Sakmann, and J.H.Steinbach. 1978. The extracellular patch clamp: a method for resolving currents through individual open channels in biological membranes. *Pflugers Arch.* 375:219-228.

126. Nilius,B., J.Sehrer, P.De Smet, W.Van Driessche, and G.Droogmans. 1995. Volume regulation in a toad epithelial cell line: role of coactivation of K+ and Cl- channels. *J Physiol* 487 (Pt 2):367-378.

127. O'Rourke,B., D.K.Reibel, and A.P.Thomas. 1990. High-speed digital imaging of cytosolic Ca2+ and contraction in single cardiomyocytes. *Am J Physiol* 259:H230-H242.

128. Ozaki,H., H.Zaizen, T.Kiyosue, M.Nasu, and M.Arita. 1999. Effect of bepridil on intracellular calcium concentration and contraction in cultured rat ventricular myocytes. *J Cardiovasc Pharmacol* 33:492-499.

129. Park,J.S., M.C.Bateman, and M.P.Goldberg. 1996. Rapid alterations in dendrite morphology during sublethal hypoxia or glutamate receptor activation. *Neurobiol. Dis.* 3:215-227.

130. Pascarel,C., F.Brette, O.Cazorla, and J.Y.Le Guennec. 1999. Effects on L-type calcium current of agents interfering with the cytoskeleton of isolated guinea-pig ventricular myocytes. *Exp. Physiol* 84:1043-1050.

131. Pastre,D., H.Iwamoto, J.Liu, G.Szabo, and Z.Shao. 2001. Characterization of AC mode scanning ion-conductance microscopy. *Ultramicroscopy* 90:13-19.

132. Pelkmans,L., J.Kartenbeck, and A.Helenius. 2001. Caveolar endocytosis of simian virus 40 reveals a new two-step vesicular-transport pathway to the ER. *Nat Cell Biol* 3:473-483.

133. Piner.R.D., J.Zhu, F.Xu, S.Hong, and C.A.Mirkin. 1999. "Dip-Pen" nanolithography. *Science* 283:661-663.

134. Pohl,D.W., W.Denk, and M.Lanz. 1984. Optical stethoscopy: Image recording with resolution 1/20. *Appl. Phys. Lett.* 44:651-653.

135. Pollard,T.D., L.Blanchoin, and R.D.Mullins. 2000. Molecular mechanisms controlling actin filament dynamics in nonmuscle cells. *Annu. Rev. Biophys Biomol. Struct.* 29:545-576.

136. Prater,C.B., P.K.Hansma, M.Tortonese, and C.F.Quate. 1991. Improved scanning ion-conductance microscope using microfabricated probes. *Rev. Sci. Instrum.* 62:2634-2638.

137. Premkumar,L.S. 1999. Selective potentiation of L-type calcium channel currents by cocaine in cardiac myocytes. *Mol. Pharmacol.* 56:1138-1142.

138. Proksch,R., R.Lal, P.K.Hansma, D.Morse, and G.Stucky. 1996. Imaging the internal and external pore structure of membranes in fluid: TappingMode scanning ion conductance microscopy. *Biophys J* 71:2155-2157.

139. Putman,C.A., K.O.van der Werf, B.G.de Grooth, N.F.van Hulst, and J.Greve. 1994. Viscoelasticity of living cells allows high resolution imaging by tapping mode atomic force microscopy. *Biophys J* 67:1749-1753.

140. Radmacher,M., R.W.Tillamnn, M.Fritz, and H.E.Gaub. 1992. From molecules to cells: imaging soft samples with the atomic force microscope. *Science* 257:1900-1905.

141. Reid,G.G., J.G.Edwards, G.E.Marshall, R.G.Sutcliffe, and W.R.Lee. 1997. Microvilli elongate in response to hydrogen peroxide and to perturbations of intracellular calcium. *Exp Cell Res* 236:86-93.

142. Reid,R., K.J.Ivey, R.H.Rencoret, and B.Storey. 1976. Fetal complications of obstetric cholestasis. *Br. Med J* 1:870-872.

143. Reyes,H. 1982. The enigma of intrahepatic cholestasis of pregnancy: lessons from Chile. *Hepatology* 2:87-96.

144. Richterova,Z., D.Liebl, M.Horak, Z.Palkova, J.Stokrova, P.Hozak, J.Korb, and J.Forstova. 2001. Caveolae are involved in the trafficking of mouse polyomavirus virions and artificial VP1 pseudocapsids toward cell nuclei. *J Virol.* 75:10880-10891.

145. Rioseco,A.J., M.B.Ivankovic, A.Manzur, F.Hamed, S.R.Kato, J.T.Parer, and A.M.Germain. 1994. Intrahepatic cholestasis of pregnancy: a retrospective case-control study of perinatal outcome. *Am J Obstet Gynecol* 170:890-895.

146. Routkevitch,D., A.A.Tager, J.Haruyama, D.AlMawlawi, M.Moskovits, and J.M.Xu. 1996. Nonlithographic nano-wire arrays: fabrication, physics, and device applications. *Electron Devices, IEEE Transactions* 43:1646-1658.

147. Russell,I.J. and G.P.Richardson. 1987. The morphology and physiology of hair cells in organotypic cultures of the mouse cochlea. *Hear. Res* 31:9-24.

148. Sanchez,D., P.Labarca, and A.Darszon. 2001. Sea urchin sperm cation-selective channels directly modulated by cAMP. *FEBS Lett.* 503:111-115.

149. Sariban-Sohraby,S., M.B.Burg, and R.J.Turner. 1984. Aldosterone-stimulated sodium uptake by apical membrane vesicles from A6 cells. *J Biol Chem* 259:11221-11225.

150. Saviane,C., F.Conti, and M.Pusch. 1999. The muscle chloride channel ClC-1 has a double-barreled appearance that is differentially affected in dominant and recessive myotonia. *J. Gen. Physiol* 113:457-468.

151. Schafer,D.A., M.D.Welch, L.M.Machesky, P.C.Bridgman, S.M.Meyer, and J.A.Cooper. 1998. Visualization and molecular analysis of actin assembly in living cells. *J Cell Biol* 143:1919-1930.

152. Schäffer,T.E., J.P.Cleveland, F.Ohnesorge, D.A.Walters, and P.K.Hansma. 2002. Studies of vibrating atomic force microscope cantilevers in liquid. *J Appl Phys* 80:3622-3627.

153. Schneider,H., M.Fallert, and E.D.Wachsmuth. 1994. Kinetics of intracellular Ca2+ concentration changes and cell contraction of electrically stimulated cardiomyocytes as analysed by automated digital-imaging microscopy. *J Microsc* 175 (Pt 2):108-120.

154. Schneider,M.E., I.A.Belyantseva, R.B.Azevedo, and B.Kachar. 2002. Rapid renewal of auditory hair bundles. *Nature* 418:837-838.

155. Schneider,S.W., P.Pagel, C.Rotsch, T.Danker, H.Oberleithner, M.Radmacher, and A.Schwab. 2000. Volume dynamics in migrating epithelial cells measured with atomic force microscopy. *Pflugers Arch* 439:297-303.

156. Seisenberger,G., M.U.Ried, T.Endress, H.Buning, M.Hallek, and C.Brauchle. 2001. Real-time single-molecule imaging of the infection pathway of an adeno-associated virus. *Science* 294:1929-1932.

157. Serrano,C.J., C.L.Trevino, R.Felix, and A.Darszon. 1999. Voltage-dependent Ca(2+) channel subunit expression and immunolocalization in mouse spermatogenic cells and sperm. *FEBS Lett.* 462:171-176.

158. Shaw,D., J.Frohlich, B.A.Wittmann, and M.Willms. 1982. A prospective study of 18 patients with cholestasis of pregnancy. *Am J Obstet Gynecol* 142:621-625.

159. Shevchuk,A.I., J.Gorelik, S.E.Harding, M.J.Lab, D.Klenerman, and Y.E.Korchev. 2001. Simultaneous measurement of Ca2+ and cellular dynamics: combined scanning ion conductance and optical microscopy to study contracting cardiac myocytes. *Biophys J* 81:1759-1764.

160. Sieczkarski,S.B. and G.R.Whittaker. 2002. Dissecting virus entry via endocytosis. *J Gen. Virol.* 83:1535-1545.

161. Sinniah,K., J.Paauw, and J.Ubels. 2002b. Investigating live and fixed epithelial and fibroblast cells by atomic force microscopy. *Curr. Eye Res.* 25:61-68.

162. Sinniah,K., J.Paauw, and J.Ubels. 2002a. Investigating live and fixed epithelial and fibroblast cells by atomic force microscopy. *Curr. Eye Res.* 24:188-195.

163. Sjovall,K. and J.Sjovall. 1966. Serum bile acid levels in pregnancy with pruritus (bile acids and steroids 158). *Clin Chim Acta* 13:207-211.

164. Smith,P.R., A.L.Bradford, S.Schneider, D.J.Benos, and J.P.Geibel. 1997. Localization of amiloride-sensitive sodium channels in A6 cells by atomic force microscopy. *Am. J. Physiol* 272:C1295-C1298.

165. Sobin,A. and M.Anniko. 1984. Early development of cochlear hair cell stereociliary surface morphology. *Arch. Otorhinolaryngol.* 241:55-64.

166. Sodeik,B., M.W.Ebersold, and A.Helenius. 1997. Microtubule-mediated transport of incoming herpes simplex virus 1 capsids to the nucleus. *J Cell Biol* 136:1007-1021.

167. Sorota,S. 1999. Insights into the structure, distribution and function of the cardiac chloride channels. *Cardiovasc. Res.* 42:361-376.

168. Spencer,C.I., W.Uchida, and R.Z.Kozlowski. 2000. A novel anionic conductance affects action potential duration in isolated rat ventricular myocytes. *Br. J. Pharmacol.* 129:235-238.

169. St John,P.M., L.Kam, S.W.Turner, H.G.Craighead, M.Issacson, J.N.Turner, and W.Shain. 1997. Preferential glial cell attachment to microcontact printed surfaces. *J Neurosci. Methods* 75:171-177.

170. Stang,E., J.Kartenbeck, and R.G.Parton. 1997. Major histocompatibility complex class I molecules mediate association of SV40 with caveolae. *Mol Biol Cell* 8:47-57.

171. Subramaniam,V., A.K.Kirsch, and T.M.Jovin. 1998. Cell biological applications of scanning near-field optical microscopy (SNOM). *Cell Mol. Biol. (Noisy. -le-grand)* 44:689-700.

172. Sun,X.H., F.Protasi, M.Takahashi, H.Takeshima, D.G.Ferguson, and C.Franzini-Armstrong. 1995. Molecular architecture of membranes involved in excitation-contraction coupling of cardiac muscle. *J Cell Biol* 129:659-671.

173. Synge. 1928. *Phil. Mag.* 6:356.

174. Theriot,J.A. and T.J.Mitchison. 1991. Actin microfilament dynamics in locomoting cells. *Nature* 352:126-131.

175. Theriot,J.A. and T.J.Mitchison. 1992. Comparison of actin and cell surface dynamics in motile fibroblasts. *J Cell Biol* 119:367-377.

176. Tilney,L.G. and M.Mooseker. 1971. Actin in the brush-border of epithelial cells of the chicken intestine. *Proc. Natl. Acad. Sci. U. S. A* 68:2611-2615.

177. Tousson,A., C.D.Alley, E.J.Sorscher, B.R.Brinkley, and D.J.Benos. 1989. Immunochemical localization of amiloride-sensitive sodium channels in sodium-transporting epithelia. *J. Cell Sci.* 93:349-362.

178. Tyska,M.J. and M.S.Mooseker. 2002. MYO1A (brush border myosin I) dynamics in the brush border of LLC-PK1- CL4 cells. *Biophys J* 82:1869-1883.

179. Vanderplasschen,A. and G.L.Smith. 1999. Using confocal microscopy to study virus binding and entry into cells. *Methods Enzymol.* 307:591-607.

180. von Ardenne,M. 1938. Scanning Transmission Electron Microscope. *Z. Phys.* 109.

181. Walz,B., O.Baumann, B.Zimmermann, and E.V.Ciriacy-Wantrup. 1995. Caffeine- and ryanodine-sensitive Ca(2+)-induced Ca2+ release from the endoplasmic reticulum in honeybee photoreceptors. *J Gen. Physiol* 105:537-567.

182. Wang,H.W. and M.M.Stack. 2000. The erosive wear of mild and stainless steels under controlled corrosion in alkaline slurries containing alumina particles. *Journal of Materials Science* 35:5263-5273.

183. Wehner,F. 1993. Taurocholate depolarizes rat hepatocytes in primary culture by increasing cell membrane Na+ conductance. *Pflugers Arch.* 424:145-151.

184. Welling,L.W. and D.J.Welling. 1975. Surface areas of brush border and lateral cell walls in the rabbit proximal nephron. *Kidney Int.* 8:343-348.

185. Williams,D.A., L.M.Delbridge, S.H.Cody, P.J.Harris, and T.O.Morgan. 1992. Spontaneous and propagated calcium release in isolated cardiac myocytes viewed by confocal microscopy. *Am J Physiol* 262:C731-C742.

186. Williamson,C., J.Gorelik, B.M.Eaton, M.Lab, M.de Swiet, and Y.Korchev. 2001. The bile acid taurocholate impairs rat cardiomyocyte function: a proposed mechanism for intra-uterine fetal death in obstetric cholestasis. *Clin. Sci. (Colch.)* 100:363-369.

187. Wilson,D.L., R.Martin, S.Hong, M.Cronin-Golomb, C.A.Mirkin, and D.L.Kaplan. 2001. Surface organization and nanopatterning of collagen by dip-pen nanolithography. *Proc. Natl. Acad. Sci. U. S. A* 98:13660-13664.

188. Wilson,N.F. and W.J.Snell. 1998. Microvilli and cell-cell fusion during fertilization. *Trends Cell Biol.* 8:93-96.

189. Yatziv,Y., I.Turyan, and D.Mandler. 2002. A new approach to micropatterning: application of potential-assisted ion transfer at the liquid-liquid interface for the local metal deposition. *J Am. Chem. Soc.* 124:5618-5619.

190. Ying,L., A.Bruckbauer, A.M.Rothery, Y.E.Korchev, and D.Klenerman. 2002. Programmable delivery of DNA through a nanopipet. *Anal. Chem.* 74:1380-1385.

191. You,H.X. and L.Yu. 1999. Atomic force microscopy imaging of living cells: progress, problems and prospects. *Methods Cell Sci.* 21:1-17.

192. Zabner,J., A.J.Fasbender, T.Moninger, K.A.Poellinger, and M.J.Welsh. 1995. Cellular and molecular barriers to gene transfer by a cationic lipid. *J Biol Chem* 270:18997-19007.

193. Zhang,H., l.Wu, and H.Huang. 1999. Electrochemical microprocess by scanning ion-conductance microscopy. *J. Vac. Sci. Technol. B* 17:269-272.

194. Zworykin,V.K., J.Hillier, and R.L.Snyder. 1942. A scanning electron microscope. *ASTM Bull.* 117:15.